Gas-Liquid Separation Using Axial Flow Cyclones

A Thesis Submitted By

Sin Yuan NG

to

The University of Sheffield

for the degree of Doctor of Philosophy

January 2005

University Of Sheffield

Department of Chemical and Process Engineering

Abstract

Work to improve the oil-gas extraction processes from the wellhead to basic saleable product has been a consistent area of study for over 50 years. In this project, it is aimed to develop high capacity plant to obtain low liquid entrainment levels by separating oil droplets from the dispensed gas. Commonly used gas cleaning equipment has disadvantages that inhibit its use in separating oil droplets from gas including excess bulk, too low gas handling capacities, poor separation efficiencies and the need for sophisticated maintenance.

The objective of this research is to focus on one of the more recent manifestations of a basic separation technology, the axial flow gas cyclone incorporating drainage slots in the barrel. The work enables quantitative understanding of the performance of the axial flow cyclone separating liquid droplets as an aid to intensifying oil and gas extraction processes. Experimental work was carried out to obtain the pressure drop – flowrate characteristics, data on the onset of re-entrainment and the droplet separation efficiency of the cyclone tested. Modelling work was also carried out using Computational Fluid Dynamics (CFD) and published analytical models to investigate the feasibility of modelling the pressure drop – flowrate characteristics and the grade efficiency of the tested cyclone. The methodologies to integrate individual tubes into a separating vessel and cyclone optimisation have also been covered.

It was noticed that with the centre body swirler as the swirling device, a frothing zone occurred at low air flowrates. With the occurrence of this zone, re-entrainment was bound to occur. This was the deficiency of this sort of inlet design because the airflow was not strong enough to swirl the liquid. Instead it was only enough to prevent the liquid from falling backwards and this increased the system pressure drop significantly. Therefore, tangentially oriented inlet swirl vanes with four of the slots

used as additional drainage was employed. The frothing zone was then eliminated at low air flowrates. However, at very high air flowrates re-entrainment still occurred which was due to a liquid creeping mechanism and the stripping of liquid film on the cyclone wall.

CFD and the other analytical models were able to predict the cyclone's pressure drop – flowrate characteristics well, however, the agreement of the grade efficiency curves with the experimental data was poor. Comparison of the developed axial flow cyclones with the commercially available cyclone indicated that the Sheffield design performs better in terms of droplet separation efficiency, but at the expense of pressure drop.

Acknowledgements

In order to complete this thesis with quality depends not only on the individual's determination, hard work and persistence, but also on the help and guidance from various parties who in different ways have helped me complete this PhD study. I would like to seize this opportunity to convey my sincere appreciation and gratitude to the following people for their tremendous help, guidance and co-operation in my research.

I would like to express my deepest gratitude to my supervisors; Professor R.W.K. Allen and Dr. G.H. Priestman for their invaluable support, guidance and encouragement in this project. I am indebted to them for their patience and priceless advice. Thanks should also be conveyed to the Engineering and Physical Research Council (EPSRC) and the Overseas Research Student Awards Scheme (ORS) for their financial support to this research project.

In addition, I would also like to acknowledge the technical assistance of Mr. Chris Turner for the construction of the experimental rig and Mr Chris Wright, Dr Tippetts and Dr MacInness for their technical advice. The assistance of Mrs. Anne Foletti, Miss Maria Soto and Mrs. Tracey Trodden is also appreciated.

Last but not least, I would also like to convey my appreciation to all the other research students and member of staff in the department, friends and family members for their useful and constructive suggestions and most importantly their continuous mental support.

Table of Contents

List of Figures

List of Tables

Nomenclature

Symbols	Description	Unit
A	Area	m^2
A_d	Frontal cross-sectional area of a droplet	m^2
a	Inlet height of the reverse flow cyclone tangential inlet	m
b	Inlet width of the reverse flow cyclone tangential inlet	m
C	Cunningham slip correction factor	-
C_D	Drag coefficient	-
CF	Correction factor for anisokinetic flow	-
C_{si}	Solid loading at cyclone inlet	kg solids/ kg gas
d_d	Droplet diameter	m
d_t	Tube inner diameter	m
d_p	Particle diameter	m
D_C	Diameter of the cylindrical section of the reverse flow cyclone	m
D_{ch}	Characteristic length	m
D_{CT}	Diameter of cyclone tube for the axial flow cyclone	m
D_{DE}	Diameter of the underflow aperture of the reverse flow cyclone	m
De	Dean Number	-
D_{VF}	Diameter of vortex finder	m
E_c	Field strength in which particles are charged	volts/meter
E_p	Field strength in which particles are collected	volts/meter
E_{MS}	Single wire efficiency	-
Eu	Euler Number	-
e	Voidage	-

Symbols	Description	Unit
$F_{buoyancy}$	Buoyancy force	N
F_{drag}	Drag force	N
$F_{gravity}$	Gravity force	N
FS	Flow split	%
GE	Grade efficiency	-
g	Acceleration due to gravity	m/s^2
h	Height of cylindrical section of the reverse flow cyclone or height of knitted mesh or height of drainage pipe in the separation vessel	m
H	Height of the entire reverse flow cyclone (cylinder + cone) or Total separation vessel height	m
H_{GS}	Height of gravity settler	m
k	Gas load factor	m/s
l	Length from the lip of vortex finder to the underflow aperture	m
S	Separation distance (distance between the bottom of vanes and the tip of the vortex finder)	m
L	Length	m
L % v/v	Percentage of liquid loading	vol/vol
L_{CT}	Length of cyclone tube	m
L_{GS}	Length of gravity settler	m
L_V	Length of vanes	m
L_{VF}	Length of vortex finder into cyclone tube	m
m_d	Mass of droplet	kg
N_V	Number of vanes	-
N_t	Number of tubes	-
ΔP	Pressure drop	N/m^2
P	Pressure	N/m^2
PT	Pressure tapping	-

Symbols	Description	Unit
q	Particle charge	Coulombs
Q	Volume flow rate	m^3/s
Re	Reynolds number	-
r	Radius	m
Stk	Stokes number	-
s	Distance between the wire and the collecting plate in an electrostatic precipitator	m
t	Time	s
U or V	Velocity	m/s
U_f	Flooding velocity	m/s
U_{GS}	Gas velocity in the gravity settler	m
U_o	Free stream velocity	m/s
U_{probe}	Velocity inside sampling probe	m/s
U_t	Terminal settling velocity	m/s
Q	Volumetric air flow rate	m^3/s
V	Volume	m^3
V_t	Tangential velocity	m/s
VA	Valve controlling the annulus flow	
VC	Valve controlling the centre flow (i.e. vortex finder flow)	
We	Weber Number	-
W	Width	m
w	Migration or drift velocity	m/s

Greek symbols		Unit
δ	Film thickness	m
ε	Permittivity	Coulombs/ volt-meter

Greek symbols		Unit
η	Separation efficiency	%
μ	Viscosity	Ns/m^2
θ	Angle	degree
ρ	Density	kg/m^3
σ	Surface tension	N/m
γ	Dielectric constant	-
π	Constant value = 3.142	-
ϕ	Friction factor	-

Subscripts

A	Annulus
C	Centre
CT	Cyclone tube
cr	Critical
d	Droplet
ESP	Electrostatic precipitator
f	Fluid
g	Gas
GS	Gravity settler
in	inlet
L	Liquid
l	local
M	Knitted mesh
MD	Dry knitted mesh
MW	Wet knitted mesh
mv	Measuring volume
re	Re-entrained liquid
S	Supply
s	Slot or sampling
V	Vane

VF	Vortex finder
w	Wire

Chapter 1

Introduction

1.1 Project Background

This research project was part of a joint industry programme on Intensive Integrated Process Systems for Oil and Gas (IPSO) and was funded by EPSRC. It was developed as an integrated package with a number of other projects to address the issues surrounding the subsea processing of wellhead fluids (See Figure 1.1). It is aimed to design high capacity equipment and to obtain very low liquid entrainment levels in the separation of oil from dispensed gas. The gas rich stream from the pre-separator is treated in a cyclonic gas-liquid separator. The novel design that has been developed is based on a set of axial flow cyclones operating in parallel in a large separating vessel. Pre-conditioners are also used in this application. A pre-conditioner is a device prior to the axial flow cyclones and in this project a knitted mesh pad has been used. When the liquid loading is high the mesh tends to flood, hence the cyclones are required for the separation. Therefore, the cyclones have to be properly designed for satisfactory performance (i.e. to increase the system throughput and enhance the droplet separation efficiency). In this project, axial flow cyclones were tested operating with an air-water system. The following sections give an introduction to demisting and also to axial flow cyclones.

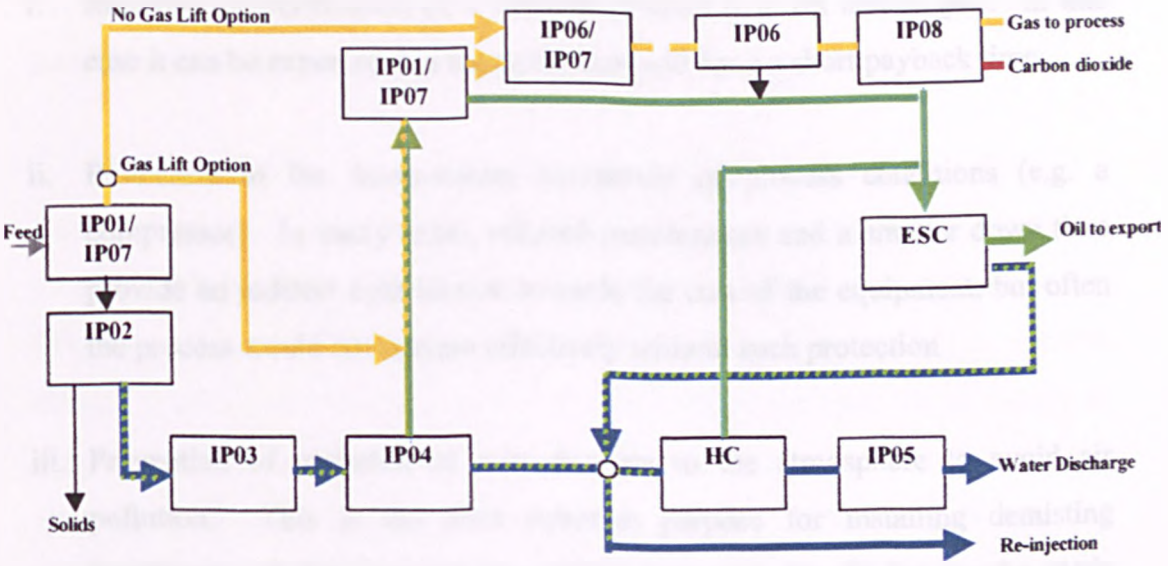

PROJECTS

IP01	Detection and Control of Multiphase Flow for the Initial Separation Stage of Advanced Phase Separators
IP02	Solids Handling in Advanced Phase Separators
IP03	Kinetics of Breakdown of Dispersions in Multiphase Flows in Pipes and Fittings. Application to a pre-coalescer
IP04	Subsea Operation of a Centrifugal Separator
IP05	Chemical Management Strategy for Produced Water Injection
IP06	Axial Flow Cyclones for Gas-Liquid Separation
IP07	Smart Process Sensors for Field Monitoring
IP08	Separation of CO_2 from Natural Gas and Conversion to Methanol

KEY

Black = solids
Blue = water
Yellow = gas
Green = oil
C = CO_2
HC = Hydrocyclone
ESC = Electro-Static Coalescer

Figure 1.1: Projects involved in the IPSO programme.

1.2 The Need for Demisting

In most chemical process plants where gases and liquids flow within the same vessel, the liquid becomes entrained into the gas. Therefore removal of the droplets (demisting) is required to avoid plant failure. "Demisting" is a separation process where liquid droplets and gas are made to move in different directions as a result of the droplets' inertia. It involves two phases and is distinct from gas purification in which two components of the same phase are separated. There are a number of possible benefits of installing demisting equipment and these are **(Allen, 2001)**:

i. Recovery or purification of a valuable product (e.g. oil and/or gas). In this case it can be expected that the equipment will have a short payback time.

ii. Protection of the down-stream equipment or process conditions (e.g. a compressor). In many cases, reduced maintenance and a smaller down time provide an indirect contribution towards the cost of the equipment, but often the process would not operate effectively without such protection.

iii. Prevention of emission of mist droplets to the atmosphere to avoid air pollution. This is the least common purpose for installing demisting equipment. It involves the least direct economic benefit but maybe made necessary by environmental regulations, concern for public relations and the legal requirements regarding air pollution.

In this project, dispensed gas has been looked at in the context of high capacity equipment requiring very low liquid entrainment levels. Therefore the equipment should be compact and able to exhibit high gas handling capacity as well as having a low maintenance requirement. It is also beneficial if the equipment can handle a broad range of liquid to gas ratios, and have a broad tolerance to changes in inlet droplet size distribution and flow rate. Hence, it has been the purpose of this research to investigate equipment, i.e. the axial flow cyclone, which can perform at the required level.

1.3 Different Types of Cyclones

There are basically two types of cyclones; the conventional reverse flow cyclone (See Figure 1.2) and the axial flow cyclone (also known as straight-through cyclone), the former being more frequently used. A typical axial flow cyclone with the commonly used nomenclature is shown in Figure 1.3.

In an extensive survey of cyclones, **Stern *et al.* (1955)** defined a cyclone in general terms as follows:

"Structurally, a cyclone must have an axial gas outlet, a discharge and a means for gas inlet which will produce the gas rotation necessary to create the vortex. These three elements may be combined in a number of different ways. Rotation may be produced by tangential gas entrance or by axial gas entrance through a set of swirl vanes. Separated dust may be removed either axially or tangentially from the periphery. Dust may be removed from either the end opposite to the axial gas outlet or from the same end. There may be one or a multiplicity of tangential inlets. The cyclone body may be completely cylindrical, completely conical or made of both cylinders and cones. The gas outlet may be either cylindrical or conical."

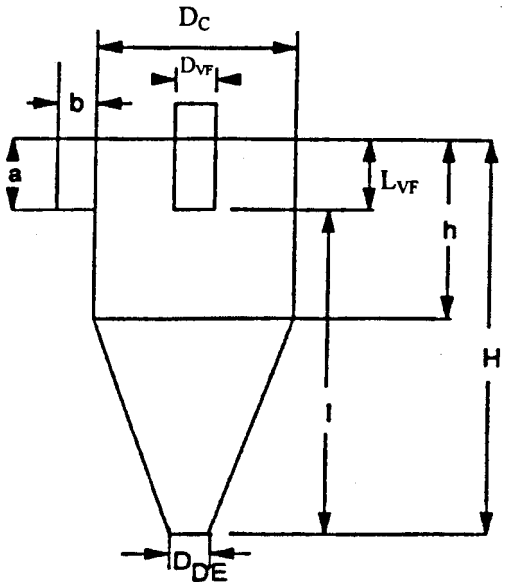

Figure 1.2: A typical conventional reverse flow cyclone.

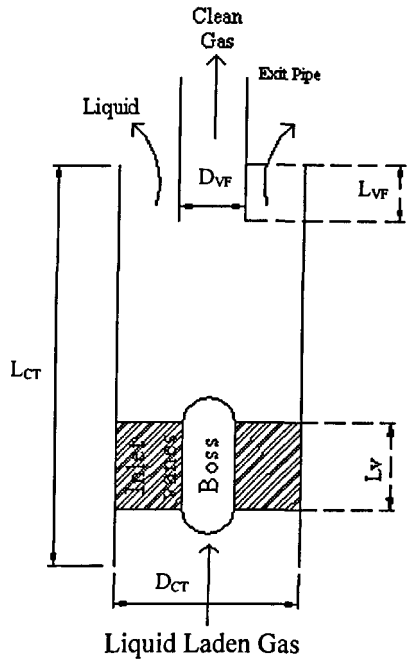

Figure 1.3: A typical axial flow cyclone.

The reverse flow cyclone **(Jackson, 1963; Phillips *et al.*, 1992)** got its name because the flow reverses its direction. The opening of the apex of the truncated cone serves as the underflow nozzle and a tube, extending partially into the centre of the cylindrical section, serves as the overflow nozzle, i.e. the vortex finder. The clean gas leaves through the vortex finder and the particles or liquid droplets leave at the opposite end through the underflow. A scroll type inlet is usually used if friable particles are present in the system so that the particles would not be broken or smeared upon entry. Also, with a scroll inlet, the dust laden gas is introduced into the cyclone smoothly, hence sticky particles would tend to stick less to the cyclone wall and erosion problems are minimised.

For an axial flow or straight-through-flow cyclone **(Gauthier *et al.*, 1990; Jackson, 1963; Stenhouse and Trow, 1979; Sumner *et al.*, 1987)**, the fluid enters at one end and leaves at the opposite end of the cyclone. The axial entry has obvious advantage of construction when many small cyclones are to be nested together. The drawback is the lower dust collection efficiency, which is attributed to lower level of swirl in practical operation.

The general principle of gas-liquid separation is identical for both the cyclones. The main object of a cyclone is to create a vortex, which will centrifuge the liquid droplets radially outwards to the walls, where they are separated. The major distinction is in the flow direction of the clean gas.

Demisting cyclones are distinguished from conventional gas cyclones collecting solid particles by the behaviour of the coalesced liquid film once the droplets have been deposited upon a surface. Solid particles will bounce back upon hitting the wall whereas liquid droplets tend to stick onto the wall upon hitting it. As a result, it is believed that if correctly designed, axial flow cyclones can provide intensive processing by exhibiting high gas handling capacities per unit volume of plant. They are relatively easy to scale up once the fundamental performance limitations of a particular geometry are understood. Hence, axial flow cyclones are regarded as the most desirable option for the gas-liquid separation considered in this project.

1.4 Proposed Demisting System

Normally, knitted meshes are used for demisting purposes. Although they are currently the primary gas demisting method employed in oil-gas production facilities, their use is limited to low superficial gas velocities and they have a tendency to flood under high loadings. To counteract these deficiencies, it is proposed to include a cyclone in a hybrid system. This is seen as a way to increase the turndown ratio while retaining the advantages of being cheap, reliable, easy to maintain and safe. In the proposed application, a set of axial-flow cyclones is to be operated in parallel inside a large vessel (Refer to Figure 1.4). An initial layer of mesh is provided immediately following the gas inlet. The cyclone tubes clean up any droplet carryover from this primary mesh. The mesh is intended to perform the required separation under conditions of low liquid or gas loading. At higher loading it can become inefficient or flooded and hence further downstream separation is then required by a combination of cyclone unit and a second mesh

layer. Clean gas in the vortex finders can bypass the second mesh layer, reducing velocity through it, and hence its propensity to flood. This requires flexibility in the design to control the flow split.

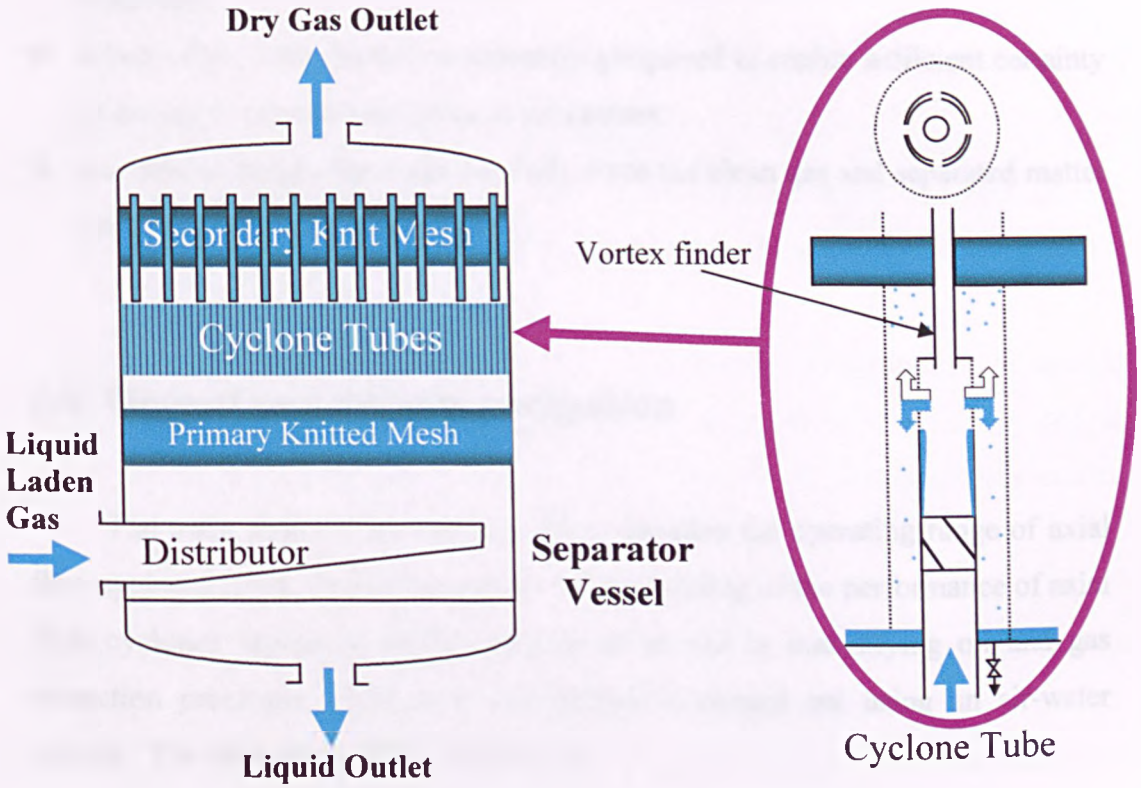

Figure 1.4: The proposed overall demisting system.

1.5 Benefits and Limitations of Axial Flow Cyclones

Axial flow cyclones are chosen to separate gases and liquid because

- ❖ they are relatively cheap compared to other separators.
- ❖ they are easily constructed with no moving parts and hence have easy maintenance.
- ❖ they are relatively easy to scale up once the fundamental performance limitations of a particular geometry are understood.
- ❖ they are more compact compared to conventional cyclones.
- ❖ if correctly designed, they can provide intensive processing by exhibiting high gas handling capacities per unit volume of the plant.

The present barriers to their application in compact or sub sea systems are

- a narrow operating range in respect of inlet drop size of the dispersion to be separated.
- a lack of the fundamental understanding required to enable sufficient certainty in design to provide performance guarantees.
- the need to design the outlet carefully since the clean gas and separated matter are taken off close to each other.

1.6 Objectives of this Investigation

The main aims of this research are to broaden the operating range of axial flow cyclones and to enable quantitative understanding of the performance of axial flow cyclones separating liquid droplets as an aid to intensifying oil and gas extraction processes. However, this project is carried out using an air-water system. The objectives of this research are:

i. to enable quantitative understanding of the performance of axial flow cyclones collecting liquid droplets as a function of drop size (grade efficiency data),
ii. to provide a model which allows predictions of the effects of cyclone geometry changes upon the low loading cyclone grade efficiency performance,
iii. to provide quantitative data on the on-set of re-entrainment in axial flow cyclones,
iv. to provide quantitative data on the axial flow cyclone pressure drop-flow rate characteristics and to investigate possible ways of extending the cyclone turndown ratio by improving on the air flow split and the separation efficiency through design modifications,
v. to acquire a realistic cyclone design for a separator system and investigate the integration of all the individual tubes into a large separation vessel so that the demisting system would work effectively over a wide range of throughputs.

1.7 Thesis Overview

Following this introductory chapter, the contents of the remaining chapters are briefly described below:

Chapter 2: This chapter reviews the work that has been undertaken by other researchers using cyclones. The findings from the literature on experimental and theoretical work concerning cyclones are outlined.

Chapter 3: This chapter describes the experimental programmes conducted within the course of this research giving details of the rig design, operating procedures and aim of each of the investigations carried out.

Chapter 4: The geometry of the axial flow cyclones studied went through a broad range of changes during the course of the project. The first few designs were similar with modification of slot dimensions and positions, which did not produce a design that met the set requirements. Consequently, a major change was made to the inlet swirling device. This chapter details the evolutionary changes that took place.

Chapter 5: The discussion of the experimental results on flooding/re-entrainment tests for the initial tested cyclone geometry.

Chapter 6: The discussion of the experimental results on flooding/re-entrainment tests for the modified cyclone geometries.

Chapter 7: The discussion of the experimental results of the grade efficiency tests for the most successful geometry tested in the flooding/re-entrainment tests.

Chapter 8: This chapter reports the numerical work carried out using Computational Fluid Dynamics and also comparing the work of other investigators with the findings obtained in this project.

Chapter 9: This covers the integration of individual cyclone tubes into a large demisting vessel, which involves calculations to determine the number of tubes to be fitted into the vessel and this requires consideration of the tube layout and tube pitch (i.e. the distance between one cyclone tube to another). The throughput for the specific cyclone design is reported here as well.

Chapter 10: Lastly, the conclusions drawn from this investigation and recommendations made for future work are outlined in this chapter.

Chapter 2

Literature Review of Demisting Technologies

2.1 Introduction

In this chapter, a range of demisting equipment will be discussed, focussing on previous work done on cyclones, axial flow cyclones in particular. The emphasis will be on the reason for employing axial flow cyclones over the other types of gas-liquid separators in the context of this research project, which focuses on the oil and gas industry. The wellhead fluids (fluids that are pumped out from the seabed) consist of crude oils, natural gas and natural gas liquids. Usually the removal of liquids from the natural gas, which consists primarily of methane, is carried out in two stages. The first stage is wellhead separation, which takes place under high pressure. At this stage, to prevent erosion, the crude oils (consisting mainly of hydrocarbon chains containing five carbon atoms or more) and the solids have to be removed before passing the fluids further downstream. When the fluids move further downstream, the decrease in pressure and temperature causes more liquid to condense (i.e. natural gas liquids or condensate that consists of two to four carbon atoms) and this is when second separation stage becomes important. It is of interest to install separation equipment that can handle large amount of fluids and can also separate the liquids from the gas efficiently into basic saleable forms. The equipment has to work efficiently in separating the fluids both in bulk and in the form of mists.

The separation of liquids from gas can be carried out either on- or offshore. For offshore applications, extra demands on the size and weight of a separator will be imposed. Hence, the focus of this work is on the separation of liquid from gas in an environment where compactness, high capacity and low maintenance equipment are essential features of design so that it is suitable for both on- and offshore applications. The definitions of the operating characteristics that will be

used to judge the capability and suitability of the various types of separators are listed below.

- *Throughput (size)*

Some separators can handle larger amount of gas flow at a certain size than others. Compactness (size and weight) is very important especially for offshore applications since it is preferred to have a small and light separator on the platform that will perform equally well if not better than the larger ones.

- *Pressure Drop*

Pressure drop across the separator determines the energy required to run the equipment, hence the operating cost. In cases where pressure drop is critical, it will be beneficial to be able to predict it and in most situations there are empirical correlations that could be used for certain geometries. This will be discussed later in Section 2.7.1.

- *Separation Efficiency*

The separation efficiency depends on the droplet size distribution, the physical properties of the gas and the liquid, the liquid and gas flows and the geometry of the separator. It is usually defined in gravimetric term as the ratio of the liquid captured in the separator to the liquid going into the separator. The effect of drop size is described through the use of a grade efficiency curve. This will be further discussed in Section 2.7.2.

- *Capital and Running Costs*

The cost invested in any piece of equipment is of concern in any industry. It has a strong influence on the selection of the separator for certain applications. Capital cost is usually associated with the size, construction technique, installation difficulties, and so on of the separator and the running cost is associated with utilities, maintenance and so on. It is always desirable to choose a separator with the lowest balance of capital and running costs that will perform the required tasks for maximum profit.

Minimum capital costs involve smaller equipment, which will give higher separation efficiency due to higher inlet gas velocities. However, at higher velocities most types of demisters will have higher pressure drops and may flood, hence re-entraining the collected liquid and reducing efficiency. Therefore, a trade-off in the design needs to be reached to meet the target of the gas cleaning process. These important parameters will be discussed in this chapter. The basic gas-liquid separation mechanisms are briefly discussed in the following section.

2.2 Gas – Liquid Separation Mechanisms

Generally, a droplet is considered to be separated from the gas when it comes into contact with obstacles in the gas flow or when it hits one of the walls of the separator in which the fluid flows and is drained from the separator. To do this the droplet has to be subjected to external forces large enough to separate it from the gas stream during its residence time in the control unit. The particle transport mechanisms can be divided into six categories namely gravitational settling, centrifugal separation, inertial impaction, direct interception, diffusion and electrostatic migration.

- *Gravitational Settling*

This is the simplest form of gas-liquid separation using the influence of gravity. Larger particles moving slowly enough in a gas stream can be overcome by gravity and be collected (See Figure 2.1). Gravity settling chambers separate droplets utilising this mechanism. When large assemblies of droplets are present, this enhances separation because of the heavier mass of the liquid (i.e. faster settling rate) and also there is a high tendency of droplet agglomeration occurring producing more larger droplets, hence higher efficiency. More details on gravity settling will be discussed in Section 2.3.1.

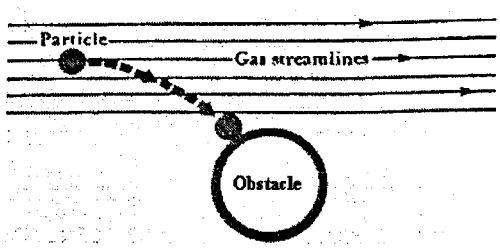

Figure 2.1: Gravitational Settling (Mycock *et al.*, 1995).

- *Centrifugal Separation*

The shape or curvature of the separator causes the gas stream to move in a spiral motion. Droplets that are in this centrifugal field will tend to travel in a straight line due to their inertia and move towards the outer wall of the separator by virtue of their momentum as shown in Figure 2.2. This is the main mechanism responsible for the droplet collection in a cyclone (See Section 2.3.5).

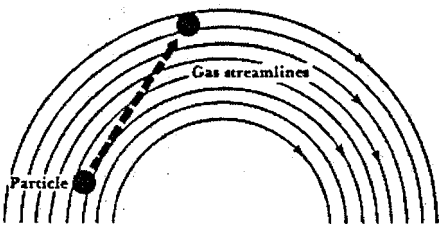

Figure 2.2: Centrifugal Separation (Mycock *et al.*, 1995).

- *Inertial Impaction*

When a gas 'sees' an obstacle in a laminar flow, it moves in streamlines around the obstacle. Droplets that are carried along at approximately the same gas velocity might not necessarily follow the streamlines around the obstacle, hence impacting on it even though the gas and the smaller droplets tend to diverge and pass around the obstacle (See Figure 2.3). Inertial impaction usually occurs in knitted mesh pads and vane separators (See Section 2.3.2 and 2.3.4). In turbulent gas flow, the droplets may also be regarded locally as if they are in a laminar regime because the slip velocity between the gas and the droplets is small.

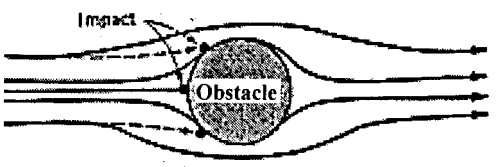

Figure 2.3: Inertia Impaction (Wark *et al.*, 1998)

The particle equation of motion is the equation, which results when the Newton's second law is applied to the motion of the small particles. Usually they can be considered small enough for Stokes drag law to apply. From Newton's second law in the vertical direction (y vertically downwards), the particle equation of motion may be expressed as in Equation 2.1.

Mass of particle x acceleration = Fluid drag + Body force

$$\frac{\pi d_p^3}{6}\rho_p\frac{dU_y}{dt} = -3\pi d_p \mu U_y + \frac{\pi d_p^3}{6}(\rho_p - \rho_g)g \qquad \textbf{- Equation (2.1)}$$

This equation can be made dimensionless by putting $U_y^* = U_y/U$, $t^* = tU/D_{ch}$ and $g^* = gD_{ch}/U^2$ in Equation (2.1) where U is the undisturbed gas velocity (i.e. mean velocity before passing the obstacle) and D_{ch} is the characteristic length and in the case of a cyclone, it is the cyclone diameter. The dimensionless particle equation of motion with the Stokes Number term is expressed as Equation (2.2). The Stokes Number is widely used to scale up similar geometries.

$$Stk\frac{dU_y^*}{dt^*} = -U_y^* + Stk\,g^* \qquad \textbf{- Equation (2.2)}$$

where $Stk = d_p^2(\rho_p - \rho_g)U/18\mu D_{ch}$

- *Direct Interception*

In direct interception, some of the smaller droplets, even though their centre may follow the gas streamlines around the obstacle, may also contact the obstacle (shown in Figure 2.4) if the distance between the droplet centre and the surface of the obstacle is less than the particle radius. This mechanism also occurs in a knitted mesh pad.

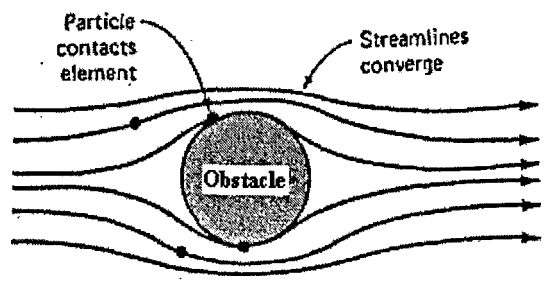

Figure 2.4: Direct Interception (Wark *et al.*, 1998).

- *Diffusion*

Collection by diffusion, better known as Brownian motion (Figure 2.5), usually occurs with very small droplets (usually < 1 μm). These droplets are so small that they become affected by collision of molecules in the gas stream. These droplets move randomly or diffuse through the gas to impact on the obstacle.

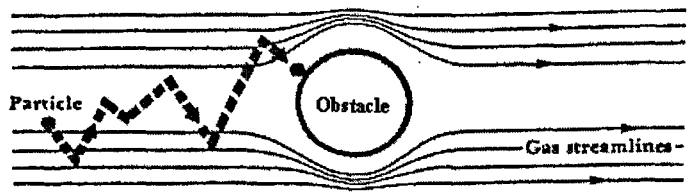

Figure 2.5: Diffusion (Mycock *et al.*, 1995).

- *Electrostatic migration*

Another collection mechanism involves electrostatic forces. The droplets can be naturally charged or be charged by subjecting the droplets to a strong electric field. These particles migrate to an opposing charged collection surface. Electrostatic precipitators (ESPs) employ this mechanism to separate out the droplets from the gas (See Section 2.3.3). However, when the inlet burden is high, special care is required in the ESPs design and operation.

2.3 Gas – Liquid Separation

The earliest demisters were packed beds **(Robinson, 1985)**. They were used to remove entrained droplets from plant discharges. They have the disadvantages that they are large, and have high capital and maintenance cost, as the beds require frequent cleaning and media changing. Over the years, a wide range of alternative demisting equipment has become available. The selection depends on the drop size range of the liquid in the gas. To set the context of this research, an assessment of other types of gas cleaning equipment will be presented.

2.3.1 Gravity Separators

Gravity settlers are widely used as first stage separators to separate out the bulk of the liquid from the gas in the oil industry because of their simplicity and effectiveness. However, they are most suitable for the separation of droplets larger than about 50 μm. Settling chambers are one of the oldest, simplest and also cheapest form of industrial gas-cleaning equipment. The system pressure drop is relatively low (major contribution will be the entrance and exit losses) for a typical horizontal flow gravity settling chamber (Figure 2.6). For a baffle chamber the pressure drop is higher due to the slightly more complicated internal design. Gravity separators operate by allowing the gas to expand into a large chamber via a nozzle, reducing the velocity considerably. Hence, increasing the residence time

of the liquid promoting better separation. The separated liquid and clean gas leave the separator via different nozzles. The denser fluid will fall to the bottom while the lighter fluid rises to the top. The separation is under the action of gravity at a rate dependent on the density and size of the droplets and also upon the physical properties of the suspending gas (viscosity and density). Theoretically, the minimum droplet size that has 100 % efficiency in laminar flow can be determined in the following manner **(Mycock *et al.*, 1995; Robinson, 1985; Wark *et al.*, 1998)**.

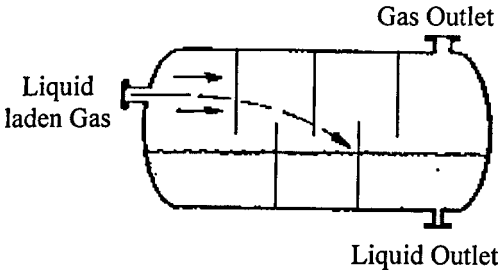

Figure 2.6: A horizontal gravity settling chamber.

The time, t, required for a droplet of diameter, d_d, to fall a distance, H_{GS}, and collected is equal to or less than the time required to move horizontally a distance, L_{GS} (i.e. droplet settling time ≤ droplet residence time) as expressed in Equation (2.3). Therefore,

$$t = \frac{H_{GS}}{U_t} = \frac{L_{GS}}{U_{GS}} \qquad \textbf{- Equation (2.3)}$$

where

U_{GS} = gas velocity in the gravity settler (m/s)

U_t = terminal settling velocity (m/s)

The terminal settling velocity, U_t, for droplets is defined as the constant downward speed that a droplet attains in a direction parallel to the Earth's gravity field as it overcomes the forces due to buoyancy and frictional drag. The force balance on a droplet can be written as follows (Equation 2.4):

$$F_{drag} + F_{buoyancy} = F_{gravity} \qquad \textbf{- Equation (2.4)}$$

The gravity force is the weight of the droplet, $F_{gravity} = m_d g$. The buoyancy force is equal to the weight of the displaced gas, $F_{buoyancy} = \rho_g V_g g = (\pi d_d^3/6)\rho_g g$. The drag force is the resistive force exerted by the gas on the droplet, $F_{drag} = \rho_g A_d U_t^2 C_D/2$ where C_D = drag coefficient and A_d = frontal cross-sectional area of the droplet = $\pi d_d^2/4$. Hence, the overall force balance in Equation (2.5) becomes:

$$\rho_g \frac{\pi d_d^2}{4}\frac{U_t^2}{2}C_D + \frac{\pi d_d^3}{6}\rho_g g = \frac{\pi d_d^3}{6}\rho_d g \qquad \textbf{- Equation (2.5)}$$

and rearranging Equation (2.5) gives the terminal settling velocity, U_t, expressed as Equation (2.6).

$$U_t = \sqrt{\frac{4}{3}\frac{d_d g(\rho_d - \rho_g)}{\rho_g C_D}} \qquad \textbf{- Equation (2.6)}$$

In the Stokes' regime (i.e. Droplet Reynolds number, $Re_d < 0.2$), $C_D = 24/Re_d$ where $Re_d = \rho_g U_t d_d/\mu_g$. Substituting C_D into Equation (2.6) and rearranging it gives an estimation of the minimum droplet size with 100 % separation efficiency expressed as Equation (2.7).

$$d_{d,min} = \sqrt{\frac{18\mu_g U_t}{g(\rho_d - \rho_g)}} \qquad \textbf{- Equation (2.7)}$$

and from Equation (2.3) $U_t = H_{GS}U_{GS}/L_{GS}$, Equation (2.7) becomes:

$$d_{d,min} = \sqrt{\frac{18\mu_g H_{GS} U_{GS}}{g(\rho_d - \rho_g)L_{GS}}} \qquad \textbf{- Equation (2.8)}$$

From Equation (2.8), it can be seen that to make the minimum particle size removed with 100 % efficiency smaller, the value of H_{GS}/L_{GS} has to be reduced (i.e. having a low and long chamber). This will take up a lot of space, which is not

desirable especially in offshore applications. However, baffle plates can be put across the chamber for a shorter and higher chamber. Although more efficient, it is more costly to construct and more difficult to clean which again is not desirable for demisting for offshore applications. The above prediction is for laminar flow inside the gravity settler. Details on separation efficiency for turbulent flow can be obtained from **Mycock *et al.* (1995); Svarovsky (1981); Wark *et al.* (1998); Zhao and Pfeffer (1997).** In turbulent flow, with mixing taking place this prevents the settling of particles except those entering the laminar boundary layer at the bottom of the chamber **(Svarovsky, 1981).** Assuming a well-mixed flow region (i.e. uniform droplet distribution exists for all particle sizes in any cross-section perpendicular to the flow) and performing a mass balance for a differential length, dx, of the settler, the change in droplets flux in the horizontal direction must be equal to the settling flux through the boundary layer as expressed in Equation (2.9) **(Wark *et al.*, 1998).**

$$\frac{dN_p}{N_p} = -\frac{U_t dx}{U_{GS} H_{GS}} \qquad \textbf{- Equation (2.9)}$$

where

dN_p/N_p = fraction of the total number of droplets of size d_p that reaches the laminar sublayer and removed while flowing in a distance dx.

dx/U_{GS} = time required for the main flow to travel a distance dx with U_{GS} is the gas velocity in the gravity settler.

Integrating Equation (2.9) at $x = 0$, $N_p = N_{p,0}$ and at $x = L_{GS}$, $N_p = N_{p,L_{GS}}$ leads to Equation (2.10).

$$N_{p,L_{GS}} = N_{p,0} \exp\left(-\frac{U_t L_{GS}}{U_{GS} H_{GS}}\right) \qquad \textbf{- Equation (2.10)}$$

The fractional collection efficiency of droplet size d_p is expressed as Equation (2.11).

$$\eta_p = 1 - \frac{N_{p,L_{GS}}}{N_{p,0}}$$
$$= 1 - \exp\left(-\frac{U_t L_{GS}}{U_{GS} H_{GS}}\right)$$

- Equation (2.11)

Conventional gravity separators are judged to be too bulky, having a low gas handling capacity, hence they must be very large in order to reduce the gas sufficiently enough for the finer droplets to settle. Therefore when it comes to demisting (separation of droplets smaller than 20 microns, which is the interest of this project), the gravity separators are not the solution.

2.3.2 Vane Separators

Vane separators (Figure 2.7) are also one of the more traditional means of mist removal used in the oil industry. They generally consist of a labyrinth of narrowly spaced uniformly corrugated plates positioned in parallel to the direction of the gas flow. They operate by diverting the gas stream several times introducing changes in the gas flow direction. The heavier liquid droplet will not follow the gas streamlines. It tends to move in a straight line due to its inertia, and hence impinges onto the vanes (inertial impaction). As more droplets impinge on the walls of the demister, the liquid will drain in a counter-current manner if the gas flow is in the vertical direction. If the gas flow is horizontal, the drainage will occur perpendicularly to the flow.

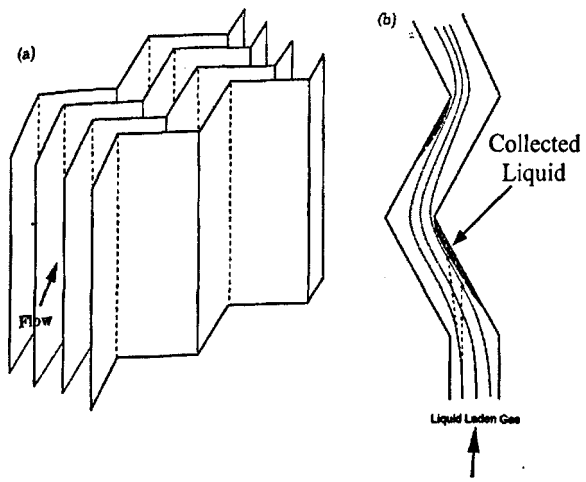

Figure 2.7: (a) Basic structure of a vane type separator. (b) Liquid separated from the gas stream in a vane type separator (Wang and Davies, 1996).

It is clearly seen from the Stokes Number (Equation 2.2) that if the operating pressure is increased, the gas density will increase and for the same Stokes Number the grade efficiency curve will shift to the right meaning a decrease in the separation efficiency because of the smaller density difference.

At low gas flowrates, collection efficiency will decrease due to the decrease in inertial impaction efficiency and at high gas flowrate the collection efficiency will reduce due to increased re-entrainment. The re-entrainment mechanism of vane separators basically occurs at the tip of the corrugated plates (See Figure 2.8). The separated liquid gets torn off due to the shear forces exerted by the gas on the liquid. As the gas density increases, the maximum gas velocity has to decrease (See Equation 2.12) in order to avoid re-entrainment. This equation used by Calvert, as quoted by **Swanborn (1988)**, to determine the maximum gas velocity allowable before re-entrainment occurs.

$$U_{g,max} = \sqrt{\frac{\sigma \cos\theta}{\rho_g \delta}} \qquad \textbf{- Equation (2.12)}$$

where δ is the thickness of the liquid film and θ is the angle between the vane to the horizontal axis.

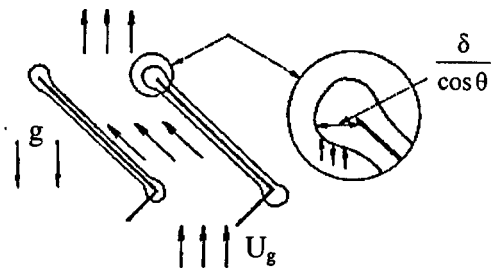

Figure 2.8: Re-entrainment on vane edges (Swanborn, 1988).

Additionally when low surface tension fluids are being separated, the maximum allowable gas velocity drops, hence giving a lower turn down ratio. This is the problem generally seen with vane packs at higher operating pressures and temperatures because surface tension decreases with temperature rise, which is a very common operating condition in the oil and gas industry. Since gas viscosity increases with temperature, this will decrease the separation efficiency for the same Stokes number.

A very common way of predicting the collection efficiency of a vane type separator is to estimate the efficiency of a single bend and add up the cumulative effect of all bends. Investigations on predicting collection efficiency of the vane separators have been carried out by various researchers: Calvert and Bürkholtz developed the turbulent mixing model and Gardner developed the laminar flow model as quoted in **Robinson (1985)**. Alternatively, computational fluid dynamics (CFD) can be used to predict the performance of the vane separator. Recently, **Wang and Davies (1996)** have used this method to study the influence of rear pockets, bend angle (α) and flow velocity on the pressure drop and the separation of mists from gases. The authors found that rear pockets (See Figure 2.9) can greatly improve the performance of the vane type separators compared to increasing the bend angle, α, in terms of both the separation efficiency and the pressure drop. For the tested vane geometry, the separation efficiency increases as the flow velocity increases until a value (say 'x' m/s) where the efficiency does not increase much with the flow velocity, but the pressure drop increases greatly. Therefore, the gas flow in this geometry should not exceed 'x' m/s since it increases the pressure drop significantly without improvement in the separation efficiency.

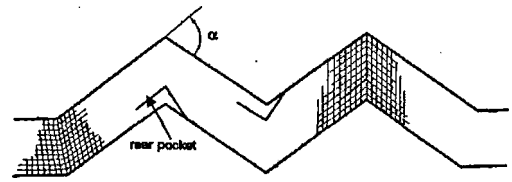

Figure 2.9: Vane type separator with rear pockets (Wang and Davies, 1996).

The pressure drop for the vane separators is low which is around 5 – 10 mbar for air-water system under atmospheric condition. The cut size, d_{50}, obtained from these separators is typically between 7-20 μm depending on the design and the physical properties of the gas and liquid **(Swanborn, 1988)**. However, both the pressure drop and the cut size will increase if operating under high pressure. Due to these reasons, they are not considered in the demisting process of this project.

2.3.3 Electrostatic Precipitators (ESPs)

The electrostatic precipitator (Figure 2.10) is an apparatus consisting of a corona electrode (usually a wire) and a collection plate (usually a large surface electrode or a tube), which cleans gases by using electrostatic forces to remove the solid or liquid particles suspended in a gas stream. It is used in cement plants, pulp and paper industry, steel plants and coal-fired power stations in separating fly ash **(Allen, 2001)**. In this equipment, an electrostatic field is set up by applying a high voltage across an electrode system. Both the charging and collection processes are strongly dependent on the electric field established in the precipitator.

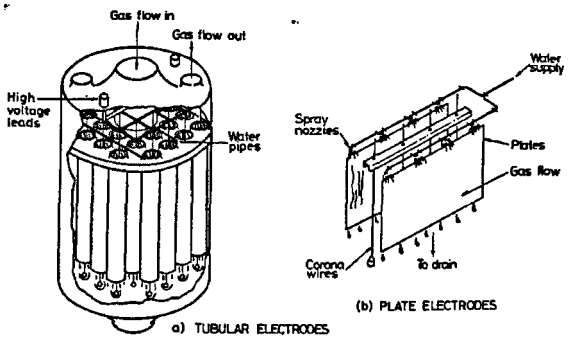

Figure 2.10: Irrigated ESPs (Robinson, 1985).

There are four distinct stages to electrostatic precipitation. First, the particles are given an electric charge. Secondly they are passed through an electric field in order to apply a precipitating force on them. Thirdly, they are captured and agglomerated on to the collecting surface, normally an electrode. Finally, the particles are removed from the electrode surface, usually by vibration or by washing, so that other particles may be collected.

Particle charging is accomplished by means of a corona electrode, which produces ions that become attached to the particles. The electrons near the wire are accelerated to a velocity sufficient to cause ionisation of the gas upon collision, producing a positive ion and an additional free electron. The electrons leave the corona region and enter the interelectrode region. When these electrons impact on the gas molecules in the interelectrode region negative gas ions are created and these negative ions serve as the principal mechanism for charging the particle. As the negative gas ions move towards the collection electrode, they will collide with and become attached to the suspended particles in the gas stream along the way.

The collected particles can be removed by periodic rapping (i.e. short sharp blows) or by coalescing and draining for liquids.

The charged particle migrates to the collection electrode and this movement is termed the migration velocity or the drift velocity, w. The migration velocity is expressed as Equation (2.13).

$$w = \frac{qE_p}{3\pi\mu_g d_p} = \frac{p\varepsilon E_c E_p d_p}{3\mu_g} \qquad \textbf{- Equation (2.13)}$$

where

q = particle charge (Coulombs) = $p\pi\varepsilon E_c d_p^2$

$p = 3\gamma/(\gamma + 2)$, γ = dielectric constant

ε = permittivity (Coulombs/volts-meter)

E_c = field strength in which particles are charged (volts/meter)

E_p = field strength in which particles are collected (volts/meter)

d_p = particle diameter (m)

μ_g = gas viscosity (Ns/m^2)

Equation (2.13) shows that the migration velocity is sensitive to the field strength (appearing twice). It is directly proportional to the particle diameter and inversely proportional to the gas viscosity. It is desirable to have high migration velocity, therefore larger particles are collected more easily than smaller ones. Gas viscosity increases with temperature, hence reducing the migration velocity, which is undesirable. Equation (2.13) is valid for particles in the Stokes' flow regime (i.e. $Re_p < 1$). When $Re_p > 1$, the prediction of the migration velocity will deviate. Nevertheless, this theoretical equation is useful in predicting the performance of the electrostatic precipitator.

When particles are deposited onto the collecting electrode, the knowledge of the particle resistivity is important to determine the resistance of the collected particle layer to the flow of the electric current. Particles with low resistivity (between 10^4 to 10^7 ohm·cm) are difficult to collect because they loose their charge upon arrival at the collection electrode **(Mycock *et al.*, 1995)**. Thus

insufficient electrostatic charge remains on the collected particles to hold them together. Re-entrainment into the gas stream results and collection efficiency suffers. Examples of low resistivity dusts are unburned carbon in fly ash and carbon black **(Mycock *et al.*, 1995; Wark *et al.*, 1998)** and low resistivity liquids are water, ethanol and crude oil **(Lees, 1996)**. High resistivity particles (above 10^{10} ohm·cm) are difficult to charge and once they are charged, they do not readily give up their charges upon arrival at the collection electrode **(Mycock *et al.*, 1995)**. A phenomenon referred to as back corona can occur whereby localised electric fields in the particle layer become sufficiently strong that they cause a positive corona discharge. Any positive ion formed will tend to migrate away from the collector electrode reducing both the space charge and also the charge on the particles. This prohibits collection of the particles, hence reduced efficiency.

The most common equation for calculating efficiency in an electrostatic precipitator is the Deutsch-Anderson equation as expressed in Equation (2.14).

$$\eta_{ESP} = 1 - \exp\left(-\frac{A_{ESP}\, w}{Q_g}\right) \qquad \textbf{- Equation (2.14)}$$

where

A_{ESP} = area of the collection electrode (m^2)

w = migration velocity (m/s)

Q_g = Gas flowrate through the precipitator (m^3/s)

The A/Q term is called the specific collection area (SCA). It can be seen that increasing the SCA and the migration velocity will increase the collection efficiency. However, this will also increase the capital cost. The length can be roughly estimated from a knowledge of the drift velocity, w. The time required for particles to migrate to the collection electrode must be less than the residence time of the particles in the precipitator. When the migration time is equal or less than the residence time, the separation efficiency will be 100 % and this is because of no turbulence (i.e. laminar flow).

Equation (2.14) assumes even distribution of particles across the interelectrode space, which is not always valid and assumes that the gas flowrate is uniform across the precipitator with no bypassing. It also completely ignores the fact that re-entrainment may occur, which is very likely because of turbulence and the cleaning process. Nonetheless, its simplicity is so appealing that it is normally used for making preliminary estimates of the collection efficiency.

The disadvantages of ESPs are that they are not easily adaptable to varying loads and operating conditions, they are relatively more expensive to build and they require a large installation area **(Wark *et al.*, 1998)**. They are not widely employed in the oil and gas industry since they require proper maintenance, large space requirement and a low gas handling capacity (the gas velocity in ESP usually varies between 0.3 – 3 m/s in order to avoid flooding and re-entrainment) **(Wark *et al.*, 1998)**. However, safety issues surrounding the high voltages required to run ESPs and the tendency to get an explosion because of sparking are the main reasons why they are not used. Hence, this type of separator is not being considered in this project.

2.3.4 Mesh Type Eliminators

One of the most common types of demisters used in chemical process industries is the knitted mesh demister, which is made from interlocking loops of wire (Figure 2.11) with a diameter in the range of 80 – 280 microns **(Brunazzi and Paglianti, 2000)**. The wire can be formed from a wide range of materials depending on the application, temperature and corrosive nature of the medium in which it operates. Metal meshes are typically constructed from mild steel, stainless steel and nickel whereas non-metallic meshes are made of nylon, propylene, mineral wool and glass fibre (See Figure 2.12) **(Davies and Papadopoulos, 2000)**. The wire filaments are knitted to produce a lay flat sock

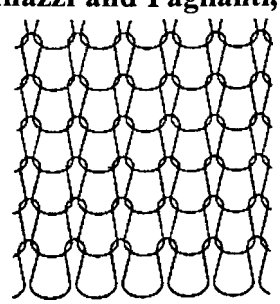

Figure 2.11: Interlocking loops of wire (KnitMesh Catalogue, 2001).

(Davies and Papadopoulos, 2000) (See Figure 2.13a). Before they are used to make knitted mesh pads, they are passed through corrugated rollers to impose a ribbed pattern upon the wires (See Figure 2.13b). This is called crimping. This not only provides a tortuous path for the gas stream, but also increases the surface area per unit volume for capture of droplets (i.e. enhances separation).

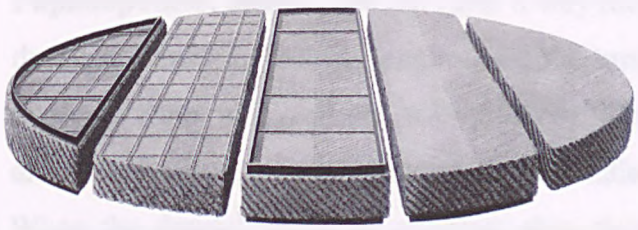

Figure 2.12: Knitted Wire Mesh (KnitMesh Catalogue, 2001).

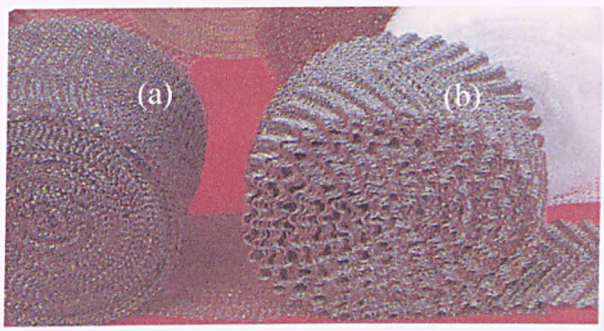

Figure 2.13: (a) Lay flat sock, (b) Crimped wire mesh (KnitMesh Catalogue, 2001).

Knitted mesh demisters are produced by knitting the wires to form a layer that can be rolled up around itself to form a cylinder (commonly used for small diameter applications) or folded into several layers (i.e. placed on top of another) until the desired thickness is reached. The size of the mesh varies from 25 mm to 10 m diameter and the depth of pad used varies from 50 to 300mm, with 100 to 150mm pads being the most common and a free volume of 75 – 99 % **(Robinson, 1985; Strauss, 1977)**.

The separation process can be broken down into three different stages **(Davies and Papadopoulos, 2000)**:

(i) Capturing of droplets by the wires,

(ii) Coalescence of the droplets,

(iii) Drainage of liquid.

The droplets are captured on the knitted wire mesh demisters through a combination of gravity deposition, direct interception, inertial deposition and

diffusional deposition (details were discussed in Section 2.2) **(Davies and Papadopoulos, 2000)**. The gas finds it way round the wires very easily, while the droplets, which are heavier cannot take the turns and impinge on the wires. The liquid droplets will coalesce with previously captured droplets to create pendant drops. This increases the chances of the smaller, lighter droplets being collected. When the droplets grow to a certain size, they are large enough for gravity to exceed the combined forces of surface tension and gas drag, they will fall into a collection sump as shown in Figure 2.14. This is the ideal working condition. When the gas velocity is just enough to handle a specified liquid loading. If this gas velocity is increased at a high liquid loading, three distinct situations will take place. There are listed below **(York and Poppele, 1963)**:

(i) Liquid enters the mesh and gets collected in a reservoir at the bottom of the wire mesh.

(ii) The liquid in the reservoir will rise higher into the knitted mesh with any additional increase in the gas velocity. The mesh is significantly filled with liquid and becomes flooded internally. The pressure drop rises more sharply.

(iii) As the gas rate is further increased, the liquid reservoir will be lifted to the top surface of the knitted mesh. At this point, the liquid is re-entrained back into the gas stream.

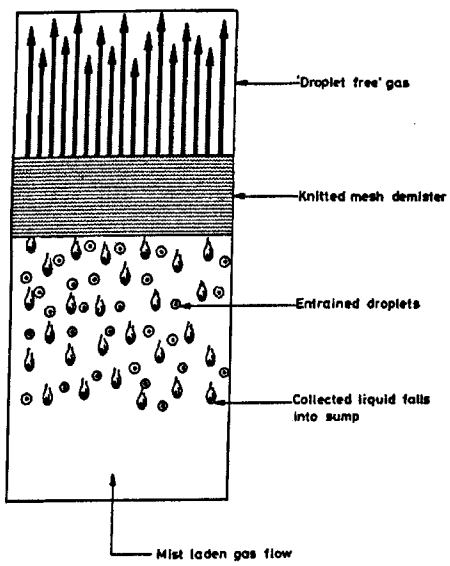

Figure 2.14: Normal operation of knitted mesh demister (Robinson, 1985)

As previously noted, the gas velocity is one of the most important factors affecting the design of a demister. If the gas velocity is too low, the separation efficiency will be low because the smaller droplets will move with the gas streamlines, hence escaping. If it is too high this will lead to flooding. The upper limit to the gas stream velocity is determined by the re-entrainment and flooding characteristics of the packing. The Souders-Brown equation **(Souders and Brown, 1934)** (Equation 2.15) is most commonly used to predict flooding.

$$U_f = k\sqrt{\frac{(\rho_L - \rho_g)}{\rho_g}} \qquad \textbf{- Equation (2.15)}$$

where U_f is the gas velocity at flooding (m/s), ρ_g is the gas stream density (kg/m^3), ρ_L is the liquid density (kg/m^3) and k is an empirical constant with the dimensions of velocity (m/s). Its value depends upon the operating conditions. Unfortunately, the literature for values of the coefficient k, also referred to as gas load factor, is very limited. However, the value of k provided by the manufacturers is about 0.1m/s for most vertical flow applications for water droplets in air **(Davies and Papadopoulos, 2000)** and some recommended 'k' values are given in Table 2.1 **(KnitMesh, 2001)**. This way of designing is very rough since it does not take into consideration either the drop size, on which the collection efficiency is strongly dependent, or the liquid loading that can influence flooding on the pad. It is suggested that good performance is obtained for all velocities between 30 and 80% of the flooding velocity, U_f, to allow for surges **(KnitMesh, 2001)**.

Duty	k value (m/s)
Clean conditions	0.107
Vacuum operation	0.061-0.085
Plastic demisters: highly corrosive conditions	0.064
High pressure: > 20 bars	0.085

Table 2.1: Different 'k' values for different operating conditions.

The gas flowrate and the liquid loading going through the knitted mesh influences the pressure drop across the mesh. Pressure drop increases significantly when the mesh is flooded. The total pressure drop, ΔP_M, through a knitted mesh is

taken as the sum of the dry pressure drop, ΔP_{MD} and the pressure loss due to the liquid load within the mesh, ΔP_{MW} **(York and Poppele, 1963)** expressed as Equation 2.16.

$$\Delta P_M = \Delta P_{MD} + \Delta P_{MW} \qquad \textbf{- Equation (2.16)}$$

The dry pressure drop, which includes all the relevant mesh geometrical properties, is expressed in Equation (2.17).

$$\Delta P_{MD} = 4\phi \frac{h}{d_w} \rho_g U_g^2 \frac{(1-e_m)}{e_m^3} \qquad \textbf{- Equation (2.17)}$$

where

h = height of mesh (m)

d_w = diameter of the wire (m)

e_m = mesh voidage

ϕ = friction factor

ρ_g = gas density (kg/m^3)

U_g = gas velocity (m/s)

It is clearly shown in the above equation that the dry pressure drop depends significantly on the mesh voidage (e_m). In order to handle a high throughput, e_m has to be large, but this will not trap the smaller droplets. If e_m is too small (high specific surface area) this will increase the pressure drop. However, the dry pressure drop is usually only a small fraction of the mesh total pressure drop. There is no generalised correlation for the wet pressure drop for wire mesh demisters **(Robinson, 1985)**. However, it would be expected that at higher liquid loading and gas velocity, the wet pressure drop is higher. For high pressure system, the total pressure drop will be higher compared to atmospheric conditions because the pressure drop is affected by the gas and liquid densities. Pressure drop also increases with the pad thickness. A pressure drop-flowrate characteristic graph of various knitted meshes at different liquid loadings can usually be obtained from various manufacturers. In general, the pressure drop through knitted mesh pads is small due to their open structure and typically lies in the range 12-50 mm water **(Robinson, 1985)**.

The separation efficiency is believed to be affected by the gas velocity, the system properties (density and viscosity of fluid), the type of mesh used (the effect of crimp and effect of pad construction involving combined meshes). The efficiency of the knitted mesh can be estimated by extending the analysis for the efficiency of a single wire **(Robinson, 1985)**. The single wire efficiency, E_{MS} (Equation 2.18) can be expressed in terms of Stokes Number (Stk):

$$E_{MS} = Stk^3 (Stk^3 + f_1 Stk^2 + f_2 Stk + f_3)^{-1} \quad \textbf{- Equation (2.18)}$$

where

$f_1 = -0.0133 \ln (Re_w) + 0.931$

$f_2 = 0.0353 \ln (Re_w) + 0.360$

$f_3 = -0.0537 \ln (Re_w) + 0.398$

Re_w = wire Reynolds number = $\rho_g U_g d_w / \mu_g$

And the efficiency of the wire mesh demister, E_M, is expressed as Equation (2.19).

$$E_m = 1 - \exp\left(-\frac{8\rho_b h}{3\pi\rho_w d_w} E_{MS} \right) \quad \textbf{- Equation (2.19)}$$

where

ρ_b = demister bulk density (kg/m^3)

ρ_w = wire true density (kg/m^3)

h = thickness of the demister (m)

As expected, the separation efficiency increases as the droplet diameter, demister height and the bulk density increases. Since the separation efficiency is a function of Stokes number, this means that at high operating pressure and temperature, the efficiency will decrease because of the reduced density difference between the gas and liquid and the increased gas viscosity. Further information (both general and complex details) on the work carried out both experimentally and numerically on knitted wire mesh separators can be obtained from **Carpenter and Othmer (1955); Brunazzi and Paglianti (1998; 2000); Feord *et al.* (1996) and York (1954).**

Knitted wire meshes are simple to use, low in cost and in pressure drop across the mesh and they are also efficient in capturing small droplets ($d_{50} \approx 5$ microns) **(Swanborn, 1988)**. They can be used as a coalescer operating at high velocity above the flooding point where re-entrainment occurs as well as increased collection efficiency of small droplets, which will pass through a standard mesh. These re-entrained droplets will be of a much larger size compared to the original mist, hence can be separated easily by a standard mesh further downstream, operating below flooding conditions. This method was adopted by **York and Poppele (1970)** to improve removal efficiency in sulphuric acid plants.

2.3.5 Cyclone separators

Cyclones have been a popular and valuable tool in the separation industries as described in Chapter 1. The rate of particles settling in a gas stream can be significantly increased if centrifugal rather than gravitational forces are used. Increasing separation rate reduces vessel size (compactness) by reducing retention times. In a cyclone, the liquid laden gas performs a spiral movement after being fed through a tangential inlet or passing through swirl vanes. The liquid droplets are flung to the walls of the containment under the action of centrifugal force and the liquid will be collected at the bottom of the vessel from where it is drained.

A lot of work has been done on reverse flow cyclones; looking at the flow pattern **(Hoffmann *et al.*, 1996; Iozia and Leith, 1989; Shepherd and Lapple, 1939)** and the effect of each design parameter on the separation efficiency of solid-gas separation **(Hoffmann *et al.*, 1995)**. Studies on uniflow cyclones, however, are relatively few. The principle of operation of demisting cyclones is very similar to that of dust cyclones. They are distinguished from conventional gas cyclones collecting solid particles by the behaviour of the coalesced liquid film once the droplets have been deposited upon a surface. It is easier to separate a gas-liquid mixture because

(i) it is easier for droplets to coalesce producing larger droplets, hence reduced residence time.

(ii) liquid droplets tend to coagulate with the liquid film on the cyclone wall in which their kinetic energy will be dissipated. This reduces turbulence mixing, which brings the liquid back into the main flow upon hitting on the cyclone wall. However, liquid film is prone to creep to areas of lower pressure (i.e. across cyclone top all the way down the vortex finder and leave through the vortex finder). The film is also susceptible to re-entrainment due to the shear effect between the gas and the liquid surface especially in areas having a small radius of curvature. Therefore, in this work slots are introduced to strip off the liquid film before droplets are detached from it. The presence of the film may alter the effective roughness of the cyclone wall, which will have an influence on the pressure drop characteristics.

There are thus two important differences between the operations of a dry or wet cyclone. The first regards the role of boundary layer flow in promoting the 'annular eddy' in the region between the cyclone barrel and the vortex finder. This eddy causes flow of the collected film over the roof of the cyclone and down the vortex finder. Often a serrated skirt is placed around the vortex finder to prevent short-circuiting by this flow. The second difference concerns the need to avoid stripping of the collected liquid film, particularly at the cyclone inlet. This places an effective limit on the inlet velocity that can be used for mists. It is suggested that for a well-designed mist-removing cyclone, the product of the gas density (kg/m^3) and the square of the inlet velocity (m^2/s^2) should be less than 1860 for air/water systems and less than 3700 for air/oil systems **(Stairmand, 1951)**.

This suggests that Stairmand's criteria could be re-expressed in terms of a critical gas Weber number (We), which is given by Equation (2.20).

$$We = \frac{t\rho_g U_g^2}{\sigma} \qquad \textbf{- Equation (2.20)}$$

where t = characteristic dimension (usually taken as film thickness)

σ = surface tension (N/m)

The drag required to re-entrain liquid from the liquid film to the main air flow will depend on the surface tension and the viscosity (film thickness is dependent on viscosity). Since the surface tension of water is approximately twice that of oil, the observed difference between oil and water by Stairmand is most probably due to the difference in viscosity leading to a different film thickness, i.e. 't' .

Critical Weber number criteria for the initiation of droplets entrainment in two-phase flow have been proposed by **Ishii and Grolmes (1975)** and by **Andreussi (1980)**. The characteristic dimension has been taken as the film thickness, which is not known in practical cyclones. However, it may be assumed that the film thickness will increase with increasing inlet concentration which in turn suggests that the droplet initiation criterion might be more easily exceeded at higher inlet concentrations.

2.3.6 Combination of separators

The number of separation stages depends on the nature of the operating system (i.e. the amount of liquid fed to the separator and the maximum amount of liquid allowed in the outlet of the separator). For example, if only slugs of liquid are to be separated from both slugs and fine mists, a single separator is usually sufficient. If mists are not allowed or if the gas must be free of any liquid, then two or three separation stages will be necessary.

In the case of this research, a combination of knitted meshes and axial flow cyclones is used to separate liquid droplets from air. The knitted mesh should separate out the liquid droplets at low liquid loading, but when it is flooded the axial flow cyclones will have to perform the separation process, but on the larger, entrained droplets. The details of the separation have been discussed in Chapter 1, Section 1.4.

2.4 Historical Background of Cyclones

The use of cyclones for gas cleaning has been common for more than a century. They are very popular because there are no moving parts that can wear out or break. Consisting of a cylindrical body, an inlet and exit port, a cyclone separator is fairly simple, inexpensive to build and to maintain. They are capable of collecting particles above 10μm with 99.9 % efficiency depending on particle density.

The first applications employing the cyclone principles date back to 1885. The first cyclone design was seen in German patent 39 219 granted in 1885 to the Knickerbocker Company of the USA **(Jackson, 1963)**. The patent shows a simple cyclone with just a cone, both with and without an inserted exit pipe **(Jackson, 1963)**. Figure 2.15 shows that in the cyclone with an inserted exit pipe, there is a special exit on the top plate for collecting coarse particles that had climbed to the top of the walls.

Most of the industrial applications and research work in the past have used cyclones mostly for solid-gas separation. The main difference between liquid and solid collection is that liquid may re-entrain under high shear conditions whereas dusts may rebound at a broader range of conditions. Reverse flow cyclones with tangential inlet are usually used. There has been very little work carried out using cyclones of any geometry for gas-liquid separation and the applications of axial flow cyclones for either liquid or solid separation in particular are not well understood.

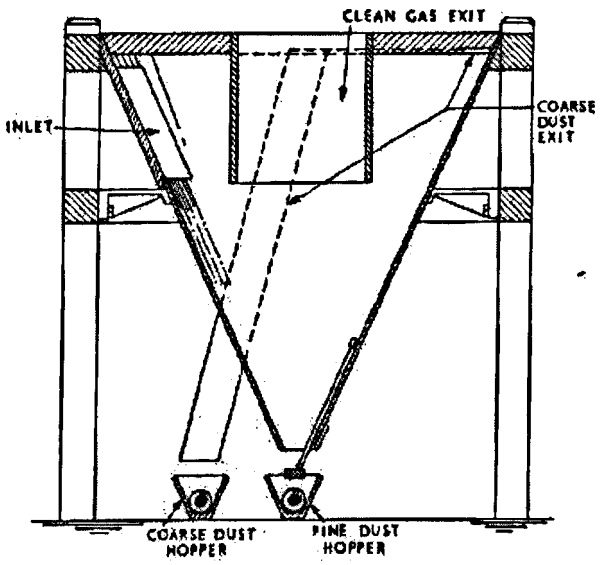

Figure 2.15: First cyclone seen in German patent 39 219 (1885) granted to the Knickerbocker Company (Jackson, 1963).

The size of practically useful cyclone bodies can vary from 25mm to greater than 3m. The pressure drop across a cyclone ranges from 10 to 200mm water gauge (wg) with inlet velocities in the range of 7 to 30 m/s. Cyclones can be designed to operate in temperatures up to 1000^0C and pressures up to 500 bar **(Phillips *et al.*, 1992)**. Hence, they are fabricated according to need from a wide range of materials allowing for flexibility of usage in hostile environments.

Cyclones are able to cope with a wide range of dust loadings. This makes them very suitable for use as pre-cleaners. However, the turn down ratios on the gas flow are generally limited to around 3:1 depending on operating conditions and the required duty.

2.5 Types of Cyclones Configurations

Cyclones have been used in industry for over 100 years and more recently the designs have become more standardised. There are basically two major variations in the designs. The first concerns the mechanism for creating the gas vortex, which can be formed by a tangential inlet or by stationary swirl vanes. The second difference concerns the type and the position of the gas exit. The gas exit

can be either on the same end as the inlet or at the opposite end. The gas may leave the cyclone either peripherally or axially. Figure 2.16 illustrates some possible variations of the inlet and outlet designs of cyclone.

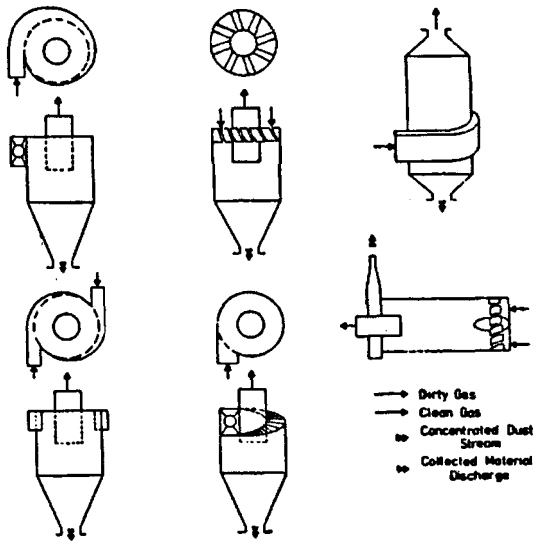

Figure 2.16: Variations in cyclone design (Allen, 2001)

2.5.1 Conventional Reverse Flow Cyclones

The main characteristics that differentiate conventional reverse flow cyclones from axial flow cyclones would be the flow direction of the cleaned exit gas. The principle of operation of this type of device is shown in Figure 2.17. The gas, loaded with solid particles/liquid droplets, enters the upper part of the cylindrical vessel tangentially or in some cases it can enter axially through a system of stationary vanes. The gas goes down the vessel following a helical path. The spiralling flow goes downward between the walls of the gas exit pipe (vortex finder) and the body of the cyclone. The spiral continues down the outside of the unit. While the gas spirals down the unit, a portion of the flow continually goes into the central, inner vortex. When the spiral gets to the lower zone (the conical section), the gas turns and goes up, again following a helical trajectory with a smaller radius. Finally, it leaves the device through a cylindrical duct coaxial to the cyclone barrel as clean gas. The inner vortex is usually estimated at being 0.5 to 1.0 times the diameter of the vortex finder. An annular eddy is often found in

the annular space between the cyclone body and the vortex finder flowing upwards along the cyclone wall, across the roof and down the vortex finder. This is only relevant for reverse flow cyclones with tangential inlet and axial flow cyclones. The particles/droplets, which are heavier than the gas, are thrown towards the cyclone wall by centrifugal forces. The particles move downwards on the wall following a helical path. The particles' inertia makes them travel in a straight line (i.e. fly off at a tangent). It is the balance between the centrifugal force and the drag force that determines whether the particles are collected or not.

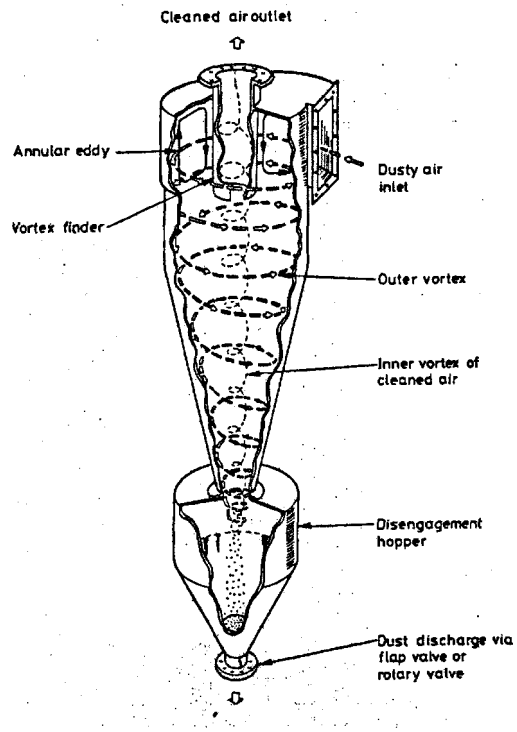

Figure 2.17: Three-dimensional view of a reverse flow gas cyclone (Allen, 2001).

For reverse flow cyclones, the longer the cyclone when inlet and outlet dimensions are constant the greater the volume of the outer vortex which leads to increased residence times and hence increased chance of particle capture. However, there is also a limit where increasing cyclone length does not lead to increased efficiency. This is explained by the concept of 'natural length' of the vortex. This length of the vortex is measured from the bottom of the vortex finder to the point where the flow reverses. Relative length ratios (H/D_C) above 5 cannot be justified economically **(Doerschlag and Miczek, 1977)**.

2.5.2 Axial Flow Cyclones

The operation fundamentals of an axial flow cyclone are similar to that of the conventional reverse flow cyclone. However, there are some major

distinctions between the two devices. The flow in a reverse flow cyclone comprises two vortices; an outer vortex moving downwards and an inner vortex in the opposite direction. On the other hand, in an axial flow cyclone, there is only one vortex flowing in one direction and the flow direction of the clean gas out is different for both type of cyclones. The main drawback of the reverse flow cyclone is the large pressure drops, requiring a higher expenditure of energy **(Klujszo *et al.*, 1999)**. Therefore, uniflow cyclones have been developed **(Gauthier *et al.*, 1990; Gauthier *et al.*, 1992; Sumner *et al.*, 1987)** such that by eliminating the flow reversal, the pressure drop is reduced and one likely cause of re-entrainment is eliminated because there is no mixing of cleaned gas with the liquid laden gas.

Axial flow cyclones consist only of the cylindrical section. The gas is caused to spin when it enters, either through a tangential inlet or through a set of stationary swirl vanes. It has been found that tangential entry reduces particle bounce and hence gives a higher efficiency than the vane inlet **(Daniels, 1957)**. However, such an advantage is inappropriate when considering the collection of droplets. Tangential inlet cyclones suffer from the fact that the inlet is at right angle to the outlet and, hence, they cannot be easily placed in-line with the flow. This is an advantage for the vane inlet axial flow cyclone geometry when multi-cyclones are required to handle high gas flow capacities. The clean gas leaves the cyclone through a cylindrical duct coaxial to the cyclone barrel opposite from the gas inlet. The particles/droplets are collected either axially or at the periphery of the cyclone barrel. Figure 2.18 and 2.19 illustrate the wide variety of inlet designs and various forms of gas exit used.

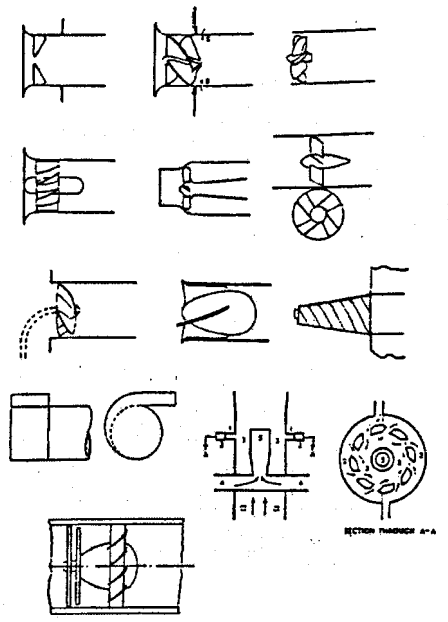

Figure 2.18: Various forms of axial flow cyclone inlet (Jackson, 1963).

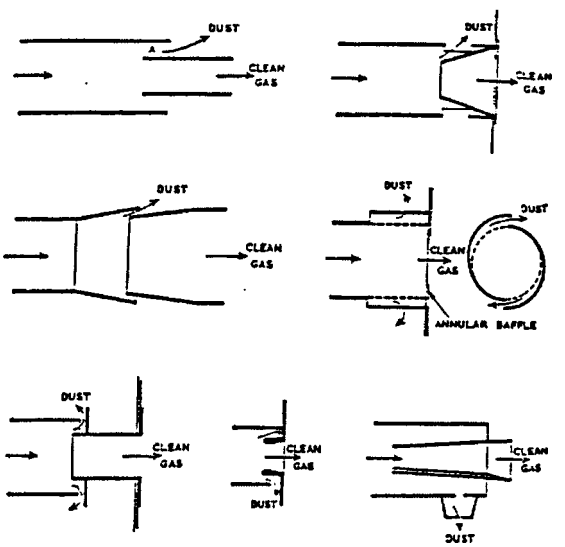

Figure 2.19: Various forms of axial flow cyclones gas exit (Jackson, 1963).

2.6 Axial Flow Cyclones

2.6.1 Flow Pattern

The gas flow pattern in cyclones, mostly reverse flow cyclones, has been studied extensively both experimentally and also computationally over decades. However, some of the general findings can also be applied to axial flow cyclones where appropriate and will be discussed below.

The axial velocity is either an upward or a downward flow depending on the flow direction. For the tangential velocity, V_t, it was assumed that the gas flow constitutes a simple form of vortex in the earlier calculations of Seillan, Lissman and Barth as quoted in **Jackson (1963)**, which is given by Equation (2.21):

$$V_t = \frac{C}{r^n} \qquad \textbf{- Equation (2.21)}$$

where

V_t = tangential velocity at any point

C = constant

r = radius corresponding to V_t

n is determined by the form of the flow pattern

The index 'n' is 1 for free vortex and –1 for forced vortex (solid body rotation). The forced and free vortices are two types of ideal swirling flows. For a real swirling flow, there is always a central core of near solid body rotation surrounded by a free vortex flow. This is called a 'Rankine vortex', which is expressed as Equation (2.22). The combined Rankine vortex satisfies the forced vortex equation at small 'r' and the free vortex equation for larger 'r'.

$$V_t = \frac{C'}{r}\left[1 - \exp\left(\frac{r^2}{r_o^2}\right)\right] \qquad \textbf{- Equation (2.22)}$$

where

C' = constant

r_o = core radius (m)

r = radius at any point in the cyclone(m)

Like the reverse flow cyclone, an annular recirculation zone is often found in the annular space between the cyclone body and the vortex finder. Unlike gas-solids cyclones, in gas-liquid cyclones some liquid tends to deposit along the upper cyclone wall and on the roof forming a wall film. The recirculating gas will drag the liquid film up the wall and then radially inwards across the roof and down the vortex finder. The liquid will either creep into the vortex finder or re-entrain back

to the gas flow in the cyclone body. Since, the mechanism leading to separation of liquid droplets from the gas is the spinning of the gas within the cyclone it is, therefore, useful to consider how far the pattern of gas flow in a cyclone is known before making changes in the geometries. Besides getting measurements from experiments, numerical simulations are also used to give insight to the flow pattern in cyclones. As for the creeping effect, which is disadvantageous to the overall separation performance, it can be avoided using 'anti-creep skirt' or 'roof-skimmer', which will be discussed later.

The following sections will describe the different components of a straight through flow cyclone in terms of the importance of the design of each section to the performance of the cyclone.

2.6.2 Cyclone Body

The cyclone body is the main section of this centrifugal separator. There are only two parameters that could be changed which are the tube diameter and length. With smaller diameter, it is believed that the separation efficiency will increase, but there is an increased threat of blockage with dust and flooding with liquid. The system pressure drop will also increase due to the increased swirl energy.

Theoretically, one would imagine that with a shorter tube the separation efficiency would drop because there is not enough residence time for the droplets to travel to the wall. On the other hand, with a long tube, the swirl would decay. This increases the turbulence and hence results in a drop in the separation efficiency **(Jackson, 1963)**.

There does not seem to be much published information on optimum dimensions in the open literature. However, **Daniels (1957)** stated that a length/diameter ratio of just under 5:1 is preferred because from his work he discovered that with a 2-inch diameter cyclone tube, an increase in the tube length

beyond 9.5 inches gave poorer separating efficiency due to the decreased swirl intensity. From **Akiyama and Marui (1989)**, in straight-through swirl tubes it has been found that doubling the dimensionless length, L/D_{CT}, from 3 to 6 led to a reduction of separation efficiency for a 0.185m diameter cyclone tube (See Figure 2.20). This is because of the decay in the swirl. If swirl is induced in a fluid flowing along a tube, the swirl decays in an exponential manner in the flow direction. A dimensionless length of around 3 was recommended.

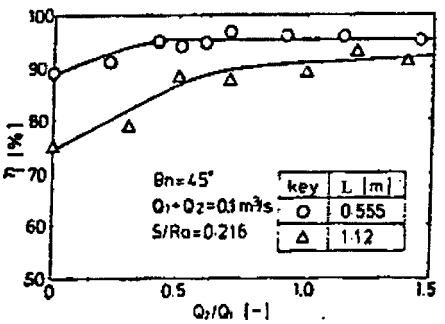

Figure 2.20: Effect of cyclone length on dust collection efficiency (Akiyama and Marui, 1989).

Klujszo *et al.* (1999) reported that the separation distance required for 50.8 mm diameter cyclone tube is less than one diameter as shown in Table 2.2 and **Sumner *et al.* (1987)** also stated that the optimal separation length for their cyclone design was around one cyclone diameter as shown in Figure 2.21.

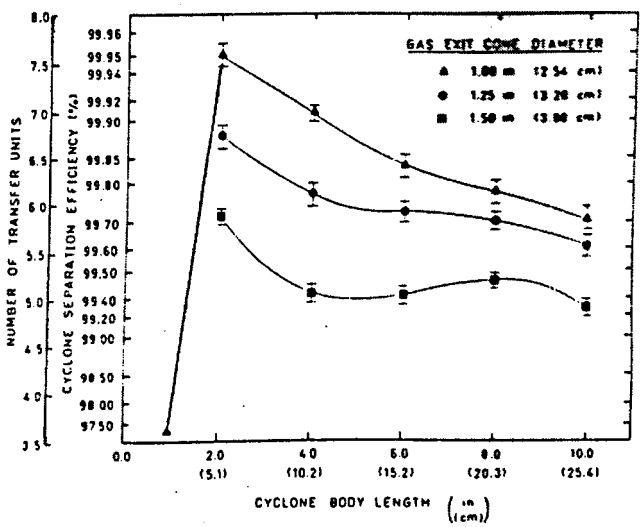

Figure 2.21.: Effect of body length on the separation efficiency (Sumner *et al.*, 1987).

Blade Geometry	Inlet Velocity (m/sec)	Separation Distance (mm)	Mass Recovery (%)
6 (30°-20°-10°)	4.2	31.8	80.0
8 (20°-20°-20°)	4.2	38.1	82.0
6 (30°-20°-10°)	4.2	57.2	80.3
8 (20°-20°-20°)	4.2	88.9	81.3
8 straight	4.2	108.0	79.9

Table 2.2: Effect of separation distance on collection efficiency (Klujszo *et al.*, 1999).

The uniflow cyclone, with a tangential inlet equipped with a volute, investigated by **Gauthier *et al.* (1990)** could achieve collection efficiencies of 99.9 % or more with a separation length of 1.5 cyclone diameters (See Figure 2.22). They believed that the reduced efficiency at longer separation lengths was likely due to the reduced vortex intensity in the gas exit region, which was consistent with the results obtained by **Daniels (1957)** and **Sumner *et al.* (1987)**.

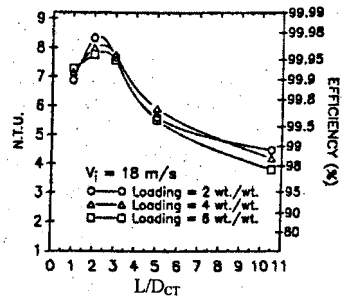

Figure 2.22: Effect of separation length on collection efficiency at various loadings (Gauthier *et al.*, 1990).

There is no rule as to which ratio is the optimum value. The value that was suggested by previous workers was based on their specific operating conditions, dust distributions and cyclone designs (especially the vane design since different designs give different swirl intensities). Therefore, to find an optimum ratio, experiments have to be carried out to meet the specific requirements.

2.6.3 Cyclone Inlet

The main characteristic of the inlet is that it provides the means to swirl the gas. The inlet has to be smooth to avoid causing the droplets in the boundary layer to break away from the walls and to flow radially inwards, hence re-entraining them. Usually swirl vanes are fixed around an axial boss, which is used to provide support for the vanes. There is no published work as to what the dimensions of the boss should be to achieve optimum performance (i.e. length and diameter). A larger boss and hence a shorter vane height (distance from the root of the vane to the top in the radial direction) would increase efficiency due to greater centrifugal force caused by the increase in velocity follow-on from the narrower annulus. However, an aggressive swirl may cause the coarser particles to bounce off the wall or might break them into smaller particles, hence reducing separation efficiency. This phenomenon might have less effect on mist separation. There is

work done showing that using a tangential entry had the advantage of reducing particle bounce upon hitting the wall since the particles were projected at a much shallower angle. On the other hand, this type of inlet introduces problems like maldistribution when grouping the cyclones into banks (multicyclones) and it would not be as compact as using static swirl vanes.

2.6.3.1 Swirl Vanes

For a given throughput and body diameter, the swirl intensity for cyclones having tangential entry can be varied by changing the inlet cross-sectional area. For cyclones using guide vanes to create swirl, the vane turning angle (angle between the vane plane and the axial direction) is the main determining factor. An increase in this angle will give a higher separation efficiency as well as a greater pressure drop. However, there will be a limit where a further increase will not enhance the separation efficiency and will create excessive pressure drop. Therefore, there is always a trade-off between pressure drop and the swirling energy.

Another cause of pressure drop is the air velocity and acceleration through the gap between the vanes. The larger the reduction in the flow area (i.e. smaller vane angle, larger number of vanes), the larger the flow acceleration and more friction loss the vanes generate, and hence the larger the pressure drop **(Akiyama *et al.*, 1986)**. When designing the vanes, there should not be any gap left between two successive vanes in the axial direction (See Figure 2.23). Although having a gap between vanes will decrease the pressure drop, part of the incoming flow would pass right through the gap without turning, reducing swirl intensity. If fewer blades are used, they have to be extended a longer distance axially to ensure there is no gap between two successive blades, which will induce a problem if there is a design limitation on the total length of the cyclone tube **(Klujszo *et al.*, 1999)**.

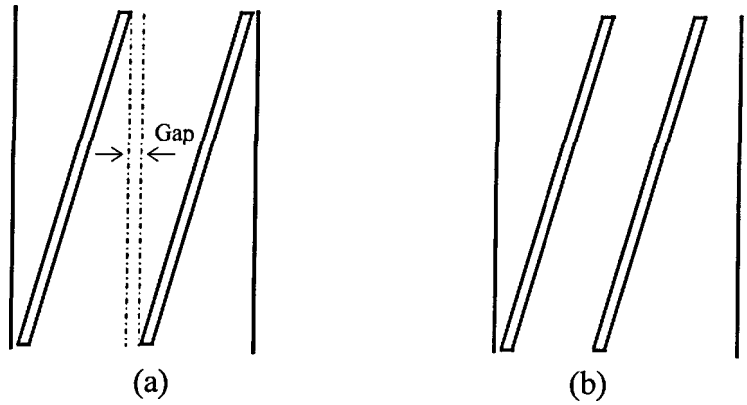

Figure 2.23: (a) Undesirable vane design with gap between successive vanes and (b) appropriate design without gap in between vanes.

Daniels (1957) found that increasing the vane angle from 30^0 to 45^0 created a greater swirl and hence a greater centrifugal force producing a marked increase in efficiency as illustrated in Figure 2.24. A further increase to 50^0 produced no further significant increase instead increases the system pressure drop from 7 in (45^0 vane angle) to 7.5 in water gauge. Therefore, care should be taken when designing the vanes to minimise trailing eddies which would increase turbulence without improving the cyclone's performance or might even reduce its efficiency due to bouncing or liquid droplets being sheared off the liquid film.

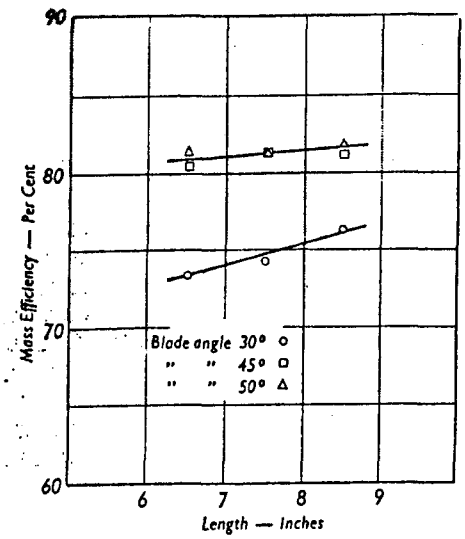

Figure 2.24: Effect of blade angle on separation efficiency (Daniels, 1957).

Klujszo *et al.* (1999) experimentally assessed performance of an axial flow cyclone used for dust collection using three different blade designs (the angle between the blade plane and the axial direction was fixed at 60^0); straight blades (entire blade surface is contained in a single plane), a 3-plane design (the first blade plane forms an angle of 20^0 with the axial direction, the second blade turns 20^0 with respect to the first one and the third one turn for another 20^0 with respect to the second one) and 3-plane (30^0-20^0-10^0 blade). Both the gradually turning

blades demonstrated a very large decrease in pressure drop (See Figure 2.25). The blades were mounted on a hub, which had a conical front and a cylindrical and conical back section (See Figure 2.26). However, the authors did not show evidence of the effect of different vane configurations on the separation efficiency.

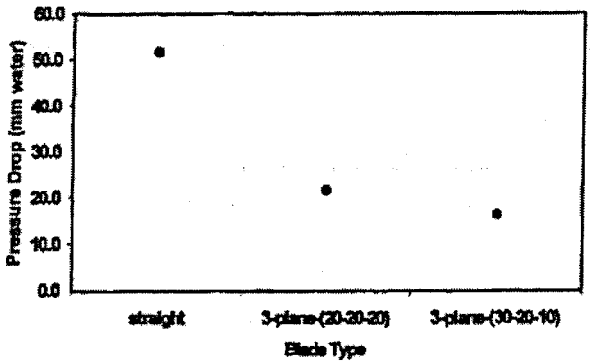

Figure 2.25: This figure clearly shows that the gradually turning vanes gives lower pressure drop (Klujszo et al., 1999)

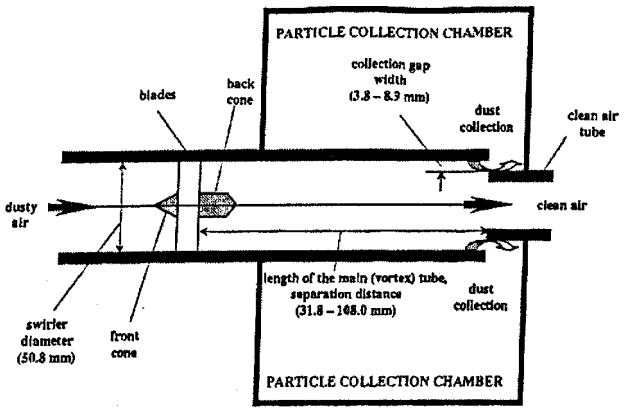

Figure 2.26: Schematic of the swirler separator used by Klujszo *et al.* (1999).

2.6.4 Cyclone Exit

Extra attention has to be paid to the exit design of an axial flow cyclone because the liquid is separated out in the same direction as the clean gas. As a result, there is a higher probability of getting liquid re-entrained if the outlet is not properly designed. The simplest design is shown in Figure 1.3 with just an annulus to drain out liquid, which spins at the periphery of the cyclone body.

There are more sophisticated outlet designs, but there is no one particular design that will give satisfactory results for all operating conditions. One might outperform the others under certain condition. Some forms of gas and liquid exits are illustrated in Figure 2.19. Some exits allow liquid to escape all around the periphery (coaxial outlet) and some escape through longitudinal slots.

Most of the work done so far has used a coaxial outlet. The gap width (distance between the cyclone tube and the vortex finder) is very crucial. A smaller than required gap will lower the efficiency, however, a larger than required gap will not improve the efficiency, but will increase the pressure drop. **Daniels (1957)** and **Klujszo *et al.* (1999)** are some of the researchers that have investigated the influence of gap width on separation efficiency.

According to **Swanborn (1988)**, a limiting phenomenon was identified inside the coaxial discharge cyclone. At high liquid loadings the interfacial friction in the gap is not high enough to carry all the liquid out of the cyclone, causing heavy re-entrainment just underneath the vortex finder (Figure 2.27). Therefore, it was decided to use longitudinal slots in the wall of the cyclone tube as the liquid outlet in this project.

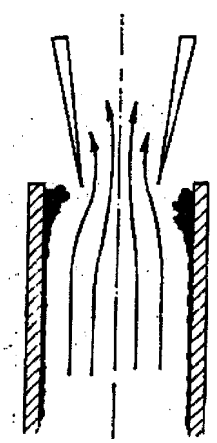

Figure 2.27: Re-entrainment in coaxial discharge (Swanborn, 1988).

2.7 Cyclone Performance

The performance of cyclones is judged by two major criteria **(Jackson, 1963)**: the pressure drop and the efficiency. Under normal circumstances, knowledge of pressure drop through a cyclone is important for the selection of the fan that needs to be installed. However, this is not a major problem in the oil industry since there is a large amount of pressure from the wellhead that is used to drive the fluids. The efficiency determines whether the equipment will deal with

the dust/liquid concentrations present in a satisfactory manner. It is desirable to keep the pressure drop a low value and the efficiency high, but these requirements are contradictory because the two factors are related in a sense opposite to that which would be desired.

2.7.1 Pressure Drop

The pressure drop across the cyclone is an important parameter, but exact prediction is still not available. The total pressure is made up from static and dynamic pressure, P and $\frac{1}{2}\rho U^2$ respectively. The Bernoulli equation for steady flow of a frictionless fluid states that:

$$\frac{P}{\rho} + gh + \frac{1}{2}U^2 = \text{constant} \qquad \textbf{- Equation (2.23)}$$

This shows that the static and dynamic pressures (first and last term respectively on the left hand side) can be interchanged in the flow field. Static pressure will be low in high velocity areas and vice versa. However, in real application, the fluid is not frictionless. Therefore, the RHS of Equation (2.23) is not constant, but decreases along a streamline due to energy losses. The losses across the cyclone can be considered separately and additively in

(i) the entrance
(ii) the vanes
(iii) the separation space
(iv) the gas exit

The entrance losses are often insignificant compared to the other losses with the major losses occurring in the vortex finder **(Hoffmann and Stein, 2002)**. Pressure drop is normally obtained by measuring the static pressure upstream and downstream of a pipe. However, for cyclonic systems the swirling motion complicates the measurement. The static pressure is reasonably uniform over the

tube cross-section and can normally be measured with a pressure tapping in the wall. Difficulties arise in measuring the pressure in the vortex finder due to the swirl present at the pressure tapping point. The static pressure is not uniform in the swirling zone; in fact it is highest at the wall **(Hoffmann and Stein, 2002)**. This problem has been tackled in various ways. **Stairmand (1949)** ignored the swirl and measured the pressure at the outlet wall. Another approach is to use a flow straightener to recover the static pressure as the dynamic pressure stored in the swirling motion in the vortex finder can be very significant **(Hoffmann and Stein, 2002)**. **Hoffmann *et al.* (1992)** stated that the static pressure at the pressure tapping point in the wall is close to the cross-sectional mean of the static pressure and the dynamic pressure stored in the swirl. Therefore, in the absence of a flow straightener the pressure at the vortex finder wall minus the static pressure at the inlet gives the true dissipative loss between the inlet and the measurement point in the outlet.

Pressure drop is usually expressed as a number of inlet velocity heads, N_H. N_H is related to pressure drop (Equation 2.24):

$$\Delta P = \frac{1}{2}\rho_g U_g^n N_H \qquad \textbf{- Equation (2.24)}$$

where U_g is the gas inlet velocity and the exponent 'n' varies between 1.5 and 2. Usually it is taken as 2 and this makes N_H a dimensionless factor, often called the Euler Number (Eu) or the pressure loss coefficient (Equation 2.25).

$$Eu = \frac{\Delta P}{\frac{1}{2}\rho_g U_g^2} \qquad \textbf{- Equation (2.25)}$$

The Eu can be divided into two independent factors. One accounts for the pressure losses due to the clean gas, being constant at fixed cyclone geometry and other depends on the liquid inlet concentration (i.e. the liquid loading).

A lot of pressure drop models have been developed over the years and they are mostly for predicting the pressure drop in reverse flow cyclones. Some of the

work in which experimental data have been correlated against cyclone geometry to give an empirical expression were carried out by **Shepherd and Lapple (1939)** and **Casal and Martinez-Benet (1983). Shepherd and Lapple (1939)** claimed that the dry pressure drop (expressed as Euler number, Eu_g) across a cyclone varies directly with the inlet height and width, and inversely with the vortex finder diameter, D_{VF}, given in Equation (2.26). This expression only correlates the losses from the inlet to the entrance of the vortex finder. However, it has the advantage of being very simple, while providing good accuracy **(Casal and Martinez-Benet, 1983; Phillips *et al.*, 1992).**

$$Eu_g = \frac{16ab}{D_{VF}^2} \qquad \textbf{- Equation (2.26)}$$

Casal and Martinez-Benet (1983) correlated the published experimental data of other workers with geometrical parameters: a/D_C, b/D_C, D_C/D_{VF} and ab/D_{VF}^2. The best results were obtained with the dimensionless group ab/D_{VF}^2, deriving the following expression for pressure drop (See Equation 2.27).

$$Eu_g = 11.3\left(\frac{ab}{D_{VF}^2}\right)^2 + 3.33 \qquad \textbf{- Equation (2.27)}$$

Work which accounted for the energy losses by modelling the fluid dynamics in the cyclone has been described by researchers like **Stairmand (1949)** and **Alexander (1949). Stairmand (1949)** assumed that the total energy loss is due to the losses in the vortex plus the entrance and exit losses. Stairmand's proposed pressure drop correlation was as expressed in Equations (2.28) and (2.29).

$$Eu_g = 1 + 2\phi^2\left(\frac{2(D_C - b)}{D_{VF}} - 1\right) + 2\left(\frac{4ab}{\pi D_{VF}^2}\right)^2 \qquad \textbf{- Equation (2.28)}$$

where

$$\phi = \frac{-\left(\frac{D_{VF}}{2(D_C - b)}\right)^{\frac{1}{2}} + \left(\frac{D_{VF}}{2(D_C - b)} + \frac{4GA}{ab}\right)^{\frac{1}{2}}}{\frac{2GA}{ab}}$$ **- Equation (2.29)**

'G' is a friction factor roughly equal to 0.005 and 'A' is the internal surface area of the cyclone exposed to the spinning gas, which can be calculated from Equation (2.30).

$$A = \frac{\pi}{4}(D_C^2 - D_{VF}^2) + \pi D_C h + \pi D_{VF} L_{VF} + \frac{\pi}{2}(D_C + D_{DE})\left[(H-h)^2 + \left(\frac{D_C - D_{DE}}{2}\right)^2\right]^{\frac{1}{2}}$$ **- Equation (2.30)**

Alexander (1949) assumed that all pressure losses were due to kinetic energy losses in the gas stream and came up with a relationship expressed in Equations (2.31) to (2.33).

$$Eu_g = 4.62\frac{ab}{D_C D_{VF}}\left[\left\{\left(\frac{D_C}{D_{VF}}\right)^{2n} - 1\right\}\left\{\frac{1-n}{n}\right\} + f\left(\frac{D_C}{D_{VF}}\right)^{2n}\right]$$ **- Equation (2.31)**

where

$$n = 1 - \left(1 - \frac{(39.4D_C)^{0.14}}{2.5}\right)\left(\frac{T}{283}\right)^{0.3}$$, T is the temperature (K) **- Equation (2.32)**

and

$$f = 0.8\left[\frac{1}{n(1-n)}\left(\frac{4-2^{2n}}{3}\right) - \left(\frac{1-n}{n}\right)\right] + 0.2\left[(2^{2n}-1)\left(\frac{1-n}{n}\right) + 1.5(2^{2n})\right]$$ **- Equation (2.33)**

The study done by **Ramachandran *et al.* (1994)** on rotary flow cyclones was the closest to the working mechanisms of axial flow cyclones. However, this rotary cyclone did not have a vortex finder like the design this project is addressing. The pressure drop across the rotary flow cyclone is the sum of the change in the velocity head and the head loss due to friction as the gas stream

moves through the cylinder, with a negligible potential head. The pressure drop is given by Equation (2.34):

$$\Delta P = P_1 - P_2 = \rho_g \left(\frac{U_2^2 - U_1^2}{2} \right) + \rho_g g h_f \qquad \textbf{- Equation (2.34)}$$

with 1 and 2 denoting the flow in and out respectively (Refer to Figure 2.28). At point 1 the gas has only an axial velocity in where $U_1=U_g$. It is assumed that the gas stream exits the cyclone with an average helical velocity, U_{avg}, which is calculated as an area weighted average of the net velocity of gas, U, a vector sum of the axial and tangential components of velocity. It is assumed that there is no radial component of velocity. The detailed of the derivations can be found in **Ramachandran *et al.* (1994)**. U_{avg} can be calculated from Equation (2.35) below:

$$U_{avg} = U_g \frac{4\pi}{3R^2 P_t} \left[\left(\frac{P_t^2}{4\pi^2} + R^2 \right)^{\frac{3}{2}} - \left(\frac{P_t^2}{4\pi^2} \right)^{\frac{3}{2}} \right] \qquad \textbf{- Equation (2.35)}$$

where P_t = the axial distance travelled by the gas in one revolution of the helix

R = radius of the rotary flow cyclone

The head loss due to friction, h_f (Equation 2.36), is obtained from the modified Darcy-Weisbach relationship for flow through a cylinder:

$$h_f = \frac{f L_{hel} U_{avg}^2}{2 D_h g} \qquad \textbf{- Equation (2.36)}$$

where L_{hel} is the average length path of gas through the helical structure (Equation 2.37), U_{avg} is the average velocity of gas in the helix, D_h is the hydraulic diameter of the rotary flow cyclone (Equation 2.38), and f is the friction factor.

$$L_{hel} = U_{avg} \left(\frac{H}{U_g} \right) \qquad \textbf{- Equation (2.37)}$$

$$D_h = \frac{2\pi R}{\pi + 2}$$ **- Equation (2.38)**

f is given by Equation (2.39):

$$\sqrt{\frac{1}{f}} = -1.8\log_{10}\left[\frac{6.9}{Re_g} + \left(\frac{\varepsilon/D_{CT}}{3.7}\right)^{1.11}\right]$$ **Equation (2.39)**

where ε/D is the relative roughness of the walls and Re_g is the Reynolds Number for the gas expressed in Equation (2.40).

$$Re_g = \frac{\rho_g U_{avg} D_h}{\mu}$$ **- Equation (2.40)**

Substitute the above relationships into Equation (2.34), the pressure drop can be expressed as follows (Equation 2.41):

$$\Delta P = \frac{\rho_g U_g^2}{2}\left[\left(\frac{U_{avg}}{U_g}\right)^2\left(1 + \frac{L_{hel}}{D_h} f\right) - 1\right]$$ **- Equation (2.41)**

where ρ_g is the gas density

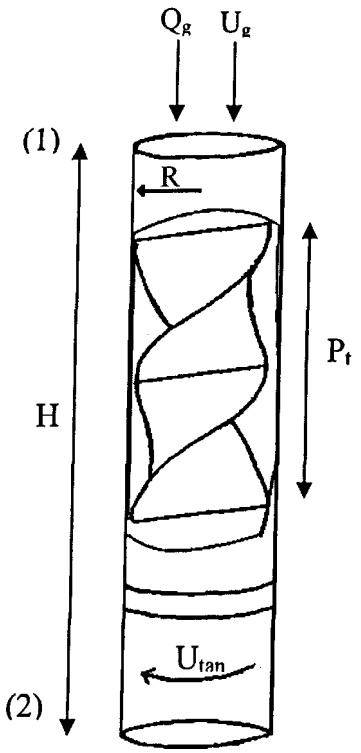

Figure 2.28: Diagram of a rotary flow cyclone (Ramachandran et al. (1994)

Most of the correlations in the literature are for predicting dry pressure drop or pressure drop with low concentration of dust/liquid, which does not affect the pressure drop significantly (Cyclone pressure coefficient, $Eu_c = Eu_g \cdot Eu_s$, Eu_g = pressure drop resistance due to clean gas and Eu_s = pressure drop resistance due to solids). However, there are some literature correlations to calculate the influence of the solid loading in the cyclone pressure drop as investigated by **Gil *et al.* (2002)**.

When solid is injected to the air stream, a decrease in pressure drop is observed. Many are surprised because it would be expected that the increase of loading will cause an increase in the frictionless loss hence higher pressure drop, the same case with an increase in the wall roughness in pipe flows. It is thought that the work done in accelerating the solids would have lowered the vortex energies and also would disrupt turbulent energy dissipation (i.e. occurrence of turbulent damping) **(Allen, 2004)**. The increase in loading will also increase the wall friction along the cyclone wall, which will also reduce the tangential velocity in the cyclone body **(Gauthier et al., 1992; Yuu *et al.*, 1978)**. The drag between the particles and gas takes away a significant amount of the gas energy, hence a reduction in the static pressure loss. Therefore, it is generally required to maintain the wall surfaces as smooth as it is practical to get the highest core spin velocity and best separation performance (i.e. avoid any disturbance in the boundary layer as described earlier).

There are correlations to predict the effect of solid loading on the overall cyclone pressure drop (reported by **Gil *et al.* (2002)**), which are tabulated in Table 2.3 below. However, no publications have been found so far reporting on correlations to calculate influence of liquid loading in the cyclone pressure drop.

Reference	Equation
Briggs	$Eu_s = \frac{1}{1 + 0.0086(C_{si}\rho_g)^{0.5}}$
Smolik	$Eu_s = 1 - 0.02\,(C_{si}\rho_g)^{0.6}$
Baskakov et al	$Eu_s = \frac{1}{1 + 3.1C_{si}^{0.7}} + 0.67C_{si}$

C_{si} = solid loading at cyclone inlet (kg solids per kg gas)

Table 2.3: Literature predictions for the solid loading effect quoted from (Gil *et al.*, 2002)

- ***Re-entrainment***

When there is liquid present in the cyclonic system, there is a tendency for re-entrainment to occur. Entrainment refers to liquid droplets breaking away from a gas/liquid interface to become suspended in the gas phase. Re-entrainment is used generally to assume that droplets have settled to the liquid phase, then are detached and returned to the gas phase. It is caused by rapid momentum transfer from gas to liquid. These droplets can be responsible for corrosion, erosion and mechanical failure of the equipment downstream. The means by which re-entrainment/flooding takes place are as listed below **(Calvert, 1978)**:

(i) When the gas flowrate is high, the aerodynamic drag forces can cause carryover of drops from the liquid films flowing down the separator. This becomes more dominant when liquid hold-up in the separator is too much, decreasing the cross-sectional area available for the gas flow. The high relative velocities cause liquid to be blown out.

(ii) Drops may break due to direct collision with one another forming smaller droplets that escape with the clean gas.

There are many papers concerning the experimental results of cyclone collection efficiency, but not many regarding the experimental results of the re-

entrainment. **Ishii and Grolmes (1975)** proposed correlations for predicting the minimum gas velocity required for re-entrainment to occur in concurrent flow, which is useful in determining the limit of the cyclone design for various gas-liquid properties. The correlations used a film Reynolds number, Re_L and a viscosity number, N_μ to characterise the two-phase flow. These are defined as follows (Equations 2.42 to 2.48);

$$Re_L = 4\rho_L U_L \delta_t / \mu_L \quad \textbf{- Equation (2.42)}$$

$$N_\mu = \mu_L / [\rho_L \sigma (\sigma / g\Delta\rho)^{0.5}]^{0.5} \quad \textbf{- Equation (2.43)}$$

where δ_t is the average film thickness and σ is the surface tension of the gas-liquid interface.

For the low liquid Reynolds number regime ($Re_L<160$),

$$(\mu_L U_g/\sigma)(\rho_g/\rho_L)^{0.5} \geq 1.5 Re_L^{-0.5} \quad \textbf{- Equation (2.44)}$$

For the transition regime ($160 \leq Re_L \leq 1635$ for the horizontal and vertical upward flow and $2 \leq Re_L \leq 1635$ for downward flow),

$$(\mu_L U_g/\sigma)(\rho_g/\rho_L)^{0.5} \geq 11.78 N_\mu^{0.8} Re_L^{-1/3} \text{ if } N_\mu \leq 1/15 \quad \textbf{- Equation (2.45)}$$

and

$$(\mu_L U_g/\sigma)(\rho_g/\rho_L)^{0.5} \geq 1.35 Re_L^{-1/3} \text{ if } N_\mu \geq 1/15 \quad \textbf{- Equation (2.46)}$$

For the rough turbulent regime ($Re_L > 1635$),

$$(\mu_L U_g/\sigma)(\rho_g/\rho_L)^{0.5} \geq 0.1146 \text{ if } N_\mu \geq 1/15 \quad \textbf{- Equation (2.47)}$$

and

$$(\mu_L U_g/\sigma)(\rho_g/\rho_L)^{0.5} \geq N_\mu^{0.8} \text{ if } N_\mu < 1/15 \quad \textbf{- Equation (2.48)}$$

Liquid Reynolds number, Re_L, is a measure of the liquid phase turbulence and indicates which mechanism of re-entrainment is most likely for the flow conditions considered. For simplification, it is generally supposed that the liquid film is evenly distributed across the separator wall. However, this assumption is not always applicable. The liquid will flow in strings when the liquid loading is low and not all the surface is wetted. The surface will eventually be wetted when

the liquid loading increases. There is a limit above which further increase in liquid loading will result in ripples on the film surface and eventually leading to formation of small droplets. According to **Ishii and Grolmes (1975)** for Re_L<160, a wave undercut mechanism was proposed where gas impinges on the gas-liquid interface, undercutting it and breaking displaced liquid away from the interface. In the transition regime, the dominant mechanism is the shearing off the top of the roll waves from the wave crests by high relative velocities between gas and liquid. The other types of entrainment mechanisms include the bursting of gas bubbles, the impingement of the liquid drops to the film interface and when the counter-current flow reaches the flooding condition forming a bulge or a liquid film between the walls and when these liquid bulges and bridges disintegrate into smaller droplets, they are re-entrained into the gas stream (See Figure 2.29 for the mechanisms of droplet formation). Typically, the re-entrained droplets from the mechanisms mentioned will be in the range of 5 to 100 μm.

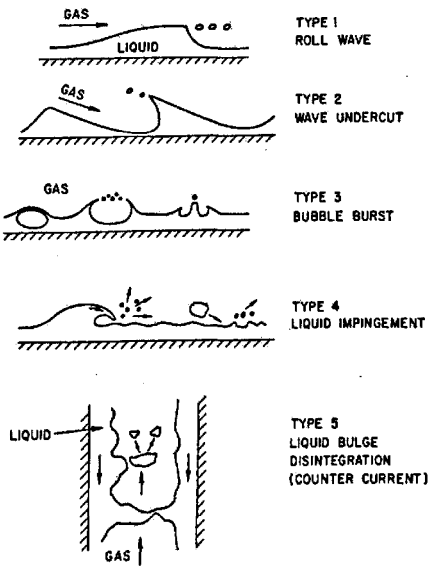

Figure 2.29: Various mechanisms of droplet formation.

It is recommended that to significantly reduce re-entrainment, an anti-creep skirt should be placed around the vortex finder as shown in Figure 2.30 **(Calvert, 1978; Stairmand, 1951; Van Dongen and Ter Linden, 1958)**.

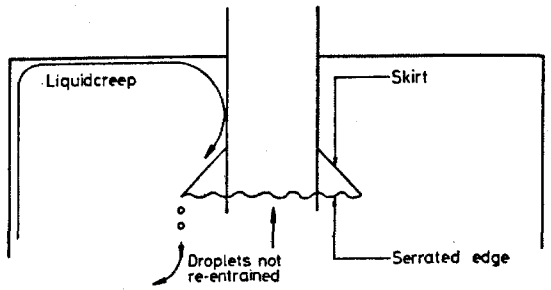

Figure 2.30: Using a serrated skirt to counteract the re-entrainment problem.

2.7.2 Grade Efficiency

In most industries involving transport of particles by a gas stream, the ability to collect a representative sample for analysis is an essential step in any assessment of particle size. The common method of obtaining the concentration readings is to insert a sampling probe into the gas stream. A typical system will generally have at least one bend to change the flow direction from parallel to the duct axis to perpendicular to the axis. When an aerosol stream is forced to change direction, large particles of high inertia are unable to follow the streamlines, hence might collide with walls and be removed depending on the initial position at the bend inlet and other parameters such as Stokes number (Stk) and flow Reynolds number (Re). On the other hand, small particles with low inertia can follow the streamlines closely and penetrate through the bend and are hence sampled. Extensive experimental and modelling work has been carried out to look at the flow inside sampling probes, the effect of the probe geometry and how these affect particle deposition in both laminar and turbulent flows **(Armand *et al.*, 1998; Cheng and Wang, 1975; 1981; Dean, 1927; 1928; Dennis and Ng, 1982; Gore and Jurewicz, 1983; Yanase *et al.*, 1989)**. Sampling errors usually result from;

(i) Deviations from isokinetic sampling
(ii) Misalignment of the sampling probe
(iii) Sample line losses (inertial deposition, losses in bend)

- ***Sampling from flow environment***

It is desirable to have the velocity within the probe (U_{probe}) equals the free stream velocity (U_o) so that a minimum disturbance is created in the flow field. This condition is referred to 'isokinetic' sampling. Unfortunately, there are situations where it is impossible to sample isokinetically because of the difficulties in matching probe size and flow conditions properly **(Shahnam and Jurewicz, 1986)**. When operating at anisokinetic conditions, the streamlines will be distorted

and droplets will not follow the distorted streamlines. If $U_o<U_{probe}$ (subisokinetic), large particles are undersampled since they can not follow the streamline because of their significant inertia and miss the probe entrance altogether. If $U_o>U_{probe}$ (superisokinetic), large particles are oversampled since they cross the streamlines and enter the probe. Figure 2.31 illustrate the gas streamlines and particle trajectories for both isokinetic and anisokinetic situations. In general, significant over- and under-sampling can be accepted if the particles are smaller than 10 micron aerodynamic diameter **(Krishnan, 1999; Mitchell and Morris, 1994)**.

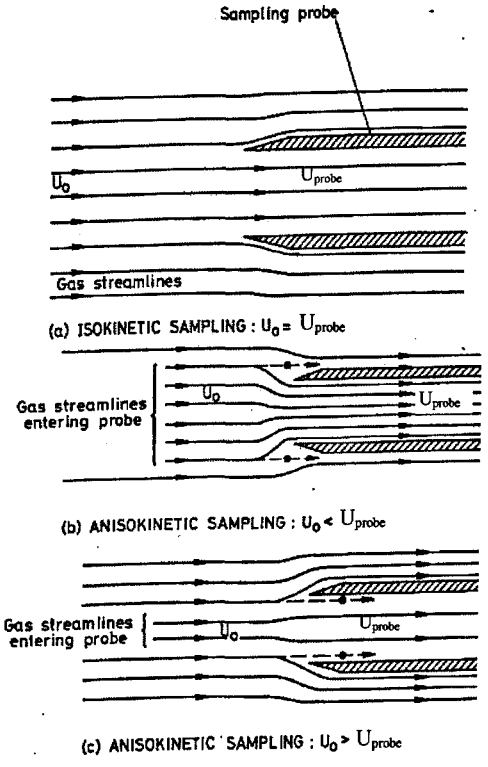

Figure 2.31: Sampling from a flow of aerosol (Mitchell and Morris, 1994).

❑ *Misalignment of sampling probe*

Probe misalignment (Figure 2.32) is usually due to technical error and could be avoided by careful setting of the probe in the duct. Figure 2.33 can be used as a guide to estimate errors if θ is known **(Mitchell and Morris, 1994)**. This is not a serious problem if the probe is aligned within 5^0 of the actual gas flow **(Sparks, 1984)**.

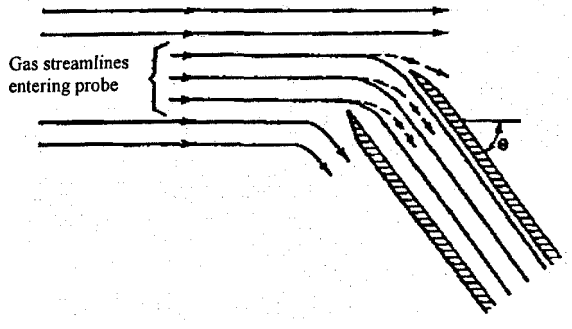

Figure 2.32: Probe misalignment (Mitchell and Morris, 1994).

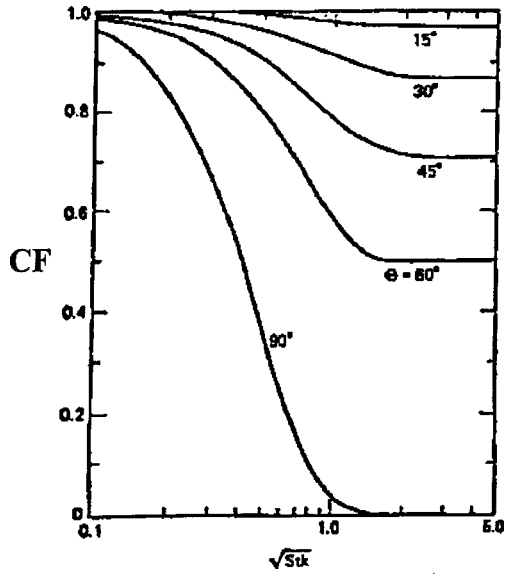

Figure 2.33: Estimation of effect of misalignment on sampling efficiency (Hinds, 1999)

- ***Sample line losses***

Sampling lines should be kept to a minimum length because particle losses could be very significant due to inertial deposition. For flow through straight pipes, Reynolds number ($Re = \rho_f U d_t/\mu$) is used to characterise whether the flow is laminar (Re less than 2000), turbulent when Re is greater than 3000 and transition between those values **(Coulson *et al.*, 1999)**. Here, ρ_f is the fluid density, U is the average fluid velocity, d_t is the pipe inner diameter and μ is the fluid viscosity. The flow in curved pipes is characterised by a secondary flow in a cross sectional plane normal to the main flow and by the shift of the maximum axial velocity to the outside owing to the centrifugal force. This type of flow nature depends the Re and the curvature of the bend, which can be characterised as the Dean number (De) expressed in Equation (2.49):

$$De = Re/\delta^{1/2} \qquad \textbf{- Equation (2.49)}$$

where $\delta = R/a$ = curvature ratio of the bend

R = radius of curvature of bend (m)

$a = d_t/2$ = tube internal radius (m)

The flow field in bends of circular cross section depends only on the Dean number for bends of curvature ratio greater than five. Three different flow regimes for the flow around circular bends have been defined **(Pui *et al.*, 1987)**. Dean number plays the role of the "Re" of the flow in a curved pipe. For De ≤ 370, the flow is considered laminar **(McFarland *et al.*, 1997; Pui *et al.*, 1987)**. Both experimental and numerical work has been carried out by various workers **(Cheng and Wang, 1981; McFarland *et al.*, 1997; Pui *et al.*, 1987)** investigating the deposition efficiency of particles in bends. The impaction efficiency of a bend for particles of finite sizes depend on the following dimensionless groups **(Cheng and Wang, 1975)**:

(i) Stokes Number (Stk) = $C\rho_p d_p^2 U_{probe}/18\mu a$

(ii) Particle Reynolds number (Re_p) = $d_p U_{probe}/\nu$

(iii) Flow Reynolds number (Re) = $2aU_0/\nu$

(iv) Curvature ratio (δ) = R/a

where C is the Cunningham slip correction, ρ_p the particle density, d_p the particle diameter, ν the kinematic viscosity of the fluid. Among these groups, the Stokes number is the most important parameter. For small values of Stk (≤ 0.1) and large values of Re, the impaction efficiency, I, of a 90^0 bend can be approximated by (Equation 2.50);

$$I = (1 + \frac{\pi}{2\delta} + \frac{2}{3\delta^2})Stk \qquad \textbf{- Equation (2.50)}$$

Cheng and Wang (1981) concluded from their work that the impaction efficiency of a 90^0 bend is mainly a function of the Stokes and the flow Reynolds number for $4 \leq \delta \leq 30$ and $Re_p << 1$.

The numerical work of **Tsai and Pui (1990)**, covering only the laminar region, agreed with the work of **Cheng and Wang (1981)**, but they think that the curvature ratio plays an essential role in determining the deposition efficiency as well. They also found out that the inlet velocity profile also influences the deposition efficiency and they looked at the effect of Reynolds number and

curvature ratio, δ, expressed as Dean number. At a fixed Stokes number, the deposition efficiency increases with an increasing De because the axial velocity profile is skewed more toward the outside of the bend and also due to the increase of the secondary flow strength. The efficiency will decrease with an increasing curvature ratio, δ, at a fixed Dean number because the increase of δ is expected to decrease the secondary flow strength while maintaining the essentially the same axial velocity profile. The efficiency is always higher in the case of a parabolic inlet velocity profile compared to a uniform profile. This is due to the increased skewness of the axial velocity profile toward the outside of the bend. Tsai and Pui found that all the deposition curves obtained (De = 38 to 869 and δ = 5.7 to 50) could be fitted by the following function (Equation 2.51);

$$\eta_{dep}\ (\%) = \frac{100}{\{1 + Stk^{[f_1(De,\,\delta)Stk_m + f_2(De,\,\delta)]}\}} \qquad \textbf{- Equation (2.51)}$$

where $Stk_m = Stk/Stk_{50}$ is a modified Stokes number. For a uniform inlet profile,

$$Stk_{50} = [-0.44\exp(-0.086\delta)+0.403] \times \exp[(-1.82\times10^{-5}\delta^2+1.18\times10^{-3}\delta-0.024)De] + 3.92\times10^{-6}\delta^2 + 5.67\times10^{-3}\delta + 0.41$$

and for a parabolic inlet profile;

$$Stk_{50} = [3.59\times10^{-5}\delta^2 + 6.95\times10^{-3}\delta + 0.24] \times \exp[(-7.3\times10^{-6}\delta^2 - 2.47\times10^{-5}\delta - 0.0077)De] - 0.65\exp(-0.039\delta) + 0.775$$

Pui *et al.* (1987) found experimentally that the deposition efficiency was independent of the flow Reynolds number for the turbulent flow regime. They have concluded that for the turbulent regime, the deposition efficiency, η_{dep}, approaches zero as the Stokes number goes to zero. Their experimental data could be fitted by a straight line of log P = -0.963Stk where P is the aerosol penetration. Therefore, η_{dep} = 1-P. All these imply that in order to have negligible particle losses in bends, the Stk should be kept small. Or said in another way: larger particles are subject to proportionately larger errors.

McFarland *et al.* (1997) have also studied aerosol deposition in bends with turbulent flow, both numerically and experimentally. They claimed that the effect of Reynolds number is sufficiently small such that it can be neglected from their numerical studies. Experimental results show that a bend with curvature ratio, δ, of 4 should be satisfactory for aerosol transport. Further increase of δ will not have a significant improvement on the aerosol penetration. They have also accounted the effect of flattening of the bend cross-section. The degree of flattening is the amount by which a diameter is reduced by the original tube diameter. Data suggest that if a bend is somewhat flattened less than 25% during the fabrication process, the aerosol penetration characteristics would not be significantly impacted. They have also come up with a correlation model based on numerical calculations as seen below (Equation 2.52):

$$\ln P = \frac{4.61 + a\theta Stk}{1 + b\,\theta Stk + c\,\theta Stk^2 + d\,\theta^2 Stk} \qquad \textbf{- Equation (2.52)}$$

where θ = radians

P = Penetration in percent.

$$a = -0.9526 - 0.05686\delta$$

$$b = \frac{-0.297 - 0.0174\delta}{1 - 0.07\delta + 0.0171\delta^2}$$

$$c = -0.306 + \frac{1.895}{\sqrt{\delta}} - \frac{2}{\delta}$$

$$d = \frac{0.131 - 0.0132\delta + 0.000383\delta^2}{1 - 0.129\delta + 0.0136\delta^2} \quad \text{(a)}$$

Therefore, to obtain accurate data it is important to correct for losses of particles in bends as well as other parts of a sampling system.

(a) Please note that there is a mistake in the expression for the coefficient 'd' in McFarland et al.'s paper, which has been corrected here.

2.7.2.1 Grade Efficiency Curve

The grade efficiency curve is obtained by measuring the separation efficiency of each particle size. The efficiency is plotted against the diameter of the particles. The grade efficiency curve provides a more complete description of cyclone collection efficiency since it quantifies the efficiency at different particle diameters. It is normally independent of size distribution and is constant for a particular set of operating conditions. The curve is usually S-shaped as shown in Figure 2.34. The grade efficiency curve gives the probability at which particles of a given size in the gas stream will be separated from or escape with the gas stream. The value of the curve generally increases from zero for finest particles to 100% for the coarser particles. Important points such as cut size, x_{50}, limit of separation, x_{max}, and sharpness of cut can be obtained from the grade efficiency curve.

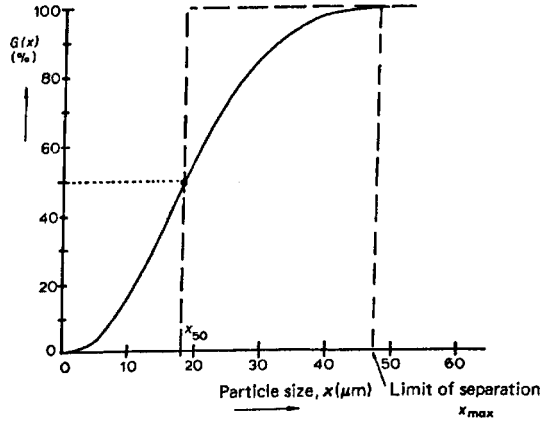

Figure 2.34: A typical grade efficiency curve (Svarovsky, 1981).

- ***Cut Size, x_{50}***

The cut diameter or cut size, x_{50}, is defined as the size of the particle that has an equal chance of being collected or of escaping the collection (i.e. 50% probability of separation on the grade efficiency curve). It is taken as the most significant single parameter to describe both the difficulty of dust separation and the performance of the separator.

- ***Limit of Separation, x_{max}***

In a grade efficiency curve, there is a particle size above which the grade efficiency is 100% regardless of x. This is known as the limit of separation, x_{max} (See Figure 2.33). It is the size of the smallest particle that will be separated from the gas stream with 100% efficiency.

- ***Sharpness of Cut***

The general slope of the grade efficiency can be expressed in terms of a 'sharpness index'. It can be defined in several ways. Sometimes it is defined as the gradient of the tangent to the curve at x_{50}. It is also sometimes defined as the ratio of two sizes corresponding to two different percentages on the grade efficiency curve on either side of 50%, for instance:

$$H_{25/75} = x_{25}/x_{75} \text{ or } H_{10/90} = x_{10}/x_{90} \text{ or } H_{35/65} = x_{35}/x_{65}$$

or on the other hand, defined as the reciprocal values of these.

2.7.2.2 Performance analysis of axial flow cyclones

A lot of numerical work has been carried out to analyse the performance of axial flow cyclone separators in terms of total and fractional collection efficiencies (grade efficiencies). **Dobbins *et al.* (1979)** have formulated a calculation method that permits extensive computational trials of proposed designs to be run, which permits a rapid evaluation and more thorough analysis of proposed designs. They have reported the calculations on three vane turning angles; 45^0, 54^0 and 60^0 with gravimetric collection efficiencies of 95.7%, 98.4% and 97.3% respectively. According to their analysis, efficiency falls off at a vane angle of 60^0 because of the adverse effects of particles bouncing off the wall. A large particle can be thrown to the wall at a very high velocity and after few bounces might either be separated into the foul stream or passed into the clean stream. On the other hand, when the vane angle is 45^0 the smaller particles are separated less effectively because they have a low particle Reynolds number, hence a very high particle drag

force. However, the authors did not discuss the coefficient of restitution used in their simulations. If a coefficient of 1 is used, this will increase the chances of particles leaving through the vortex finder compared to a coefficient of lower value. Therefore, the reduced efficiency at vane angle 60^0, which is expected to give stronger swirl, hence improved separation, is questionable.

Besides carrying out experiments to get empirical equations for the grade efficiency curves, various researchers have developed models to predict the curve to save time and money from the laborious experimental work. Like the models to predict cyclone pressure drop the bulk of the work is concerned with the reverse flow tangential entry cyclones **(Dietz, 1981; Leith and Licht, 1972). Dirgo and Leith (1985)** have carried out collection efficiency tests for a Stairmand high-efficiency cyclone and compared the results with the predictions of four theories (Lapple theory, Dietz theory, Leith-Licht theory and Barth theory). The authors found that the Leith-Licht theories worked best for the Stairmand high-efficiency cyclone. From the Leith-Licht theory, the fractional efficiency curve can be determined using the expression below (Equation 2.53 to 2.56).

$$\eta = 1 - \exp\left[-2(C\psi)^{1/(2n+2)}\right] \qquad \textbf{- Equation (2.53)}$$

where

$$\psi = \frac{\rho_p d_p^2 U_{in}(n+1)}{18\mu_g D_C} \qquad \textbf{- Equation (2.54)}$$

$$C = \frac{\pi D_C^2}{ab}\left[\begin{array}{l} 2\left\{1-\left(\frac{D_{VF}}{D_C}\right)^2\right\}\left(\frac{L_{VF}}{D_C}-\frac{a}{2D_C}\right) \\ +\frac{1}{3}\left(\frac{L_{VF}+l-h}{D_C}\right)\left(1+\frac{d_l}{D_C}+\frac{d_l^2}{D_C^2}\right) \\ +\frac{h}{D_C}-\left(\frac{D_{VF}}{D_C}\right)^2\frac{l}{D_C}-\frac{L_{VF}}{D_C} \end{array}\right] \qquad \textbf{- Equation (2.55)}$$

$$d_l = D_C - \frac{(D_C - D_{DE})(L_{VF}+l-h)}{(H-h)} \qquad \textbf{- Equation (2.56)}$$

and the natural length of the cyclone, l, was defined by **Alexander (1949)** as the furthest distance the spinning gas extends below the vortex finder, which is expressed as (See Equation 2.57);

$$l = 2.3 D_{VF} \left(\frac{D_C^2}{ab} \right)^{\frac{1}{3}} \qquad \textbf{- Equation (2.57)}$$

and d_l is the diameter of the conical section of that point. If the natural length exceeds (H-L_{VF}), l in Equations (2.53) and (2.54) is replaced by (H-L_{VF}). **Alexander (1949)** presented an empirical expression to calculate the vortex exponent, n, for any cyclone diameter and gas temperature (See Equation 2.32). Despite its popularity, this model has been pointed out by **Clift *et al.* (1991)** to have flaws in their derivations. The modified model is much more simpler and reflects the shape of the grade efficiency curve better.

The Dietz model **(Dietz, 1981)** calculates cyclone efficiency as follows (Equation 2.58 to 2.61).

$$\eta = 1 - \left[K_o - (K_1^2 + K_2)^{0.5} \right] \exp \left[\frac{-\pi (2L_{VF} - a) \rho_p d_p^2 U_{in}}{18 \mu_g ab} \right] \qquad \textbf{- Equation (2.58)}$$

The 'K' terms are functions of particle and gas properties as well as cyclone dimensions expressed as:

$$K_o = \frac{1}{2} \left[1 + \left(\frac{D_{VF}^2}{D_C} \right)^{2n} \left(1 + \frac{9 \mu_g ab}{\pi \rho_p l d_p^2 U_{in}} \right) \right] \qquad \textbf{- Equation (2.59)}$$

$$K_1 = \frac{1}{2} \left[1 - \left(\frac{D_{VF}^2}{D_C} \right)^{2n} \left(1 + \frac{9 \mu_g ab}{\pi \rho_p l d_p^2 U_{in}} \right) \right] \qquad \textbf{- Equation (2.60)}$$

$$K_2 = \left(\frac{D_{VF}}{D_C} \right)^{2n} \qquad \textbf{- Equation (2.61)}$$

Similar to the Leith-Licht theory, if the natural length exceeds (H-L_{VF}), l should be replaced by (H-L_{VF}) and 'n' can be calculated using Equation (2.32). Various

theories have been developed, but unfortunately there is no single correlation or theory that predicts accurately the collection efficiency for any cyclone design up to this moment.

One of the earlier piece of work to predict uniflow cyclone's grade efficiency curve was carried out by **Stenhouse and Trow (1979)**. They assumed that the vortex in the cyclone is forced and by assuming that the particle and gas tangential velocities are equal, the authors obtained the following theoretical model for predicting a uniflow cyclone's collection efficiency (See Equation 2.62):

$$\eta = 1 - \left[\exp\left(- \frac{2\rho_p U_o d_p^2 L (\cot\theta)^2}{9\mu D_{CT}^2} \right) \right]^2 \qquad \textbf{- Equation (2.62)}$$

where θ is the angle of the fixed vane to the axial direction.

Besides using analytical models as described above, numerical models could also be used to evaluate the cyclone's performance. Computational Fluid Dynamics (CFD) has been widely used for this purpose. **Hoekstra *et al.* (1999)** have carried out experimental and numerical studies of turbulent swirling flow in gas cyclones. The tangential and axial velocity components along the radius of the cyclone were measured by use of two-component laser-Doppler velocimetry. The turbulence models used in his work are the standard k-ε model, RNG-k-ε model and the Reynolds stress transport model (RSM). The performance of the three turbulence models in predicting the strongly swirling flow in a cyclone was evaluated by comparison with the velocity measurements. Both the k-ε model and the RNG-k-ε model predicted an unrealistic distribution of axial and tangential velocities (See Figure 2.35). Results obtained from the RSM are in reasonable agreement with the experimental data. However, there are still some differences and further improvement is needed.

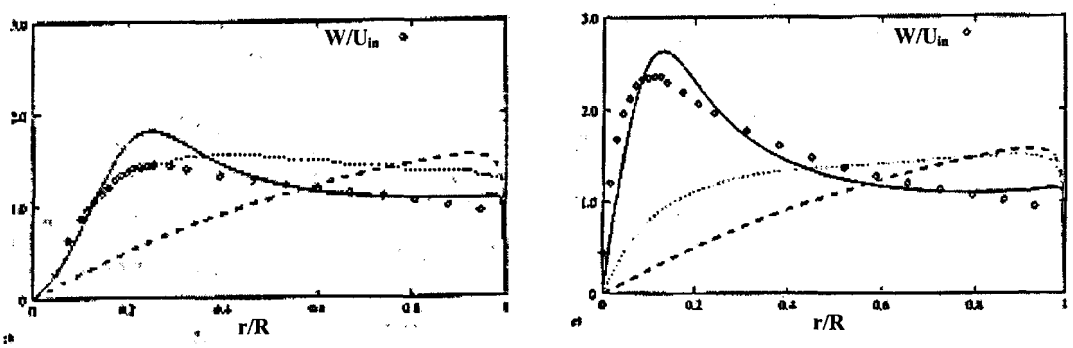

Figure 2.35: Comparison of numerical predictions and measurements of mean tangential (W) velocity normalised by inlet velocity, U_{in}. Results presented for swirl number = 2.2 (a) and 1.8 (b). (◊) LDV measurements, (-) RSM, (· ·) RNG k-ε, (– –) k-ε (Hoekstra *et al.*, 1999).

Modigell and Weng (2000) performed the calculations of pressure loss and separation efficiency of a uniflow cyclone with a CFD method. The turbulence models used are the standard k-ε model and the Reynolds stress model (RSM). The comparison of simulated and experimental data taken from a uniflow cyclone show that the standard k-ε turbulence model even at low swirl numbers is not able to reproduce tangential velocity profiles properly (See Figure 2.36). The RSM gives a correct velocity distribution in agreement with the pressure loss calculation. The separation efficiency calculation errors diminish when the effect of gas-phase turbulence on particle motion and additional simulations of fluid flow inside the swirl generator are taken into account. These improvements cause significantly higher processing times and numerical effort. Although the RSM allows swirling flow to be adequately modelled it also has one major drawback, which is the amount of computing power required. This model takes 50–60 % more CPU time per iteration and 15-20 % more memory compared to the standard k-ε model.

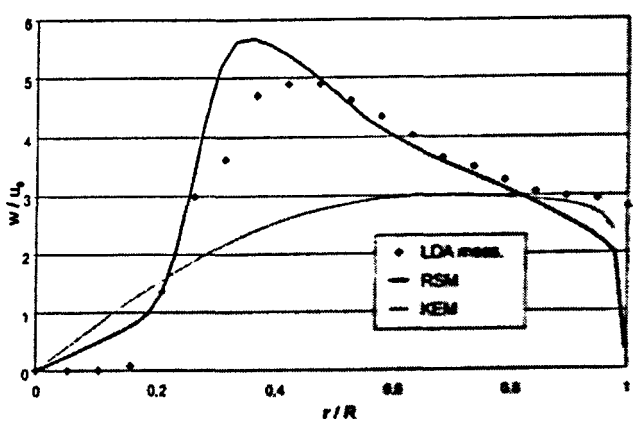

Figure 2.36: This figure shows the comparison between experimental and numerical data. LDA = Laser Doppler Anemometry, RSM = Reynolds Stress Model, KEM = k-ε model (Modigell and Weng, 2000).

Most of the CFD work carried out was on modelling conventional reverse flow cyclones. Even for uniflow cyclones, the area investigated was more on predicting the system pressure drop. Hence it is still necessary to investigate whether CFD could correctly predict the cyclone's separation efficiency using the geometry tested in this project. Although some work has been done on this type of cyclone, the difference in the complexity of the geometry will affect the mesh generation and also the computational power required to model the entire cyclone system. Like the analytical model, there is no one model that is superior for all types of designs and conditions. Therefore, investigations have to be carried out to see whether it is feasible to model the tested geometries and how accurately CFD could predict the cyclone's performance. All the details can be found in Chapter 8.

2.8 Conclusions

A detailed review of various gas-liquid separation equipment was conducted and considered the issues of handling capacity (size), pressure drop, separation efficiency and capital cost. A review of the different types of particle transport mechanisms was also carried out and it was shown that any gas-liquid separation process will fall into one or more of five categories; gravitational settling, centrifugal impaction, inertia impaction, direct interception, diffusion and electrostatic migration. The standard derivation of an important dimensionless parameter, Stokes Number ($Stk = d_p^2 (\rho_p - \rho_g) U/18\mu D_{ch}$), which is used to scale up similar geometries, was shown starting from the particle equation of motion (Equation 2.1). This shows that density difference is important for good separation. For a particular droplet size the separation efficiency is higher in a system with higher density difference. The equipment that was reviewed included gravity settlers, vane separators, electrostatic precipitators, knitted mesh demisters and cyclone separators.

Gravity settlers are commonly used because of their simplicity and effectiveness as first stage separators in the oil industry to separate out the bulk of

the liquid from the gas. However, they are only efficient in separating droplets larger than about 50 μm. When it comes to demisting purposes (i.e. separating droplets smaller than 20 μm as required for the application of this project) they are not very suitable because they will need to be very large in order to reduce the gas velocity sufficiently to allow the fine droplets to settle.

Vane separators use the inertial impaction mechanism to collect the liquid droplets by diverting the gas flow several times, altering the direction of the gas flow. The drawback of this separator is that in high-pressure systems, the fluid density difference decreases (i.e. smaller Stk Number) hence decreasing efficiency. Furthermore, as the gas density increases and the liquid surface tension decreases due to the high pressure and temperature, the maximum gas velocity going through this separator has to decrease in order to avoid re-entrainment, hence lowering the system throughput. For these reasons, they are not considered for demisting in the oil industry where the operating pressure is very high.

Electrostatic precipitators (ESPs) clean gases by using electrostatic force to remove the droplets suspended in the gas stream. They are not suitable for gas-liquid separation in the oil industry, especially offshore applications, because high voltages are required to run them, hence increasing the chances of an explosion. In addition, they are relatively more expensive, require more maintenance and have low gas handling capacity (i.e. low throughput per unit volume).

Knitted mesh demisters, made from interlocking loops of wire, are also a common type of demister. They are simple to operate, low in cost and pressure drop and also efficient in capturing small droplets. The separating mechanisms are a mixture of gravity deposition, direct interception, inertia deposition and diffusional deposition. However, the knitted wire mesh demisters can only work efficiently up to a certain velocity referred to as flooding velocity. Flows above this will cause entrainment of droplets into the downstream process. On the other hand, if the velocity is too low the smaller droplets will move with the gas

streamlines and not be collected. The limiting velocity is governed by the Souders-Brown equation (Equation 2.15).

For this project, knitted wire mesh demisters are used upstream of the cyclone units to collect droplets. At lower velocities they collect in the normal way, and they act as coalescers at the higher velocity, operating above the flooding point. In this regime smaller droplets will coalesce and larger drops leave the meshes. These re-entrained droplets can then be easily separated by another separator downstream.

Cyclone separators are well known for their simple construction, easy maintenance and for being relatively cheap to build and run. In common industrial practice, there are two types of cyclones namely reverse flow cyclone and uniflow cyclone (also known as axial flow cyclone or straight through flow cyclone). It is easier to separate a gas-liquid mixture because droplets coalesce with the liquid film on the cyclone wall, reducing the effect of turbulence mixing which for solid particles bring collected material back into the core gas flow. However, this film itself is susceptible to re-entrainment due to the shear effect between the gas and the liquid and this reduces the separation efficiency. Liquid creeping across the cyclone roof, down the vortex finder and radially inward into the vortex finder will reduce the efficiency as well. The common way around this problem is to have an anti-creep skirt around the vortex finder. Most of the previously published work was carried out on gas-solid separation using the reverse flow cyclone. Studies on uniflow cyclones on gas-liquid separation are relatively few.

Uniflow cyclones have lower pressure drop because there is no flow reversal within these cyclones. Therefore, they are chosen for the purpose of this research. Furthermore, they are easily placed in line with the flow when multicyclones are required to handle high gas flow capacities whereas the tangential inlet reverse flow cyclones introduce problems like maldistribution and would not be as compact as axial flow cyclones.

The pressure drop and the separation efficiency are the two major criteria determining the performance of the cyclones. It is desired to keep the pressure drop a low value and the efficiency high.

The total pressure drop is made up of the static and dynamic pressure with the losses across the cyclone in the entrance, the vanes, the separation space and the gas exit. There have been a lot of models developed over the years for predicting the pressure drop in reverse flow cyclones based on the cyclone geometry or based on the fluid dynamics in the cyclone. No model has been found yet to predict the pressure drop of the uniflow cyclones showing that the operation of this type of cyclone is not well investigated and understood. The closest prediction work carried out was the study by **Ramachandran *et al.* (1994)** on rotary flow cyclones.

In determining the system collection efficiency, the measurements are usually carried out under isokinetic sampling conditions. Probe misalignment and sampling line losses could be very significant due to inertial deposition; hence this has to be taken into account as well. Correlations have been developed to predict the collection efficiency of the sampling probe.

Like the pressure drop predictions, most of the models were developed to predict the separation efficiency of reverse flow cyclones. Among them were the Leith-Licth theory and the Dietz model. For uniflow cyclones, the earliest work done to predict their efficiency was carried out by **Stenhouse and Trow (1979)**. Besides using analytical models to predict the cyclone's performance, numerical models could serve this purpose as well, for instance using Computational Fluid Dynamics.

From the analysis of the available literature, it can be concluded that axial flow cyclones have a potential advantage in demisting processes over the other separation devices even the reverse flow cyclones. Therefore, in this work, there have been investigations to explore their potential in the oil industry and also to

gain a more thorough understanding of their behaviour. In the next chapter, the experimental methodology for this work is presented.

Chapter 3

Experimental Methodology

3.1 Introduction

This chapter specifies all the experiments carried out during the course of this research. The setup, procedures and aims of each of the experiments are described comprehensively. An overview of each type of experiment is tabulated in Table 3.1.

Flooding Studies	
Experiments	**Objectives**
Pressure drop measurement	To determine the pressure drop-flowrate characteristics for each cyclone geometry for both dry and wet operation.
Flow split measurement	To determine the amount of clean air leaving the vortex finder for various cyclone designs.
Onset of entrainment/re-entrainment	To find out the limitation of each cyclone geometry (i.e. the maximum liquid loading that could be handled before entrainment/re-entrainment occurs).
Grade Efficiency Studies	
Experiments	**Objectives**
Bench scale testing	To ensure that the particle analyser is in good working condition.
Grade efficiency measurement	To determine the performance of axial flow cyclone collecting liquid droplets as a function of drop size.

Table 3.1: Summary of experimental work undertaken.

3.2 Flooding/Re -entrainment studies

Figures 3.1 and 3.2 illustrate the overall experimental rig for the cyclone flooding/re-entrainment studies. The rig took up an area of 3 x 4 meters. In the proposed demisting system discussed earlier, a set of axial flow cyclones is to be operated in parallel inside a large vessel. However, in carrying out all the present experiments, only one axial flow cyclone was tested, operating with an air-water system. The support structure used to hold the cyclone consisted of a platform that was raised 1.6 m from the ground. The platform was raised so that a water tank could be slotted in under the cyclone. The tank was used to hold water flowing from the drainage system. The tank had a dimension of 1.63 x 0.81 x 0.51 meters. The water supply was taken straight from the mains supply. The raised platform was the core of the rig where readings and observations were made. Almost all the experimental apparatus was put on this platform. The framework was constructed from carbon steel. The platform tier was made of chequered plates. Flat boards were built around the edges of the framework for safety. This formed the basic structure for all the major experimental tests carried out.

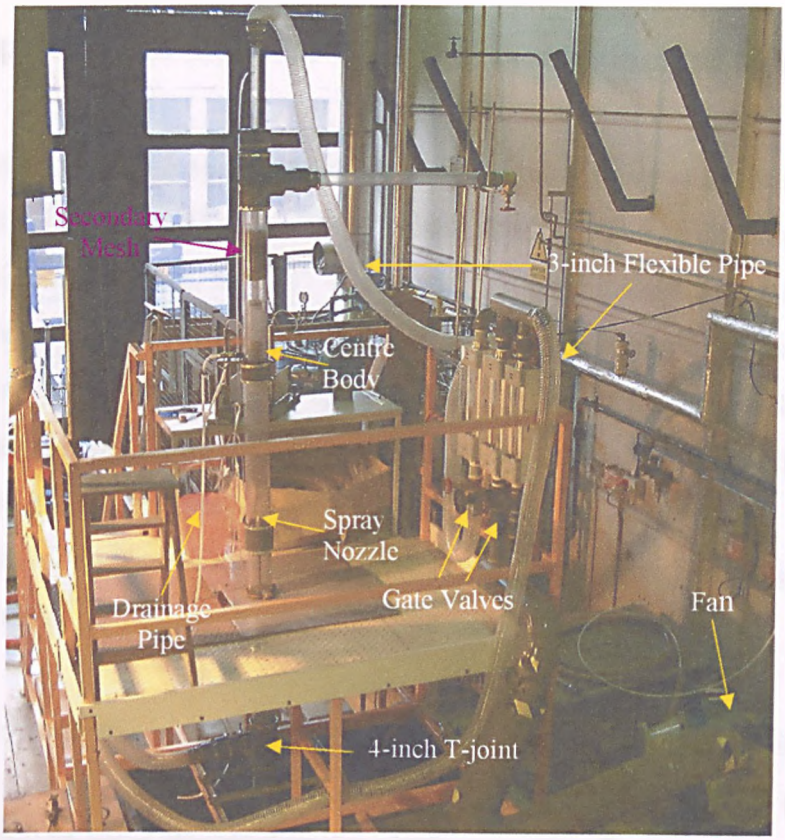

Figure 3.1: Experimental rig for flooding test (Overall view).

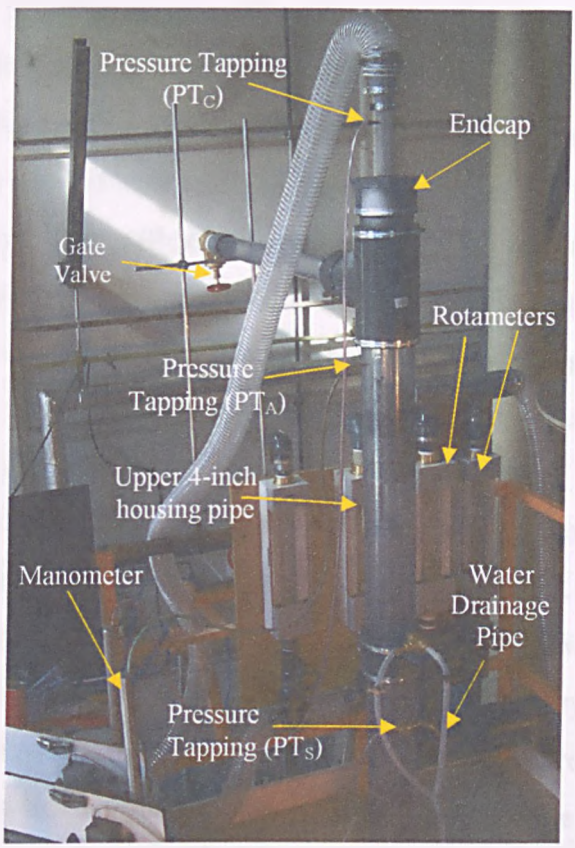

Figure 3.2: Experimental rig for flooding test (core section).

3.2.1 Experimental setup for flooding/re-entrainment tests

The work reported here focused on a single tube, representative of one unit in the bank of actual cyclones, operating in parallel. The cyclone was tested, operating with an air-water system. The primary knitted mesh was not included in the system for the flooding experiments because a great volume of water needed to be introduced and knitted meshes tend to flood under such high loadings. The cyclone alone was tested for its operability under such high loadings. The various cyclone designs investigated will be discussed in Chapter 4 (Cyclone Development). Figure 3.3 illustrates the overall rig assembly for the flooding/re-entrainment tests.

Air was supplied by a centrifugal blower via air rotameters providing inlet velocities within the 52 mm (inner diameter) cyclone tube of up to 20 m/s. The inlet air rotameters were mounted on the platform so that flows could be adjusted easily. The outlet air rotameters, used to determine the flow split, were also on this tier. The air flowrate was controlled using gate valves. Gate valves were used because they introduce only a small pressure drop when they are fully open. The pipe connecting the inlet air rotameters to the cyclone inlet is a 76 mm transparent, flexible ducting pipe (Crystaflex® ducting pipe from ARCO Limited). The rotameters were connected via a plain reducing socket and a 101 mm T-joint. This type of ducting was chosen because it would be a problem to bend a large diameter rigid pipe from the upper platform to below the platform. Furthermore, if there was water flowing into the air line it could be detected easily. This type of pipe was also used to connect the gas exit pipe (also known as the vortex finder) to the air rotameters to minimise the dynamic pressure at the outlet and any trace of water in the gas outlet could then be detected easily as well. Water was supplied beneath the separator through spray nozzles giving a solid spray cone. Different types of nozzle, as shown in Figure 3.4, were used in order to provide the flowrate required for different liquid loading tests. The water flowrate was set, via the pressure regulator, to give the liquid loading required. Liquid loading is defined as

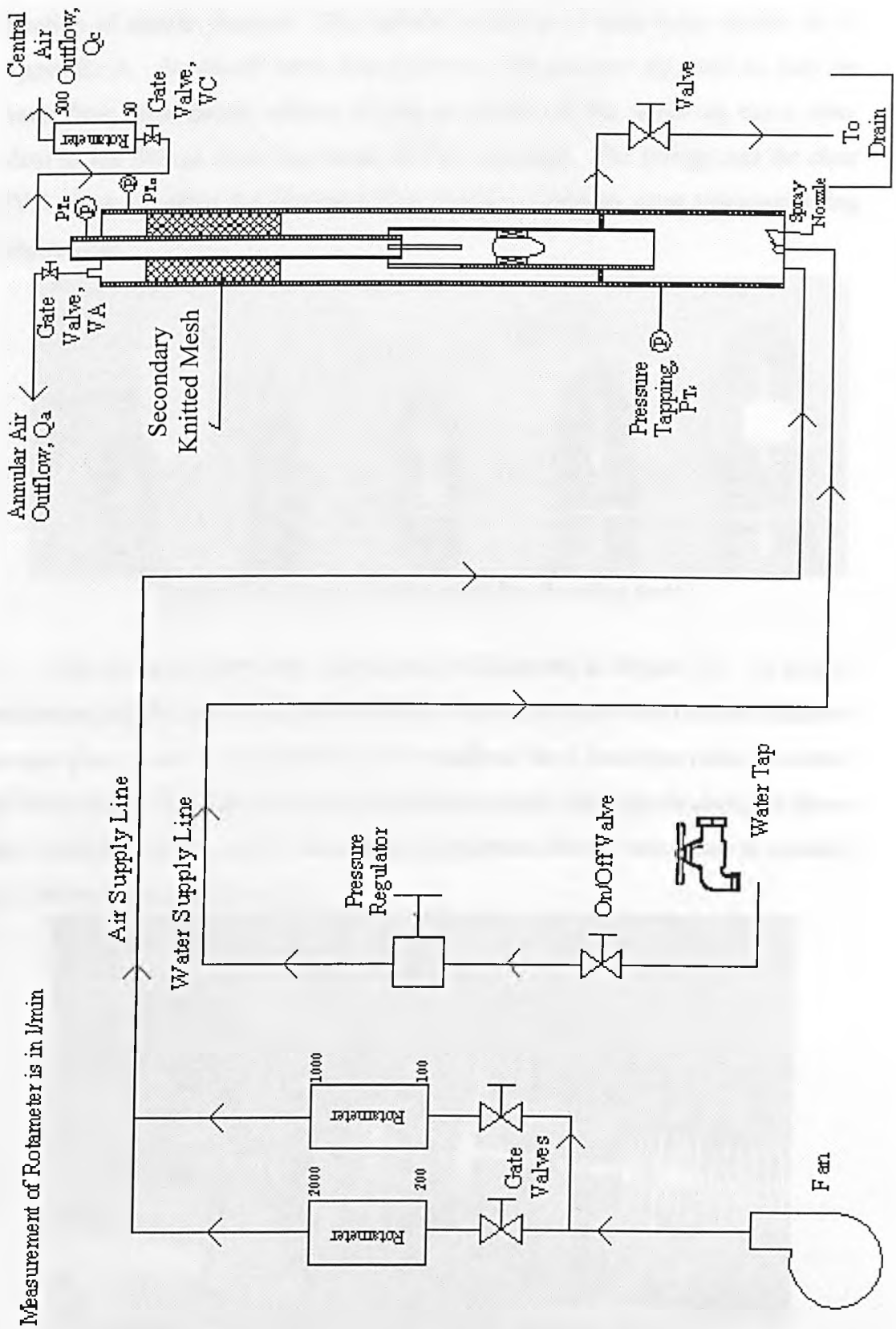

Figure 3.3: Overall rig assembly for flooding/re-entrainment test.

the ratio of water to air in volume percent (L % v/v). The water flow rate is a function of nozzle pressure. The calibration curves of each spray nozzle are in Appendix A. An on-off valve was put before the pressure regulator to stop the water flow immediately without having to switch off the water tap every time. Most of the fittings used were made of PVC durapipe. The fittings and the clear PVC pipes (supplied by Glynwed Pipe Systems Limited) were tightened using jubilee clips.

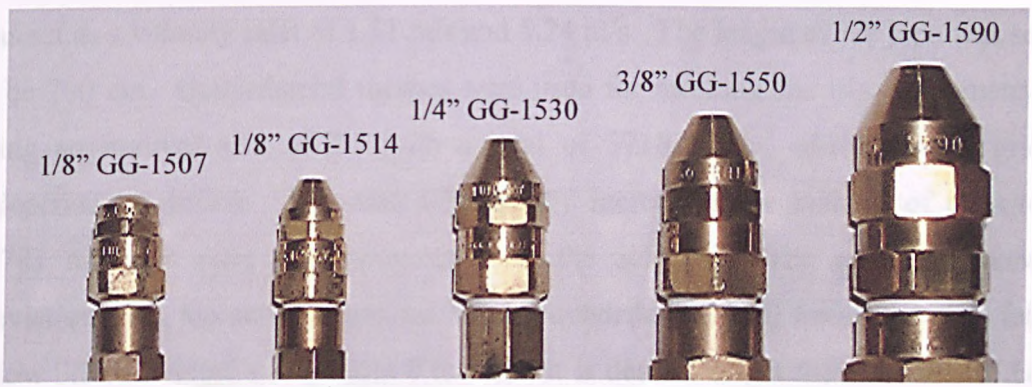

Figure 3.4: Spray nozzles used for flooding tests.

The air and water inlet connection is illustrated in Figure 3.5. A nylon-reinforced polyethylene pipe connected the water tap to a 9 mm internal diameter copper pipe, which was inserted into the middle of the 4-inch pipe (inner diameter of 101.6 mm). The pipe insertion to the bottom 4-inch pipe was located just above the Tee-joint. At the end of the copper pipe, enots fittings were used to connect the different spray nozzles used.

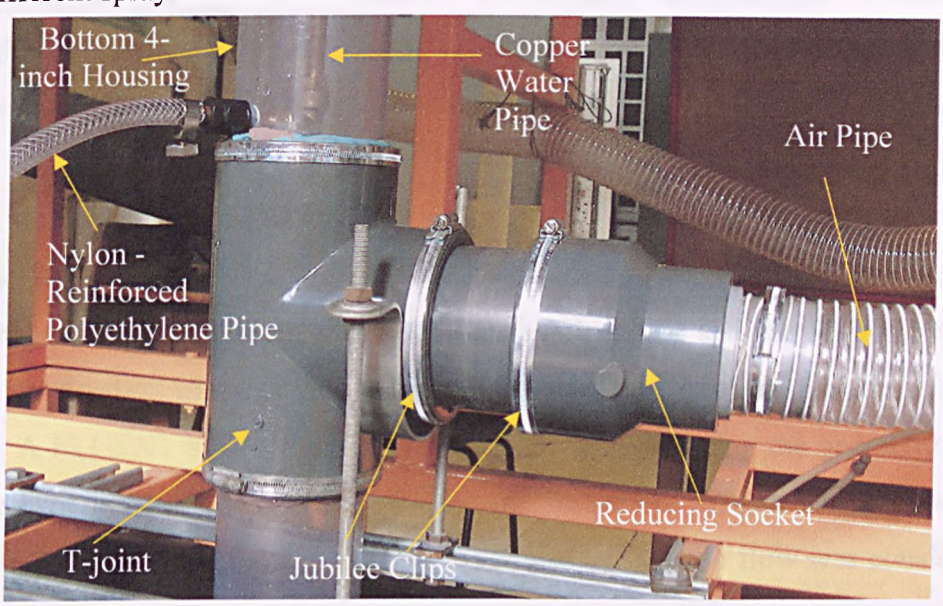

Figure 3.5: Connections of the air and water inlet.

It was intended to have a fairly uniform gas flow upon reaching the cyclone tube. Therefore, a FLUENT simulation was conducted to obtain the required pipe length that gives a uniform flow distribution. The lowest and the highest inlet velocities investigated were 5 m/s and 20 m/s respectively through the cyclone tube, which corresponded to 1.31 and 5.24 m/s in the housing pipe. This is the typical velocity range that the actual cyclone in the multicyclone arrangement is required to handle **(Davies, 2000)**. Therefore, the inlet boundary of the geometry was set as a velocity inlet of 1.31 m/s and 5.24 m/s. The length of the pipe was set to be 200 cm. Quadrilateral meshes were used for meshing the whole geometry, using an interval size of 2.5 with a total of 37187 cells, which gave a grid independent solution. This was achieved by increasing the number of cells to 55781 and this gave no improvement to the solution. The equiangle skew (deviation from the actual angle, i.e. 90^0 for quadrilateral cell) for all the cells fell below 0.1 (the range varies from 0 to 1.0). It is desired to get the skewness to be as small as possible to avoid a diverged solution. At 1.31 m/s and 5.24 m/s, the Reynolds number is 8,873 and 35,492 respectively (inner diameter = 0.1016 m, ρ = 1.2 kg/m^3, μ = 1.8 x 10^{-5} Ns/m^2), which is a turbulent flow. Therefore, the standard k-ε model with standard wall function was selected for solving this 2D problem because this is just a simple turbulent problem and a 2D solution is sufficient to give the information required. The velocities were plotted and it is clearly shown in Figure 3.6a, b that the flow is fairly uniform after 140 cm. The length of the housing pipe used for all the experiments was 190 cm. This was a lot longer than required. It was made so for the ease of visualisation by the operator.

On the same piece of the housing pipe, there is a pressure tapping (PT_S). It is not desirable to have water going into the pressure tapping and since there will be recirculation in the annulus of the 101-mm housing pipe and the 52-mm cyclone pipe, the position of the pressure tapping was designed to avoid the recirculation area. A FLUENT simulation was again conducted replicating the geometry used in the experiment. The cyclone tube was inserted about 82 mm into the housing pipe (diameter = 100 mm and length = 750 mm). Since the flow was considered uniform upon reaching the cyclone tube, the length was not a critical parameter.

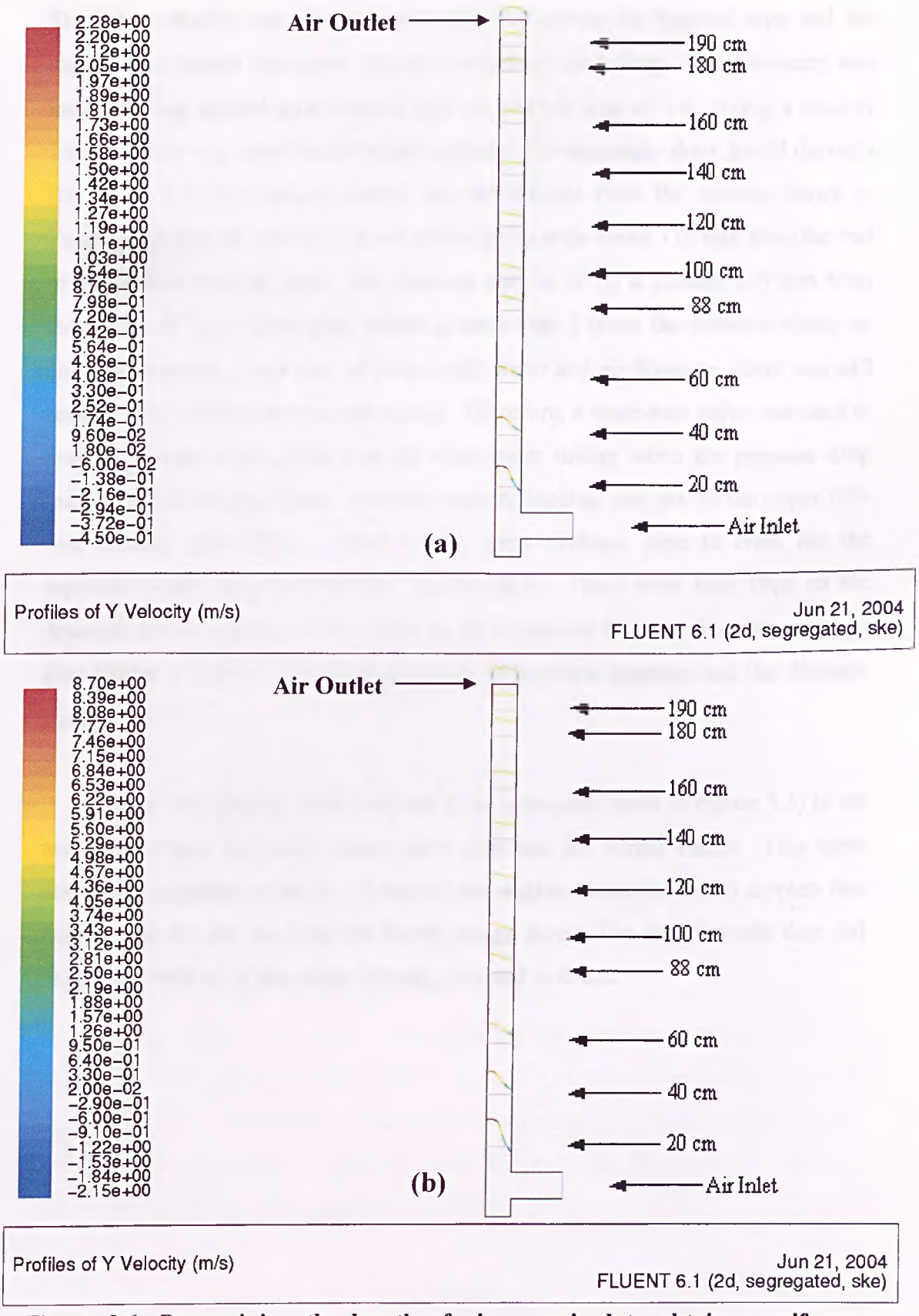

Figure 3.6: Determining the length of pipe required to obtain a uniform velocity profile (a) at the lowest inlet velocity of 1.31 m/s and (b) the highest inlet velocity of 5.24 m/s.

The inlet velocity was set at 5 m/s uniformly across the housing pipe and the standard k-ε model was again used for turbulence modelling. This geometry was meshed using quadrilateral meshes with an interval size of 2.0, giving a total of 19652 cells to a get grid independent solution. The equiangle skew for all the cells fell below 0.1.The velocity vector was plotted and from the results, shown in Figure 3.7 it can be seen that the air recirculation ends about 113 mm from the end of the bottom housing pipe. The pressure tapping (PT_S) is located 235 mm from the mouth of the cyclone tube, which is more than 2 times the distance where re-circulation occurs. However, at a very high water and air flowrate, water was still seen flowing into the manometer tubing. Therefore, a three-way valve was used to avoid the water from going into the manometer tubing when the pressure drop reading was not being taken. Another pressure tapping was put on the upper 100-mm housing pipe (PT_A). There was a water drainage pipe to drain out the separated water droplets from this housing pipe. There were hose clips on the drainage pipe to regulate flow so that the air would not flow out from the drainage pipe (Refer to Figure 3.2 for the positions of pressure tappings and the drainage pipe).

There was another mesh (referred to as secondary mesh in Figure 3.3) in the annulus between the upper 4-inch outer pipe and the vortex finder. This mesh acted as a secondary collector. It trapped and agglomerated the liquid droplets that flowed with the air out from the liquid escape slots. The liquid would then fall back to the bottom of the upper housing pipe and to drain.

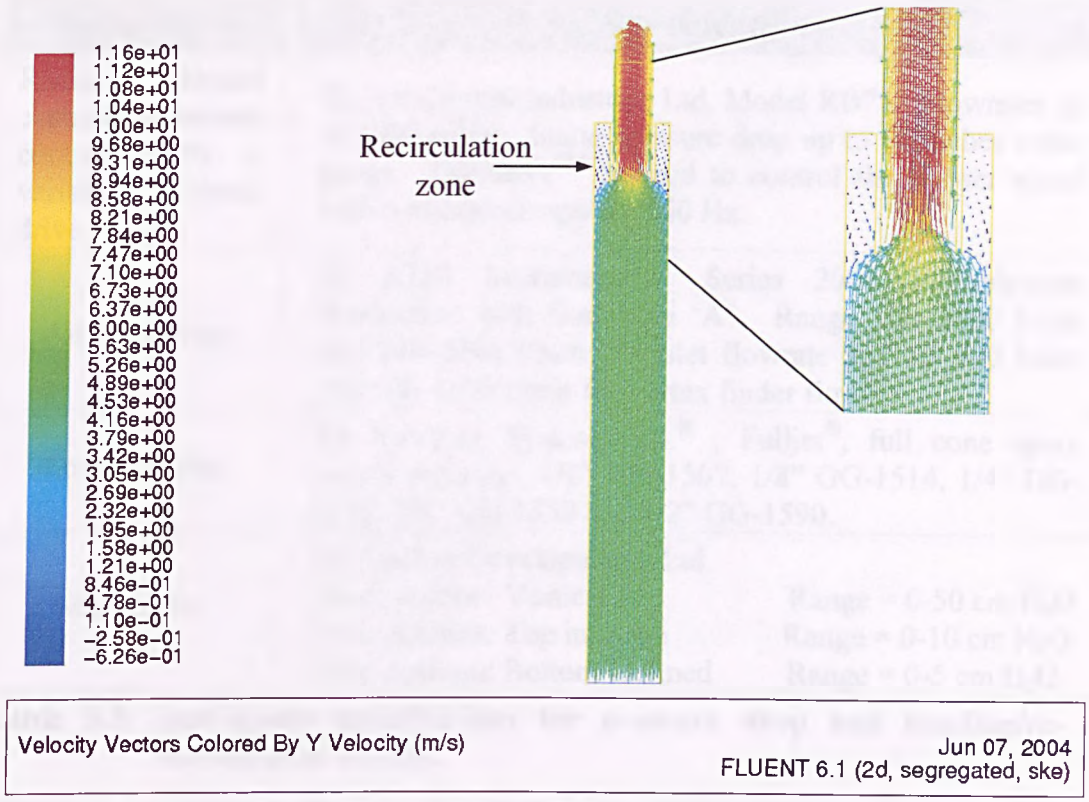

Figure 3.7: Determining the position of the inlet pressure tapping (PT_S) avoiding the recirculation zone in the annulus of the housing pipe and the cyclone tube.

The vortex finder was either connected to a 50 - 500 l/min or a 100 – 1000 l/min rotameter via gate valves (VC) depending the amount of air flowing out from the vortex finder. Only one of these valves was opened at any time. Another pressure tapping (PT_C) was put on the vortex finder. The gas that came out through the liquid escape slots flowed out of the upper housing pipe via a 90^0 Tee. The straight end of the Tee was blocked with an endcap. The gas flow was also controlled by a gate valve (VA). The pressure drop measurements were taken from PT_S to PT_A and from PT_S to PT_C. The static pressures were also measured from PT_A to PT_C. Manometers were used to measure the system pressure drop. Details of the instrument used for pressure drop-flowrate characteristics and the flooding/re-entrainment tests are given in Table 3.2.

Instrument	Specifications
Radial bladed centrifugal blower controlled by a variable speed drive	By Air Control Industries Ltd, Model RB75. Flowrates up to 1000 m^3/hr. Static pressure drop up to 65 inches water gauge. Optidrive™ is used to control the blower speed with a maximum speed of 60 Hz.
Air rotameters	By KDG Instruments. Series 2000 Variable-area flowmeters with float type 'A'. Range 100–1000 l/min and 200–2000 l/min for inlet flowrate and 50–500 l/min and 100–1000 l/min for vortex finder flow.
Spray nozzles	By Spraying Systems Co.® , Fulljet®, full cone spray (small capacity). 1/8" GG-1507, 1/8" GG-1514, 1/4" GG-1530, 3/8" GG-1550 and 1/2" GG-1590.
Manometer	By Airflow Developments Ltd. Tube position: Vertical Range = 0-50 cm H_2O Tube position: Top inclined Range = 0-10 cm H_2O Tube position: Bottom inclined Range = 0-5 cm H_2O

Table 3.2: Instrument specifications for pressure drop and flooding/re-entrainment studies.

The first geometry to be tested was the initial design with a centre body swirler made up of six stationary guide vanes to create centrifugal force and liquid escape slots as detailed in Figures 4.5 and 4.6 in Chapter 4.

3.2.2 Experimental Measurements

For flooding/re-entrainment tests, the variables of interest are as follows:

(i) Air Flowrate
(ii) Water Flowrate
(iii) Liquid Loading (L % v/v)
(iv) Pressure drops across the cyclone
(v) Euler Number, Eu

The air flowrate was measured using the rotameters with control available through the adjustment of gate valves. The velocity range to be tested inside the

52 mm inner diameter cyclone pipe was from 5 to 20m/s. The volumetric air flowrate, Q_g, can be obtained from the product of velocity, U_{in}, and the cross-sectional area of the cyclone tube (A_{CT}). The relationship is expressed as (Equation 3.1):

$$Q = U_{in} A_{CT} \qquad \textbf{-Equation (3.1)}$$

Therefore, the lower and upper limits for the air volumetric flowrate are 637 l/min to 2548 l/min respectively with the cross-sectional area of the cyclone tube being $\pi(0.052)^2/4 = 0.002124\ m^2$.

From the conservation of mass, the amount of air flowing into the 2-inch diameter cyclone pipe will equal the air flowing into the bottom 4-inch outer pipe. The amount of liquid required depends on the liquid loading. Equation 3.2 defines liquid loading, which is the ratio of water to air in volume percent (v/v %).

$$\text{Liquid Loading} = \frac{\text{Volume of Liquid}}{\text{Volume of Air}} \text{x} 100\% \qquad \textbf{- Equation (3.2)}$$

The dimensionless Euler number, Eu, when both water and air are present is expressed below.

$$Eu = \frac{\Delta P_{cyclone}}{0.5 \rho_f U_{in}^2}$$

where

$\Delta P_{cyclone}$ = Pressure drop across cyclone (Pa)

U_{in} = cyclone inlet velocity (m/s)

ρ_f = Fluid density (kg/m^3)

$= \rho_g(1-L) + \rho_W L$

ρ_g = air density (1.2 kg/m^3)

ρ_W = water density (1000 kg/m^3)

L = Liquid loading (m^3 water/m^3 air)

A conventional manometer was used to measure the pressure drop across the cyclone and a 3-way valve was used to prevent the water from going into the

manometer tubing. The experimental procedures for flooding/re-entrainment test can be found in Appendix B.

3.3 Grade Efficiency Studies

Grade efficiency measurements required the introduction of a much smaller quantity of finer droplets of diameter of the order 0.4 to 20 microns. The fine droplets were produced using a nebuliser. The grade efficiency tests used a water aerosol stabilised with glycerol, $C_3H_5(OH)_3$, in order to avoid drop size changes from evaporation. The composition of this aerosol was 87% water and 13% glycerol **(Krishnan, 1999)**. The drops of glycerol-water represent an ideal spherical particle system, hence the droplet size distribution can be measured accurately. An optical particle analyser (Polytec HC-15), which has also been used by other researchers **(Buttner and Ebert, 1989; König, 1991; Mitchell *et al.*, 1989)**, is used to measure the fractional efficiency. The detailed operating instructions for this equipment are discussed in Appendix C. According to **König (1991)**, the light scattering particle analyser has two great advantages:

(i) The aerosol is analysed without any contact with the measuring system and
(ii) The particles are analysed very fast on-line.

Isokinetic sampling is required to ensure that sample is removed at the same velocity as that of the local bulk flow in the pipe and thus is a true representation of the total flow in the pipe. Grade efficiencies can be determined by comparing inlet and outlet measurements. Prior to these tests, significant effort was spent on validation of the calibration of Polytec by means of an appropriate nebuliser system.

3.3.1 Introduction to Bench Scale Testing

For grade efficiency measurements, a light scattering particle analyser, Polytec HC-15 was used. The analyser was tested at a bench scale before it was used for the large scale grade efficiency tests to ensure that it was working well in measuring the droplets in the desired range, 0.4 – 20 μm. This section gives an overview of the particle analyser, the calibration process and the repeatability tests. Figure 3.8 shows the schematic diagram of the setup of the calibration rig.

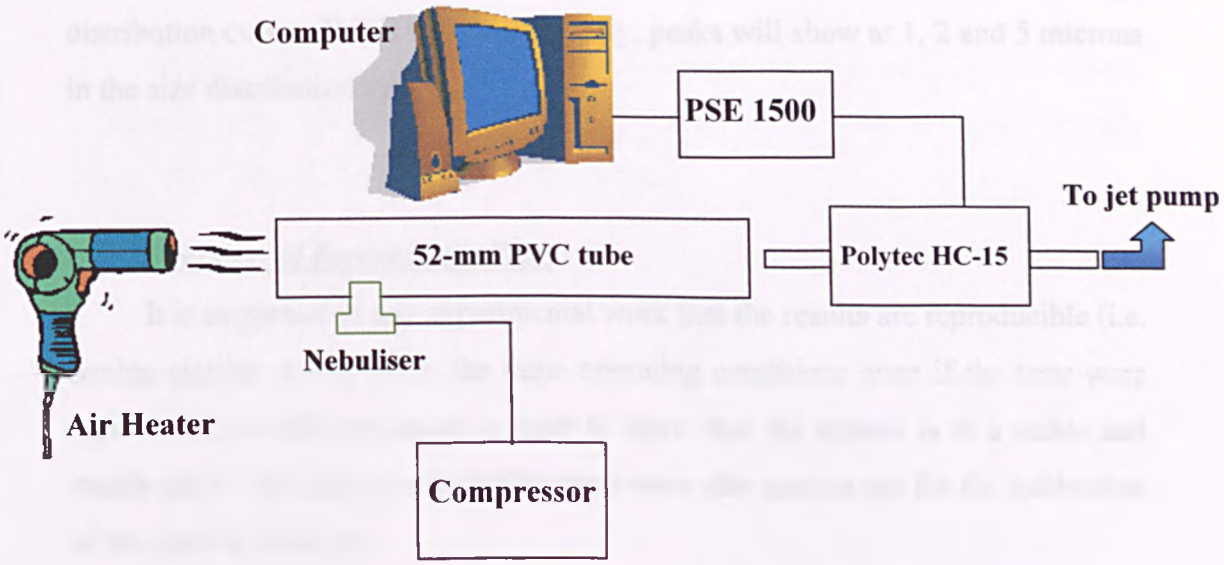

Figure 3.8: Schematic diagram of the calibration rig to determine the reliability of the analyser.

- *Overview of Polytec HC-15*

Measurement using Polytec HC-15 is performed on individual particles as they move through a small measuring volume. The measuring volume is defined optically in the flow field. The lenses of two optical systems are set at right angles. One system (illumination system) illuminates the measuring volume and the other detects the scattered light (observation system). The light scattered by the particles is collected and amplified by the photomultiplier and transformed into electrical pulses, which are a measure of the individual particle size. A more detailed description is provided in Section 3.3.2.

- *Overview of Calibration*

Before using the particle analyser, it was tested with some known sizes of latex particles using a specially set up calibration rig. A mixture comprising latex particles of 1, 2 and 5 microns was passed through the Polytec. The cocktail of latex particles (1, 2 and 5 microns) was supplied by LGC Promochem. The data provided by LGC Promochem can be found in Appendix D. Distilled water was used for the dilution of the suspensions. The drops were produced using a nebuliser. The nebuliser system was supplied by Glenmore Health Limited. The results from Polytec HC-15 were then analysed for the peaks in the size distribution curve. If it is working properly, peaks will show at 1, 2 and 5 microns in the size distribution curve.

- *Overview of Repeatability Tests*

It is important in any experimental work that the results are reproducible (i.e. having similar results under the same operating conditions even if the tests were carried out on different days) in order to show that the system is in a stable and steady state. Therefore, repeatability tests were also carried out for the calibration of the particle analyser.

3.3.2 Polytec HC-15 Description

The Polytec HC15 (Figure 3.9) is suitable for the investigation of all types of aerosol, for example droplets from sprays and nozzles, solid and liquid particles in smoke and gases, and air dispersed powders. The droplet concentration (by number) and size distribution were obtained by measuring the light scattered by a single particle moving through a small, optically defined measuring volume located in the flow. The two important parts of this analyser are its optical head (where the particle detection takes place) and the electronic controller unit (where data are received and stored).

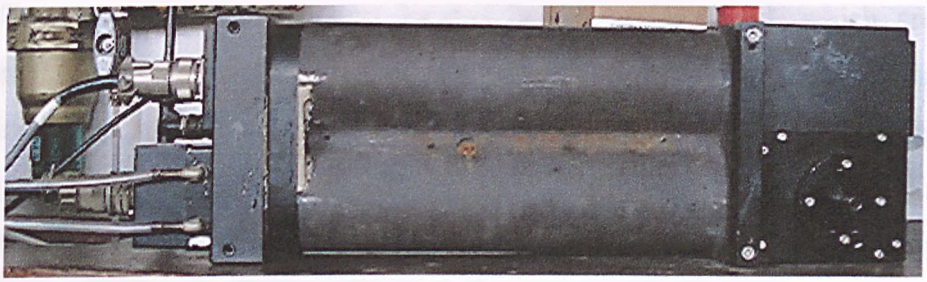

Figure 3.9: View of the particle size analyser Polytec HC-15.

3.3.2.1 Function of Optical Head

The analyser is a black rectangular box with dimensions of 555mm in length, 192mm in height and 100mm in width (See Figure 3.10). It weighs approximately 16kg. The optical head is shown in Figure 3.11.

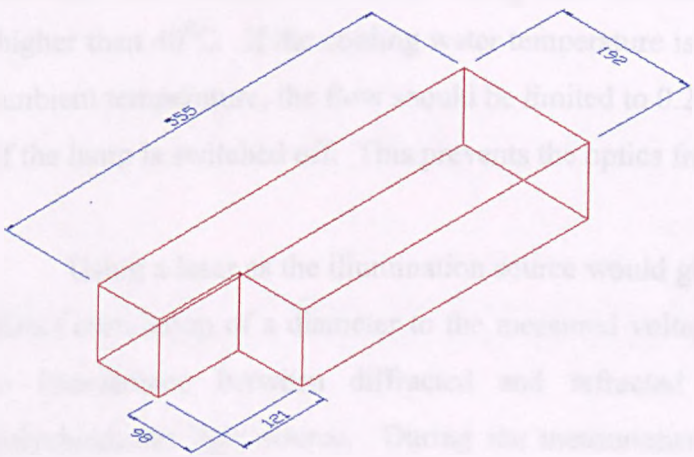

Figure 3.10: Dimensions (in mm) of the analyser.

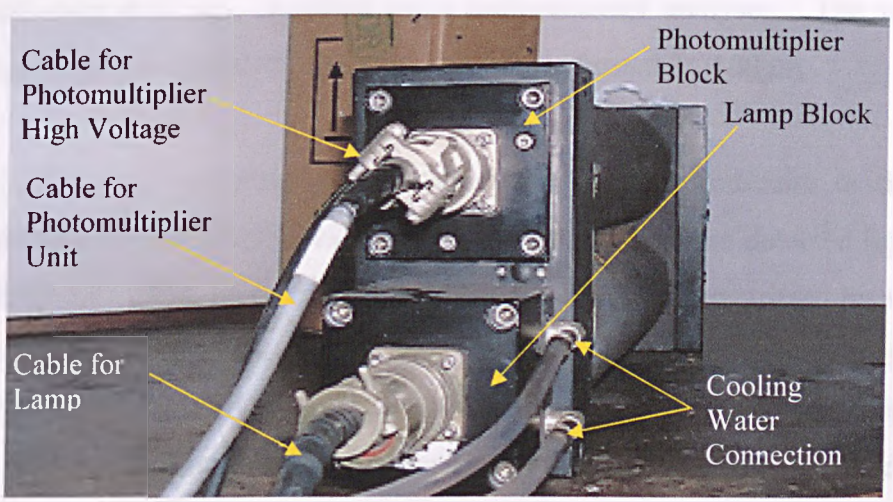

Figure 3.11: Optical head shown from the connection end (lamp and photomultiplier unit).

There are 2 optical systems located in the optical head, which are the illumination system and the observation system. Both the optical systems are positioned perpendicular to the flow direction. The illumination system images a rectangular aperture, which is illuminated by a 100W halogen lamp. The optics of both of the illumination and observation systems are located in a stable aluminium case. It is because of this housing that the need for further adjustment during operation and frequent cleaning of the optics inside is unnecessary. The lamp module is cooled by running tap water through it to prevent overheating of the optical head and prolong the lifetime of the lamp. A rubber tube of 6 mm inner diameter was used to connect the water tap to the cooling water connectors. A thermo switch in the lamp module switches off the lamp if it is overheated. The high heat capacity of the optical head allows operation without cooling for 10 minutes. The temperature of the casing near the halogen lamp should never be higher than 40^0C. If the cooling water temperature is significantly colder than the ambient temperature, the flow should be limited to 0.2 l/min and should be stopped if the lamp is switched off. This prevents the optics from being coated by moisture.

Using a laser as the illumination source would give a higher sensitivity, but a direct correlation of a diameter to the measured voltage would be impossible due to interference between diffracted and refracted light. The HC uses a polychromatic light source. During the measurement, peak values of scattered light are measured and classified by a multi-channel analyser. The range of measurable drop diameter of the Polytec HC-15 is from 0.3 - 100μm.

The lens of the observation system is set up perpendicular to the flow direction and the illumination system. The mirror reflects the detected light onto the cathode of a photo multiplier, the visual field of which is restricted by a square aperture. This configuration produces a small cubic measuring volume inside the flow channel in which all the particles are both illuminated by the light source and also within the detection aperture of the photomultiplier. The light scattered by the particles is collected and amplified by the photomultiplier and transformed into electrical pulses. The optical head is suitable for measuring particles in the wide

velocity range of 0.1 to 20m/s. In the standard version, the controller PSE 1500 is adjustable for the velocity range of 2 to 10m/s. The calibration is at 5m/s; hence for best results the measurement should also be at 5m/s. The particle velocity, in this range, has a negligible influence on the calibration (Polytec manual) and tests were also carried out to prove this (See Figure 3.12).

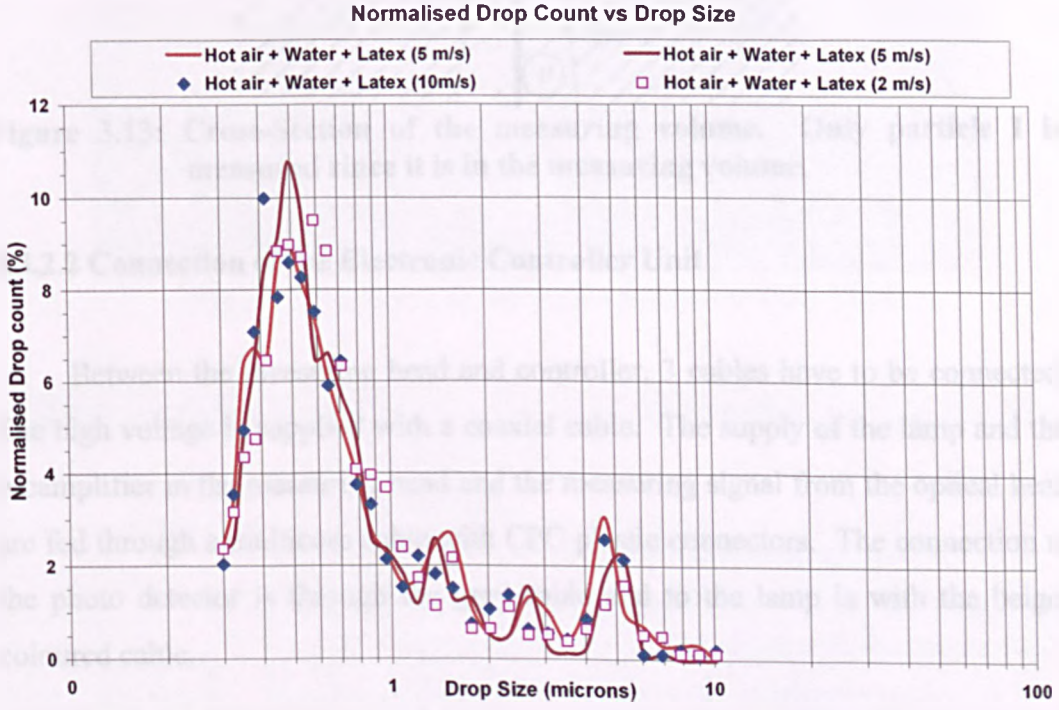

Figure 3.12: Tests showing that measurements will not be influenced by the varying of velocity in the range of 2 – 10 m/s.

Only particles on the intersection area of both optical paths will be detected. Figure 3.13 further illustrates the measuring volume for the particles. Let area I be the optical path of illumination system and area II shows the optical path of the observation system. Particles, which are located into area I are illuminated, and particles located in area II are observed. Particles outside the measuring volume are only either illuminated or observed. So, these particles are not measured. Particles neither in area I nor II are also not measured.

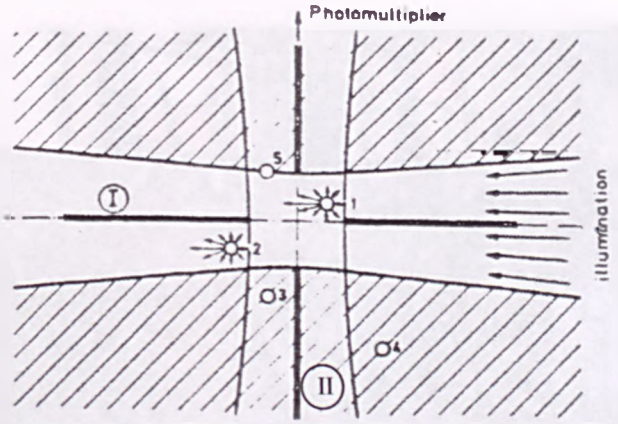

Figure 3.13: Cross-Section of the measuring volume. Only particle I is measured since it is in the measuring volume.

3.3.2.2 Connection of the Electronic Controller Unit

Between the measuring head and controller, 3 cables have to be connected. The high voltage is supplied with a coaxial cable. The supply of the lamp and the preamplifier in the measuring head and the measuring signal from the optical head are fed through a multicore cable with CPC plastic connectors. The connection to the photo detector is through the grey cable and to the lamp is with the beige-coloured cable.

The connections to the detector and the lamp have a different pin-configuration so that the instrument cannot be damaged, as the cables cannot be inserted into the wrong sockets. Figures 3.14, 3.15 and Table 3.3 show and list the function of the different sections of the signal processor PSE 1500. Besides using a computer, data can be keyed in from the signal processor using 16-key keyboard. Further details can be found in Appendix C.

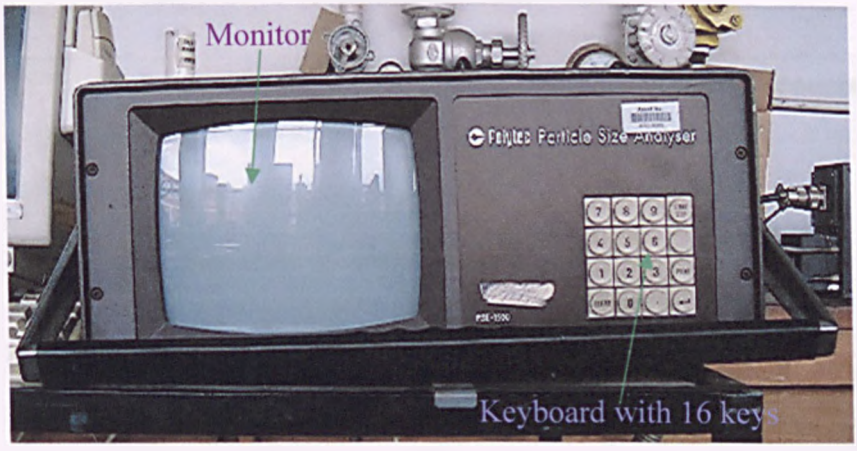

Figure 3.14: Front view of the signal processor PSE 1500.

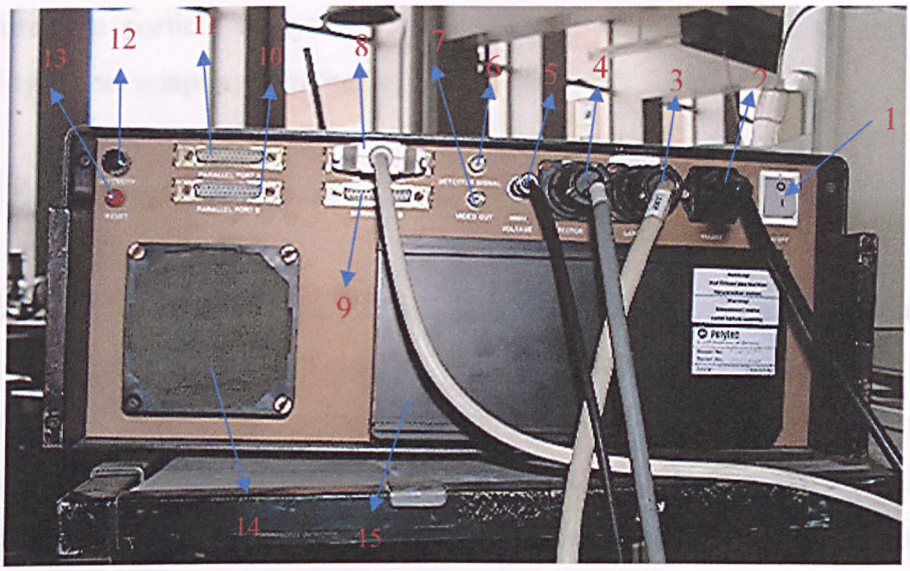

Figure 3.15: Back of the signal processor PSE 1500.

Part Number	Functions
1	AC Power Switch
2	AC-Connector
3	Connector for the lamp in the measuring head
4	Connector for the photomultiplier in the measuring head
5	HV-Connector for the photomultiplier in the measuring head
6	Signal from the photo detector, monitor output
7	Connection for additional monitor
8	Connection for serial interface "Port A" (external computer)
9	Connection for serial interface "Port B" (printer)
10	Parallel interface "Port A" (Option)
11	Parallel interface "Port B" (Option)
12	Intensity adjustment for the screen
13	Reset-Button
14	Ventilator with filter
15	Lamp power supply

Table 3.3: Function of each part of the signal processor PSE 1500.

3.3.3 Calibration of Polytec HC-15

Calibration is essential for any measuring device to ensure that the values showing on the scale of the device correspond to the actual measured value.

Therefore, the particle analyser, Polytec HC-15, was calibrated to ensure its reliability before adapting it to the large scale grade efficiency tests.

3.3.3.1 Experimental Apparatus

A cocktail of latex particles comprising particles of 1, 2 and 5 microns was used for calibrating the particle analyser. Distilled water was used for the dilution of suspensions because dissolved impurities will form separate sub-micron particles as well as coating the surface of the latex particles to make them larger. The experimental set up for the calibration test is shown in Figure 3.8 and the detail of the jet pump connection is shown in Figure 3.16. Polymer latex particles are easily aerosolised from suspension by nebulisation, providing adequate provision is made to dry the particle containing droplets produced by the nebuliser. For this, an air heater (Vidal Sassoon Maximum, Model VS543UK) with multiple heat settings was used to vapourise the mists from the nebuliser. The latex particles, mixed with distilled water, were sucked through the Polytec, which was connected to a jet pump via a tube of 52 mm diameter and 600 mm in length. When air flows through the jet pump, a low pressure region occurs at the junction due to a reduction in the area, hence the suction. The jet pump was connected to a rotameter, which was connected to the Polytec outlet (Figure 3.16). Compressed air at 2 bar was passed through the jet pump. The flowrate was controlled using an on/off valve so that the velocity inside the Polytec channel was around 5 m/s.

The nebuliser system is supplied by Glenmore Health Limited. The commercial name of the nebuliser is AquaTOWER2^{TM}. A piston compressor was used to produce the water droplets (See Figure 3.17). Care should also be taken when selecting an appropriate suspension concentration for use with nebuliser. The probability of nebulised droplets containing the formation of multiple particles (duplets, triplets, etc.) is a significant inconvenience when generating calibration aerosol. The mist from the AquaTower2^{TM} is mainly in the range of 0.5 to 5 microns range.

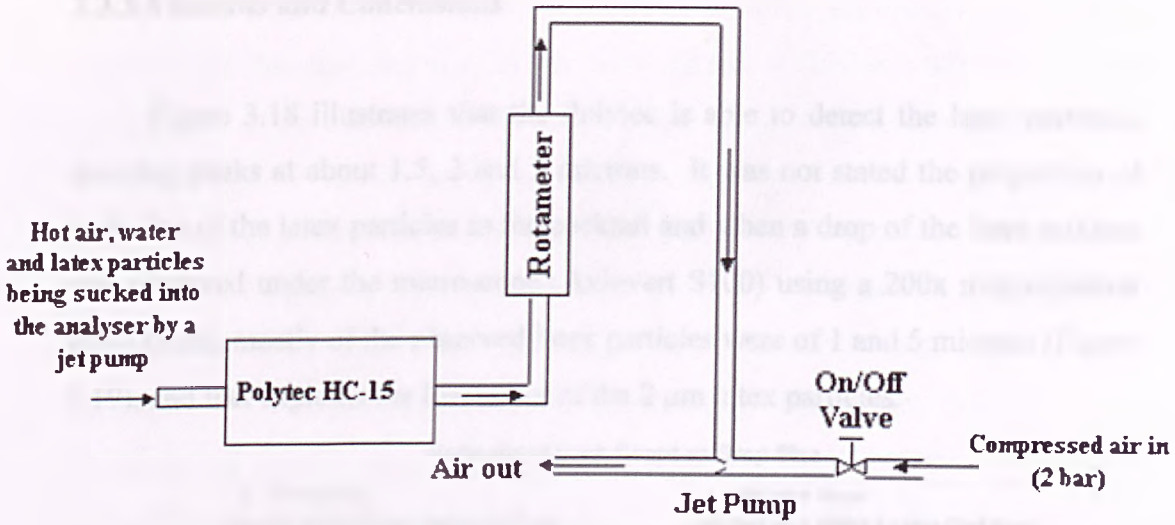

Figure 3.16: The jet pump connection for the calibration tests.

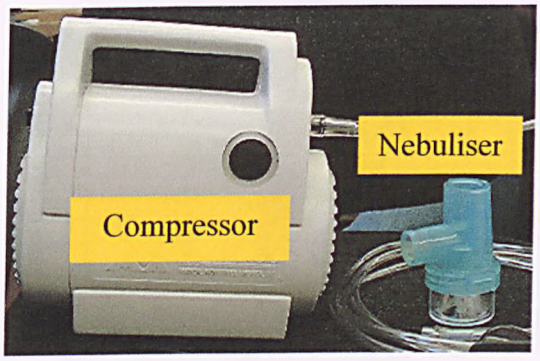

Figure 3.17: The nebuliser system used to produce droplets for the calibration tests.

3.3.3.2 Calibration Method

1. One drop of latex from the cocktail was mixed with distilled water in the nebuliser container and topped up to 10 ml.
2. The Polytec was connected to the jet pump and compressed air at 2 bar was used to suck air through the measuring volume.
3. The flowrate is controlled using an on/off valve so that the velocity passing through the Polytec is around 5 m/s for best results because the equipment calibration is at that velocity.
4. The air heater is switched on to evaporate the water suspending the latex particles and then the nebuliser is switched on.
5. Measurements were taken with different heat settings to make sure that all the water droplets are vaporised before going into the measuring volume.
6. A graph of drop count vs. particle size was plotted.

3.3.3.3 Results and Conclusions

Figure 3.18 illustrates that the Polytec is able to detect the latex particles, showing peaks at about 1.5, 2 and 5 microns. It was not stated the proportion of each size of the latex particles in the cocktail and when a drop of the latex mixture was observed under the microscope (Axiovert S100) using a 200x magnification lens (Zeiss), mostly of the observed latex particles were of 1 and 5 microns (Figure 3.19), and that explains the low count of the 2 μm latex particles.

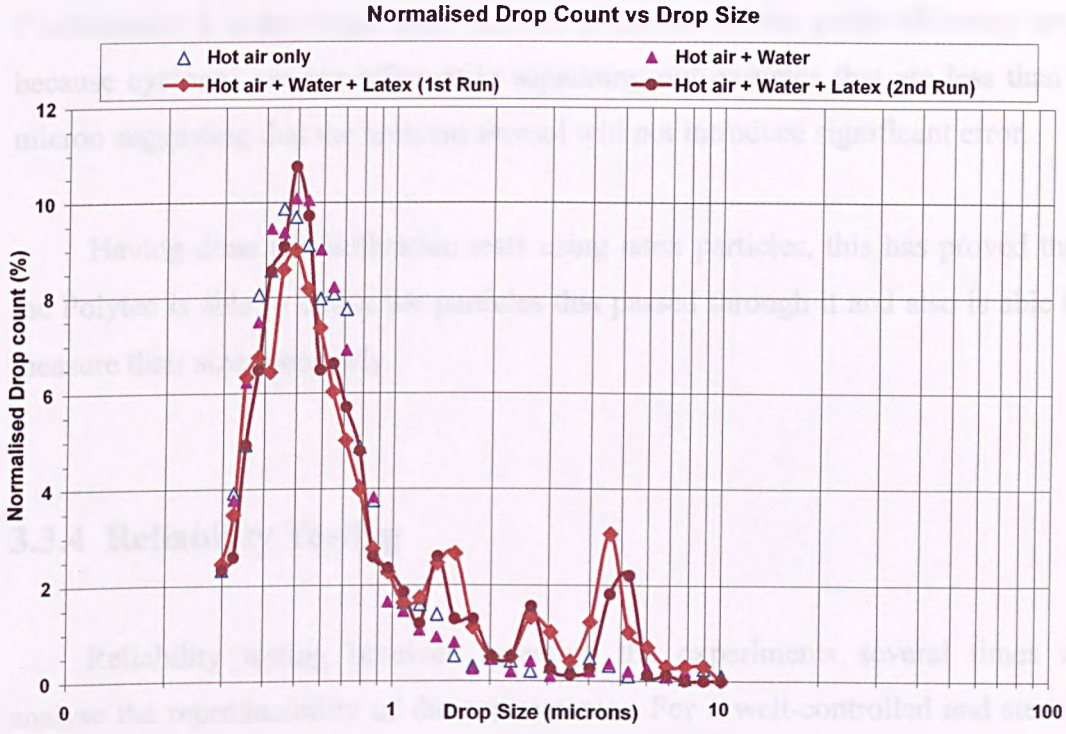

Figure 3.18: Polytec showing peaks at 1.5, 2 and 5 microns.

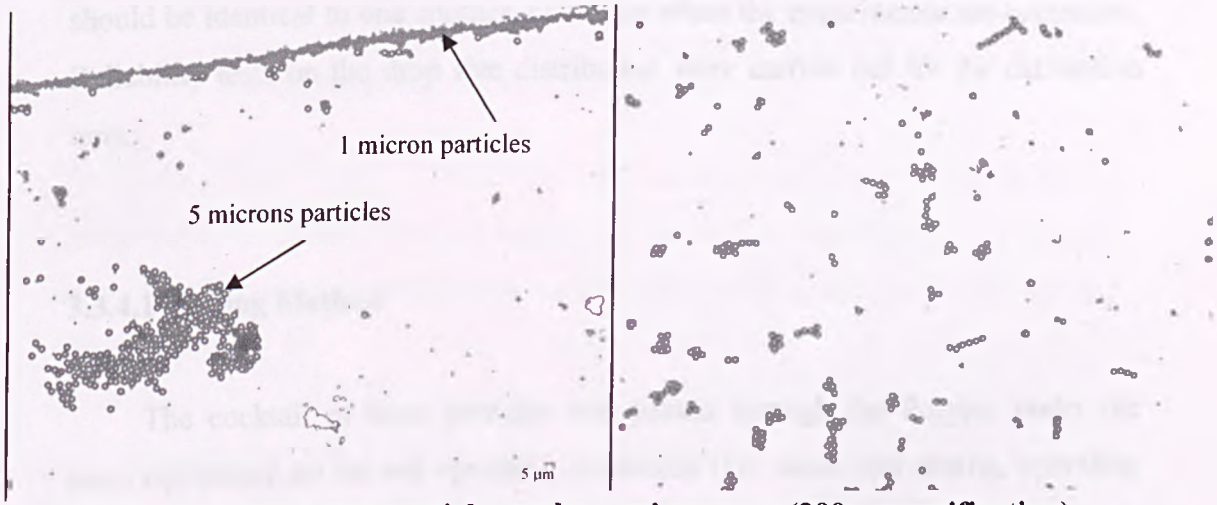

Figure 3.19: Latex particles under a microscope (200x magnification).

There were relatively higher numbers of particles detected below 1 micron because of the dust present in the atmosphere. This is confirmed by the background count carried out with just pure air being sucked through the Polytec. From Figure 3.18, it also shows that the air heater managed to evaporate the water droplets and only the latex particles went through the Polytec since both the curves, hot air with water droplets and the hot air only curve are identical. Although dust is bound to be detected, this is not substantial because the total count of water droplets in the actual experiment is significantly higher than the dust count. Furthermore, it is the larger sizes that are of interest in the grade efficiency tests because cyclones are not efficient in separating out particles that are less than 1 micron suggesting that the ambient aerosol will not introduce significant error.

Having done the calibration tests using latex particles, this has proved that the Polytec is able to detect the particles that passed through it and also is able to measure their size accurately.

3.3.4 Reliability Testing

Reliability testing involves repeating the experiments several times to analyse the reproducibility of the experiments. For a well-controlled and steady system, the results obtained, under the same setting and operating conditions, should be identical to one another, no matter when the experiments are conducted. Reliability tests on the drop size distribution were carried out for the calibration tests.

3.3.4.1 Testing Method

The cocktail of latex particles was passed through the Polytec under the same equipment set up and operating conditions (i.e. same heat setting, operating

pressure, method of preparing the solution, and so on) for several continuous runs and also the same experiment was repeated on different days.

3.3.4.2 Results and Conclusions

All the tests (i.e. air only, mixture of air and water and mixture of air, water and latex particles) were carried out several times to determine the reproducibility of all the tests. The results are plotted in Figures 3.20 and 3.21 below.

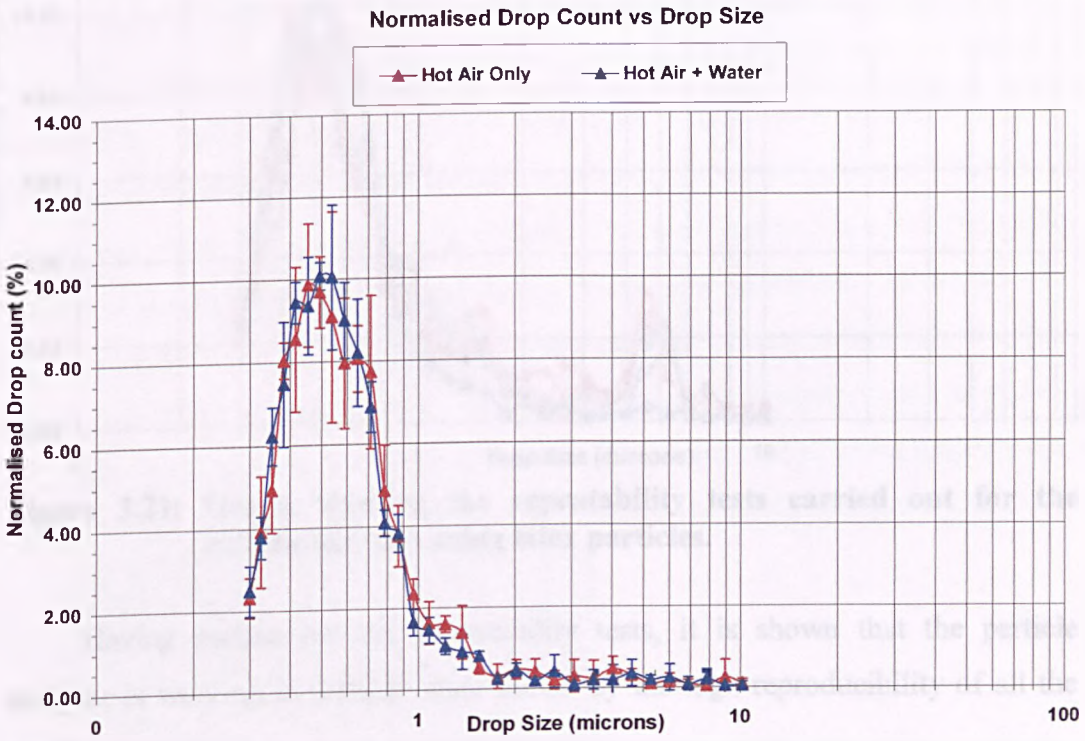

Figure 3.20: Results showing that the reproducibility of the tests is high at larger drop size and also all the water droplets are evaporated before reaching the Polytec channel.

From Figure 3.20, it shows that the repeatability is very high since the standard deviations for the larger droplets are small under the same set up and the same operating conditions (for both hot air alone and a mixture of hot air and water droplets).

Similarly from Figure 3.21, the reproducibility is reasonably good. With the latex particles going through the Polytec, peaks were detected at approximately 1.5

and 5.0 microns for all the different runs conducted. However, the peaks at 2 microns were not very distinctive. Nevertheless, this happens for all the tests carried out. It might be due to the smaller proportion of 2 microns latex particles in the mixture as discussed previously.

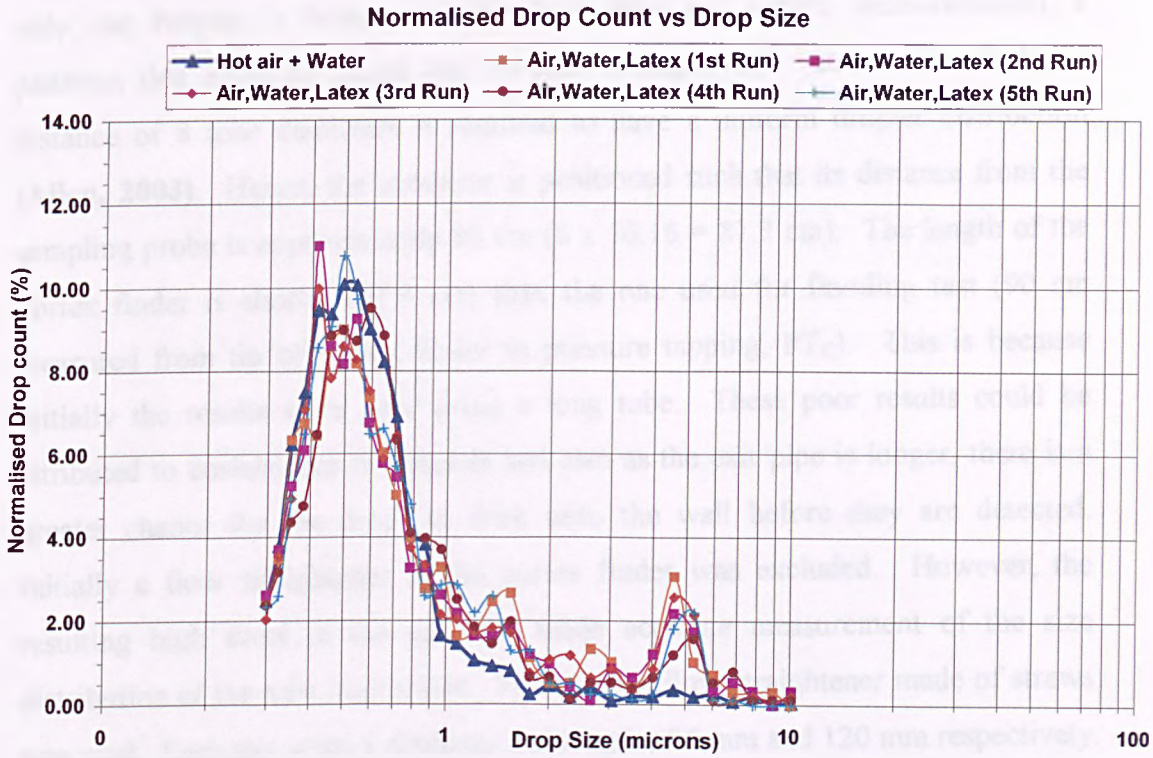

Figure 3.21: Graph showing the repeatability tests carried out for the calibration tests using latex particles.

Having carried out the repeatability tests, it is shown that the particle analyser is working in a stable state shown by the high reproducibility of all the results.

3.3.5 Grade Efficiency Tests

Grade efficiency is a measure of separation efficiency of each particle size. From the grade efficiency tests, one can tell the range of particle size that a specific design is capable of separating. The experimental set up and measurement procedures are documented in the following sections.

3.3.5.1 Experimental Setup for Grade Efficiency Tests

The bulk of the experimental setup (Figure 3.22) is very similar to the setup for flooding tests with an additional framework built to support the Polytec. Since only one Polytec is being used (for both inlet and outlets measurements), a platform that could be raised and lowered is employed. It is believed that a distance of 8 tube diameters is required to have a uniform droplet distribution **(Allen, 2003)**. Hence, the nebuliser is positioned such that its distance from the sampling probe is approximately 88 cm (8 x 10.16 = 81.3 cm). The length of the vortex finder is shorter (67.8 cm) than the one used for flooding test (90 cm measured from tip of vortex finder to pressure tapping, PT_C). This is because initially the results were poor using a long tube. These poor results could be attributed to coalescence of droplets and also as the exit pipe is longer, there is a greater chance for the drops to stick onto the wall before they are detected. Initially a flow straightener in the vortex finder was excluded. However, the resulting high swirl in the gas exit made accurate measurement of the size distribution of the mist impossible. Therefore, a flow straightener made of straws was used. Each straw has a diameter and length of 6 mm and 120 mm respectively. Table 3.4 lists the details of the instruments used for the grade efficiency tests.

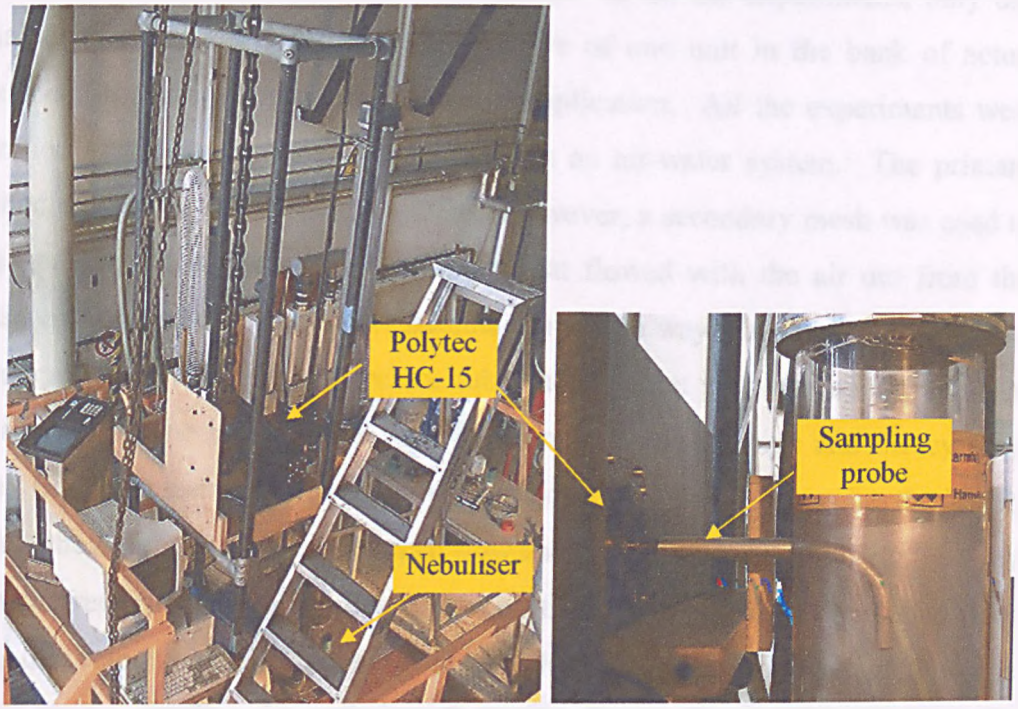

Figure 3.22: Experimental setup for grade efficiency tests.

Instrument	Specifications
Radial bladed centrifugal blower controlled by a variable speed drive	Same as flooding tests.
Particle Analyser and Signal Processor	Particle analyser model Polytec HC 15 and signal processor model PSE 1500 manufactured by Polytec.
Nebuliser and Compressor	Nebuliser model 1004 AquaTower2™. Compressor model 3050 Super SportNeb with 50 psi average pressure and 15 l/min minimum flow. Both are manufactured by Glenmore Healthcare Ltd.

Table 3.4: Instrument specifications for grade efficiency studies.

The experimental procedures for the grade efficiency test can be found in Appendix E.

3.4 Conclusions

At the beginning of this chapter, all the experiments that were carried out in this research and their objectives were listed. In all the experiments, only one axial flow cyclone was tested, representative of one unit in the bank of actual cyclones, operating in parallel in the real application. All the experiments were operated under atmospheric conditions, with an air-water system. The primary knitted mesh was omitted in the system. However, a secondary mesh was used to trap and agglomerate any liquid droplets that flowed with the air out from the liquid escape slots. The rig was assembled in such a way that the air flow is fully developed upon reaching the cyclone tube and the inlet pressure tapping (PT_s) is far away from the recirculation zone between the housing pipe and the cyclone tube. Both of these requirements were ensured using CFD to determine the length of the tube required to get a developed flow and the length to be significantly away from the recirculation zone. It was proven that the flow was a developed flow from the velocity profile measured across the cross sectional area of the pipe which gave a profile of a turbulent flow (details can be found in Chapter 7).

However, water was seen flowing into the pressure tapping tubing at very high air and water loadings although the pressure tapping was located far away from the recirculation zone indicated from CFD. This was counteracted using a three-way valve to stop the water flowing into the tubing when measurements were not taken.

The flooding and grade efficiency studies were the two major studies in this research. The important measurements for the flooding tests were the system pressure drop, flow split and the onset of entrainment/re-entrainment. The pressure drop was measured using manometers, flow split was measured using air flowmeters and the onset of entrainment/re-entrainment was determined from visual observations. The experimental procedures for the flooding/re-entrainment tests are documented in Appendix B.

The experimental setup for the grade efficiency tests was very similar to the flooding tests, with an additional framework built to support the particle analyser, Polytec HC-15. A flow straightener was used to straighten the swirl in the vortex finder in order to get a representative measurement in the vortex finder. A significant effort was spent on calibrating the Polytec prior to any grade efficiency tests. The experimental apparatus for the calibration tests and the calibration procedures are elaborated in Section 3.3.3.1 and 3.3.3.2 respectively. Repeatability tests were also conducted for the calibration work and the method can be found in Section 3.3.4.1. The results suggest that the Polytec is in good working condition and the reproducibility of the results is very high. After making sure of the Polytec's reliability, the grade efficiency tests were performed. The operating procedure can be found in Appendix E.

In the next chapter, the important parameters that determine the performance of the axial flow cyclone are discussed in detail (i.e. pressure drop, flow split, entrainment/re-entrainment and separation efficiency) and the evolution of all the designs of the axial flow cyclone that have been tested in this project are also presented.

Chapter 4

Cyclone Design Development

4.1 Structure of Chapter

In this chapter, the important parameters in determining the performance and design of the axial flow cyclone will be covered in detail. These parameters include the system pressure drop, the flow split, re-entrainment of droplets and the grade efficiency. These parameters are determined by the cyclone's geometry and the application characteristics (i.e. gas and liquid flowrates, gas and liquid physical properties). Any changes made to the geometry and the application characteristics will change the parameters involved; increasing certain parameters, but this might affect other parameters in an undesirable way. For instance, changing the geometry to increase the grade efficiency will increase the system pressure drop as well and this may be undesirable, which will be further discussed below. Therefore, it is of interest to find a compromise among all these parameters to obtain the best cyclone design, which will give the optimum performance.

4.2 Development Philosophy

The proposed demisting system has been briefly covered in Chapter 1 (Section 1.4). The design of the cyclonic gas-liquid separator will be based on a set of axial flow cyclones operating in parallel in a separating vessel. They are seen to be more compact (omitting the conical section) than conventional cyclones. The overall cyclone performance is very much dependent on the cyclone geometry, which results in a numbers of consequences for design as follows:

4.2.1 Pressure Drop

The pressure drop across a cyclone is an important parameter to judge the performance of the cyclone. However, exact prediction of the pressure drop for axial flow cyclones is still not possible. The issue of the pressure distribution in cyclones is complicated by the presence of swirl. Under normal situations, a lower pressure drop means a lower energy requirement. However, in the oil industry there is a large amount of pressure from the wellhead to drive the fluids. The reason for keeping the pressure drop as low as possible is to avoid problems concerning drainage in the vessel separator. If the pressure drop is high, then a large vessel (in terms of height) is required to prevent the liquid in the collection sump of the vessel travelling up the drainage pipe and flooding the vessel. A larger vessel requires more complication in construction, which evidently increases the capital cost and this is unfavourable. From Figure 4.1, if the system pressure drop is greater than $h\rho_L g$ (ρ_L = liquid density, kg/m^3 and g = gravitational acceleration, m/s^2) then the cyclone area will be flooded. Therefore, a knowledge of the system pressure characteristics is important.

Besides the influence of the cyclone geometry, the pressure drop also depends on the physical properties of the fluids. The liquid density and viscosity does not change significantly, but the gas density and viscosity changes as a function of temperature and pressure. The operating pressure for a subsea operation can range from 70 – 130 bar **(Nooijen, 2003)**. Gas density and viscosity increases as the pressure and temperature increases. From Equation (2.25), it shows that the system pressure drop increases as the density increases and from Equation (2.2) with an increase in the gas viscosity due to an increase in the temperature, this will lower the separation efficiency for the same Stokes number. The effect of the physical properties on the separation efficiency is discussed in Section 4.2.4.

The Euler number remains constant for a specific design under any conditions. Therefore, it is beneficial to know the gas density under the real

working conditions in order to predict the pressure drop, hence determining the size of the vessel required for normal operation. Some of the common pressure drops data for commercial gas-liquid cyclone separators are tabulated in Table 4.1.

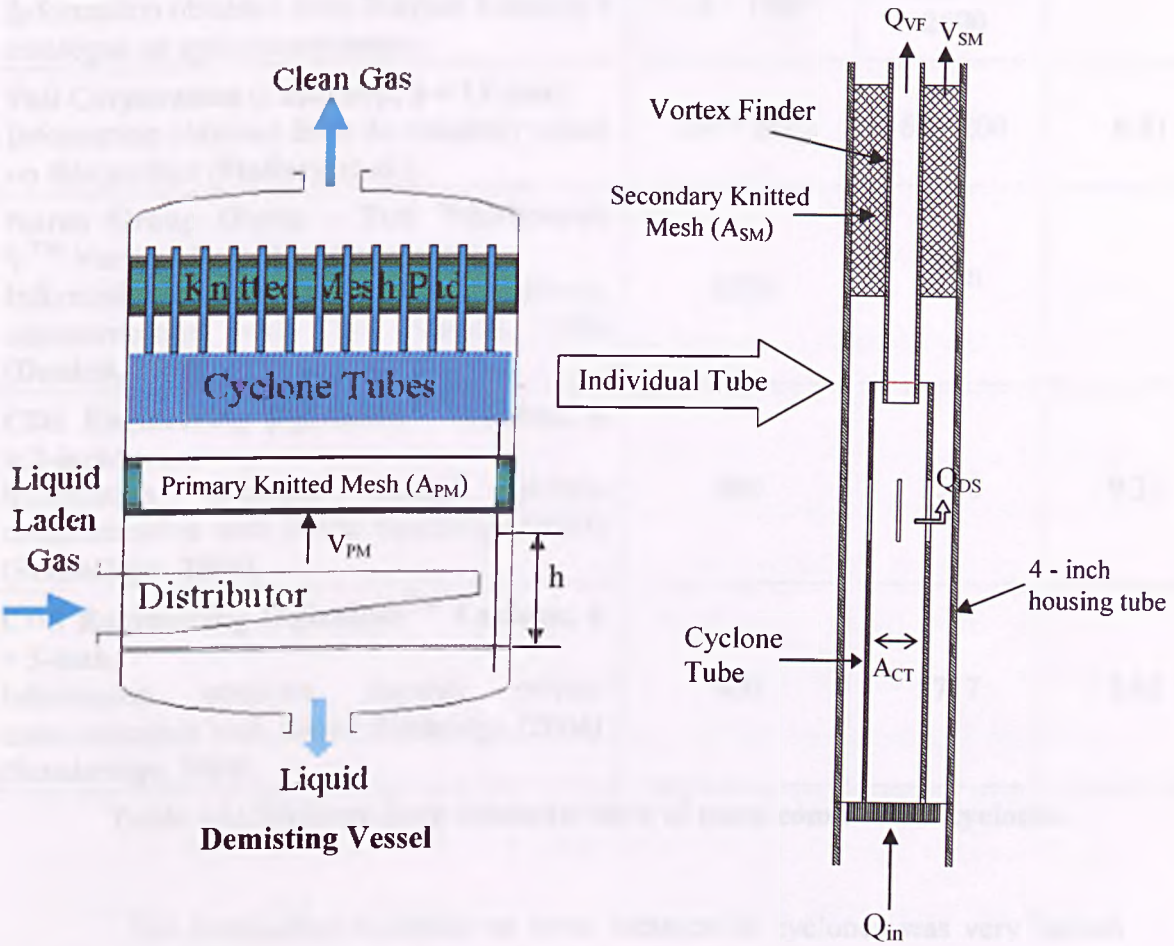

Figure 4.1: Important variables in the demisting system.

Company (Product Name)	Dry Pressure Drop (Pa)[1]	Flowrate per tube (l/min)	Euler Number (Eu)
Burgess Manning (BM A-X) Information obtained from Burgess Manning's catalogue on cyclone separators.	18 – 1600	166.7 - 2500	-
Pall Corporation (Centrisep, ϕ = 13 mm) Information obtained from the company report on this product **(Stallard *et al.*)**.	250 - 2875	67 - 200	6.81
Narco Group (Porta – Test Whirlyscrub V^{TM} Vertical Recycling Separator) Information obtained through private communication with Ian Daniels 2004 **(Daniels, 2004)**.	3500	NI[2]	-
CDS Engineering (Spiraflow^{TM} Cyclone, ϕ = 2-inch) Information obtained through private communication with David Stanbridge (2004) **(Stanbridge, 2004)**.	800	1520	9.37
CDS Engineering (Spiraflow^{TM} Cyclone, ϕ = 3-inch) Information obtained through private communication with David Stanbridge (2004) **(Stanbridge, 2004)**.	800	5717	3.05

Table 4.1: Pressure drop characteristics of some commercial cyclones.

The information available on these commercial cyclones was very limited because it was obtained either from the manufacturers' catalogues, which were very vague in every aspect (for example the cyclone's geometry, operating pressure and temperature were not usually given) or from private communication with the company. Therefore making comparison with the tested axial flow cyclone very difficult. Since the size of the cyclone tube was not specified, the Euler number (Eu) could not be calculated accurately because the cyclone inlet area is required to obtain the inlet velocity. Even though some of the pressure drop seems lower than the rest at the same inlet flowrate, this might be because a larger cyclone tube is used. A larger diameter cyclone tube gives a lower pressure drop, but this does not mean it is a better design. Their Euler number might be a

[1] Assuming that the test gas is air.
[2] No information about pressure drop characteristics is given for these cyclones.

lot higher, like the case of the Centrisep and the Spiraflow™ cyclone. The Spiralflow™ cyclone gives a lower pressure drop because it has a larger diameter. However, its resistance is higher than the Centrisep as shown by the Euler number. Therefore, it is most representative to compare Eu number in order to determine the resistance in the cyclone.

4.2.2 Flow split

Flow split (FS) is defined as the ratio of the air leaving through the vortex finder to the air supplied. It is crucial to determine the flow split because when the inlet velocity is too high, V_{PM}, the primary mesh will flood. Hence, the cyclones come into play separating the liquid from the gas. Splitting the flow in the cyclone is important because this reduces the load on the secondary knitted mesh pad, reducing velocity and hence the propensity to flood the secondary mesh. There is, however, a maximum velocity above which entrainment will occur from the secondary knitted mesh. Therefore, depending on the cross sectional area of the mesh, A_{SM}, a certain flow split has to be achieved to avoid mesh failure. It is aimed to achieve a high flow split because with a high split ratio, the cyclone can handle a much higher throughput even when the initial layer of knitted mesh is flooded. However, this will increase the system pressure drop and might reduce separation efficiency due to the increased turbulence. The frequently used variables in calculating the suitable flow split for a specific system are listed in Figure 4.1 and Table 4.2.

Symbol	Description	Unit
A_{PM}	Area of primary knitted mesh	m^2
A_V	Area of vessel	m^2
A_{CT}	Area of cyclone tube	m^2
A_{VF}	Area of vortex finder	m^2
A_{SM}	Area of secondary knitted mesh	m^2
V_{PM}	Velocity through primary mesh	m/s
V_{SM}	Velocity through secondary mesh	m/s
Q_{in}	Airflow into the system	m^3/s
Q_{DS}	Airflow out to the disengagement space	m^3/s
Q_{VF}	Airflow out from vortex finder	m^3/s
h	Height of liquid inside the drainage pipe	m

Table 4.2: Description of variables.

If we assume that the primary mesh fills up the entire vessel (i.e. $A_{PM} = A_V$), a relation between the primary and secondary velocity ratio, mesh area ratio and flow split can be derived as follows (Equation 4.1):

$$A_{PM} = A_V$$

$$V_{PM} = \frac{Q_{in}}{A_V} = \frac{Q_{in}}{A_{PM}}$$

$$V_{SM} = \frac{Q_{DS}}{A_{SM}}$$

Therefore,

$$\frac{V_{SM}}{V_{PM}} = \frac{Q_{DS}}{A_{SM}} \cdot \frac{A_{PM}}{Q_{in}}$$

$$= \frac{A_{PM}}{A_{SM}} \cdot \frac{Q_{DS}}{Q_{in}}$$

$$\frac{V_{SM}}{V_{PM}} = \frac{A_{PM}}{A_{SM}}(1 - FS) \qquad \textbf{- Equation (4.1)}$$

where

$$\text{Flow Split, FS} = \frac{Q_{VF}}{Q_{in}} = \frac{Q_{in} - Q_{DS}}{Q_{in}} = 1 - \frac{Q_{DS}}{Q_{in}}$$

Equation (4.1) shows that the suitable flow split depends on the primary to secondary mesh area and the velocity ratio. The area ratio depends on the cyclone geometry (i.e. diameter of cyclone tube and vortex finder) and the tube layout in the demisting vessel, which determines the number of tubes to be fitted inside the vessel. The mesh velocity ratio depends on the mesh characteristics.

- ***Mesh Characteristics***

To avoid flooding the secondary mesh for a constant V_{PM}, the secondary mesh velocity V_{SM} should be less than the flooding velocity, U_f, calculated using Equation (2.15) (Souders-Brown equation). It is suggested that the design velocity should be 75-80% of U_f to allow surges and the minimum velocity should not be less than 30% of U_f **(KnitMesh, 2001)**. If the operating velocity is over the upper limit, this will most probably flood the mesh and if the velocity is lower than the lower limit, droplets will probably follow the gas streamlines and will not impact on the wire mesh, hence will not be collected.

For example, an air-water system operating under clean atmospheric condition using Equation (2.15) with k = 0.107 gives a critical velocity of 3.09 m/s (air and water density of 1.2 kg/m^3 and 1000 kg/m^3 respectively). The design velocity will be 0.8·U = 2.47 m/s and the minimum velocity should not be less than 0.93 m/s (30 % of 3.09 m/s). These velocity values correspond with the characteristic curves of the knitted mesh efficiency and pressure drop data in the manufacturer's catalogue (See Figures 4.2 and 4.3).

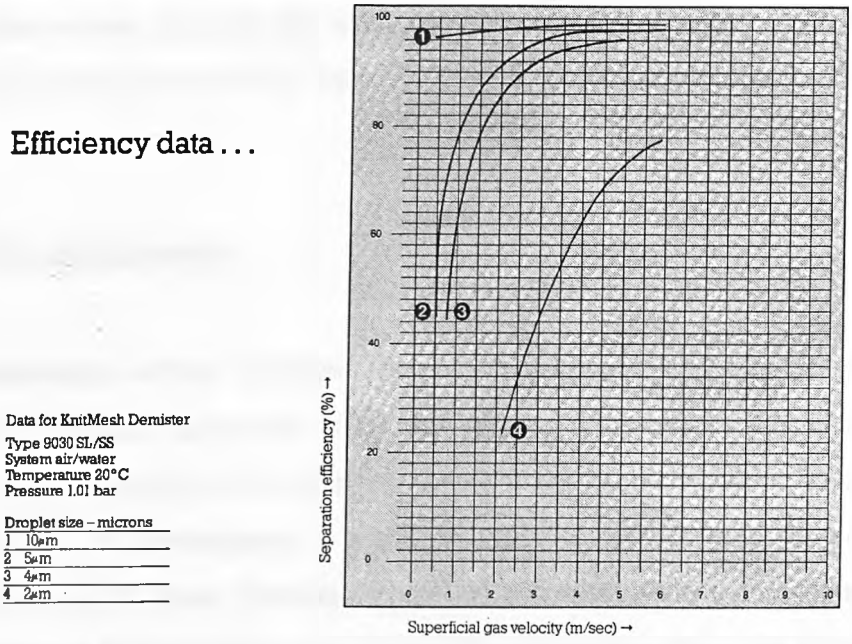

Figure 4.2: Graph showing efficiency data for air/water system at atmospheric conditions (KnitMesh, 2001).

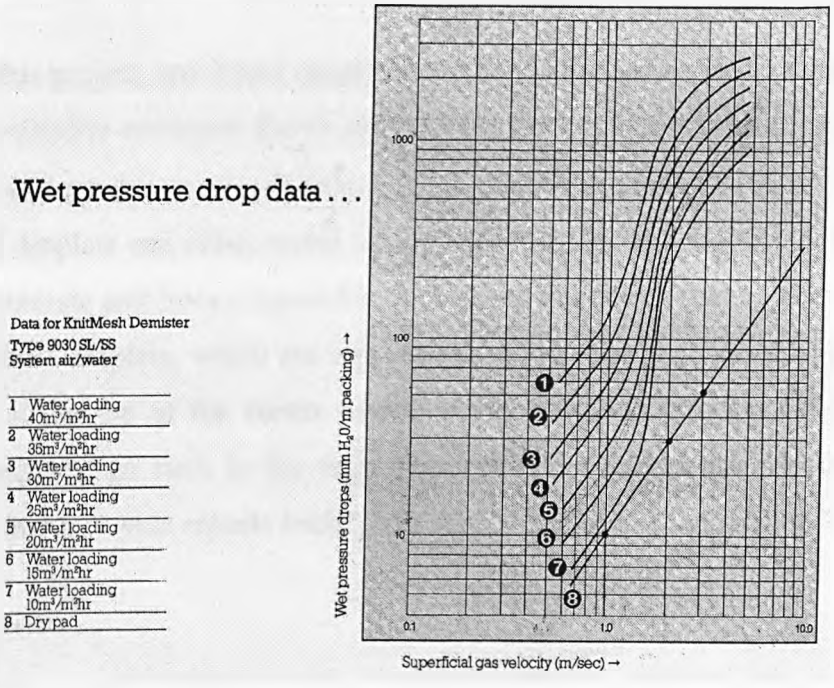

Figure 4.3: Graph showing pressure drop data for air/water system at atmospheric conditions (KnitMesh, 2001).

There is a lot to consider when determining the suitable flow split for a system (the system pressure, the maximum velocity that the secondary mesh can handle, the area of the meshes). This will be elaborated in more detail in Chapter 9.

4.2.3 Re-entrainment

Entrainment refers to liquid droplets breaking away from a gas/liquid interface to become suspended in the gas phase. This occurs when the liquid droplets are too small to be collected, hence these droplets escape through the vortex finder. Re-entrainment is used generally to assume that droplets have settled to the liquid phase, then are dispatched and returned to the gas phase. Re-entrainment can be due to film stripping and liquid creeping (from the cyclone roof, down the vortex finder wall and into the vortex finder) due to the pressure difference both axially and radially in the cyclone.

In this project, any liquid droplet found inside the vortex finder is considered to be entrained/re-entrained due to any of the three mechanisms mentioned above. Figure 4.4 illustrates the liquid behaviour in the vortex finder. The entrained/re-entrained droplets can either travel up the vortex finder in small droplets or they can agglomerate and form a liquid film moving up the vortex finder. However, the agglomerated droplets, which are significantly larger than their original size, may fall back to the lip of the vortex finder. From here, the droplets can either be stripped off and go back to the main gas flow or be thrown back to the vortex finder so that the cycle repeats itself.

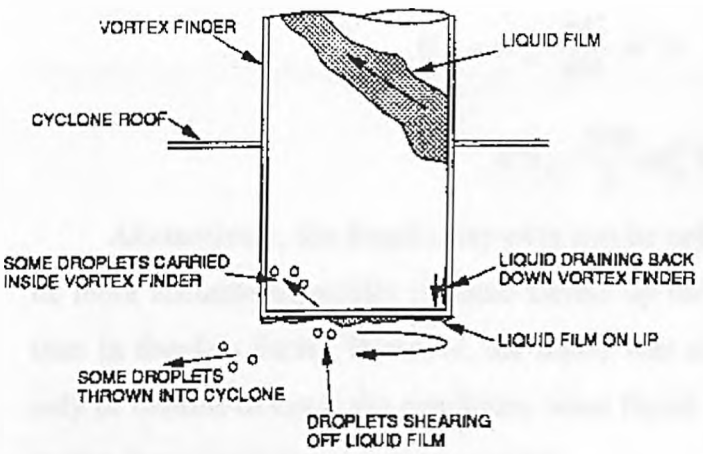

Figure 4.4: Re-entrainment from the lip of the vortex finder.

Re-entrainment of droplets should be avoided because the drops will damage the compressor downstream and as the entrained drop gets larger, the effect is greater. Serious flooding should be eliminated because this will promote liquid to be entrained into the gas stream not in the form of droplets, but in a continuous film of liquid, which will be disastrous if it enters the compressor. **Ishii and Grolmes (1975)** have studied the inception criteria for droplet entrainment and they have presented an extensive review of available data and correlations in their publication. **Andreussi (1980)** has also carried out an investigation of the onset of droplet entrainment in annular downward flows. Details of the prediction of onset of re-entrainment can be found in Chapter 2. All this work could only predict the velocity above which re-entrainment will be induced under certain operating conditions. The prediction of the amount of the re-entrained liquid is still not possible.

For this project, the liquid re-entrainment rate is roughly estimated by the following method:

(i) By visual observation, the number of droplets (N_{re}) of diameter, d_p, travelling up the vortex finder in 60 seconds was calculated.

(ii) The volume of the re-entrained liquid was calculated using Equation (4.2);

$$V_{re} = N_{re} \frac{\pi d_p^3}{6} \qquad \textbf{- Equation (4.2)}$$

(iii) The flowrate of the re-entrained liquid was calculated from Equation (4.3);

$$Q_{re} = N_{re} \cdot \frac{\pi d_p^3}{360} \text{ m}^3/\text{s}$$

$$= N_{re} \cdot \frac{500}{3} \pi d_p^3 \text{ l/min} \qquad \textbf{- Equation (4.3)}$$

Alternatively, the liquid carry-over can be collected and weighed. This will be more accurate especially if liquid travels up the vortex finder in a film rather than in droplets form. However, the liquid was not collected here because it is only of interest to know the conditions when liquid is swirled up the vortex finder so that these conditions could be avoided.

4.2.4 Droplet removal (Separation efficiency)

Separation efficiency can have several definitions such as the mass fraction of fluid/solids in the feed recovered in the liquid or gas stream expressed in percentage (%). The advantage of this is that online measurement is not required. The solids/liquid can be collected and measured after each test. Hence most of the published work gives the total separation efficiency of a cyclone instead of the grade efficiency curve. However, in this project the efficiency is expressed as the number of droplets of certain size removed to the total number in the inlet in percentage (%) because the Polytec measures the droplet concentration by number. In the interest of this research, it is the size of the droplets escaping through the vortex finder that is of concern (not the mass) because there is a compressor downstream of the cyclone separators and it is not intended to have large droplets impacting on the blades of the compressor. The grade efficiency curve is obtained by measuring separation efficiency of each particle size. The efficiency is plotted against the particle size, which is the diameter of the particles.

A very straightforward method to design a geometrically similar cyclone in order to perform under the required separation is using the Stokes number (Stk) scaling method ($Stk = d_p^2[\rho_p - \rho_g]U/18\mu D_C$). Under the same operating condition

(i.e. physical properties remain constant), the effect of changing the cyclone diameter on the grade efficiency curve is predicted as in Equation (4.4):

$$\frac{d_1}{d_2} = \left(\frac{D_{C1}}{D_{C2}}\right)^{0.5} \qquad \textbf{- Equation (4.4)}$$

where the subscripts 1 and 2 refer to separate tests in cyclones of geometrically similar design. The above equation suggests that if D_{C2} is reduced, for same separation efficiency as the larger cyclone diameter (D_{C1}) a smaller droplet size will be obtained. However, by reducing the cyclone diameter this will increase the system pressure drop as described earlier on.

The degree of separation is determined by the balance of the two forces on the particle: inertia and the drag of the fluid surrounding the particle. Particle inertia depends on its mass and velocity and the drag on the particle is greatly influenced by the particle size and shape. This explains why the bigger the particle, the easier it is to be collected. Particle density also influences the degree of separation. An increase in particle density increases the collection efficiency. According to **Stairmand (1951)** for a particle of different density from the test liquid or solid, a new grade efficiency curve can also be plotted using Stokes number scaling method (See Equation 4.5) such that the points of equal efficiency will have the particle sizes on the axis in the ratio of;

$$\frac{d_{x_1}}{d_{x_2}} = \left(\frac{\rho_{p_2} - \rho_{g_2}}{\rho_{p_1} - \rho_{g_1}}\right)^{0.5} \qquad \textbf{- Equation (4.5)}$$

where d_x is the diameter of the particle which has an x% chance of being separated and the superscripts 1 and 2 refer to separate tests of different densities of the particles in cyclones of geometrically similar design.

The grade efficiency tests in this project were operated with an air-water system under atmospheric conditions. The actual grade efficiency curve for the application in the oil industry can then be plotted using Equations (4.4) and (4.5) where appropriate. The design of the cyclone body can also be adjusted using these equations to satisfy the requirements under the real working conditions. The

expected drop size that the cyclone has to handle is around 0.4 to 20 microns. The targeted cut size is around 3 microns, which is the typical cut size of cyclones in the market. It is essential that large droplets do not go through the vortex finder because failure to do so will cause damage to the compressor downstream. Table 4.3 shows the typical separation efficiency for commercial available cyclones.

Company (Product Name)	Efficiency (%)
Burgess Manning (BM A-X) Information obtained from Burgess Manning's catalogue on cyclone separators.	$d_{50} < 5$ μm
Pall Corporation (Centrisep, ϕ = 13 mm) Information obtained from company's report on the product **(Stallard *et al.*)**	Total separation efficiency = 92% for dust size between 2 – 50 μm
Narco Group (Porta – Test Whirlyscrub V™ Vertical Recycling Separator) Information obtained through private communication with Ian Daniels 2004 **(Daniels, 2004)**	Separates liquid droplet down to 10 – 15 μm
CDS Engineering (Spiraflow™ Cyclone, ϕ = 2-inch) Information obtained through private communication with David Stanbridge (2004) **(Stanbridge, 2004))**	Separates 8 μm droplets at 1520 l/min with air-water system under atmospheric conditions
CDS Engineering (Spiraflow™ Cyclone, ϕ 3-inch) Information obtained through private communication with David Stanbridge (2004) **(Stanbridge, 2004))**	Separates 8 μm droplets at 5717 l/min with air-water system under atmospheric conditions

Table 4.3: Efficiency data for some commercial cyclones

Similarly to the information for the pressure drop of these commercial cyclones, the information on the separation efficiency is not given in detail either through manufacturers' catalogues and private communication due to confidentiality. It is assumed that all the information given is obtained with an air-water system operating under atmospheric conditions. Therefore, if the operating pressure increases the efficiency will be lower than the value specified in Table 4.3. From the efficiency data of the Spiralflow™ Cyclone, it confirms that a smaller diameter cyclone gives a better separation for the same amount of flow through the cyclone. The cyclone diameter and the flowrate required giving the stated efficiency for the Porta – Test

Whirlyscrub V^{TM} are not provided. Therefore, it is not feasible to comment on their performance. In order to access the performance of the cyclones accurately, it is necessary to have the information of the cyclone geometry, the application characteristics and the operating conditions.

4.3 Initial Geometry and the Development of the Design

4.3.1 Initial Geometry

In a traditional axial flow cyclone, swirl is imparted to a gas, by static swirl vanes located on the central boss such that liquid is forced to the wall from where it can be stripped off and so separated. An initial design of a model axial cyclone tube of this design was constructed from clear PVC with an inner diameter of 52 mm and a total height of 842 mm. The cyclone itself could be considered in 5 zones, representative of the cleaning stages (See Figures 4.5 and 4.6).

Zone 1 (175 mm from tube inlet to the vanes) was the primary stream (or feed stream) where the air and water droplets were first introduced. Zone 2 was the centre body with the swirling vanes. Six-bladed guide vanes, bent to 30^0 (between blade plane and axial direction), as shown in Figure 4.7 with all the dimensions, were attached to a centre body, constructed from brass, and acted as the swirling device. The 30-mm diameter centre body had an aerodynamic hub at the front and a rounded end. The aerodynamic front was used so that the flow would move smoothly through to the blades, creating maximum swirl at minimum pressure drop. As a result, the liquid droplets were thrown to the cyclone wall by centrifugal force. This was the collection stage (Zone 3). Zone 4 was the stripping section where slots were provided to allow the collected liquid to drain from the main cyclone tube. The slots were 5mm wide and 111mm long. Figure 4.8 gives a view of the slots from the centre body swirler inside the cyclone tube. The slots were placed 53 mm away from the vanes. Having passed through the slots, the liquid was said to be in Zone 5, a disengagement space.

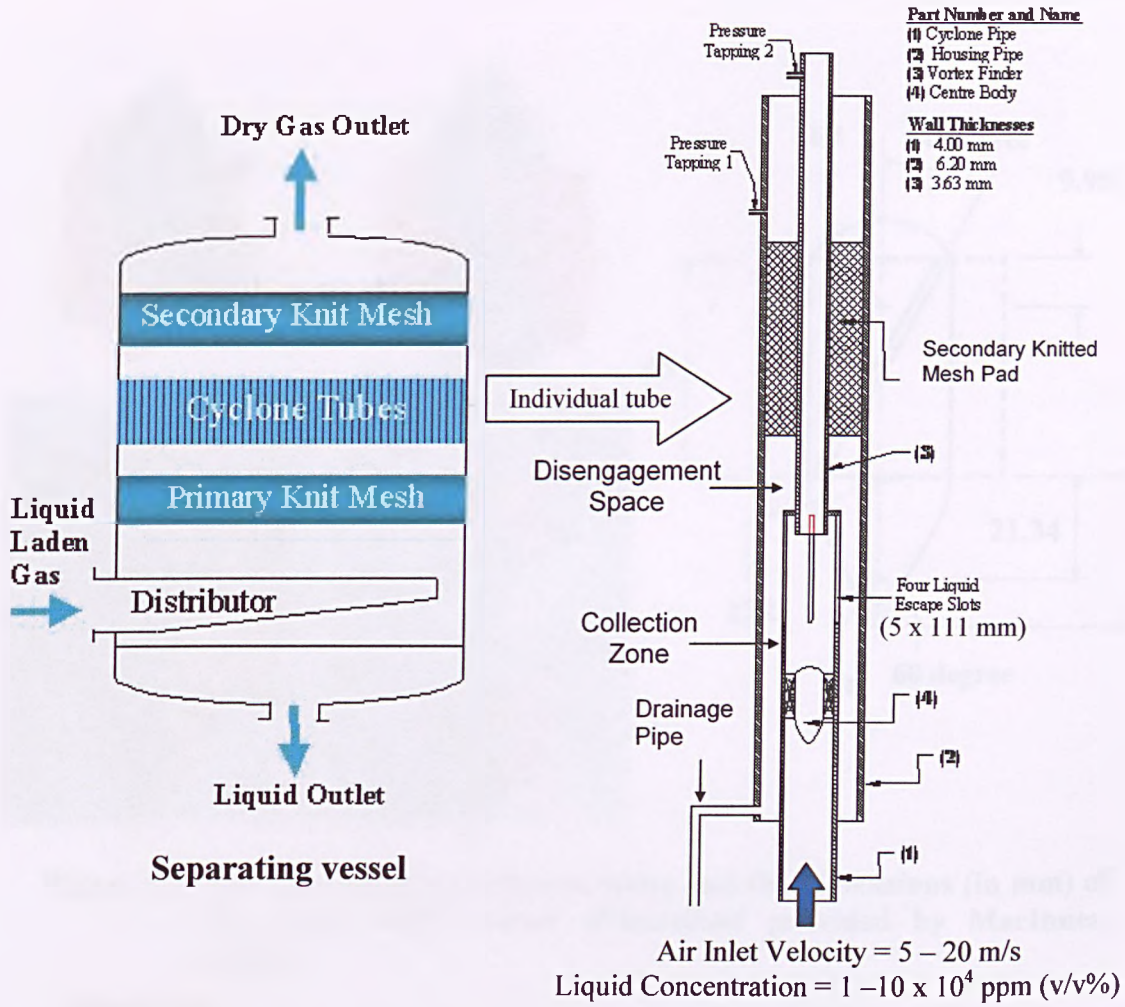

Figure 4.5: Diagram showing cyclone position inside a typical demisting vessel and the initial cyclone geometry that was investigated.

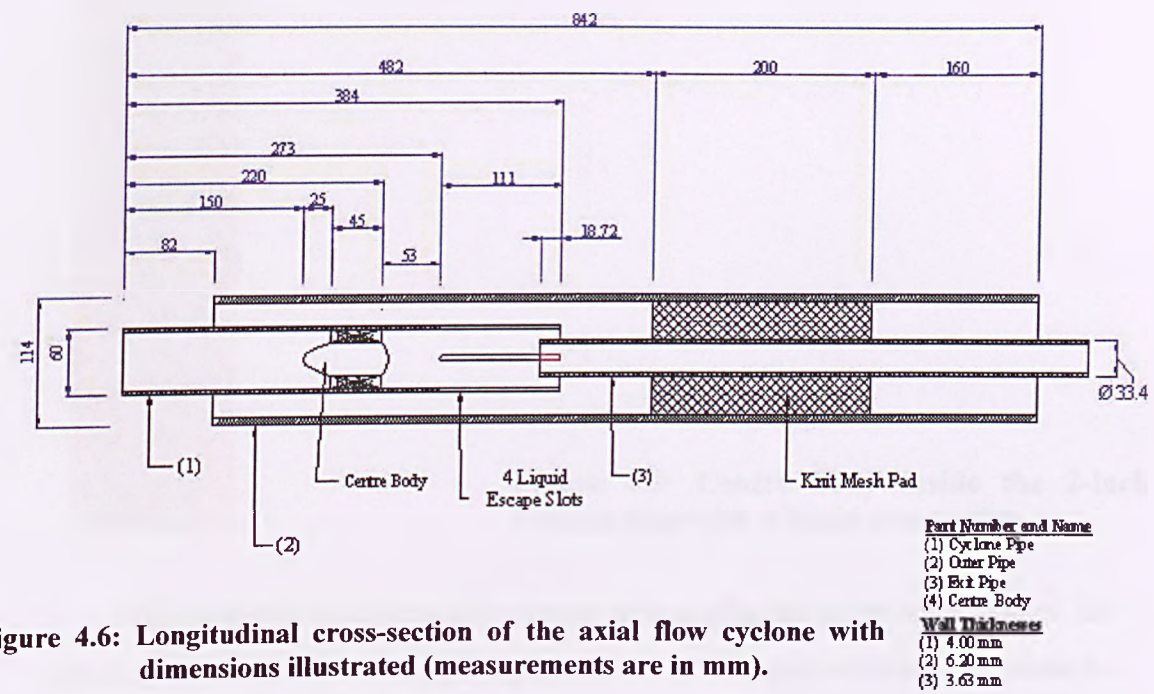

Figure 4.6: Longitudinal cross-section of the axial flow cyclone with dimensions illustrated (measurements are in mm).

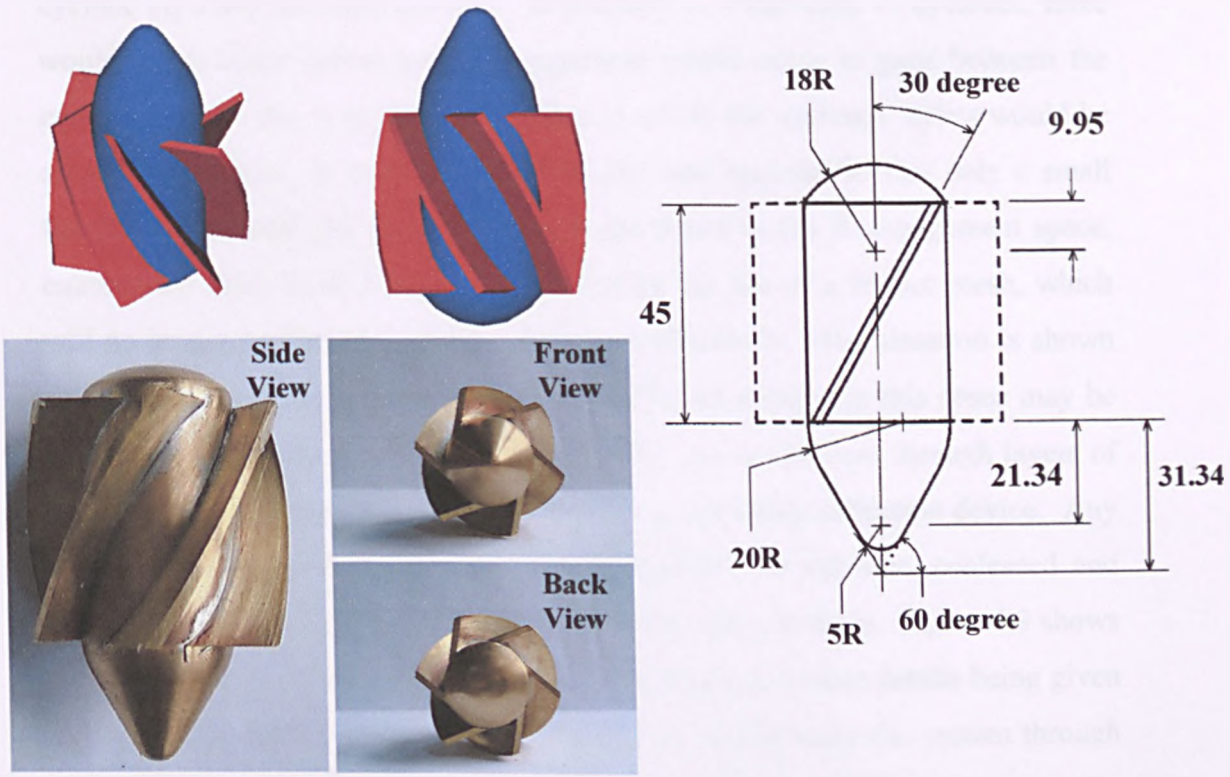

Figure 4.7: Diagrams showing different views and the dimensions (in mm) of the centre body swirler (dimensions provided by MacInnes, (2000)).

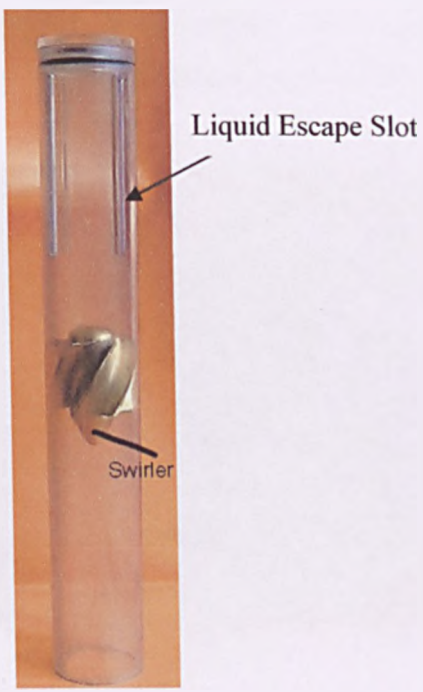

Figure 4.8: Centre body inside the 2-inch cyclone pipe with 4 liquid escape slots.

The model used in these experiments was configured as an outer tube of 100 mm inner diameter so that the disengagement zone became an annulus between the

cyclone pipe and the outer housing. In practice, in a real bank of cyclones, there would be no outer casing and disengagement would occur in gaps between the cyclones, above the vessel's plenum plate to which the cyclones' inlets would be attached. Because, as a design objective, the unit operates so that only a small fraction of the total gas flow passes with the liquid to the disengagement space, entrainment from Zone 5 may be prevented by the use of a further mesh, which will no longer be flooded and should operate effectively. The situation is shown for a single mesh in Figure 4.5. The air and liquid streams in this space may be referred to as the secondary flow streams. The gas would flow through layers of the secondary knitted mesh pad, which acts as a secondary collection device. Any liquid droplets that flowed with the air should be trapped here, coalesced and dropped back to the bottom of the disengagement space to drain. Figure 4.9 shows the mesh being used as supplied by KnitMesh Limited, further details being given in Table 4.4. Ideally, only perfectly cleaned air would leave the system through either the top of the second pad or through the gas exit pipe (also known as the vortex finder). In our model, the vortex finder had a base inner diameter of 26 mm.

The dimensions of the axial flow cyclone may be expressed as a ratio of the cyclone pipe diameter. The ratios used as the starting dimensions were provided by **Davies (2000)** and are listed in Table 4.5.

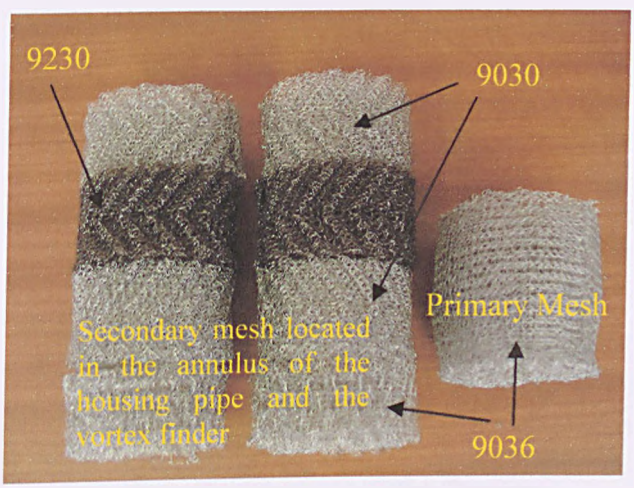

Figure 4.9: The knitted meshes used upstream and in the disengagement space.

Position of Mesh	Type Number	Mesh Depth (mm)
Initial layer of mesh	9036	100
Secondary mesh	9030	50
	9230	50
	9030	50
	9036	50

Table 4.4: Details of the type of knitted mesh used in the system.

Zones		Ratio	Measurement (nearest mm)
Cyclone Tube Inner Diameter		D_{CT}	52
Entrance Length		$2.88D_{CT}$	150
Centre Body	Leading Edge	$0.48D_{CT}$	25
	Vanes, L_V	$0.87D_{CT}$	45
	Tailing Edge	$0.12D_{CT}$	6
Diameter of Centre Body, D_{CB}		$0.58D_{CT}$	30
Collection Zone		$0.90D_{CT}$	47
Stripping Zone	Length of slots, L_S	$2.13D_{CT}$	111
	Width of slots, W_S	-	5
Vortex Finder Diameter, D_{VF}		$0.50D_{CT}$	26
Vortex Finder Length, L_{VF}		$0.36D_{CT}$	19

Table 4.5: Ratios and dimensions used in the initial design.

4.3.2 Development of the Design

In order to achieve better flow split and overcome a frothing problem that was encountered in the early programme (See Chapter 5: Experimental Results and

Discussions of the Initial Geometry), the initial cyclone geometry was modified. Attempts to avoid frothing required modifications within the device such as slot area, vortex tube diameter and the swirling device. The major changes were replacing the centre body with a set of tangentially oriented swirling vanes and to encourage drainage, four vane openings were used as additional drainage as this was found successfully to eliminate the frothing region and so avoid re-entrainment at low gas throughputs. Changes were also made to the liquid drainage slots and a larger vortex finder was introduced (from 26 mm to 34.5 mm) to achieve a higher flow split. The experimental set up and the principle of operation was otherwise similar to the previous model. All the changes to the cyclone geometry are tabulated in Table 4.6 below with a short description of the alterations made to the specific geometry. The diagrams in the table only show major changes (i.e. the slot dimensions and position, the new set of inlet vanes and the size of the vortex finder) with everything else remaining identical to the initial geometry.

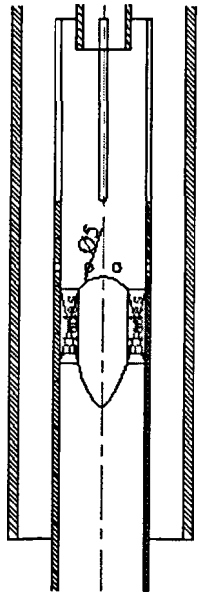	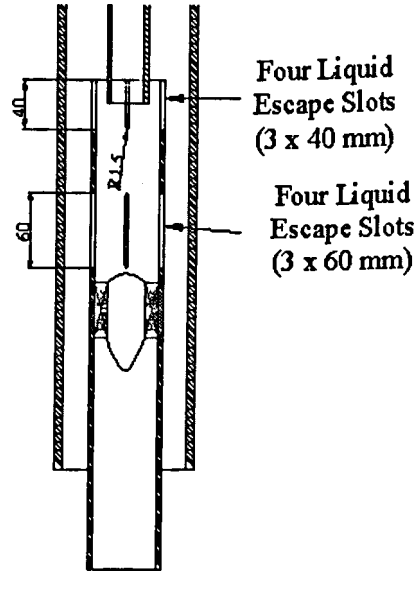
Geometry 2a, 2b: Two or four 5 mm holes are drilled in the collection zone (after the vanes).	Geometry 3a, 3b: Slot width is reduced to 3mm. Started with four 3x40 mm slots at the cyclone end and then added another four 3x60 mm slots after the vanes.

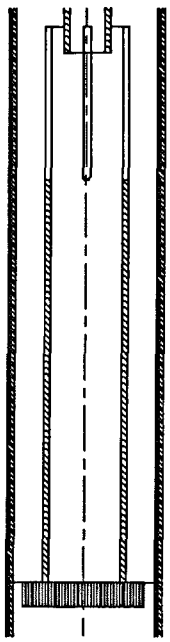

Geometry 4: A set of tangentially oriented vanes (40 blades) is used to replace centre body and the original tube is used (5x111 mm slots).

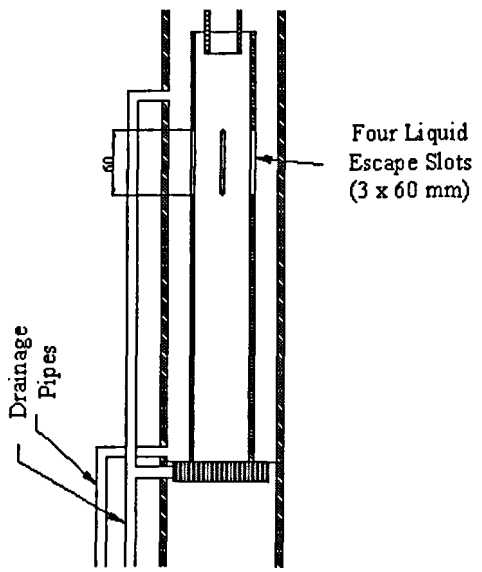

Geometry 5a, 5b: Started with the tube used in Geometry 3b, but with the slots at the end of the cyclone blocked. Then the upper halves of the slots are blocked, giving four 3x30 mm slots because liquid is seen to go out mostly from the lower half. Two vane openings are used as an additional drainage.

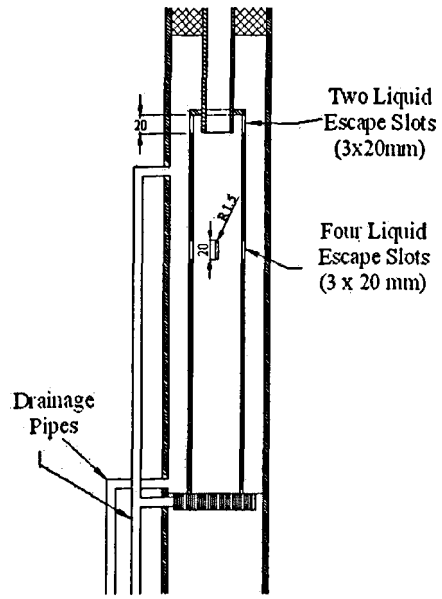

Geometry 6a, 6b: Identical to Geometry 5b but with four vane openings used as additional drainage. Liquid is seen to swirl beyond the slots, hence two extra slots are put at the end of the cyclone tube. However, the overall cross-sectional area of the slots is unchanged (i.e. having four 3x20 mm slots in the middle and two 3x20 mm slots at the end of the cyclone tube).

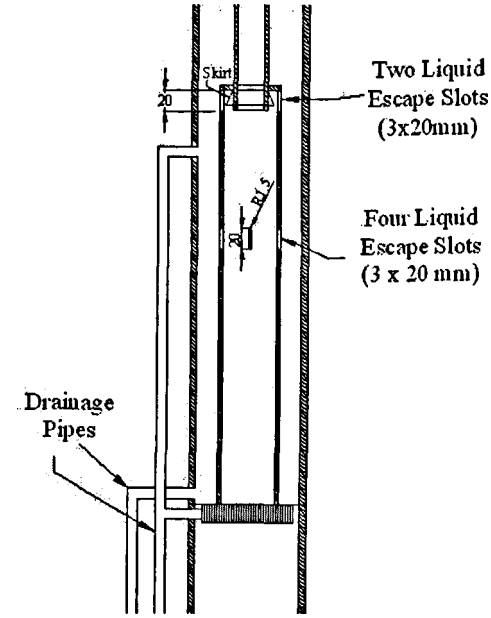

Geometry 7a, 7b: Geometry 7a has a larger vortex finder diameter (base inner diameter = 34.54 mm and outer diameter = 42.2 mm) and other measurements remain unchanged. However, liquid is still being entrained into the vortex finder, hence a skirt is placed around the vortex finder to reduce this.

Table 4.6: Summary of the geometries studied.

- ***Design of Inlet Swirl Vanes***

The centre body swirler was replaced by inlet swirl vanes because it could not provide enough swirl to centrifuge the liquid to the wall at low air flowrates. This was due to the area of the centre body blocking about 33% of the flow passage so that liquid rested on the centre body at low air flowrates and induced flooding. Therefore, a new set of inlet vanes was designed to increase the vortex strength.

Firstly, the area of the annulus between the base of the inlet vanes to the 100-mm diameter housing tube was kept the same as the area of the 52-mm diameter cyclone tube so that any difference in the pressure drop compared to the centre body design is due to the increased in vortex strength and not due to the reduction of area between the housing tube and the vanes. Therefore,

$$\pi r_{4"}^2 - \pi r_{base}^2 = \pi r_{2"}^2$$

$$\pi \left(\frac{4}{2}\right)^2 - \pi r^2 = \pi \left(\frac{2}{2}\right)^2$$

$$r^2 = 4 - 1$$

$$= 3$$

$$r = 1.732 \text{ inch}$$

$$= 43.99 \text{mm}$$

So, the outer radius of the vanes (R44) is set to be 44 mm. It was decided that the number of vanes should be set to be 40 because this kind of design was tested and worked successfully **(Tippetts, 2001)**. Hence the angle between vanes is 9°. If the number of vanes is less than 40, the vane has to be longer so that no flow will pass through these vanes without being swirled. Since the area of the annulus is fixed, the vane can only move inwards to satisfy this condition. However, this will reduce the area for the swirl to develop from the vanes into the cyclone tube. On the other hand, if the number of vanes is greater than 40 there will be less space for the flow, hence reduced throughput per unit volume. Due to the manufacturing limitation, the shortest distance between vanes is limited by an

end mill with the diameter of 3 mm. The inner radius of the vanes (R40) is fixed at 40 mm. The details of the design are shown in Figure 4.10. The height of the base to support the vanes is set to be 5 mm. The height of the vanes is determined such a way that the area of the minimum distance between vanes is equal to the area of the 52-mm diameter tube. Therefore,

$$\frac{\pi(52^2)}{4} = 40 \times 3x$$

$$x = 17.70\text{mm}$$

The finished design can be viewed in Figure 4.11.

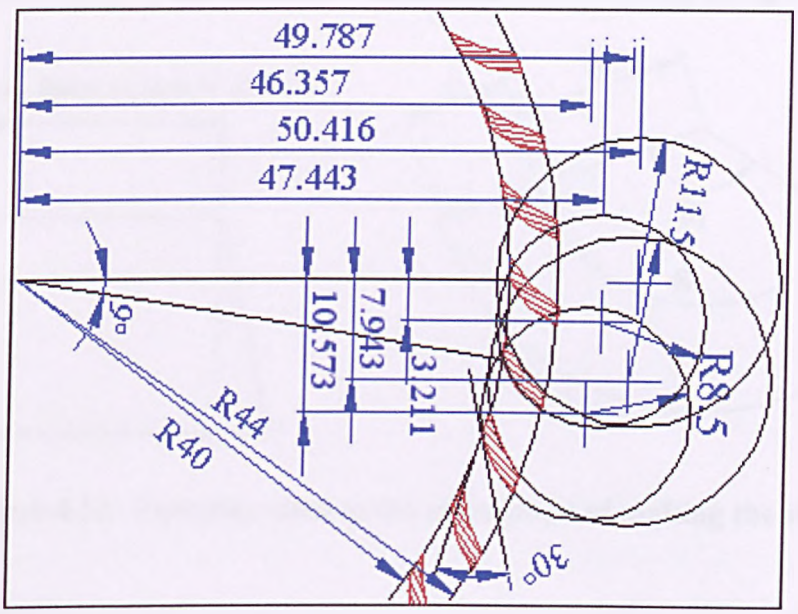

Figure 4.10: Detailed measurements (in mm) of the swirl vanes.

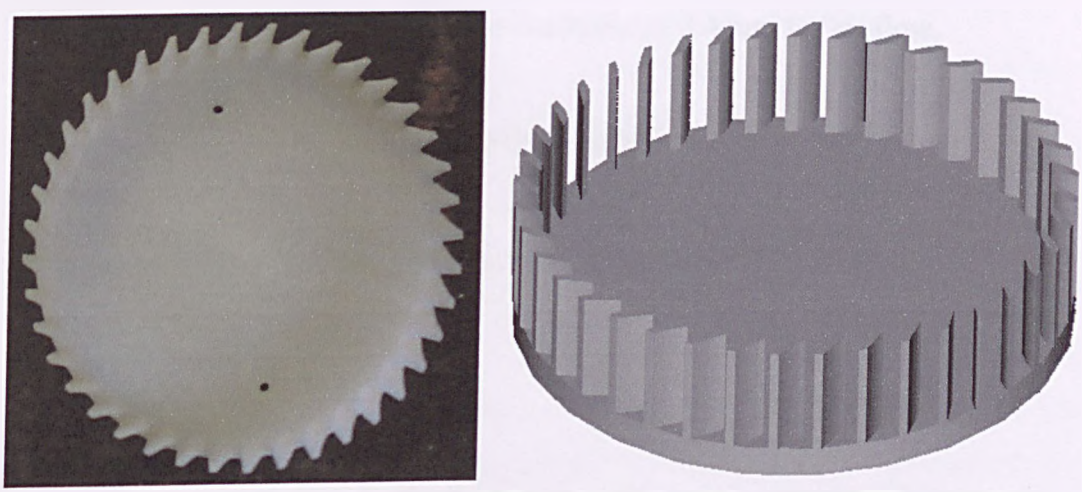

Figure 4.11: The 40-blade tangentially oriented swirl vane at different views.

- ***Design of the skirt***

Liquid that creeps across the roof of the cyclone tube and down the vortex finder has a high tendency to leave with the clean gas. Therefore, a skirt is placed around the vortex finder to reduce this liquid re-entrainment. However, with the outer vortex finder diameter of 42.2 mm and inner diameter of the cyclone tube of 52 mm there is only an annular space of approximately 5 mm to fit in the skirt. The skirt is based on calculations of a truncated cone. Since the vortex finder length is about 20 mm, the height of the skirt is set to be 10 mm. Detailed calculations are shown below and for identifying variables, refer to Figure 4.12.

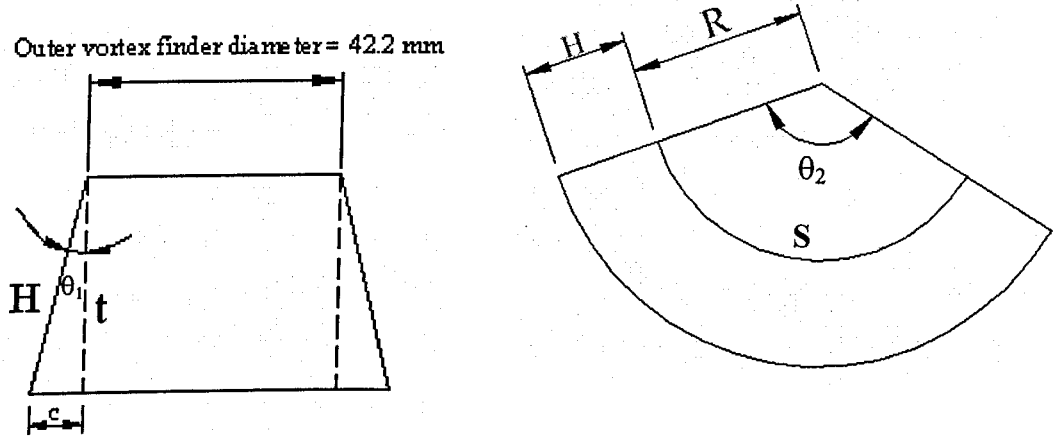

Figure 4.12: Variables used in the calculation of making the skirt.

Let t = 10 mm

$$\text{Tan } \theta = c/t$$

And c is taken as 2.6 mm so that there is a space of 2.4 mm for air flow.

Therefore,

$$\text{Tan } \theta_1 = 2.6/10$$

$$\theta_1 = 14.57^{\circ}$$

Outer vortex finder diameter is 42.2 mm, hence radius will be 21.1 mm.

$$\frac{R}{H+R} = \frac{21.1}{23.7}$$

$$\frac{H}{R} = \frac{23.7}{21.1} - 1$$

$$R = \frac{10.33}{0.123}$$

$$= 83.85 \text{ mm}$$

$$H + R = 10.33 + 83.85$$

$$= 94.18 \text{ mm}$$

Letting S = the circumference of the vortex finder.

$$S = R\theta_2$$

Therefore,

$$42.2\pi = 83.85\theta_2$$

$$\theta_2 = 1.581 \text{ radians}$$

$$= 90.59^{\circ}$$

4.4 Conclusions

In the beginning of this chapter, the development philosophy of this research has been laid out. The important parameters that determine the performance of the axial flow cyclone are discussed in detail. These include the pressure drop, flow split, re-entrainment and separation efficiency. These parameters are related to one another through the cyclone operating conditions and geometry, for example a higher flow split is associated with a higher pressure drop.

However, higher pressure drop will result a larger separation vessel in order not to flood the drainage pipe as discussed in Section 4.2.1. This will evidently increase the complexity of the vessel hence increase capital cost. Besides the geometrical contribution, pressure drop is also affected by the operating conditions. For a high pressure system, the gas density increases and this will increase the

system pressure drop. A dimensionless number, the Euler number ($Eu = \Delta P/0.5\rho_f U_{in}^2$), is used to determine the resistance of the cyclone.

Flow split, the ratio of air leaving through the vortex finder to the air supplied, is crucial in this project because a high flow split will reduce the load on the secondary knitted mesh pad and hence the tendency to flood. The mesh characteristics are very important in this case in order to design the maximum velocity that it can handle before it floods. The study on flow split is elaborated in more detail in Chapter 9.

Re-entrainment and separation efficiency are inter-related. If the re-entrainment rate is high, this will reduce the separation efficiency. Re-entrainment is unfavourable in this work because this will damage the compressor downstream. The inception criteria for droplet entrainment has been studied by **Ishii and Grolmes (1975)** and **Andreussi (1980)**, as discussed in Chapter 2.

It is of interest in this research to investigate the range of droplet size that will escape through the vortex finder, hence the separation efficiency is plotted against the diameter of the droplet. The efficiency tests were carried out with an air-water system under atmospheric conditions. The grade efficiency curve can be scaled easily using the Stokes Number scaling method as discussed in Section 4.2.4 if the physical properties of the actual conditions are known.

In the later part of this chapter, the development of all the cyclone designs tested in this research is elaborated in detail under Section 4.3, from the initial design with static swirl vanes located on a central boss to the most successful design with tangentially oriented swirl vanes. All the design details are documented including both the vanes' design and the skirt around the vortex finder.

The experimental results and discussion on the flooding/re-entrainment and the grade efficiency tests are presented in the next chapter.

Chapter 5

Experimental Results and Discussion: The Initial Geometry

This chapter draws together the results from all the experimental tests performed on the initial geometry during the course of the project. The findings are discussed extensively. The discussion will encompass the pressure drop – flowrate characteristics and the onset of entrainment/re-entrainment.

5.1 Pressure Drop Measurement

Pressure drop is one of the important parameters that determines the practical performance of a cyclone. Pressure drop is measured across the whole cyclone for all the tested geometries. The pressure drops are measured from inlet (PT_S) to both outlets (PT_C and PT_A) (See Figures 3.2 and 3.3 for the locations of all the pressure tappings). The total pressure drop is the addition of the dynamic pressure and the static pressure as described in Chapter 2. The measured pressure drops using manometers are the static pressure drops. The dynamic pressure drop is calculated and added to the static pressure drop to make up the total pressure drop across the cyclone. The total pressure drop can be related to either the vortex finder tube or the annulus (disengagement space) since the outlets are vented to a common pressure in the real application. The equations for the total pressure drop are as below:

$$\Delta P_{SC\,(Total)} = (P_S + \tfrac{1}{2}\rho U_S^2) - (P_C + \tfrac{1}{2}\rho U_C^2) = \Delta P_{SC} - \tfrac{1}{2}\rho (U_C^2 - U_S^2)$$

- Equation (5.1)

$$\Delta P_{SA\,(Total)} = (P_S + \tfrac{1}{2}\rho U_S^2) - (P_A + \tfrac{1}{2}\rho U_A^2) = \Delta P_{SA} - \tfrac{1}{2}\rho (U_A^2 - U_S^2)$$

- Equation (5.2)

Each geometry gives a value of Euler number (Refer to Section 2.7.1 for Eu definition), which corresponds to a certain value of flow split (the ratio of the flow in the vortex finder to the total flow).

The following sections will discuss the pressure drop-flowrate characteristic for the initial design with justifications from visual observations.

5.1.1 Analysis of Results (Initial Geometry)

Tests were performed with the initial design to gain an understanding of the experimental system and also the importance and influence of the design parameters (i.e. slots, swirling device, vortex finder) on the flow split. The flow split is the ratio of the air leaving through the vortex finder to the air supplied. In practice, it is crucial to get a much higher flow split so that the load on the secondary mesh is reduced substantially so that it is less likely to flood (Refer to Figure 3.3 for the rig assembly). The pressure for both the gas vents should be the same. In order to achieve this, the gate valve controlling the vortex flow, Valve VC, was fully opened while adjusting the gate valve controlling the slot flow, Valve VA, only then the pressure drop measurements were taken. With the initial design shown in Figures 4.5, 4.6 and 4.7 (Chapter 4, Section 4.3 with D_{VF} = 26 mm and four 5x111 mm slots), the dry flow split obtained was found to be around 20%. The Eu number ($Eu = \Delta P/0.5\rho_g U_{in}^2$) for this design for dry condition (i.e. only air was present) was around 10.5.

Pressure drops at different flow splits were also measured (i.e. 21%, 23%, 25%, 30%, 35% and 40%) by adjusting Valve VA with Valve VC fully opened until the required flow split was achieved in a dry condition. This test was to simulate the condition where more air went through the vortex finder when water was present because the slots would be gradually blocked. This is an estimation of the pressure drop when water is present and this term will be referred to as the adjusted dry pressure drop, ΔP^a_{dry}. Figure 5.1 shows the pressure drops for all the

dry tests carried out with the corresponding flow split stated at the end of each curve. The pressure drop is the highest when all the flow is going out through the vortex finder because of the high swirl inside the vortex finder tube. From the relation between tangential velocity and the pipe radius, the tangential velocity, U_{tan}, is inversely proportional to the radius, r. Hence, the smaller the radius the higher the tangential velocity. Since the flow is forced to pass through a smaller area (from a 52 mm tube into a 26 mm tube), the U_{tan} is higher. Therefore, the pressure drop increases significantly as more flow goes through the vortex finder.

Figure 5.2 illustrates the pressure drops with presence of water at different liquid loadings. The liquid loadings investigated are classified into various ranges. From the graph, it can be seen that even a small introduction of water into the system increases the pressure drop significantly (approximately double at low air flowrates).

- ***Behaviour at low gas flow rates***

In the initial design, which had the centre body swirler as the swirling device, visual observation showed that the liquid tended to stick onto the swirler (centre body and vanes) and also onto the cyclone wall. Therefore, energy was required to accelerate the liquid within the system to the air velocity (at most). This term was estimated using $\frac{1}{2}\rho_f U_{in}^2$ (the dynamic energy loss), where ρ_f is the fluid mixture density [$\rho_f = \rho_g (1-L) + \rho_w L$], L is the liquid loading and U_{in} is taken to be the linear air inlet velocity. From visual observation, a frothing zone (i.e. liquid hold-up) was formed in the collection zone when the air flowrate was low. This was because the strength of the vortex generated was not strong enough to throw the liquid to the wall. The air flowrate was just enough to hold the liquid from falling backwards. This phenomenon was similar to the situation in a sieve tray with the slots acting as a weir. Liquid was only separated when the liquid level built up to the beginning of the slot rather than being thrown to the wall due

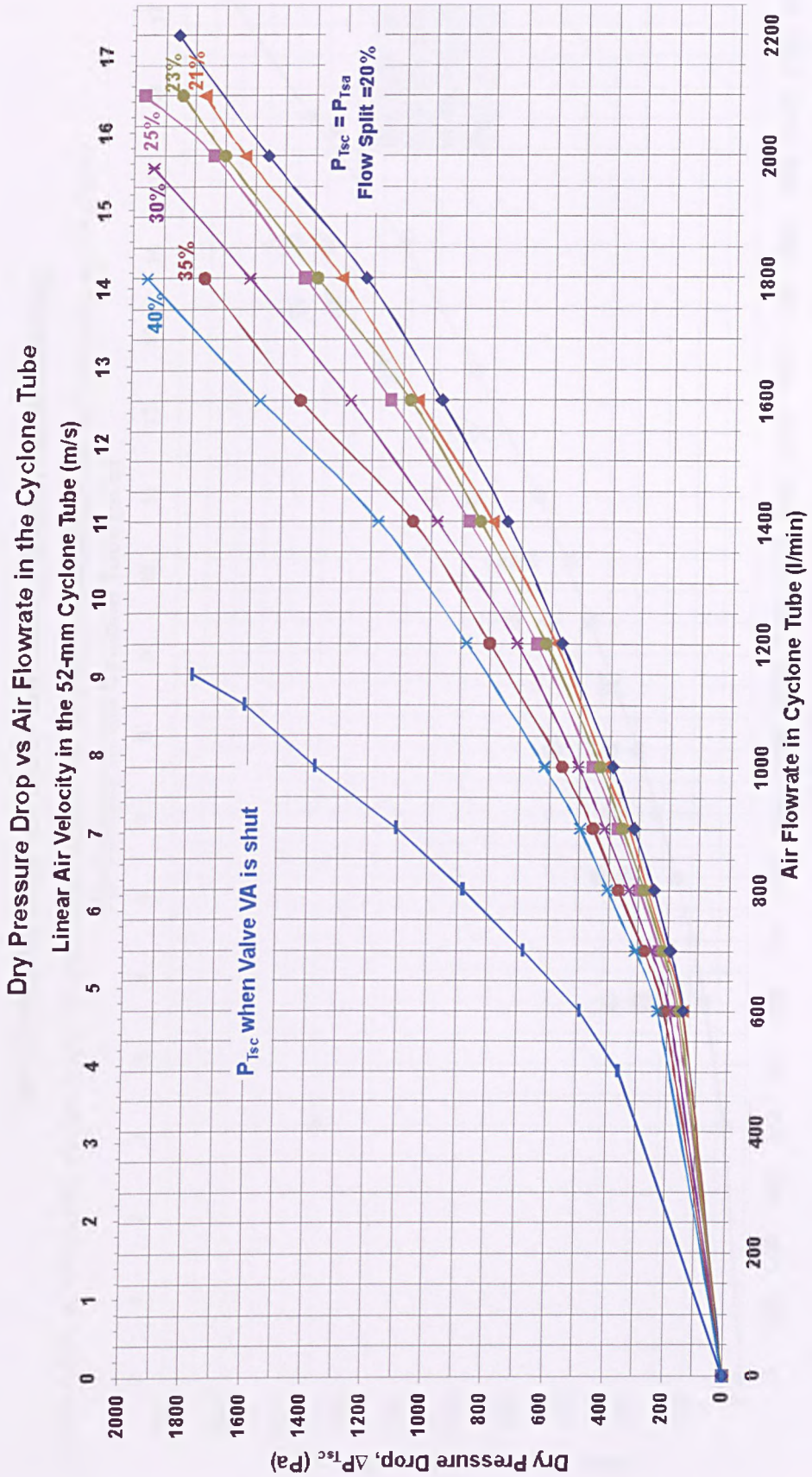

Figure 5.1: Dry pressure drop at different flow splits for initial geometry.

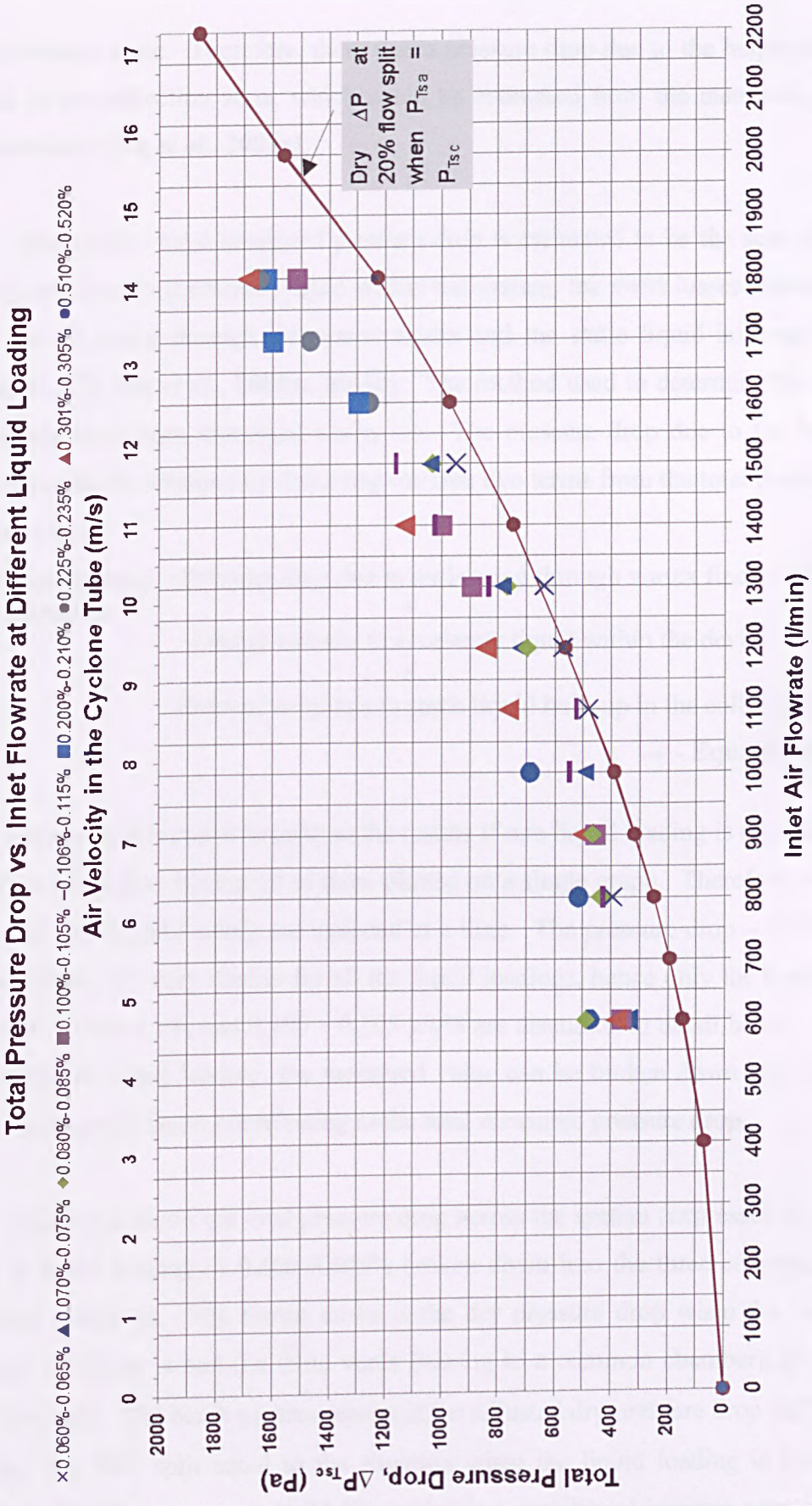

Figure 5.2: Total pressure drop measurements at different ranges of liquid loading.

to centrifugal force. Therefore, there was a pressure drop due to the height of the liquid in the collection zone, which could be estimated from the measured total pressure drop **(Ng *et al.*, 2003a)**.

The cyclone total measured pressure drop is estimated to be the sum of the energy required to accelerate liquid within the system, the swirl losses associated with the air going through the vortex finder and the static liquid hold-up (See Equation 5.3) **(Ng *et al.*, 2003a; 2003b)**. The method used to determine the first two terms have been discussed earlier on. The pressure drop due to the liquid hold-up could be obtained by deducting the first two terms from the total measured pressure drop.

Total Pressure Drop (Measured) = Pressure drop due to air leaving through vortex finder (ΔP_{VF})
+
Energy transfer to accelerate liquid within the device
+
Pressure drop due to static liquid hold-up in the collection zone
↳ **- Equation (5.3)**

However, it is easier to analyse the results if one liquid loading is considered at a time rather than having all of them plotted on a single graph. Therefore, extra graphs of one liquid loading are included at a time. The pressure drop – flowrate characteristics are very similar for all the liquid loadings, hence only the loadings of 0.060 – 0.065 v/v% and 0.100 – 0.105 v/v% are discussed in detail below. For each range of liquid loading, the measured value can be broken down into three components, each factor contributing to the total measured pressure drop.

Figure 5.3 shows the total pressure drop across the system (expressed in mm H_2O) at liquid loading of 0.600-0.605% broken down into the three components indicated earlier on. The brown curve is the dry pressure drop when the outlet pressure condition is met (i.e. both vents flowing to a common chamber), giving 20% flow split. The black squares represent the adjusted dry pressure drop (ΔP^a_{dry}) with the dry flow split equal to the situation when the liquid loading is 0.600-0.605%, which is approximately 21.5%, which is a very trivial increase compared to the dry condition. This is because water is only spun out from the bottom of the

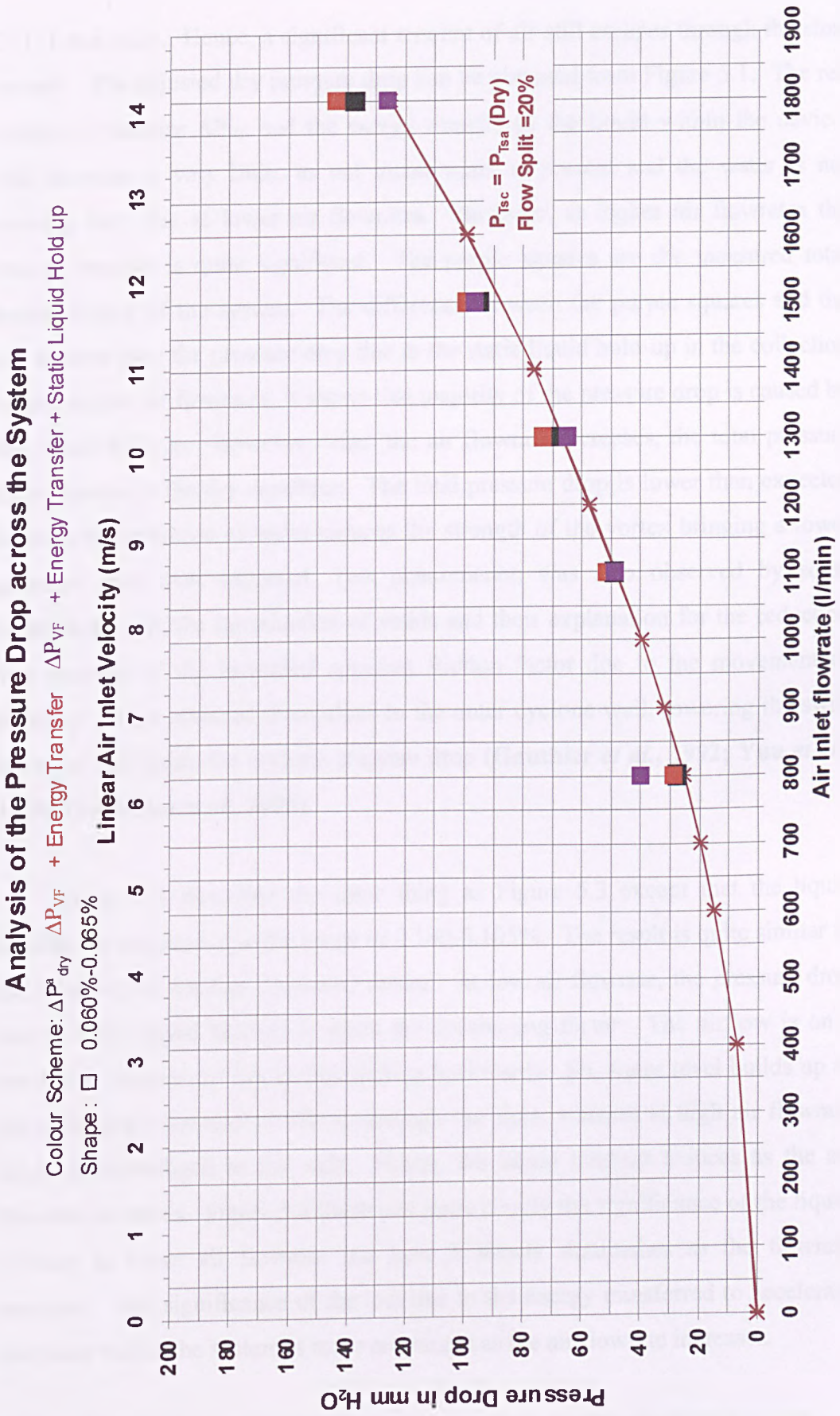

Figure 5.3: Analysis of the pressure drop at liquid loading of 0.060-0.065%.

5x111 mm slots. Hence, a significant amount of air still escapes through the slots as well. The adjusted dry pressure drop can be obtained from Figure 5.1. The red squares symbolise ΔP_{VF} and the energy transfer to the liquid within the device. The increase is very little, as not much water is present and the water is not moving very fast at lower air flowrates. However, at higher air flowrates the energy transfer is quite significant. The purple squares are the measured total pressure drop of the system. The difference between the purple squares and the red squares give the pressure drop due to the static liquid hold-up in the collection zone. At low air flowrates, it shows that majority of the pressure drop is caused by the liquid hold-up. However, when the air flowrate increases, the total pressure drop reduces to the dry condition. The total pressure drop is lower than expected because the presence of water reduces the strength of the vortex bringing a lower pressure drop than expected. This phenomenon was also observed by some researchers with the introduction of solids and their explanation for the reduction was because of the increased apparent friction factor due to the movement of particles, which attached themselves to the outer cyclone wall, lowering the swirl intensity and hence the cyclone pressure drop **(Gauthier *et al.*, 1992; Yuu *et al.*, 1978; Hoffmann *et al.*, 2001)**.

Figure 5.4 describes the same thing as Figure 5.3 except that the liquid loading investigated is in the range of 0.100-0.105%. The result is quite similar to the lower liquid loading discussed earlier. At low air flowrate, the pressure drop due to static liquid hold-up is again the dominating factor. The airflow is only enough to prevent the liquid from falling backwards. So, water level builds up in the collection zone and overflows through the slots, whereas at high air flowrate liquid is centrifuged to the wall. Hence, the liquid hold-up reduces as the air flowrate increases. Figure 5.5 illustrates more clearly the significance of the liquid hold-up at lower air flowrate and how it slowly diminishes as the flowrate increases. The significance of the loss due to the energy transferred to accelerate the water within the system is more prominent as the air flowrate increases.

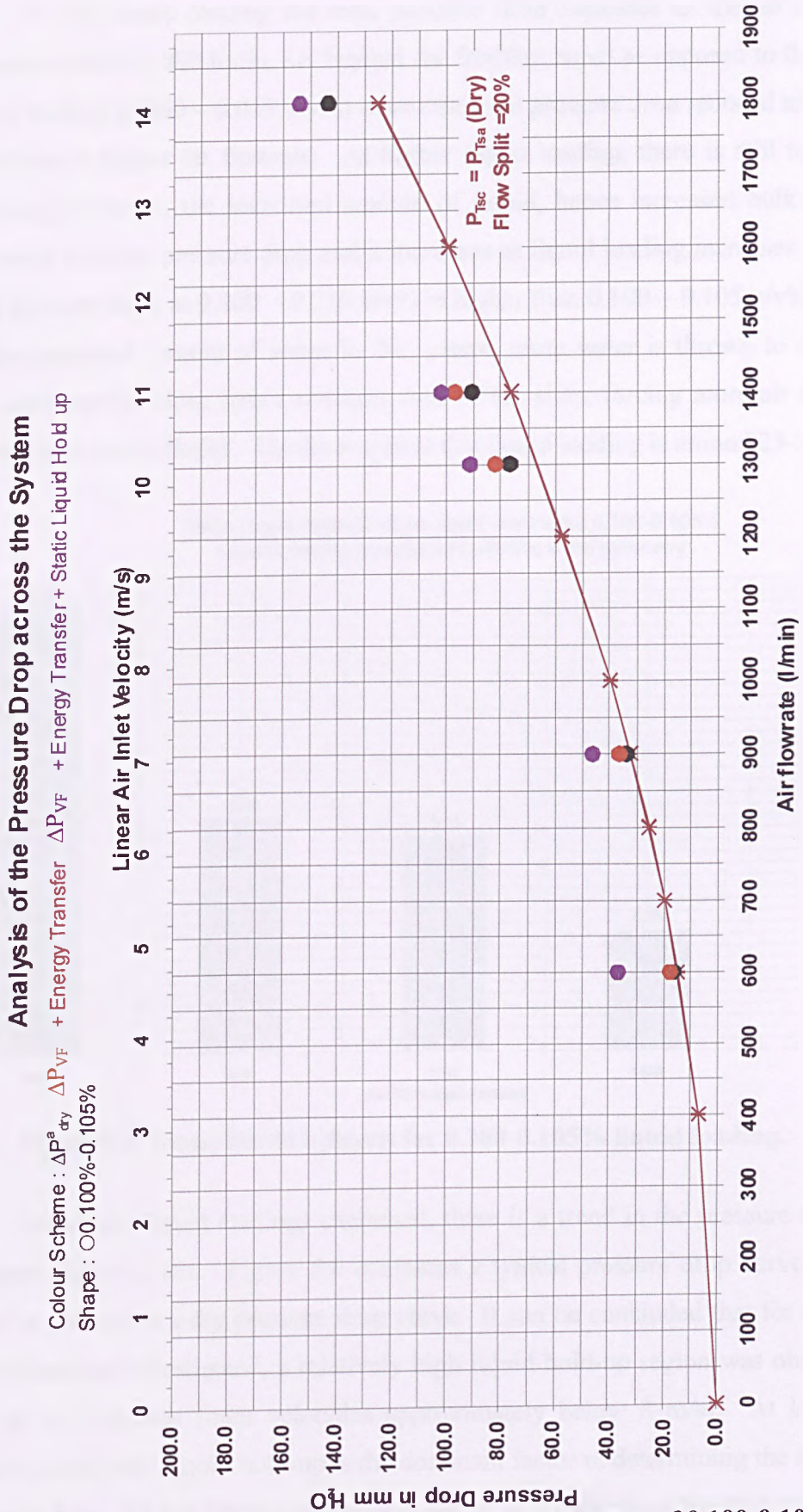

Figure 5.4: Analysis of the pressure drop at liquid loading of 0.100-0.105%.

At this liquid loading the total pressure drop increases as the air flowrate increases (above 1000 l/min, i.e. beyond the frothing zone) as opposed to the lower liquid loading (0.060 – 0.065 v/v%) where the total pressure drop reduced to the dry condition at higher air flowrate. At higher liquid loading, there is still turbulent damping, however, the increased amount of liquid, hence increased bulk density increases the total pressure drop and it increases as liquid loading increases (i.e. the total pressure drop at 0.200 – 0.210 v/v% is higher than 0.100 – 0.105 v/v%). Due to the increased amount of water in the system, more water is thrown to the wall and out from the slots, hence reducing area of the slots, forcing more air to leave through the vortex finder. The flow split at this liquid loading is around 23-24%.

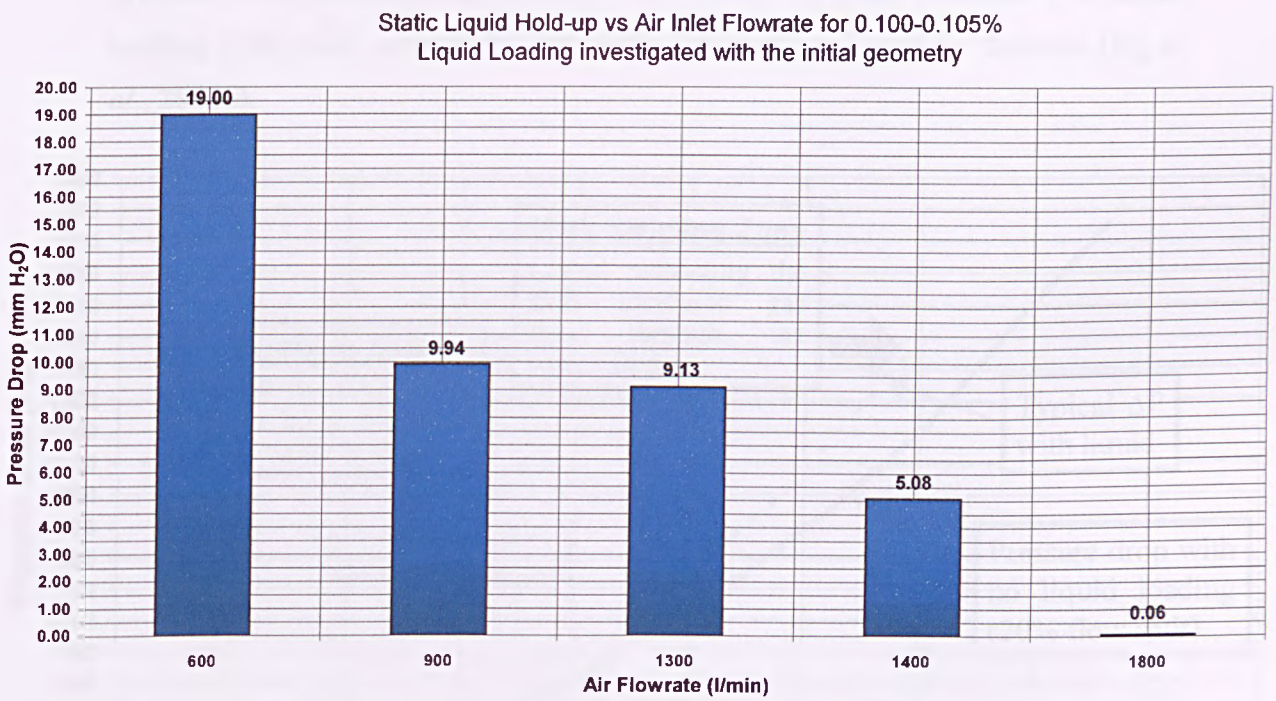

Figure 5.5: Static liquid hold-up for 0.100-0.105% liquid loading.

For all the liquid loadings examined, there is a trend in the pressure drop – flowrate characteristic. Figure 5.6 compares a typical pressure drop curve when liquid is present to a dry pressure drop curve. It can be concluded that for all the liquid loadings investigated, a relatively high liquid hold-up region was observed at low air flowrates (inlet velocities approximately below 8 m/s). At low air flowrates the static liquid hold-up is the dominant factor in determining the system pressure drop. This is a deficiency of this design of inlet because the airflow is not

high enough to swirl and entrain the liquid, but only enough to prevent the liquid from falling backwards (weeping). In this case, the slots tend to act as a weir (like the situation of a sieve tray in a distillation column). Liquid builds up in the collection zone and flows out through the slots. As the air flowrate increases, liquid starts to pulsate (frothing region) and drops are vigorously entrained/re-entrained into the vortex finder. As the air flowrate is increased above 10 m/s, the centrifugal force is high enough to throw the liquid out through the slots. At low air flowrates and low liquid loading (0.060% - 0.065%), relatively little energy is transferred to accelerate the liquid. The energy transferred becomes more significant at higher air and liquid flowrates (0.100% - 0.105% and above). The pressure drop due to the increased flow into the vortex finder increases with liquid loading (with more area of the slots being blocked) and with air flowrate **(Ng *et al.*, 2003a)**.

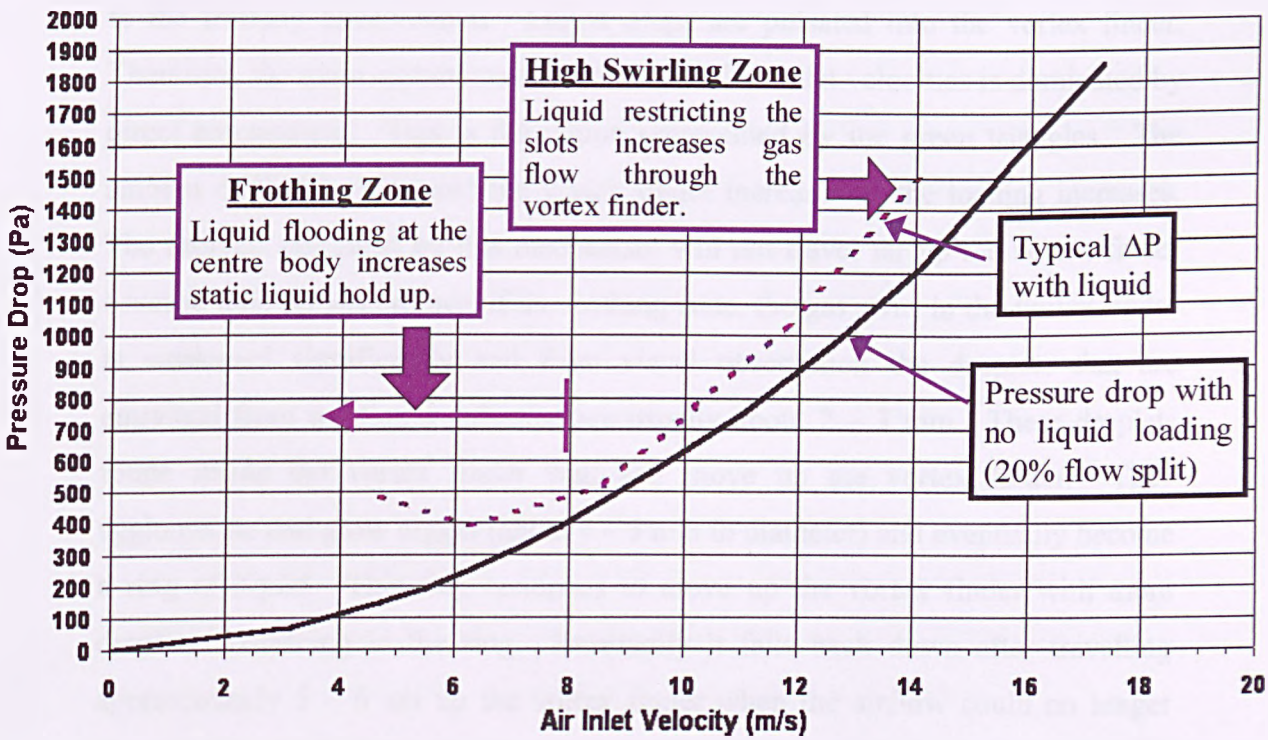

Figure 5.6: Typical dry and wet total pressure drop curves.

5.2 Onset of Entrainment/Re-entrainment (Initial Geometry)

Observations were also made of the onset of entrainment/re-entrainment. Re-entrainment is a phenomenon where liquid droplets, large enough normally to be collected by cyclonic action, leave through the vortex finder **(Ng *et al.*, 2003a)**. This can normally be detected by observation of liquid drops in the vortex finder. A significant effort was spent on determining the onset of entrainment/re-entrainment using the initial geometry. Three mechanisms could be identified, namely direct entrainment, re-entrainment due to liquid creep and re-entrainment due to stripping of the liquid film on the cyclone wall as described in Chapter 4. Figure 5.7 (onset of entrainment/re-entrainment graph) plots the liquid loading (v/v %) vs. linear air inlet velocity. It shows that at an inlet velocity lower than 8 m/s entrainment/re-entrainment occurs irrespective of the liquid loadings. This is due to the frothing phenomenon. Liquid drops are pulsated into the vortex finder. Therefore, the main entrainment mechanism at low inlet velocities is dominated by direct entrainment. This is the region represented by the green triangles. The amount of liquid going into the vortex finder increases as the loading increases. The droplets entrained by this mechanism will not travel far up the vortex finder because with the occurrence of the frothing zone, the gas swirl in the vortex finder is weakened significantly and from visual observation the droplets that are entrained from the liquid pulsation are usually about 2 – 3 mm. These droplets rotate inside the vortex finder wall and move up the vortex finder. They agglomerate and grow bigger (about 4 – 5 mm in diameter) and eventually become a ring of liquid. This ring continues to move up the vortex finder with more droplets coalescing in the ring. Eventually it falls back down after travelling approximately 5 – 6 cm up the vortex finder when the airflow could no longer support the weight of the liquid and the cycle repeats. This means that although droplets are found inside the vortex finder, they do not actually leave the vortex finder at low air flowrates (up to linear air velocity of 8 m/s) irrespective of the liquid loading (up to 0.5 v/v % investigated). This is still considered favourable since it does not induce any damage to the downstream compressor.

However, as velocity increases (above air velocity of 8 m/s) and at higher liquid loadings water droplets start to stick on the outer wall of the vortex finder, coalesce and then drain down the tube until they reach the lip. There it forms a film running around the lip of the vortex finder (See Figure 4.4 for illustration). As the film builds up it will reach a point where droplets will be sheared off into the gas stream. At this point, the liquid takes one of two different courses, either it flies outwards towards the wall of the cyclone tube or it creeps into the vortex finder where it creeps up the inside wall. At higher velocities, the chances of liquid being re-entrained due to stripping of liquid film on the cyclone wall increases. It is envisaged that some fine droplets are entrained directly into the vortex finder, but this mechanism is not dominant at high velocities. At high velocities, liquid is swirled up the vortex finder by a combination of three mechanisms. This region is illustrated by the area with the dark blue diamond-shaped icons in Figure 5.7. Once on the inner wall, the liquid in the form of mobile drops on the surface, tends to move around the inside in a swirling motion, following the gas. These drops are smaller compared to those that are entrained due to the occurrence of the frothing zone. They are approximately 1 – 2 mm in diameter (from visual observation) and they reduce in size as the air flowrate increases (down to 0.5 mm at an inlet velocity of 14 m/s). These entrained/re-entrained droplets travel all the way up the vortex finder tube and the rate increases as the inlet velocity increases. The amount of liquid travelling up is rather small (only in the order of 10^{-5} l/min) from the estimation method discussed in Chapter 4 compared to the incoming liquid. Nevertheless, entrainment/re-entrainment should be avoided by any means. Even though the amount of flow entrained/re-entrained is significant, the drop size is usually large (few mm in diameter) and this could cause damage to the downstream equipment.

The red circles represent the region with no liquid carry-over. At low liquid loadings and high inlet velocities, the drops are thrown to the wall and exit through the slots due to the high centrifugal force. Figures 5.8 and 5.9 show the swirl strength both at low and high air flowrates. There are video recordings

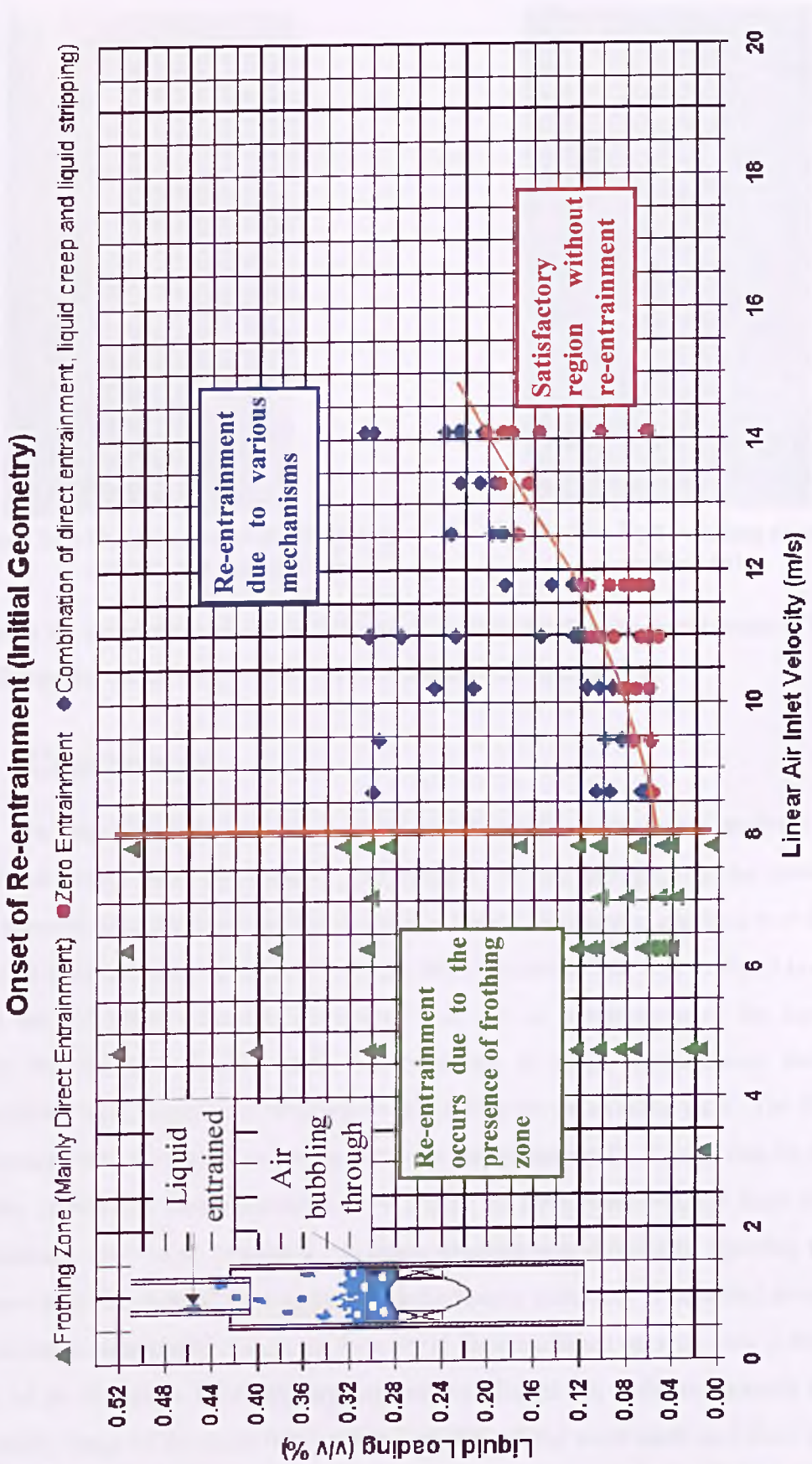

Figure 5.7: Analysis of the onset of entrainment/re-entrainment for the initial geometry.

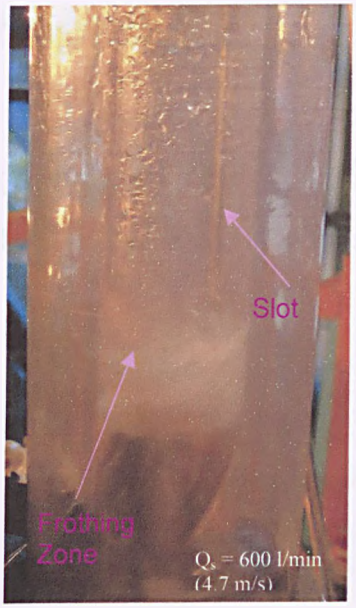

Figure 5.8: Occurrence of the frothing zone in the cyclone tube.

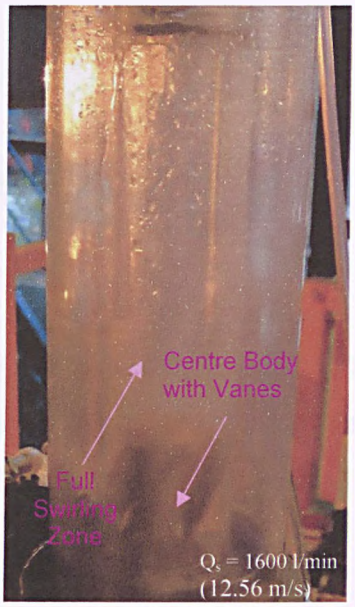

Figure 5.9: Full swirling zone in the cyclone tube.

showing the occurrence of the frothing zone and entrainment/re-entrainment of the liquid into the vortex finder of the initial geometry in Appendix H.

5.3 Conclusions

The pressure drop and the onset of entrainment/re-entrainment analyses of the initial design were discussed in this chapter. It was thought that the system total pressure drop could be broken down into three components; pressure loss due to the swirling air going through the vortex finder, pressure loss due to liquid hold-up in the collection zone and the energy loss due to acceleration of the liquid within the system. Liquid carry-over was due to three mechanisms; direct penetration, liquid creep and stripping of liquid film on the cyclone wall. The first mechanism was dominant at low linear inlet air velocities (< 8 m/s) due to the frothing region (i.e. liquid pulsation). At higher air inlet velocities, the latter two mechanisms were more dominant. A phase diagram was developed showing the region where the onset of entrainment/re-entrainment occurred. The initial design has shown a meaningful insight on how axial flow cyclones operate over a wide range of air flowrates, handling large amounts of liquid. In order to increase the operability range of the axial flow cyclone, modifications were made and these are discussed in the next chapter.

Chapter 6

Experimental Results and Discussion: The Developed Geometries

This chapter presents the results obtained from all the experimental tests performed during the course of this research work on all the developed geometries. The discussion will include the pressure drop – flowrate characteristics and the onset of entrainment/re-entrainment.

6.1 Design Modifications

Following the experiments on the initial, unsuccessful design, a series of geometric improvements was made to improve overall performance. The obvious problems with the original design were the occurrence of the frothing phenomena, inducing a significant increase in pressure drop at low air flowrates when water is present. The initial slots were too long and wide since it was observed that liquid only came out from the bottom halves of the slots. Hence, providing a lot of space for a large amount of air to escape through the slots, giving a low flow split (20%). The evolution of the cyclone design has been elaborated in Chapter 4. The following sections discuss the results of each modification in detail.

6.1.1 Geometry 2a and 2b

The initial step taken to eliminate the frothing zone was to drill holes in the collection zone to get rid of the water as soon as it left the vanes. Two holes of 5 mm diameter (Geometry 2a) were drilled just above the vanes **(Priestman, 2001)**. The dry flow split was approximately 18.41 %. The flow split with 0.100 – 0.105% v/v % liquid loading was around 22.62 %. However, this alteration did

not have any significant improvement on eliminating the frothing zone, hence there was no decrease in the pressure drop at low air velocity (See Figure 6.1).

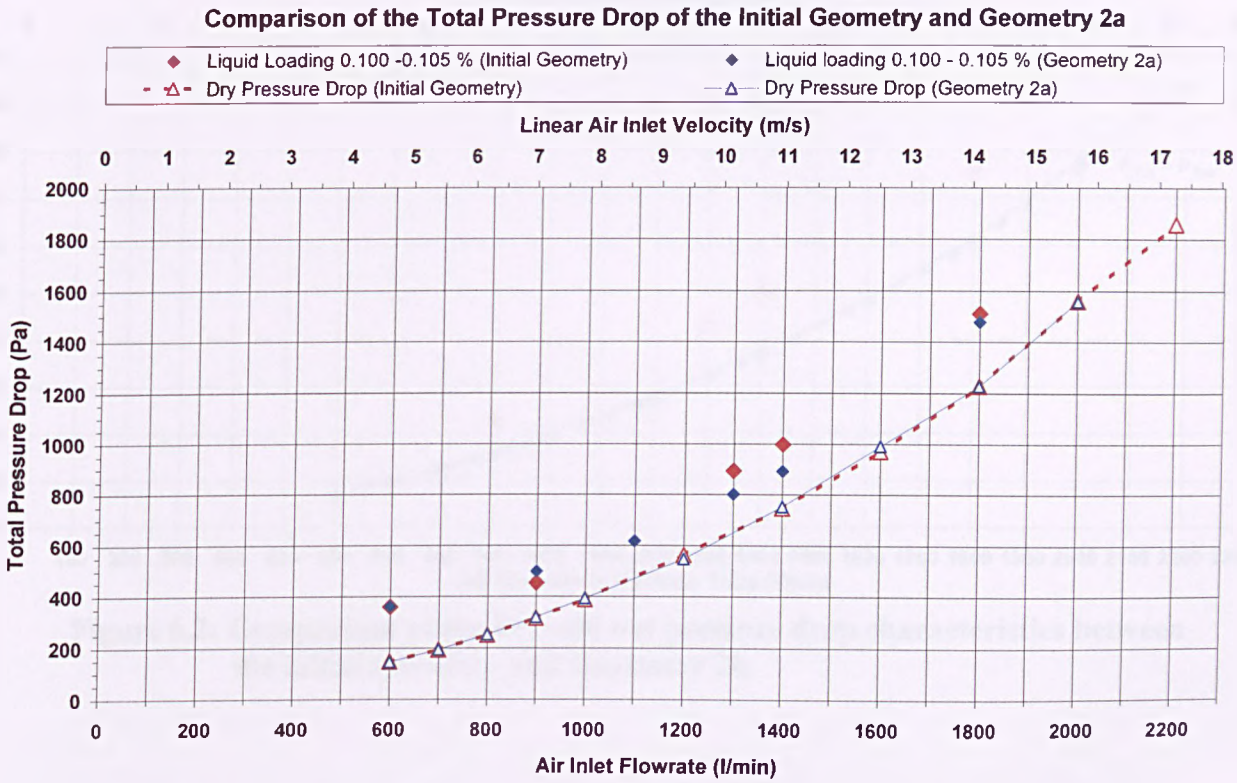

Figure 6.1: Comparing the dry and wet pressure drop characteristics of the initial geometry and Geometry 2a.

Therefore, four more equally spaced 5 mm holes were drilled in the collection zone (Geometry 2b). The top of the four 5 x 111 mm slots were blocked using adhesive tape so that the total cross sectional area for the liquid outlet equalled to the initial geometry so that any reduction in the pressure drop was due to the reduction in the liquid hold up. The dry flow split was around 19 %. Unfortunately this design also did not eliminate the frothing zone and the total pressure drop did not show any improvement from the initial geometry as shown in Figure 6.2.

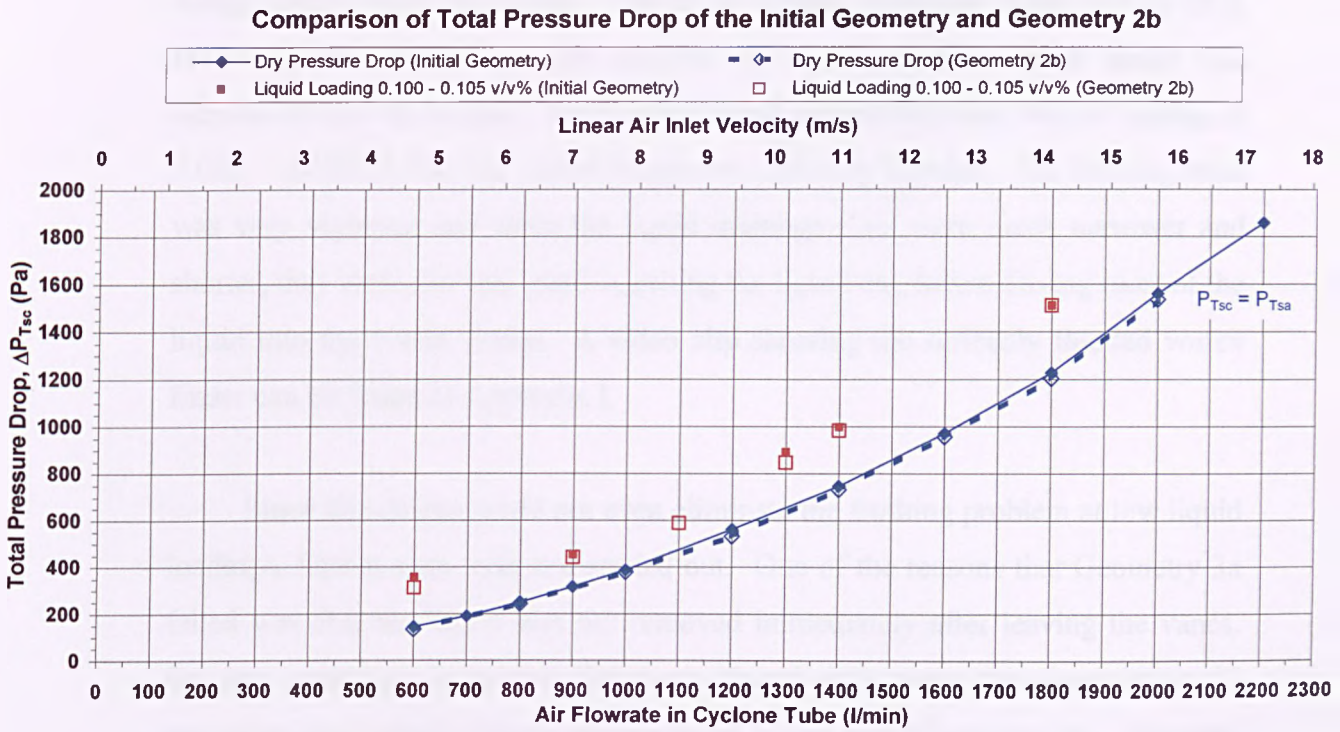

Figure 6.2: Comparison of the dry and wet pressure drop characteristics between the initial geometry and Geometry 2b.

6.1.2 Geometry 3a and 3b

The next geometry, Geometry 3a, tested was identical to the initial geometry except for the slot dimensions. Four equally spaced slots were used with a dimension of 3 x 40 mm because simulation work carried out in UMIST had shown that this design would give a good separation of about 92 % of the incoming liquid leaving through the slots **(Pokusevski, 2001)**. This was tested for flooding/re-entrainment to determine whether this design would be able to handle large amount of liquid because it was not specified in the UMIST report the amount of liquid introduced to the system and it was felt that this design might only perform very well in grade efficiency tests, but not necessarily in the flooding tests.

The dry flow split increased from 20 % to approximately 45 % due to the reduction in the slots' area, which is favourable since it was aimed at obtaining a

design with a high flow split. The Euler number increased from 10.5 to 18.8. However, this design did not perform up to expectations when water was introduced into the system. Even with a small amount of water (liquid loading of 0.060 – 0.080 v/v %), the vortex finder was seriously flooded. The frothing zone was very vigorous and since the liquid drainage slots were much narrower and shorter, they were not very good at getting the liquid out, hence driving most of the liquid into the vortex finder. A video clip showing the seriously flooded vortex finder can be found in Appendix I.

Since this design could not even eliminate the frothing problem at low liquid loadings, further tests were not carried out. One of the reasons that Geometry 3a failed was that the liquid was not removed immediately after leaving the vanes. So, four more equally spaced slots were placed right above the vanes (about 27 mm above the vanes) with the dimension of 3 x 60 mm (Geometry 3b). The total area of the liquid slots was smaller (1200 mm^2) compared to the original geometry (2220 mm^2), hence more air was forced to go out through the vortex finder, increasing the flow split to 27 % compared to 20 % for the initial geometry. The Euler number increased from 10.5 to 12.5. Like the rest, this design was tested to determine its ability in the flooding/re-entrainment tests. The wet flow split was around 28 – 29 %. Figure 6.3 compares the pressure drop – flowrate characteristics of the initial geometry and Geometry 3b.

At low liquid loadings (up to 0.080 v/v%), the liquid only went out through the bottom slots (3 x 60 mm) until an air velocity of approximately 8 m/s. Beyond this, the liquid started to swirl up to the upper slots (3 x 40 mm). The vortex finder was dry at this loading for the entire velocity range tested (up to 16 m/s). However, from visual observation, at low air flowrate when the liquid loading was increased to 0.100 v/v%, droplets of 0.5 – 5 mm in diameter were re-entrained into the vortex finder and the re-entrained drop size decreased as the air flowrate increased. This might be because a significant amount of air left through the bottom slots. When the liquid loading was increased, this liquid moved from the bottom to the top slots and some droplets were re-entrained into the vortex finder

since there was not enough air to centrifuge them to the wall. Although this design eliminated the frothing phenomena at low air flowrates, the flow split obtained was still very low and droplets were still re-entrained at high air flowrate.

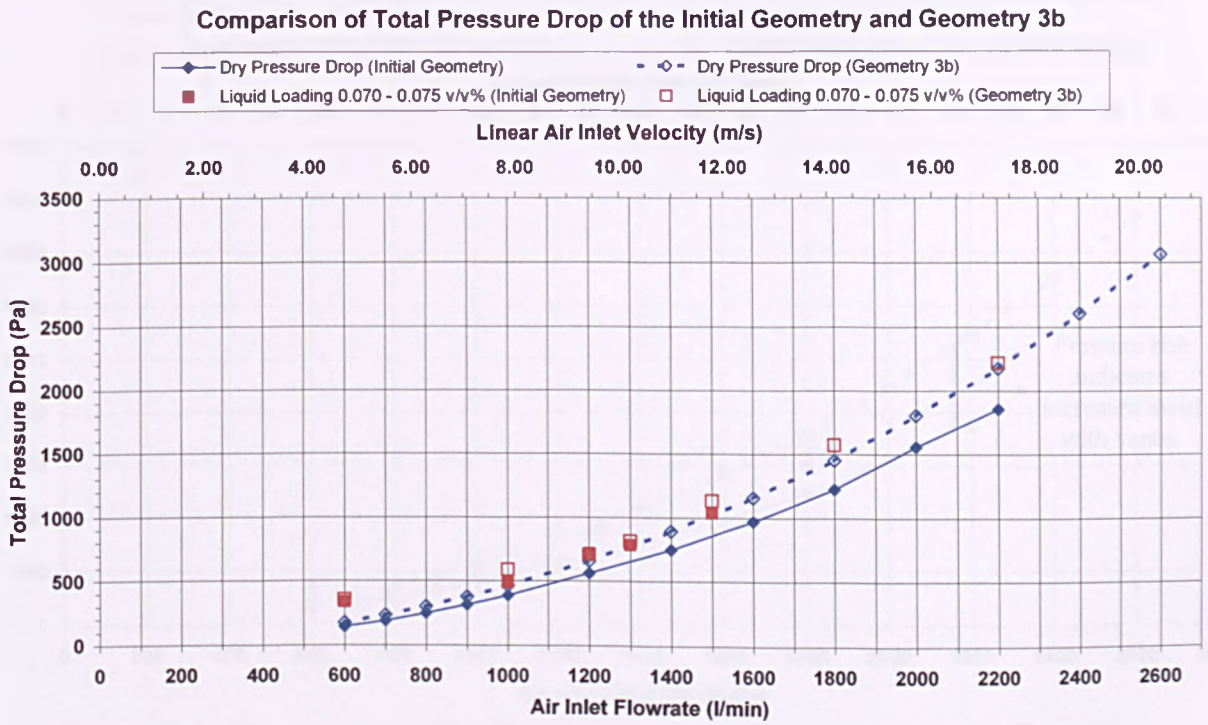

Figure 6.3: Comparison of the dry and wet pressure drop characteristics between the initial geometry and Geometry 3b.

6.1.3 Geometry 4

In all the discussed modifications, entrainment/re-entrainment still occurred and this was mostly because the air swirl was not strong enough to throw the liquid to the wall and allow drainage. Therefore, a new inlet was introduced with a tangentially oriented vane design. The design of this inlet vane was discussed in Chapter 4. It was tested for the flooding/re-entrainment using the original cyclone tube (i.e. with the 5 x 111 mm slots) and the 26 mm inner diameter vortex finder. The dry flow split for this design was around 14.3 %. The Euler number increased from 10.5 to 15.1. This showed that the new inlet design created stronger swirl throwing most of the air out through the slots. This is supported by the pressure drop – flowrate characteristics shown in Figure 6.4. Since everything remained

the same except for the vortex inducer, the pressure rise indicated increased swirl with the new inlet vanes.

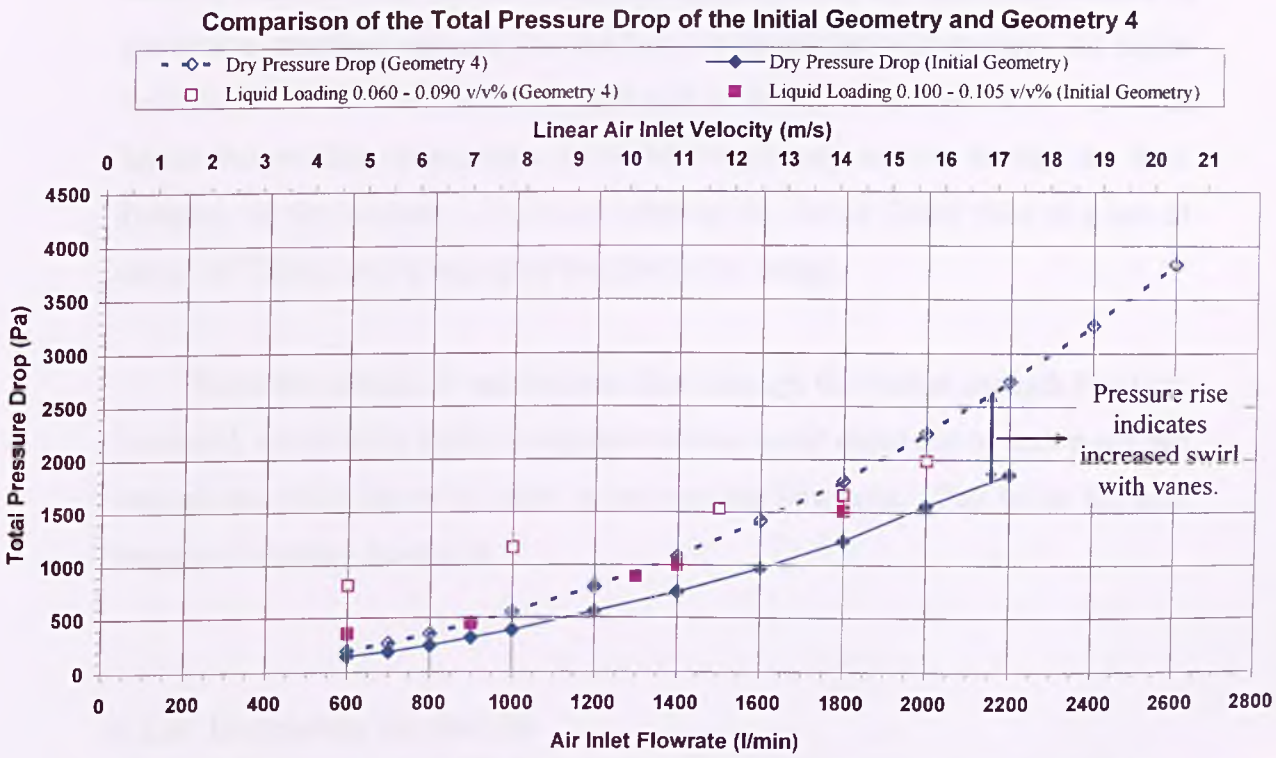

Figure 6.4: Comparison of the dry and wet pressure drop characteristics of the initial geometry and Geometry 4.

When liquid was introduced into the system, the frothing phenomena still existed at low air flowrates (up to an air flowrate of 1000 l/min). Liquid was entrained into the vortex finder due to liquid pulsation (direct entrainment). The frothing phenomenon was very serious and this caused difficulties in getting the reading of the amount of air leaving through the vortex finder because the tube was seriously flooded (See video in Appendix J). Most of the liquid was pulsated into the vortex finder because the slots were relatively further away from the vanes; 273 mm compared to 53 mm for the initial design. The swirl could have decayed before it reached the slots, hence the serious frothing. From Figure 6.4, it shows that the total wet pressure drop at low air inlet velocity is excessively higher than previous designs. The wet pressure drop is about 4 times higher than when the system is dry compared to about 2 times higher for the previous designs. This

is because the height available for the liquid hold up for Geometry 4 is longer (273 mm) for this design compared to all the previous designs (53 mm). As the inlet velocity increases, the pressure drop reduced below the dry condition because of the serious turbulent damping (i.e. the liquid weakens the swirl energy). At higher velocity (above 13 m/s), re-entrainment still occurred, but it was less serious. The liquid was swirling around the cyclone tube vigorously and out through the slots. Droplets of size around 1 – 1.5 mm crept up the vortex finder tube at a rate of about 10^{-3} l/min, which was more than the initial design.

From this design, it was realised that although the vortex strength had been increased, the frothing zone still existed because liquid could not be drawn out fast enough and effort has to be taken to increase the flow split. This led to the next designs, Geometry 5a and 5b.

6.1.4 Geometry 5a and 5b

Geometry 5a utilised a cyclone tube with four equally spaced 3 x 60 mm slots in the middle of the tube (identical to Geometry 3b, but with all the slots at the end of the cyclone blocked). In order to draw out the incoming liquid as soon as possible, two vane slots (3 x 17.7 mm) were used as an additional drainage route. The total area for liquid drainage (longitudinal slots and vane slots) was 826.2 mm^2. This design gave a dry flow split of approximately 30 %. The Euler number was calculated to be 19.2. The dry pressure drop characteristics of this design and the initial geometry are given in Figure 6.5. The dry pressure drop of Geometry 5a is a lot higher than the initial geometry since the vortex strength was higher and also more air was pushed through the vortex finder due to the reduced slots area.

Figure 6.5 also shows that when liquid is introduced into the system, the total wet pressure drop is reduced almost to the dry condition as opposed to the wet pressure drop of the initial design. This is consistent with the removal of the

frothing region, which was confirmed by observation. At low air flowrates (up to 1000 l/min) and low liquid loadings (0.060 – 0.065 v/v%), all the liquid flowed out through the additional drainage route (i.e. the two vane slots). The cyclone tube was fairly dry. Above air flowrate of 1000 l/min, liquid was seen starting to swirl up the cyclone tube. Minor frothing was still observed but entrainment did not occur until the air flowrate exceeded 2000 l/min. Drops of less than 1 mm diameter were pulsated directly into the vortex finder. The wet pressure drop was lower than the dry condition due to turbulence damping as described previously. When the liquid loading was increased to 0.100 – 0.105 v/v% the frothing zone was formed when the air flowrate was between 1200 – 1400 l/min. Droplets were entrained directly into the vortex finder due to the pulsation of the liquid. These droplets (about 2 mm in diameter) moved very quickly up the vortex finder at a rate of 10^{-6} l/min. It was also observed that all the liquid only left through the bottom halves of the slots. Therefore, the top halves of the slots were blocked, giving new slots of 3 x 30 mm with the total liquid drainage area of 466.2 mm^2 (Geometry 5b).

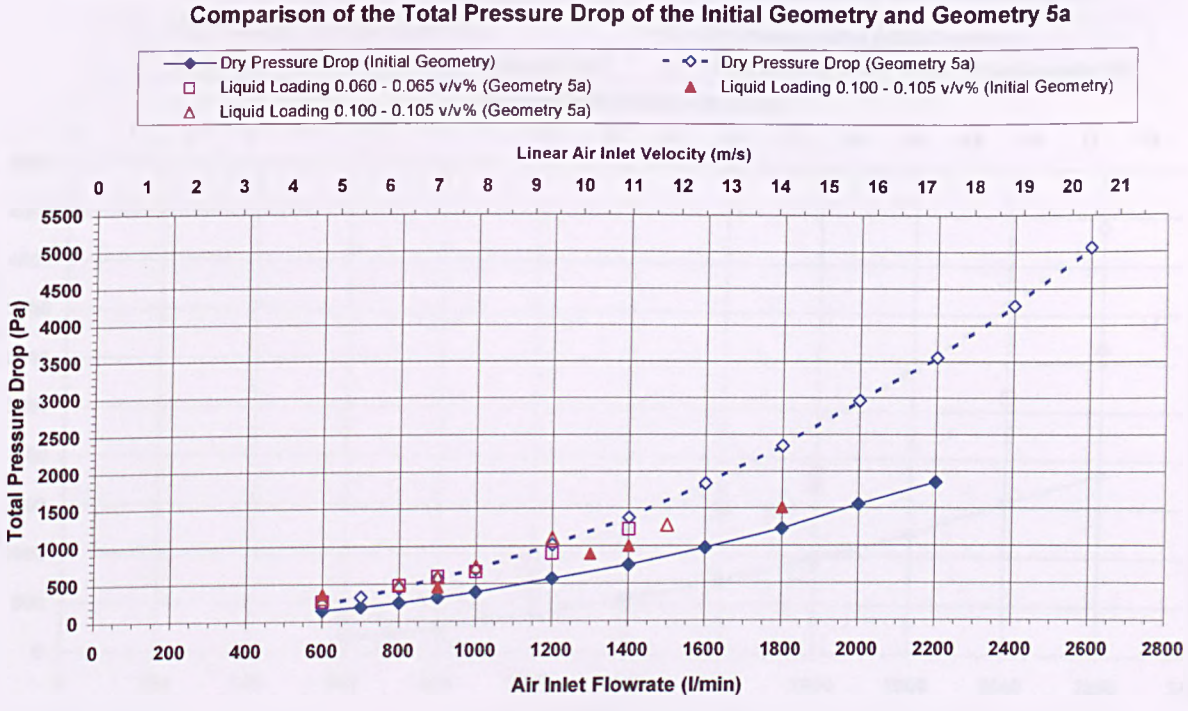

Figure 6.5: Comparison of the dry and wet pressure drop characteristics of the initial geometry and Geometry 5a.

Figure 6.6 illustrates the dry and wet pressure drop characteristics of Geometry 5b. The flow split obtained from this design was approximately 45% and the Euler number was calculated to be 24.1 due to the decreased liquid drainage area. The wet pressure drop characteristics were very similar to Geometry 5a, only slightly higher due to more air being forced to go through the vortex finder. At low liquid loadings (< 0.070 v/v%), no re-entrainment occurred within a linear air velocity of 5 – 20 m/s. As the liquid loading was increased to 0.100 – 0.105 v/v%, minor frothing still occurred. However, the frothing zone has been minimised. Re-entrainment of droplets of 1 mm diameter was observed within an air flowrate of 1400 –1450 l/min at a rate of 10^{-7} l/min. It was also observed that some of the liquid has swirled pass the drainage slots. This lead to the next modification of having four vane slots as the additional drainage (Geometry 6) so that more liquid could be taken out, hence eliminating the frothing zone entirely.

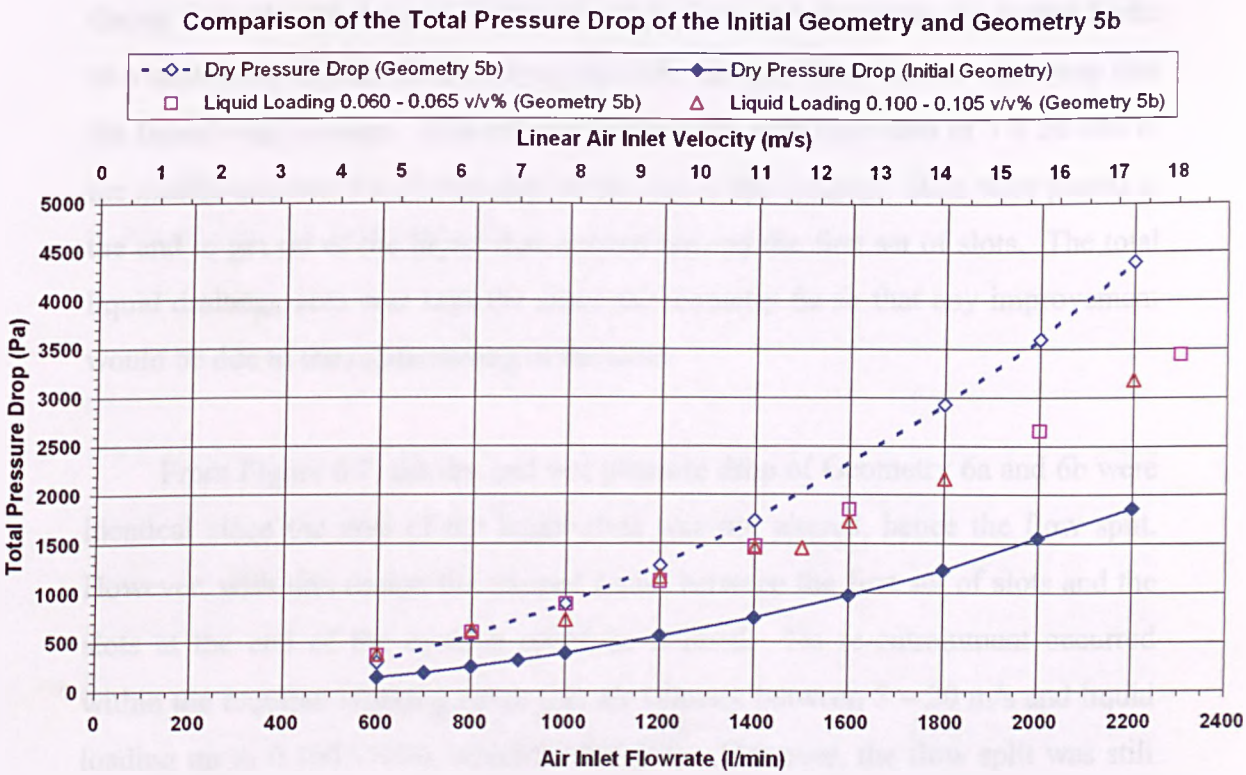

Figure 6.6: Comparison of the dry and wet pressure drop characteristics of the initial geometry and Geometry 5b.

6.1.5 Geometry 6a and 6b

Geometry 6a is identical to Geometry 5b, but with four vane slots as the additional drainage with a total area of 572.4 mm^2. The dry flow split obtained was 42.4 % with an Euler number of 25.4. Figure 6.7 shows the dry and wet pressure drop characteristics of Geometry 6a. With this design, the liquid frothing zone was totally eliminated because liquid was taken out quick enough as soon as it entered the system. Below a liquid loading of 0.100 – 0.105 v/v% no re-entrainment occurred until the air flowrate was above 2300 l/min with most of the liquid going out through the vane slots and with liquid only starting to swirl out through the four longitudinal slots above 1400 l/min. However, when the air flowrate was increased beyond 2000 l/min liquid was seen swirling beyond the slots and, as the air flowrate was increased, the amount of liquid beyond the slots also increased with a thin film spinning around the lip of the vortex finder. When the air flowrate was beyond 2300 l/min, liquid was entrained into the vortex finder in a continuous stream all the way up the tube because there was no other way that the liquid could escape. This led to Geometry 6b with four slots of 3 x 20 mm in the middle and two 3 x 20 mm slots at the end of the cyclone. Slots were placed at the end to get rid of the liquid that swirled beyond the first set of slots. The total liquid drainage area was kept the same as Geometry 6a so that any improvement would be due to the repositioning of the slots.

From Figure 6.7, the dry and wet pressure drop of Geometry 6a and 6b were identical since the area of the liquid slots was not altered, hence the flow split. However, with this design the trapped liquid between the first set of slots and the slots at the end of the cyclone could be drained. No re-entrainment occurred within the required working range (i.e. air velocity between 5 – 20 m/s and liquid loading up to 0.100 v/v%), which is desirable. However, the flow split was still considered quite low even with the addition of liquid in the system, which was approximately 50% and this lead to Geometry 7 as discussed in the next section.

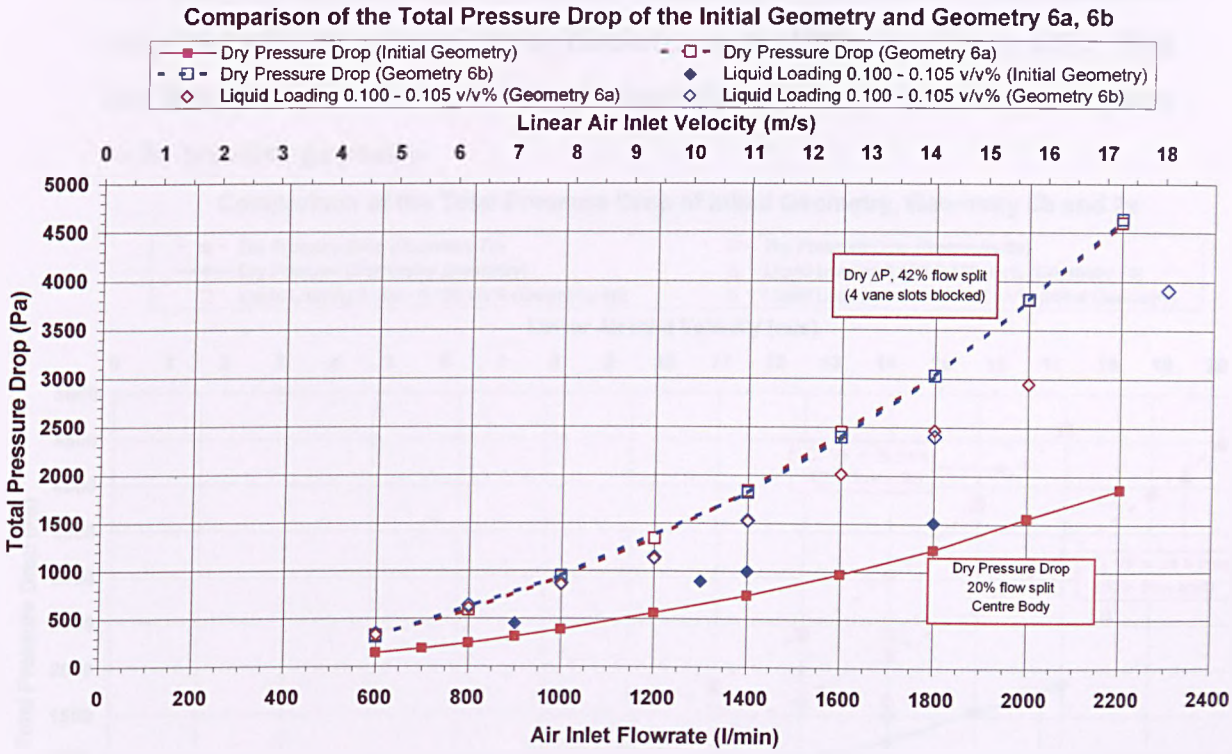

Figure 6.7: Comparison of the dry and wet pressure drop characteristics of the initial geometry and Geometry 6a and 6b.

6.1.6 Geometry 7a and 7b

In order to increase the flow split, the area of the drainage slots should be minimised or the area of the vortex finder enlarged. Since reducing the slot area would increase the tendency of the liquid swirling past the slots and increase the possibility of liquid re-entrainment, the latter option was implemented. The vortex finder diameter was increased from 26 mm inner diameter to 34.5 mm. The flow split was increased to 56%, a substantial step towards the initial targeted flow split of 70+% and the Euler number was 18 based on the linear air inlet velocity. Figure 6.8 shows the pressure drop – flowrate characteristics of Geometry 6b and 7a. It is clearly seen that the pressure drop of Geometry 7a has reduced compared to Geometry 6a although the flow split has increased. This was due to the larger vortex finder diameter as tangential velocity is inversely proportional to the radius

and also the increase in the diameter resulted in a decrease of the maximum tangential velocity as found out by **Hoekstra *et al.* (1999)** (See Figure 6.9). With this design a higher flow split was obtained with a lower pressure drop compared to the previous geometry.

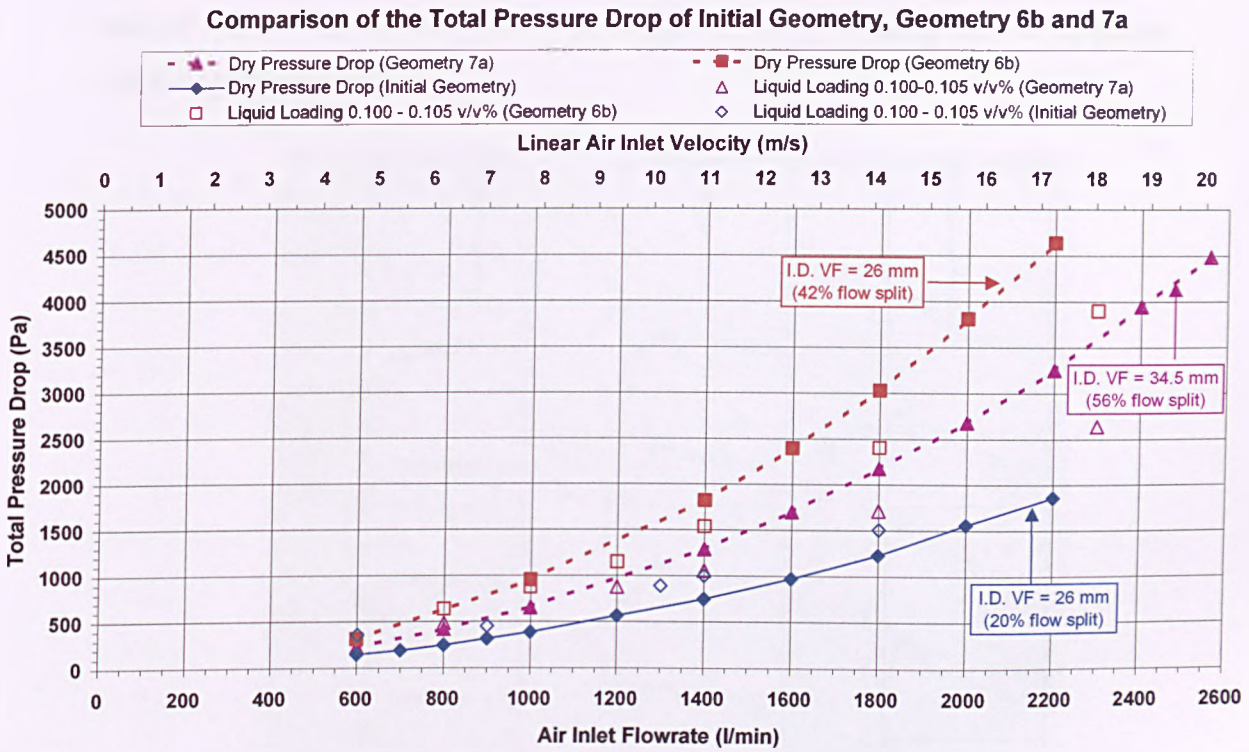

Figure 6.8: Comparison of the dry and wet pressure drop characteristics of the initial geometry, Geometry 6b and 7a.

As for the flooding/re-entrainment test, this design performed very well like the previous design in collecting and draining the liquid that entered the system. At liquid loading of 0.100 – 0.105 v/v%, all the liquid left through the slots until an air flowrate of 1700 l/min was reached. Water was seen swirling around the lip of the vortex finder and drops of less than 5 mm diameter were seen swirling up the vortex finder so quickly that it was difficult to calculate the rate of re-entrainment. However, the amount of drops moving up was quite insignificant compared to the amount re-entrained in the previous designs. This was because the droplets were re-entrained very quickly in intervals. They did not constantly swirl up the vortex finder. It was suspected that droplets were stripped off the collected film on the wall and deposited onto the wall and lip of the vortex finder or directly into the vortex finder, which covered a larger area in the cyclone tube

compared to all the previous designs. With a larger vortex finder, the tangential velocity inside the cyclone tube would be lower than the previous designs, producing a lower vortex strength; hence the re-entrainment into the vortex finder with this design, but not with Geometry 6b. When the liquid built up at the lip until its surface tension could not hold it together, drops went up the vortex finder and the cycle repeated.

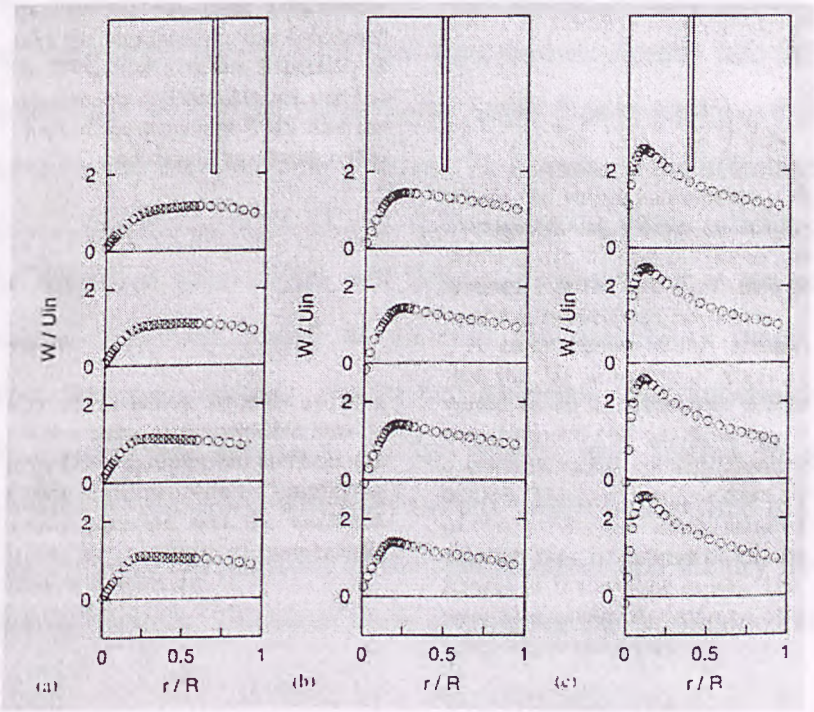

Figure 6.9: Profiles of the mean tangential velocity with a vortex finder diameter of (a) 0.190 m (b) 0.135m and (c) 0.108m. All profiles are normalised by an inlet velocity of 6.2 m/s.

From Figure 6.8, it can be clearly seen that the wet pressure drop of Geometry 7a is almost similar to the wet pressure drop of the initial geometry, but for Geometry 7a the flow split with such liquid loading in the system (0.100 – 0.105 v/v%) was approximately 61% and it was only around 23% for the initial geometry. The flow split increased by over 2.5 times, but without the expense of the pressure drop. However, minor re-entrainment still occurred with Geometry 7a. Therefore, a skirt was put around the vortex finder to eliminate re-entrainment (Geometry 7b). The detail of the skirt can be found in Chapter 4. The dry and wet pressure drop characteristics of Geometry 7b were identical to Geometry 7a as the slot area remained unchanged.

Figure 6.10 plots the onset of entrainment/re-entrainment of Geometry 7a and 7b. It is shown that below the linear air inlet velocity of 14 m/s, liquid carry-over does not occur. It is of interest to make sure that no liquid carry-over within an inlet velocity of 5 – 20 m/s below a liquid loading of 0.100 – 0.105 v/v%. With the addition of the anti-creep skirt, the range of the re-entrainment region was only slightly reduced from above 14 m/s to approximately 15.5 m/s. Above 15.5 m/s, there was no significant improvement in eliminating re-entrainment. This suggested that most of the liquid could have been thrown directly into the vortex finder or onto the outer wall of the vortex finder rather than creeping over the roof of the cyclone tube and into the vortex finder. To determine the effectiveness of the cyclone performance at around 15 m/s will require the grade efficiency data, which will be discussed later. This will determine whether it is necessary to further improve the cyclone design to increase the operability range before entrainment/re-entrainment occurs. No further alteration was undertaken after Geometry 7b because the emphasis in the project was shifted to gaining experimental results for the grade efficiency curves, which is discussed in Chapter 7. Table 6.1 below gives the summary of the specifications and the dry flow split for all the tested geometries. Details of these geometries can be obtained in Table 4.6.

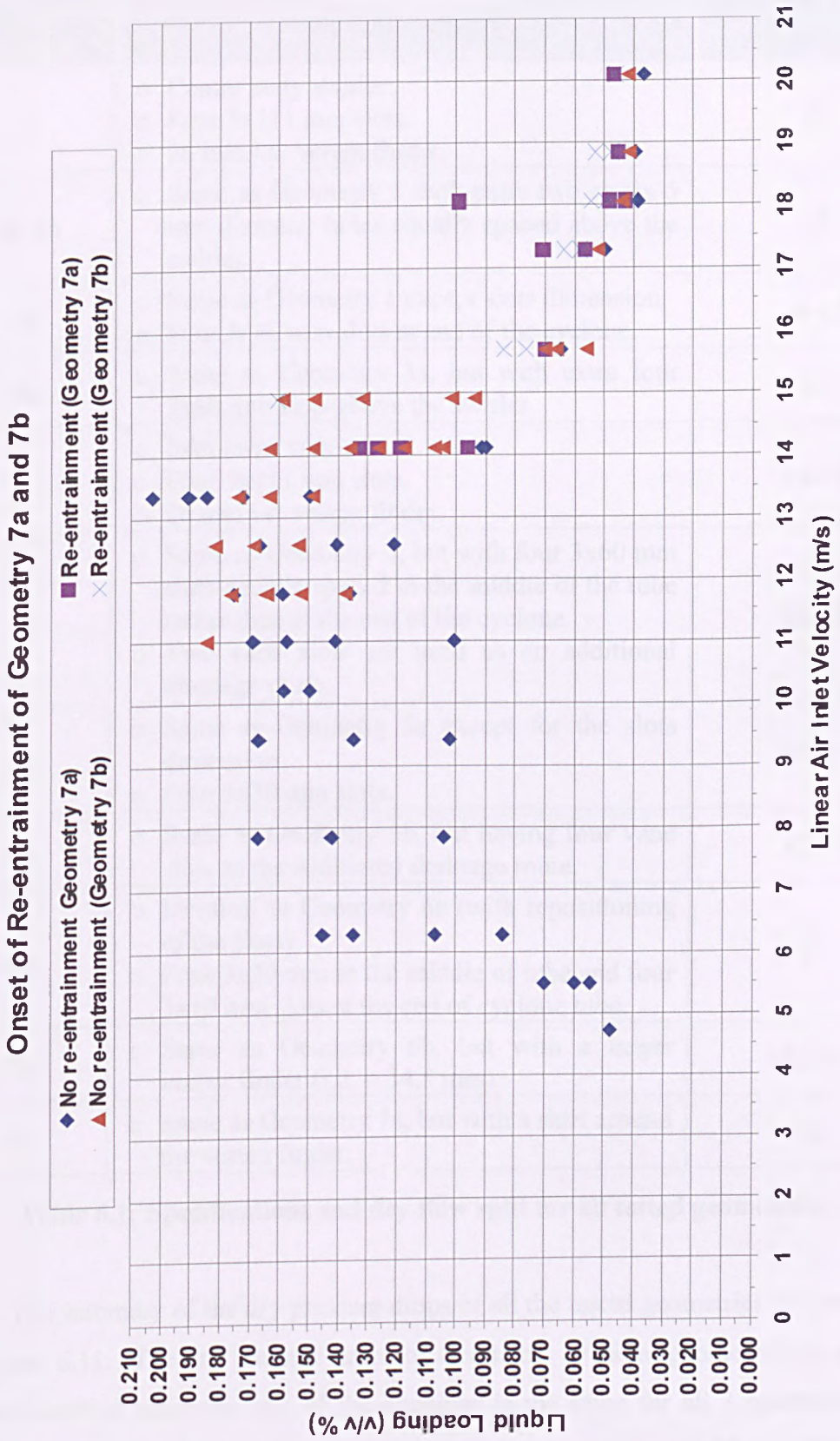

Figure 6.10: Phase diagram of Geometry 7a (without anti creep skirt) and Geometry 7b (with anti creep skirt).

Geometry	Specifications	Dry Flow Split (%)
1	o Centre body swirler. o Four 5x111 mm slots. o 26 mm i.d. vortex finder.	20
2a, 2b	o Same as Geometry 1 with extra two or six 5 mm diameter holes equally spaced above the swirler.	19
3a	o Same as Geometry 1 except slots dimension. o Four 3x40 mm slots at end of the cyclone.	44.65
3b	o Same as Geometry 3a, but with extra four 3x60 mm slots above the swirler.	27
4	o Inlet swirl vanes. o Four 5x111 mm slots. o 26 mm i.d. vortex finder.	14.31
5a	o Same as Geometry 4, but with four 3x60 mm slots equally spaced in the middle of the tube rather than at the end of the cyclone. o Two vane slots are used as an additional drainage route.	30.32
5b	o Same as Geometry 5a except for the slots dimension. o Four 3x30 mm slots.	45.01
6a	o Same as Geometry 5b, but having four vane slots as the additional drainage route.	42.36
6b	o Identical to Geometry 6a (with repositioning of the slots) o Four 3x20 mm in the middle of tube and four 3x10 mm slots at the end of cyclone tube.	41
7a	o Same as Geometry 6b, but with a larger vortex finder (i.d. = 34.5 mm).	55.91
7b	o Same as Geometry 7a, but with a skirt around the vortex finder.	56

Table 6.1: Specifications and dry flow split for all tested geometries.

The summary of the dry pressure drops of all the tested geometries is plotted in Figure 6.11. The dry pressure drops of Geometry 1 (initial geometry), 2a and 2b are identical since the area of the openings is the same for all 3 geometries. Generally, pressure drop increases as the area of slots decreases with everything else remain unchanged. This drives more air into the vortex finder (hence higher flow split) and the increase in pressure drop is associated with the greater

tangential velocity inside the tube. This is shown by the pressure drops for Geometry 3a and 3b. The slot area of Geometry 3a is the smallest compared to Geometry 1, 2a, 2b and 3b hence the highest pressure drop among the 5 geometries. Comparing Geometry 1 and 4, it is obvious that the excess pressure drop was due to the extra swirling created by the tangentially oriented swirl vanes since everything else remain unchanged. This is further supported by the lower flow split obtained with Geometry 4 because more flow leaves through the slots due to higher centrifugal force compared to the initial geometry. As area of slot openings decreases, pressure drop increases as shown by Geometry 5a, 5b, 6a, and 6b (area of openings for Geometry 6a and 6b is the same, hence same pressure drop curve). A larger vortex finder was used, from inner diameter of 26 mm to 34.5 mm, (Geometry 7) to increase the flow split. It gives a dry flow split of 56% a substantial step towards the initial targeted flow split of 70+%. The pressure drop decreases with a larger vortex finder because swirl inside the tube has decreased (tangential velocity is inversely proportional to radius). Table 6.2 below summarises all the major findings of all the tested geometries in terms of re-entrainment.

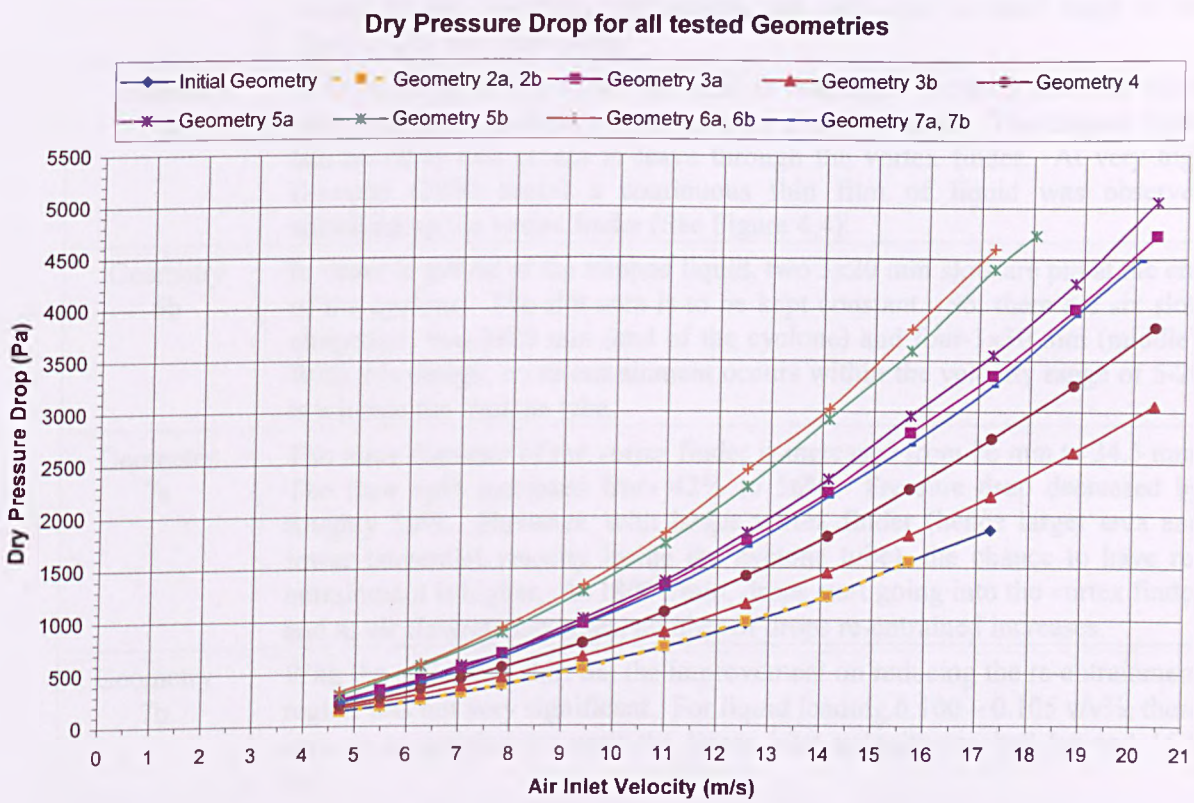

Figure 6.11: Dry pressure drops of all tested geometries.

Design	Major Findings
Geometry 1	The dry flow split is around 20%. For all the liquid loadings investigated, a liquid hold-up region is observed at low air flowrates (below 1000 l/min). This resulted a very significant increase in pressure drop (about twice the dry pressure drop). As far as re-entrainment is concerned, water drops escape through the vortex finder when the hold-up region exists (due to liquid pulsation). As air flowrate increases, liquid escapes through the slots. As liquid loading increases, re-entrainment still occurs even at high air flowrates due to liquid creeping effect.
Geometry 2a, 2b	Having holes in the collection zone does not get rid of the hold-up region. Water is not taking out fast enough.
Geometry 3a, 3b	From UMIST simulation, it seems having four 3x40 mm slots at the end of the cyclone gives the best separation. However, experiments do not agree with that. The tube was flooded straight away when water is introduced. Hence, four additional slots (3x60 mm) are put in the middle of the tube. However, liquid hold-up still occurs.
Geometry 4	The most important of these modifications was the introduction of a new tangential vane design. Inlet vanes consisting of 40 blades are used to replace the centre body. The original tube (5x111 mm slots) is used. Stronger vortex is obtained with the new vanes, but a hold-up region still exists.
Geometry 5a, 5b	Two openings in the vanes are used as an additional drainage route. The tube used is the one used in Geometry 3b, but with the four 3x40 mm slots blocked. It is seen that liquid comes out from the bottom half of the slots, so the top halves of the slots are blocked so that more air will leave through the vortex finder. Frothing still occurs, but only over a small range of air flowrates (1400-1450 l/min).
Geometry 6a	Four openings in the vanes are used as drainage. Frothing does not occur anymore, but a secondary swirl appears above the slots. The trapped liquid has no other exit except to leave through the vortex finder. At very high flowrate (2300 l/min) a continuous thin film of liquid was observed spiralling up the vortex finder (See Figure 4.4).
Geometry 6b	In order to get rid of the trapped liquid, two 3x20 mm slots are put at the end of the cyclone. The slot area is to be kept constant. So, there are six slots altogether; two-3x20 mm (end of the cyclone) and four-3x30 mm (middle). With this design, no re-entrainment occurs within the velocity range of 5-20 m/s inside the cyclone tube.
Geometry 7a	The inner diameter of the vortex finder is increased from 26 mm to 34.5 mm. The flow split increased from 42% to 56%. Pressure drop decreased by roughly 30%. However, with larger vortex finder (hence larger area and lower tangential velocity inside the cyclone tube), the chance to have re-entrainment is higher. At 1800 l/min, drops start going into the vortex finder and as air flowrate increases, number of drops re-entrained increases.
Geometry 7b	With the anti-creep skirt on, the improvement on reducing the re-entrainment region was not very significant. For liquid loading 0.100 – 0.105 v/v%, there was no re-entrainment until the linear inlet velocity reached beyond 15.5 m/s.

Table 6.2: This table summarises the major findings of the modified geometries.

6.2 Conclusions

This chapter discussed the pressure drop – flowrate characteristics and the onset of re-entrainment of all the modified geometries comprehensively. The most significant modification was the introduction of a new tangential vane design at the cyclone inlet. The most successful geometry consisted of this new inlet, four vane openings used to encourage drainage and a larger vortex finder diameter (from 26 mm to 34.5 mm) with a skirt around the tube. This had successfully eliminated the frothing region and so avoided re-entrainment at low gas throughput. This design increased the dry flow split to about 60% compared to the 20% split obtained using the initial geometry. The summaries on the findings of each design were tabulated in Tables 6.1 and 6.2.

The next chapter discusses the results acquired from the grade efficiency tests carried out.

Chapter 7

Experimental Results and Discussion: Grade Efficiency Tests

This chapter states the results obtained from the grade efficiency tests carried out in this research project. The discussion will include analysis of the collection efficiency of the entire cyclone, paying attention to the local velocity, the sampling velocity and the velocity through the measuring volume, and also the collection efficiency of the sampling probe.

7.1 Grade Efficiency Tests (Removal of Fine Droplets)

The main objective in carrying out the grade efficiency (GE) tests was to determine the cyclone's collection performance at various air flowrates. The approach used a particle analyser, Polytec HC-15, to measure the drop size distribution (DSD) at the inlet and both outlets (vortex finder and annulus). The GE curve is determined by comparing inlet and outlet measurements. Isokinetic sampling is required in which sample is removed at the same velocity as that of the local bulk flow in the pipe so that the sample is a true representation of the drop population in the pipe.

7.1.1 Analysis of Experimental Results

The separation efficiency testing was carried out using Geometry 7a since it is the best geometry tested having the highest flow split and working well without entrainment/re-entrainment over a wide range of air flowrates. The separation efficiency was tested as a function of the air flowrate. The grade efficiency curves were obtained at air flowrates of 600, 1000 and 1400 l/min. Higher flowrates were

not tested because the velocity inside the vortex finder would have exceeded the maximum velocity limit of the Polytec HC-15, which is 20 m/s. The sampling probe was approximately two diameters upstream of inlet vanes as recommended by **Hoffmann and Stein (2002)**. The velocity profile across the cross-sectional area of the inlet (i.e. the housing tube) was measured using a hot wire probe (VELOCICALC® Model 8345/8346 manufactured by TSI Incorporated) to find the local velocity for isokinetic sampling. The profiles are illustrated in Figure 7.1. The profiles for all the three flowrates were moderately constant at 1.47, 2.45 and 3.5 m/s for the flowrate of 600, 1000 and 1400 l/min respectively. The mean velocity for turbulent flow can also be predicted using Equation 7.1 for highly turbulent flow **(Coulson *et al.*, 1999)**. The mean velocity, U, is calculated from Q_{in}/A to be 1.23, 2.06 and 2.86 m/s at 600, 1000 and 1400 l/min respectively. From Equation 7.1, the maximum velocity is calculated to be 1.50, 2.52 and 3.5 m/s at the flowrate of 600, 1000 and 1400 l/min respectively. These figures are very similar to the values obtained using the hot wire probe. This confirms that the measurements taken were reliable.

$$U = 0.817U_{max} \qquad \textbf{- Equation (7.1)}$$

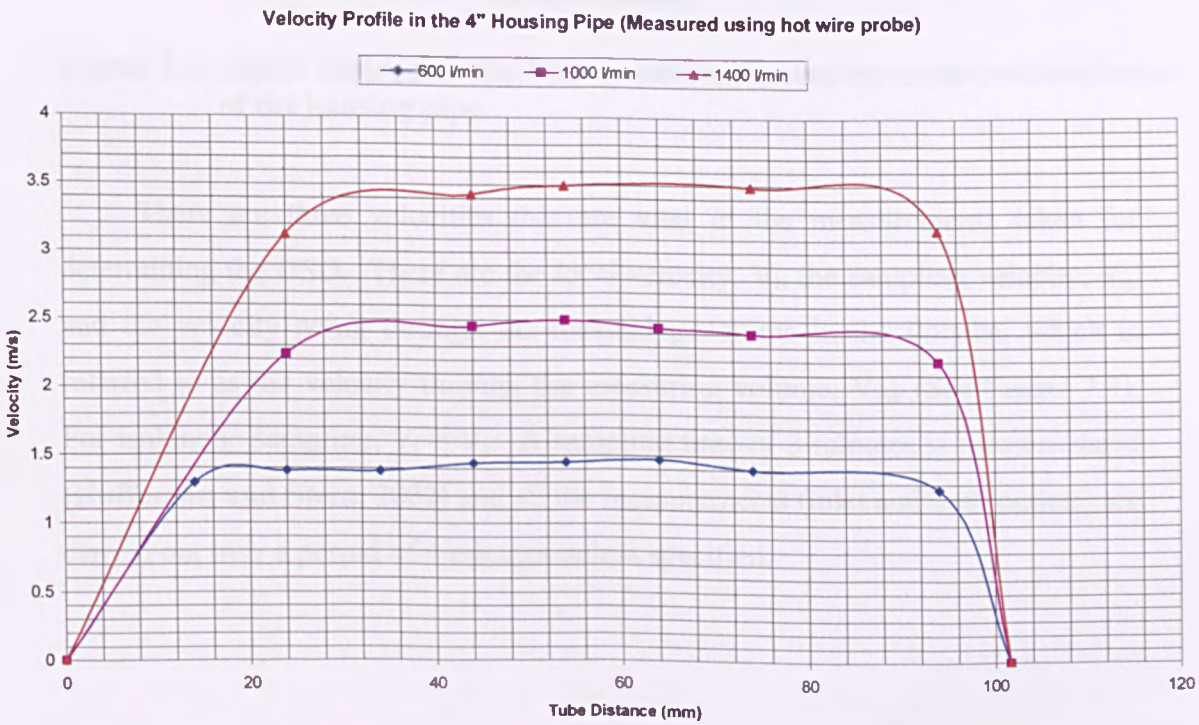

Figure 7.1: Velocity profiles at 600, 1000 and 1400 l/min over the cross-sectional area of the housing pipe.

Since the velocity variation across the width of the inlet tube is not significant, it is safe to say that the sampling is representative of the entire cross-sectional area of the pipe (i.e. the DSD at any point of the cross-sectional positions are similar) and this is proved in Figure 7.2 when sampling was carried out over the cross-sectional area of the inlet tube.

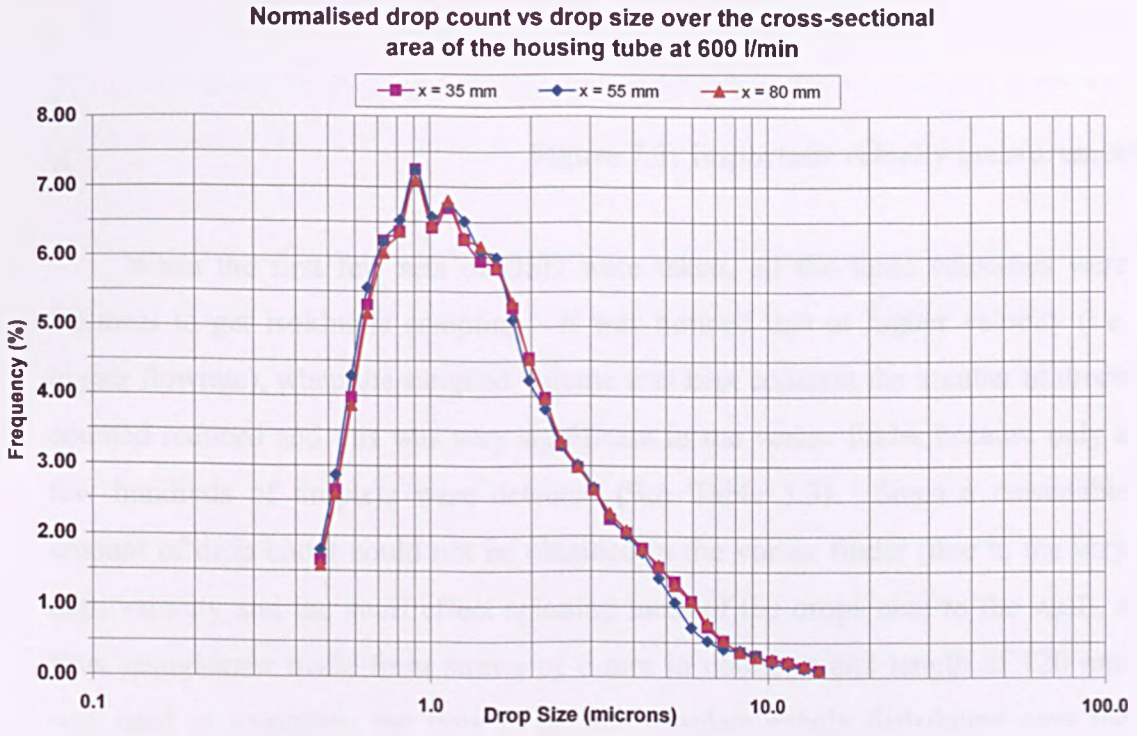

Figure 7.2: Figure shows that the DSD is uniform across the cross-sectional area of the housing pipe.

There are three velocities that are vital in the measurements taken for determining the DSD. There are the local velocity, V_l, the sampling velocity, V_s, and the velocity going through the measuring volume in the Polytec, which is referred to as the velocity through the measuring volume, V_{mv} (See Figure 7.3). For isokinetic sampling, $V_l = V_s$. A sampling time of 3 minutes is recommended **(Hoffmann and Stein, 2002)** and all the measurements (inlet and both outlets) are carried out over a period of 4 minutes unless specified.

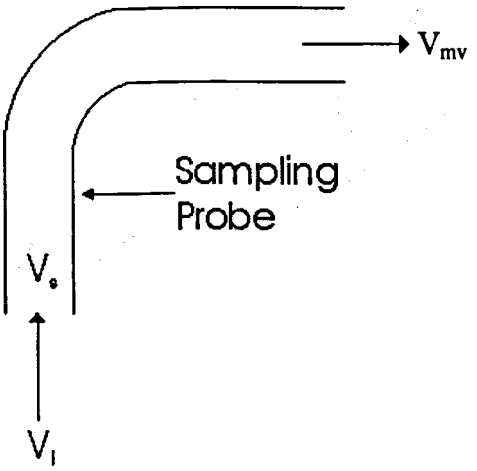

Figure 7.3: Important velocity measurements.

When the first few sets of DSD were taken, all the three velocities were identical to get isokinetic sampling. It was noticed that at higher velocity (i.e. higher flowrate), when the sampled volume was kept constant the number of drops counted reduced and this was very significant in the vortex finder because only a few hundreds of droplets were detected (See Table 5.3). Since a reasonable amount of drop count could not be obtained in the vortex finder (due to the very high velocity and the swirl effect spinning most of the drops near to the wall), a flow straightener made from straws of 6 mm in diameter and length of 120 mm was used to straighten the flow to get the droplets evenly distributed over the cross-sectional area of the vortex finder. The reduction in the inlet drop count as the flowrate increases was due to the concentration effect. As flowrate increases, the amount of drops per unit volume decreases. Even so, the number of droplets detected was large enough to give a good representation of the inlet population (> 20,000 for all three tested flowrates).

Air Inlet Flowrate (l/min)	Total Drop Count at Inlet	Total Drop Count in Vortex Finder
600	174664	643
1000	71173	-
1400	29320	-

Table 7.1: Examples showing the significant decrease of drop count at higher velocity when the sampled volume is kept constant at inlet and the vortex finder for isokinetic sampling.

However, it was not very practical to impose isokinetic sampling in the vortex finder because the required flowrate to go through the probe would exceed the rotameter range available (4 – 40 l/min) and if a larger rotameter were to be installed, this would impose a safety issue because it would create difficulty in lifting and lowering the platform with the heavy Polytec HC-15 on it and more importantly the count detected was too low (only few hundred counts) at high velocities to believe that the sample represented the population fairly. This was verified when the measurements under isokinetic sampling conditions were repeated 3 times for each inlet air flowrate (i.e. at 600, 1000 and 1400 l/min) and the drops were counted in the vortex finder. Total counts were only few hundreds for all 3 times. At this point, it was suspected that the sampling count was dependent on the velocity through the measuring volume, V_{mv}. It was then decided to go for non-isokinetic sampling (i.e. $V_i \neq V_s$) by varying the sampling velocity (6, 3, 1.5 and 1.0 m/s) but keeping the sampled volume constant for both inlet and outlet measurements (i.e. sampling time of 60, 120, 240 and 360 seconds respectively) for air flowrate of 600 and 1000 l/min. Since there was an area reduction from the sampling probe to the Polytec channel (from inner diameter of 9.8 mm to 7 mm), when the sampling velocity is 6, 3, 1.5 and 1.0 m/s, the velocity through the measuring volume is 11.76, 5.88, 2.94 and 1.96 m/s respectively. The normalised DSD's at all these various sampling velocity at the specified flowrates at the inlet and both outlets are shown in Figures 7.4a, b, 7.5a, b and 7.6a, b. These curves were the arithmetic average of 3 measurements for each measured velocity (i.e. 12 measurements in total for each flowrate at each sampling point). The normalised DSD data of the non-isokinetic sampling are compared with the isokinetic data where possible.

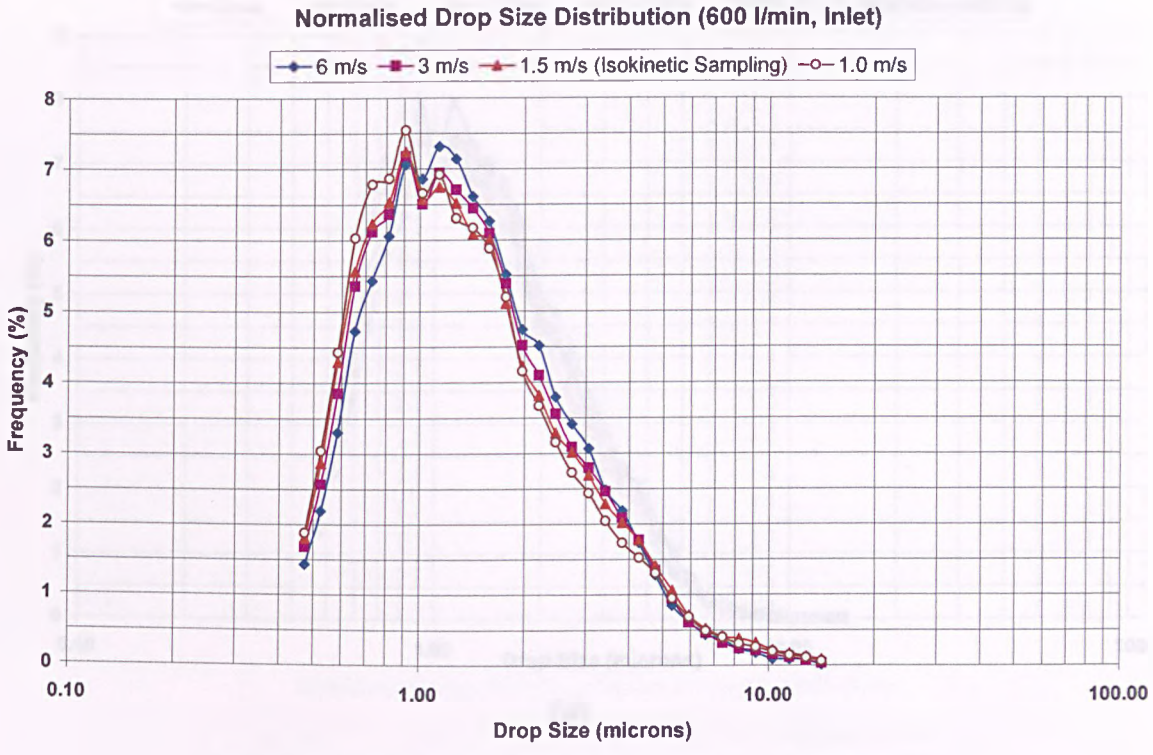

(a)

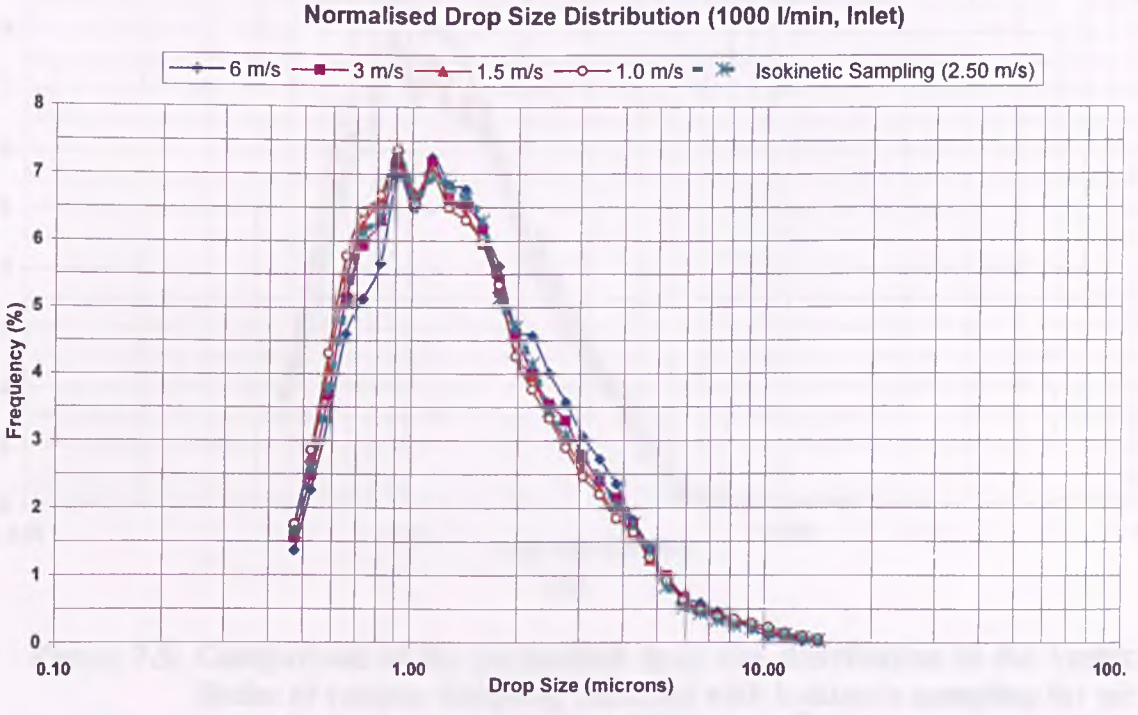

(b)

Figure 7.4: Comparison of the normalised inlet drop size distribution at various sampling velocities with isokinetic sampling for air flowrate of (a) 600 l/min and (b) 1000 l/min.

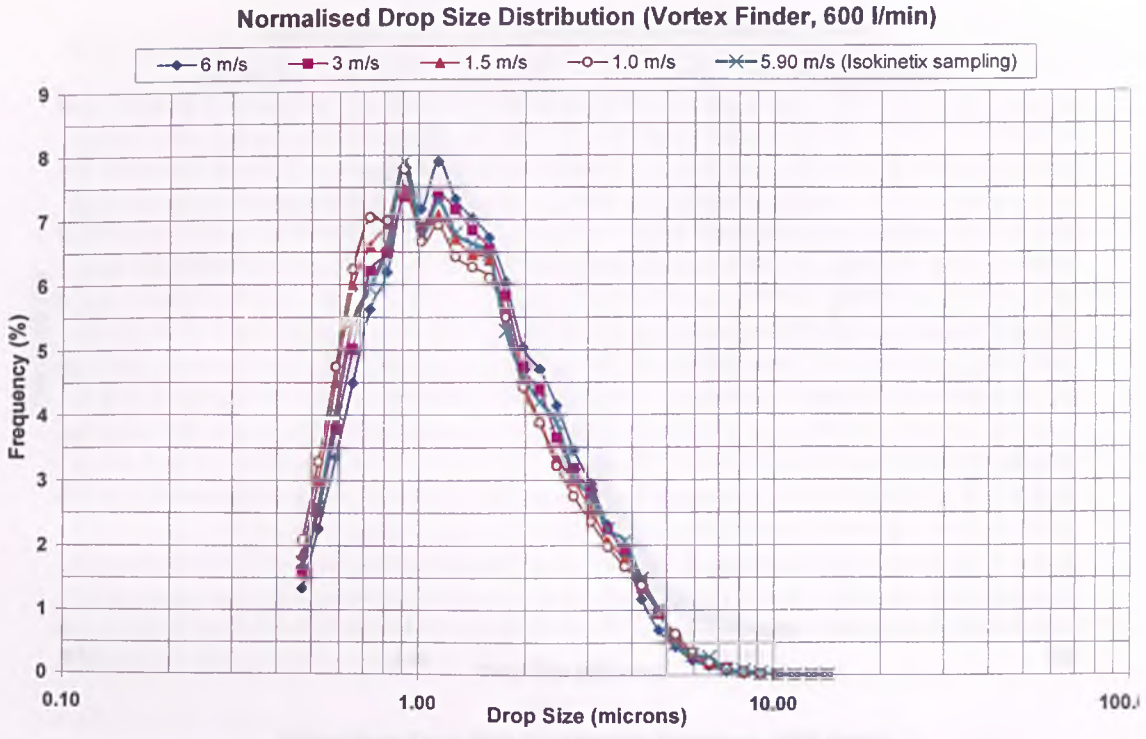

(a)

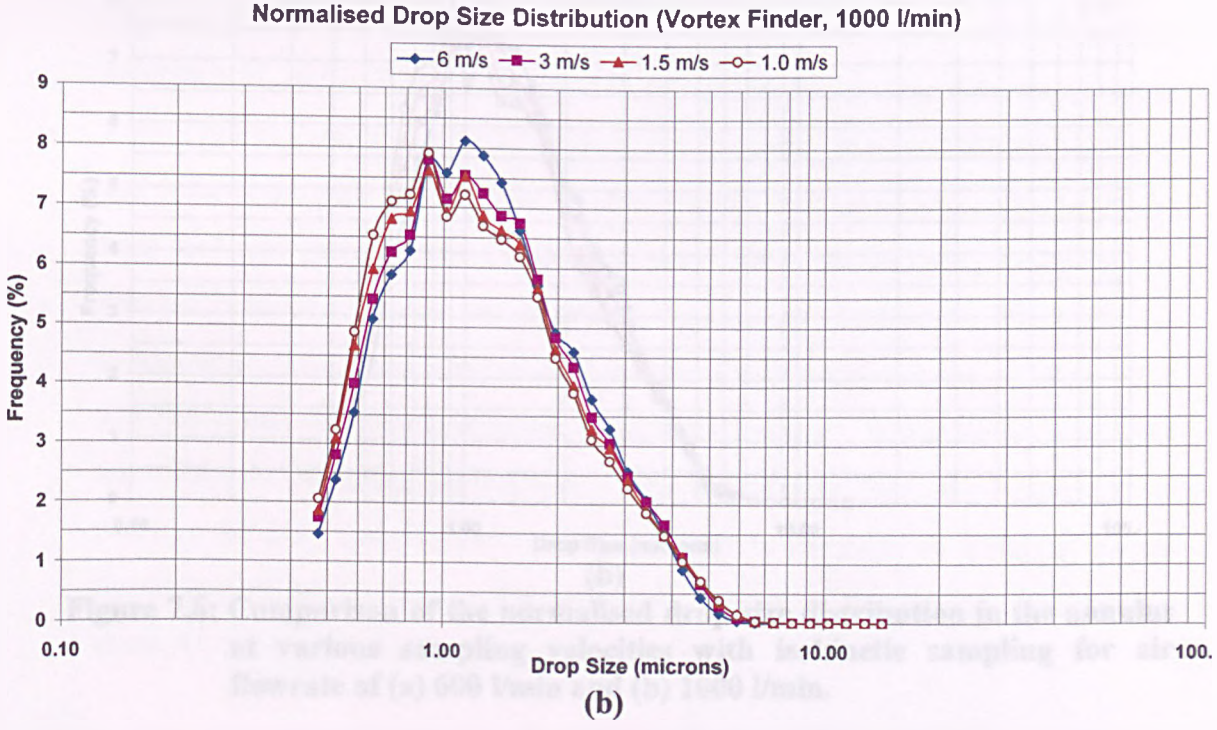

(b)

Figure 7.5: Comparison of the normalised drop size distribution in the vortex finder at various sampling velocities with isokinetic sampling for air flowrate of (a) 600 l/min and (b) 1000 l/min[3].

[3] Isokinetic data were not obtained for air flowrate of 1000 l/min because of the high velocity inside the vortex finder (10 m/s). At this velocity, the Polytec detected less than 500 counts, which is not enough to give a good representation of the drop population inside the vortex finder.

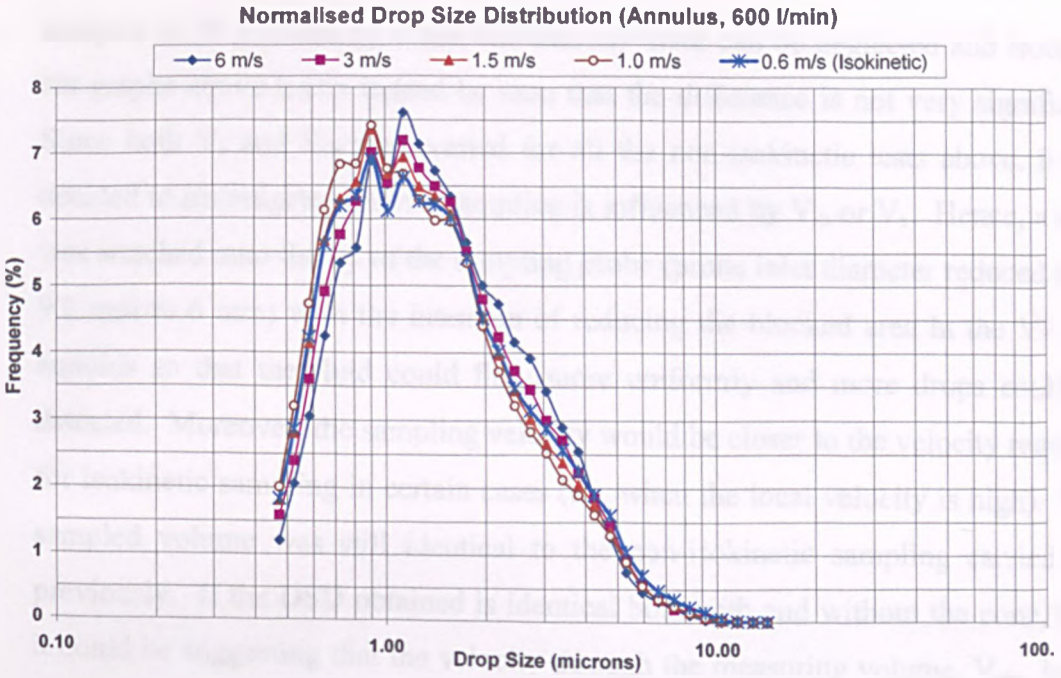

(a)

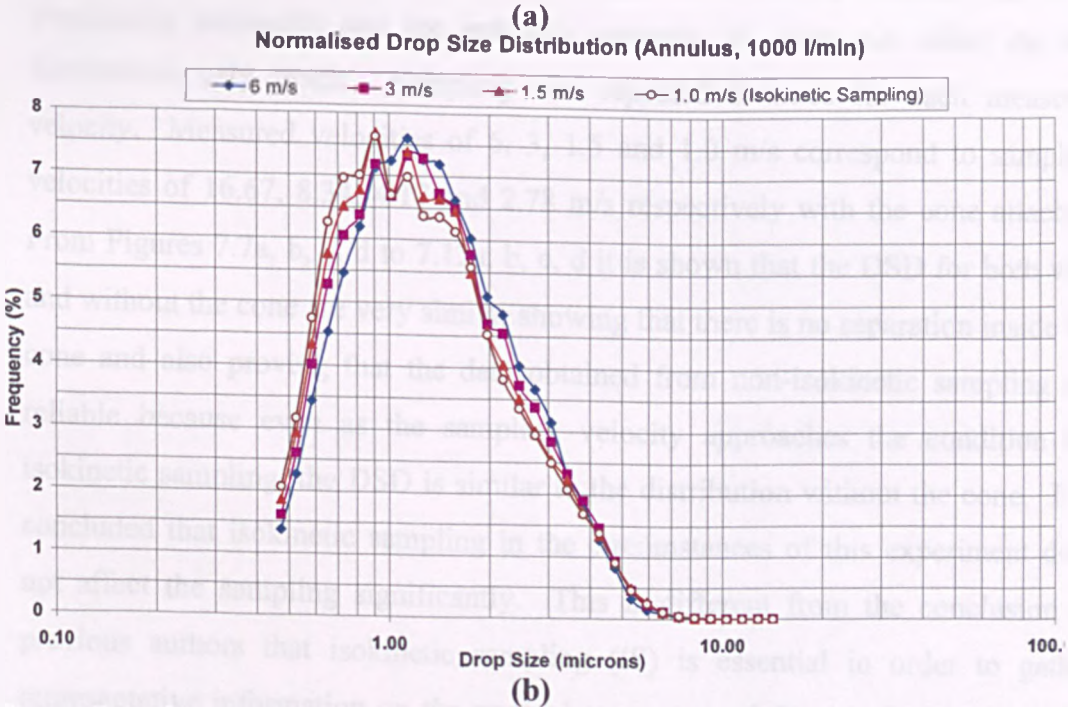

(b)

Figure 7.6: Comparison of the normalised drop size distribution in the annulus at various sampling velocities with isokinetic sampling for air flowrate of (a) 600 l/min and (b) 1000 l/min.

As shown in all the six figures above, the DSD were very similar for all sampling velocities except at 6 m/s, which varied slightly from the rest. This might be due to the limitation of the particle analyser. It was recommended to work at the calibration velocity, which is 5 m/s. Hence, this might induce a slight error as the velocity increases. However, it was stated that the upper limit of the

analyser is 20 m/s and so it was felt that any error can be neglected and from the six graphs above it can indeed be seen that the difference is not very significant. Since both V_s and V_m were varied for all the non-isokinetic tests above, it was decided to investigate whether sampling is influenced by V_m or V_s. Hence, a cone was attached onto the tip of the sampling probe (probe inlet diameter reduced from 9.8 mm to 6 mm) with the intention of reducing the blocked area in the VF and annulus so that the fluid could flow more uniformly and more drops could be detected. Moreover, the sampling velocity would be closer to the velocity required for isokinetic sampling in certain cases (i.e. when the local velocity is high). The sampled volume was still identical to the non-isokinetic sampling carried out previously. If the DSD obtained is identical both with and without the cone, then it could be suggesting that the velocity through the measuring volume, V_{mv}, is the dominating parameter and the sampling velocity, V_s, does not affect the size distribution very much. Sampling was repeated 3 times for each measured velocity. Measured velocities of 6, 3, 1.5 and 1.0 m/s correspond to sampling velocities of 16.67, 8.34, 4.17 and 2.78 m/s respectively with the cone attached. From Figures 7.7a, b, c, d to 7.12a, b, c, d it is shown that the DSD for both with and without the cone are very similar showing that there is no separation inside the cone and also proving that the data obtained from non-isokinetic sampling are reliable because even as the sampling velocity approaches the condition for isokinetic sampling, the DSD is similar to the distribution without the cone. It is concluded that isokinetic sampling in the circumstances of this experiment does not affect the sampling significantly. This is different from the conclusion of previous authors that isokinetic sampling (IS) is essential in order to gather representative information on the particulate content of flowing dusty gases **(for example, Kim *et al.*, 2001)**.

Rhodes and Laussmann (1992) claimed that IS is readily applied to steady flow of very dilute, homogeneous suspensions of fine particles in ducts where significant gas velocity gradients are absent. However, they noted that when the gas-particle suspension is at high concentrations, true isokinetic sampling is not possible. They discovered that in regions where dense suspensions are to be

sampled, higher sampling velocities may be required and the solids flux was virtually independent of the sampling velocity provided that the velocity in the sampling lines was sufficient to prevent blockage. The mean solids flux they used in their work was 30 kg/m^{2}s with particle density of 2456 kg/m^3. This is very similar to the results observed in this study with liquid flux of 40 kg/m^{2}s with liquid density of about 1034 kg/m^3. Therefore, the droplet suspension in our case was too dense for isokinetic sampling. It was observed that with the cone attached, the number of drops detected in the VF and in the disengagement space (DS) increased. Therefore, for the results shown in the rest of this chapter the measurements were taken with the cone attached.

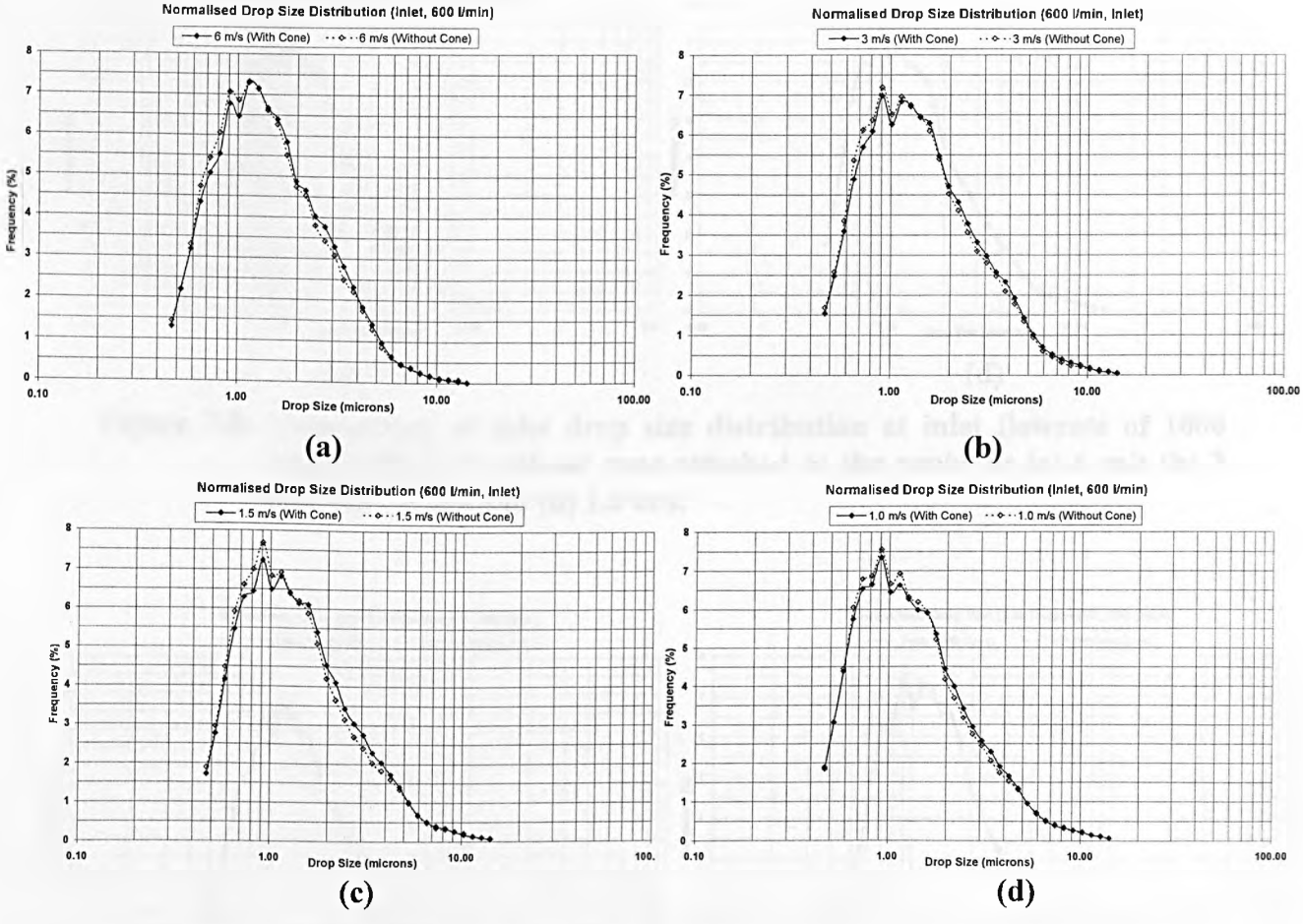

Figure 7.7: Comparison of inlet drop size distribution at inlet flowrate of 600 l/min with and without cone attached to the probe at (a) 6 m/s (b) 3 m/s, (c) 1.5 m/s and (d) 1.0 m/s. The velocity through the measuring volume, V_{mv}, is the same, but the sampled velocity, V_s, is 2.78 times higher than V_{mv}.

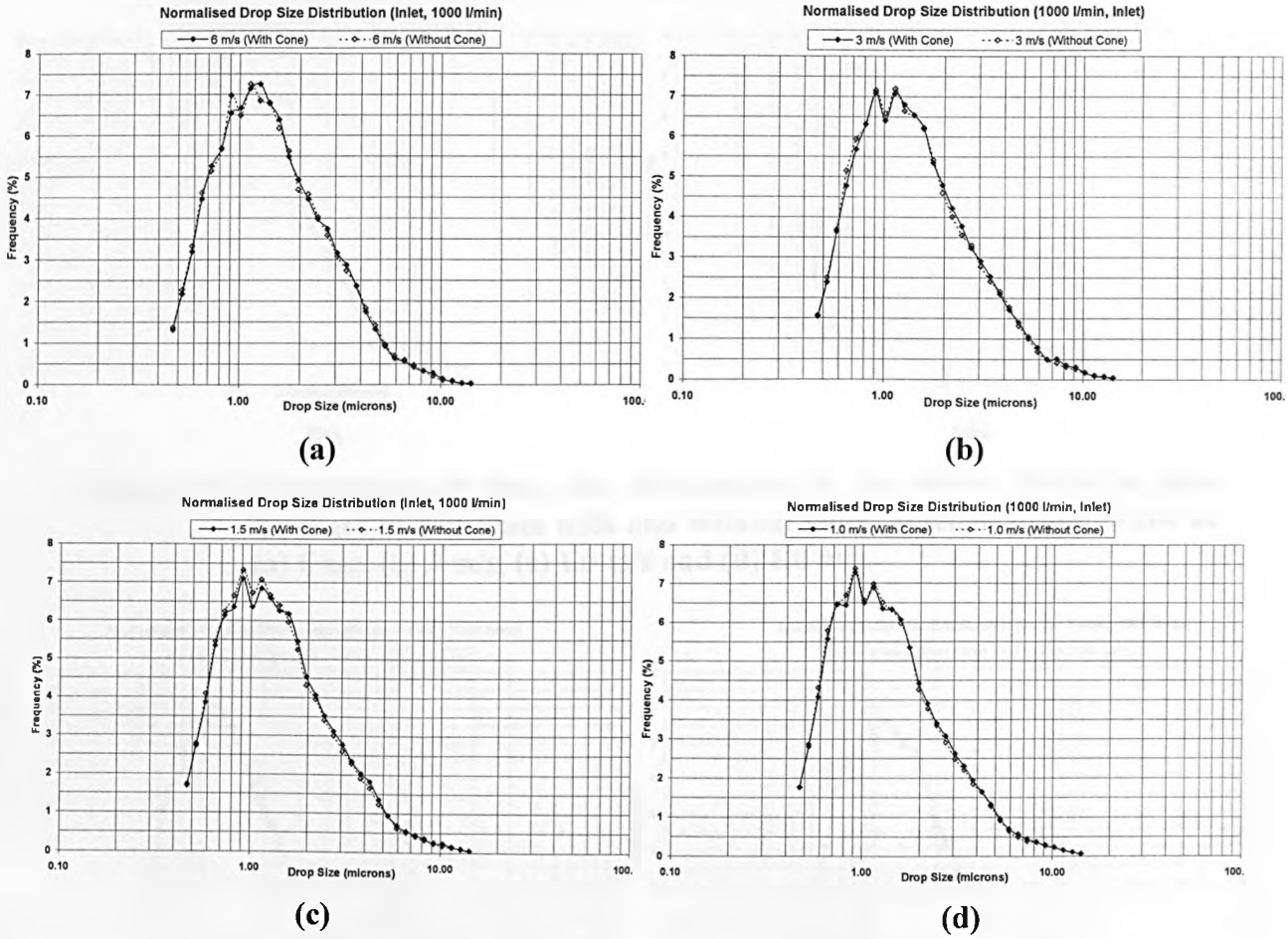

Figure 7.8: Comparison of inlet drop size distribution at inlet flowrate of 1000 l/min with and without cone attached to the probe at (a) 6 m/s (b) 3 m/s, (c) 1.5 m/s and (d) 1.0 m/s.

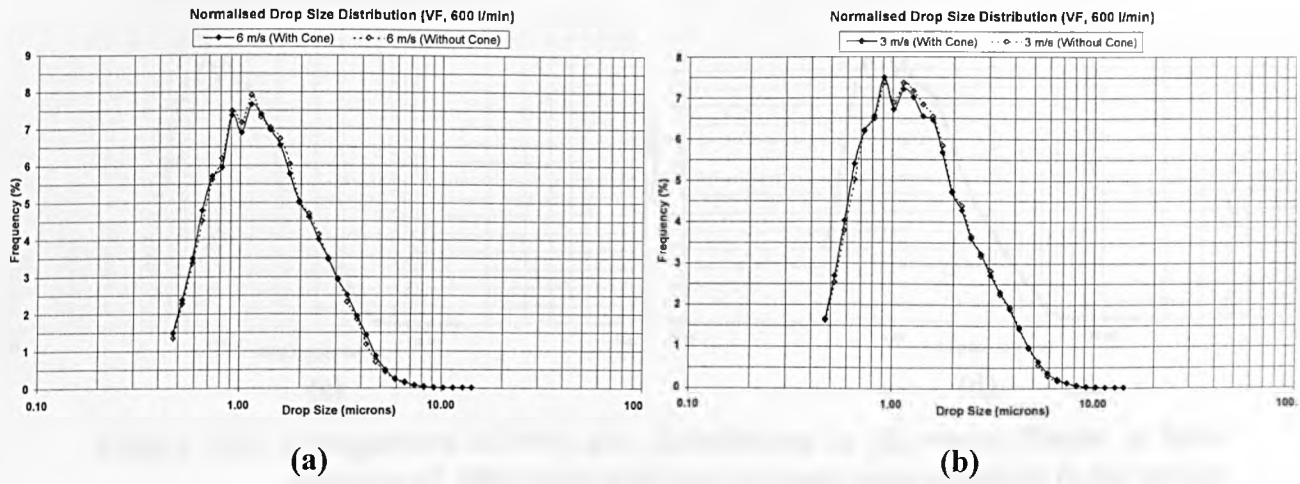

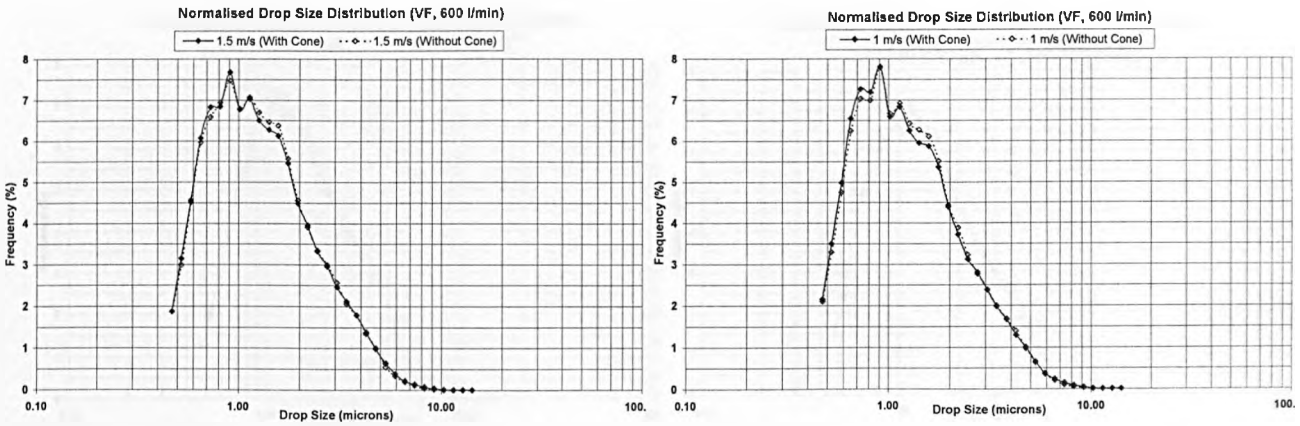

(c) (d)

Figure 7.9: Comparison of drop size distribution in the vortex finder at inlet flowrate of 600 l/min with and without cone attached to the probe at (a) 6 m/s (b) 3 m/s, (c) 1.5 m/s and (d) 1.0 m/s.

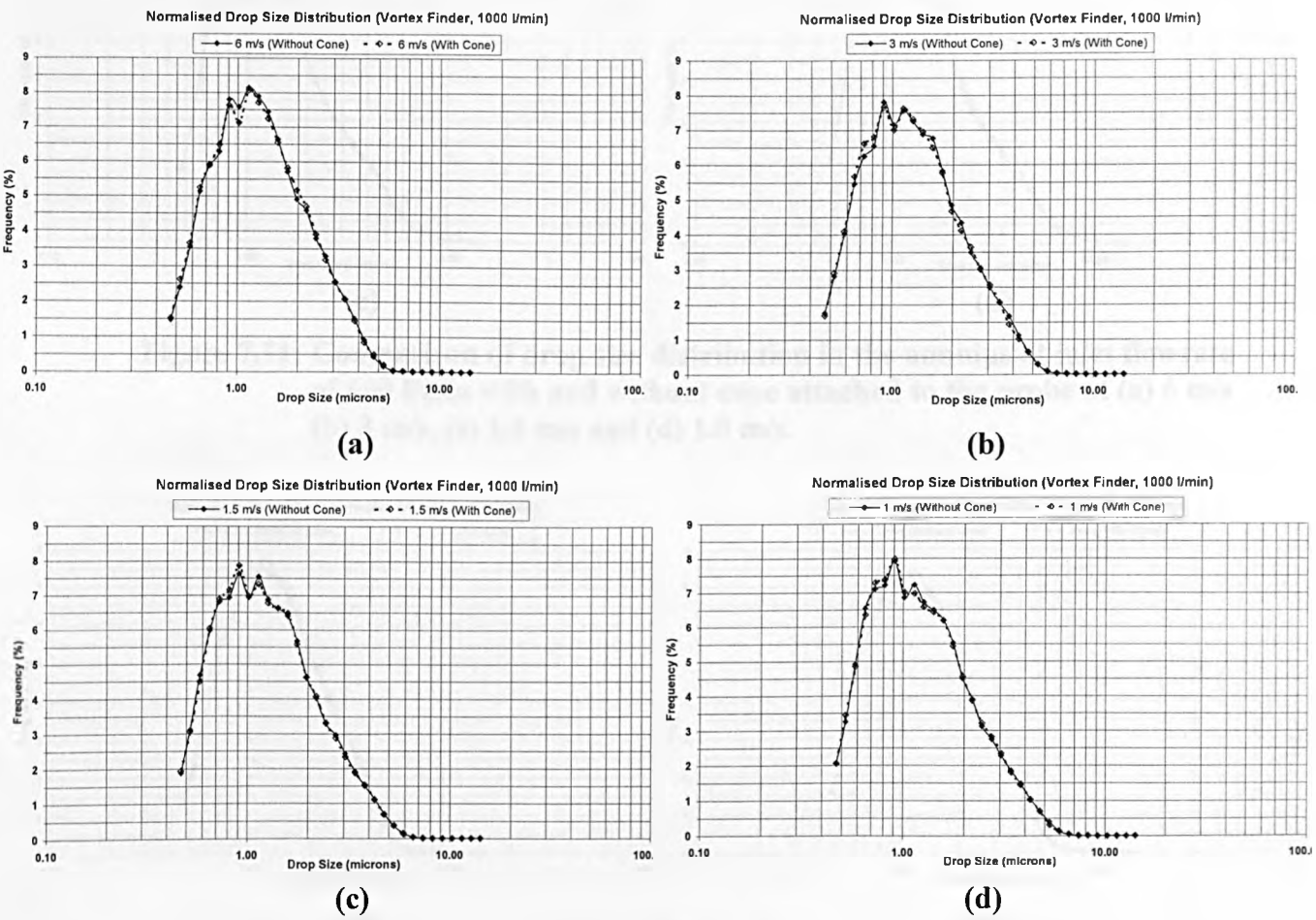

(a) (b)

(c) (d)

Figure 7.10: Comparison of drop size distribution in the vortex finder at inlet flowrate of 1000 l/min with and without cone attached to the probe at (a) 6 m/s (b) 3 m/s, (c) 1.5 m/s and (d) 1.0 m/s.

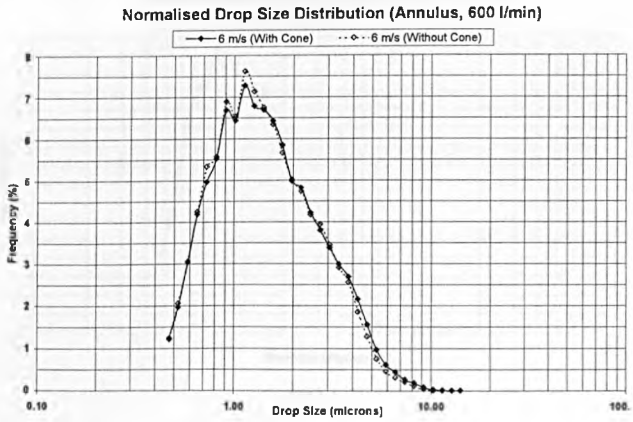

(a)

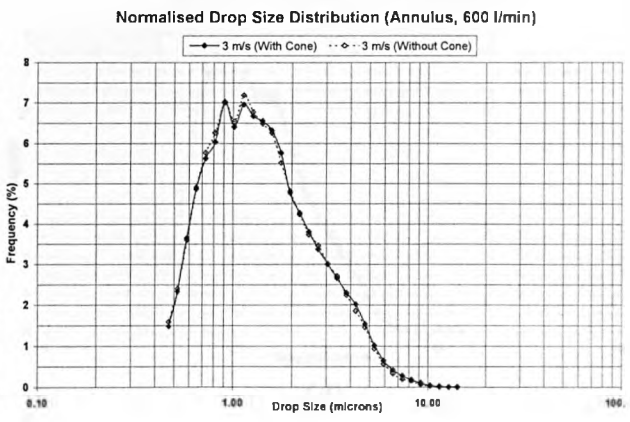

(b)

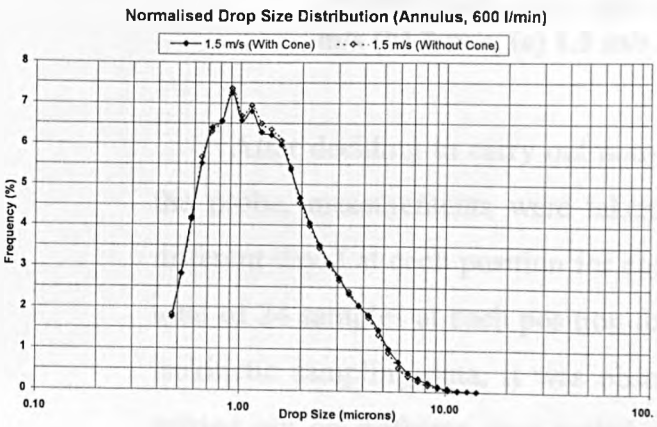

(c)

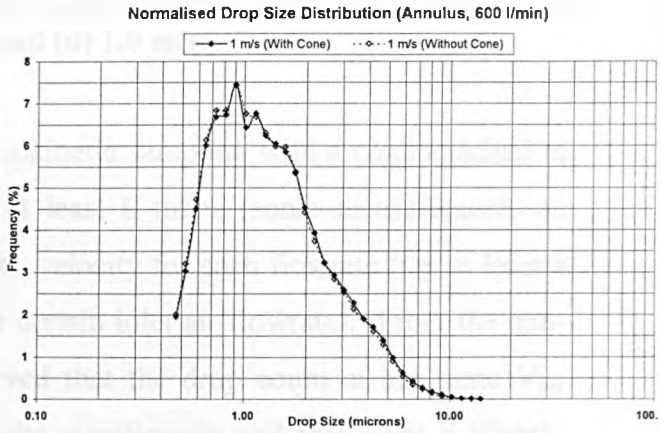

(d)

Figure 7.11: Comparison of drop size distribution in the annulus at inlet flowrate of 600 l/min with and without cone attached to the probe at (a) 6 m/s (b) 3 m/s, (c) 1.5 m/s and (d) 1.0 m/s.

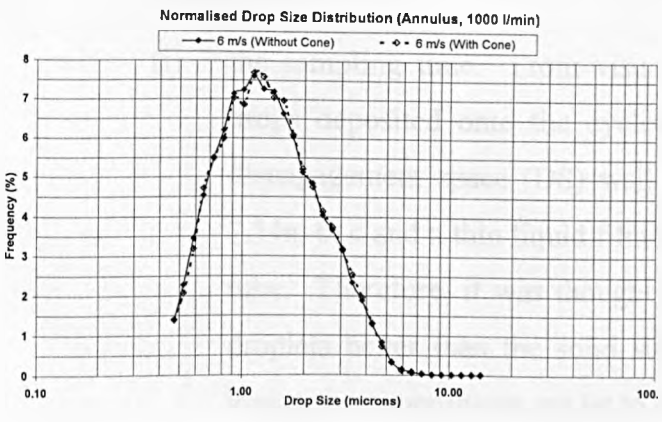

(a)

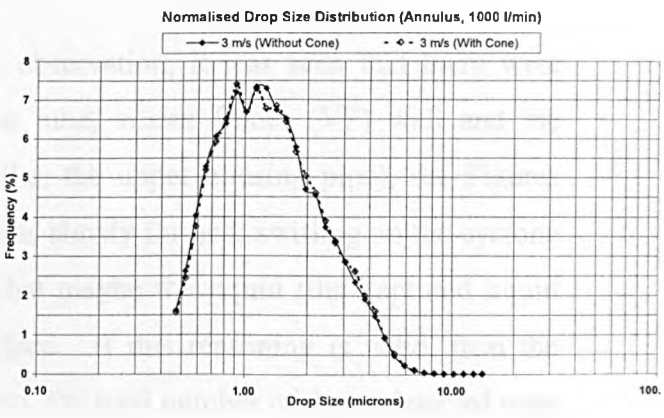

(b)

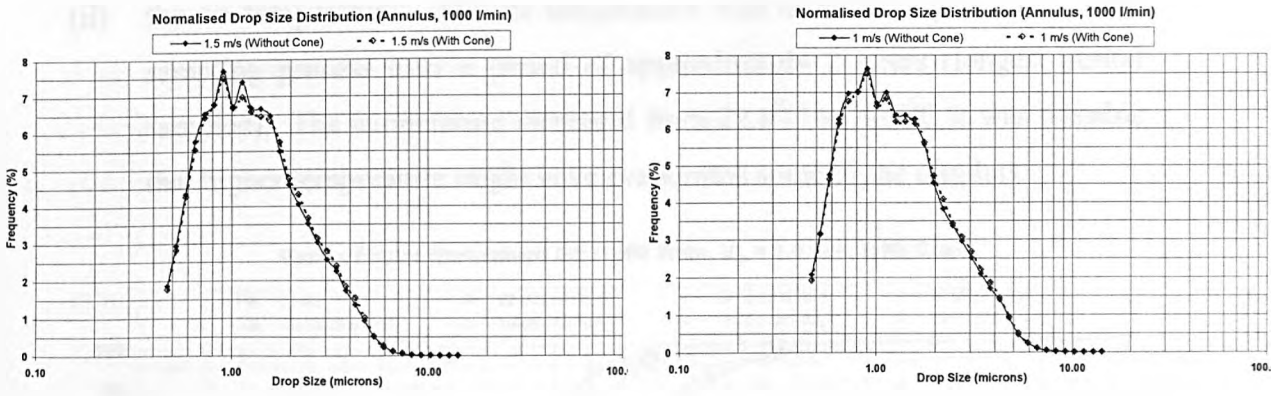

(c) **(d)**

Figure 7.12: Comparison of drop size distribution in the annulus at inlet flowrate of 1000 l/min with and without cone attached to the probe at (a) 6 m/s (b) 3 m/s, (c) 1.5 m/s and (d) 1.0 m/s.

After deciding to carry out non-isokinetic sampling with a cone attached to the probe, measurements were taken at least 6 times (some measurements on different days) at each position for each velocity for each flowrate (i.e. at least a total of 24 samples at each position for certain inlet air flowrate). From the non-isokinetic sampling data, it was observed that the drop count at the same V_{mv} carried out on different days varied quite significantly and this gives a slightly different grade efficiency curve for the same condition (e.g. See Figure 7.13).

Therefore, a significant amount of time was spent in analysing the data in terms of:

(i) the sampling time. From visual observation, it was seen that there were drops deposited onto the cyclone tube, vortex finder (VF) wall and the disengagement space (DS) wall (i.e. the upper housing pipe), see Figures 7.14a, b, c and a thin liquid film was slowly formed, swirling up the cyclone tube. Therefore, it was thought that maybe the liquid film captured liquid droplets better than the solid surface. If this reasoning is valid, then the longer the experiments are let to run, the total number of drops detected over the sampling time (4 minutes) will decrease.

(ii) the air temperature. The air temperature was taken throughout the entire sampling process over a period of approximately 2 hours (longest period

(ii) the air temperature. The air temperature was taken throughout the entire sampling process over a period of approximately 2 hours (longest period sampled). The temperature increased from 22.8^{0}C to 24.4^{0}C It was possible that higher temperature might have evaporated some of the droplets.

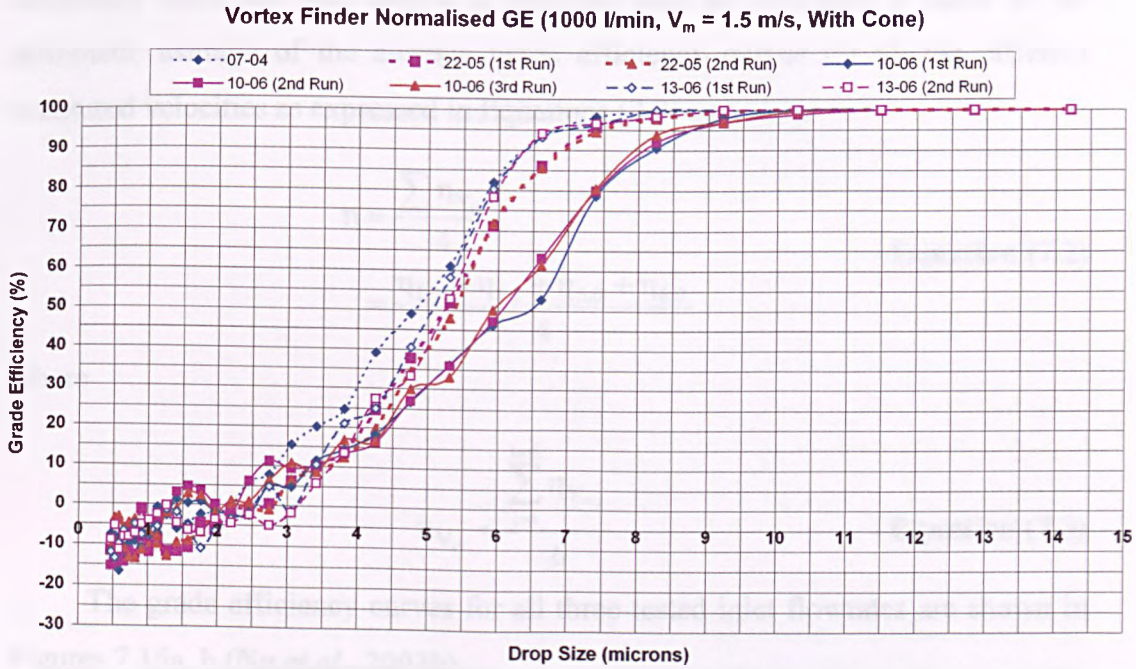

Figure 7.13: This shows the discrepancy in the measurements taken under the same condition, but on different days.

(a) **(b)** **(c)**

Figure 7.14: Droplets deposited onto the (a) cyclone tube, (b) vortex finder wall and (c) disengagement space wall.

A detailed analysis suggests that that both (i) and (ii) are not valid. In some cases, as the sampled time and temperature increases, the number of drops counted decreases. However, in some cases, it was the other way round. Therefore, it is concluded that there is inherent variability in the measurements taken. The grade efficiency curve for both outlets at different inlet air flowrates is taken as the arithmetic average of the average grade efficiency curves for all the different measured velocities as expressed in Equations (7.2) and (7.3).

$$\eta = \frac{\sum \eta_{V_m}}{4} = \frac{\eta_{1.0} + \eta_{1.5} + \eta_{3.0} + \eta_{6.0}}{4} \qquad \textbf{- Equation (7.2)}$$

where

$$\eta_{V_m} = \frac{\sum_{i=1}^{i=6} \eta_{V_{m,i}}}{6} \qquad \textbf{- Equation (7.3)}$$

The grade efficiency curves for all three tested inlet flowrates are shown in Figures 7.15a, b **(Ng *et al.*, 2003b)**.

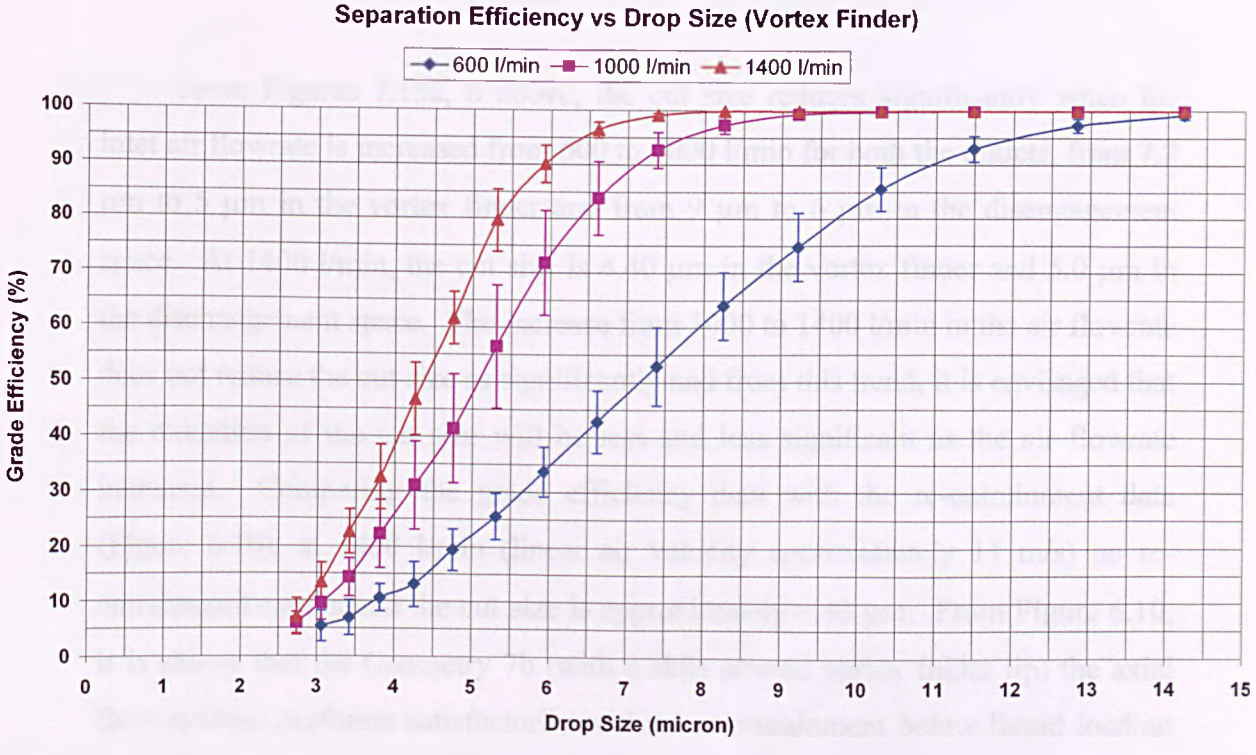

(a)

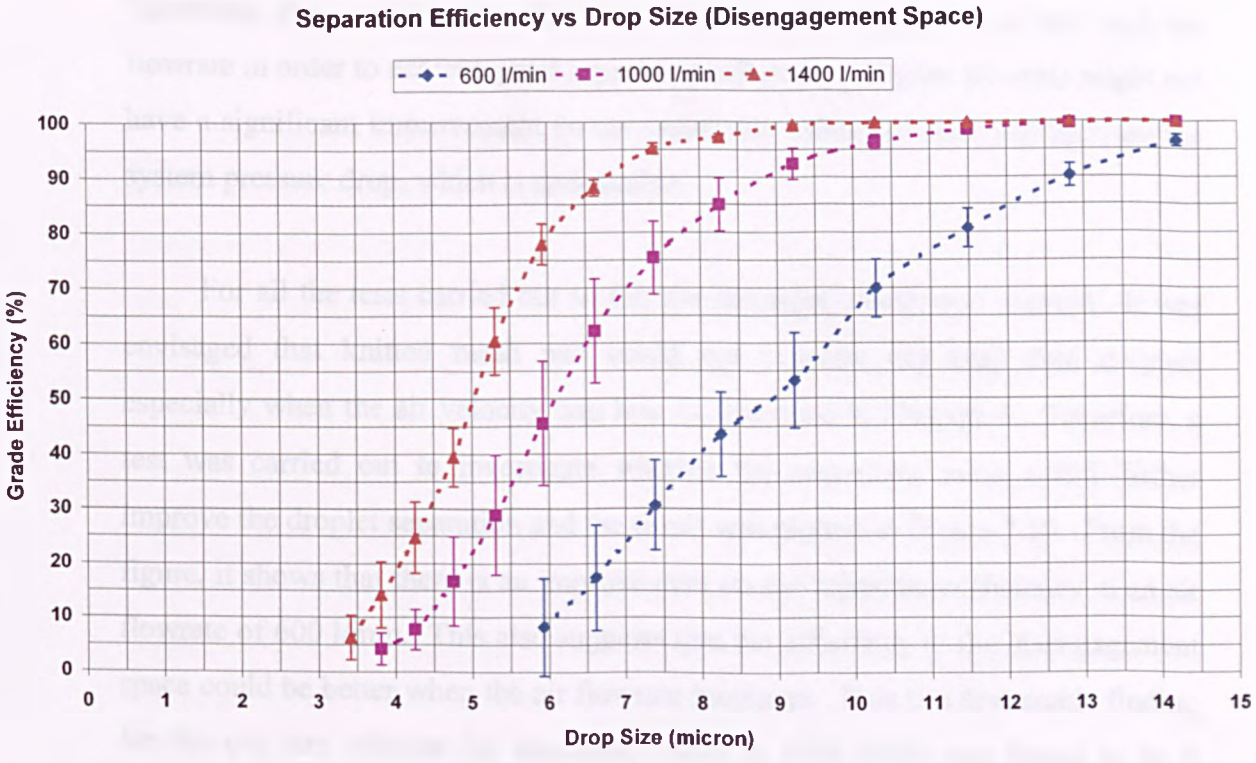

(b)

Figure 7.15: Grade efficiency curves of the (a) vortex finder and (b) disengagement space at an air flowrate of 600, 1000 and 1400 l/min (the tails of the curves at small sizes have been removed from these plots).

From Figures 7.15a, b above, the cut size reduces significantly when the inlet air flowrate is increased from 600 to 1000 l/min for both the outlets, from 7.2 μm to 5 μm in the vortex finder and from 9 μm to 6 μm in the disengagement space. At 1400 l/min, the cut size is 4.40 μm in the vortex finder and 5.0 μm in the disengagement space. The increase from 1000 to 1400 l/min in the air flowrate does not reduce the cut size as significantly and from this trend, it is envisaged that the reduction of the cut size will be less and less significant as the air flowrate increases. Comparing the grade efficiency data with the re-entrainment data (Figure 6.10), at 1400 l/min (linear air velocity approximately 11 m/s) no re-entrainment occurs and the cut size is approximately 4.40 μm. From Figure 6.10, it is shown that for Geometry 7b (with a skirt around vortex finder lip) the axial flow cyclone performs satisfactorily without re-entrainment below liquid loading of 0.100 %v/v up to linear air velocity of 15 m/s (approximately 1900 l/min).

Therefore, this is suggesting that there is no need to operate at a very high air flowrate in order to achieve good separation efficiency. Higher flowrate might not have a significant improvement on the separation efficiency, but will increase the system pressure drop, which is undesirable.

For all the tests carried out so far, the secondary mesh was omitted. It was envisaged that knitted mesh pad could not separate out very fine droplets especially when the air velocity was low as described in Chapter 4. Therefore, a test was carried out to investigate whether the secondary mesh could further improve the droplet separation and the result was plotted in Figure 7.16. From the figure, it shows that there is an improvement on the separation efficiency at an air flowrate of 600 l/min. This also suggests that the efficiency in the disengagement space could be better when the air flowrate increases. This is a favourable finding for the cut size without the secondary mesh at 1400 l/min was found to be 5 microns, hence with the mesh in the cut size will be less than 5 microns.

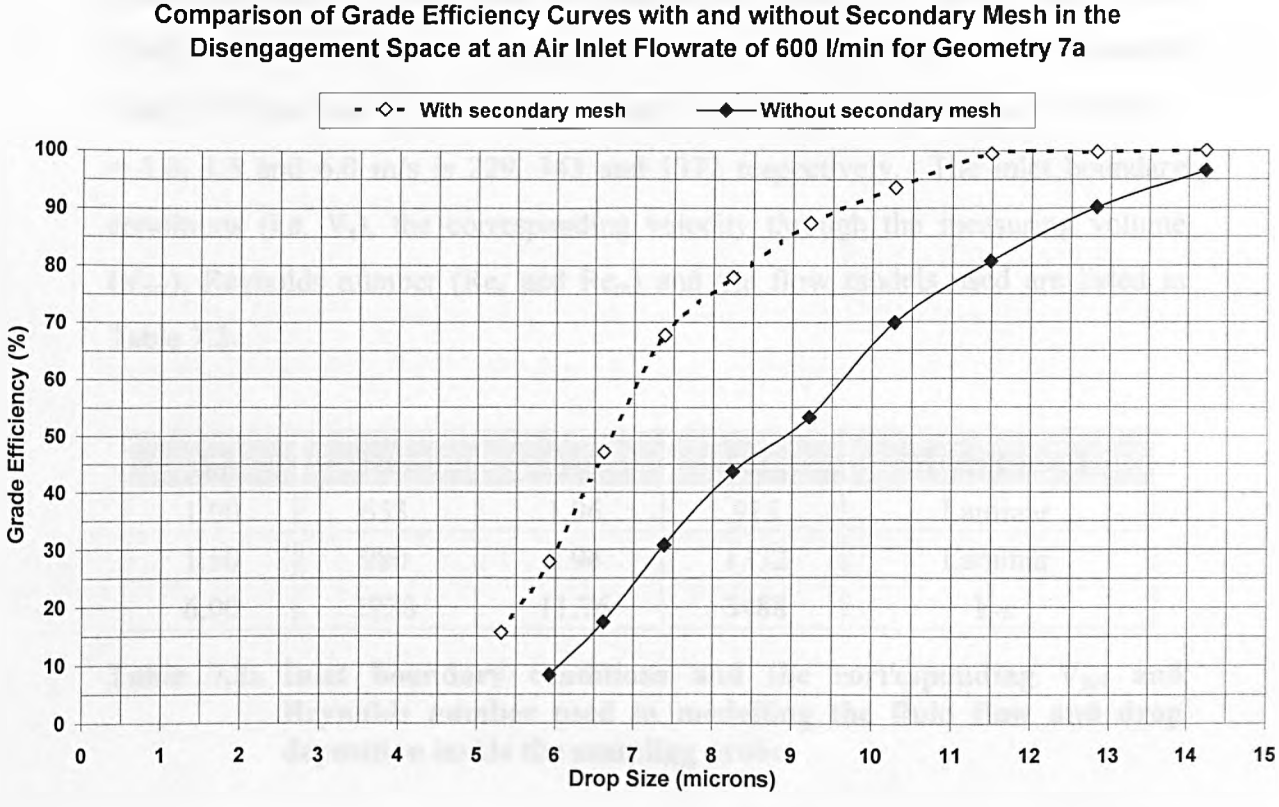

Figure 7.16: Comparison of the grade efficiency curves with and without the secondary mesh in the disengagement space.

7.1.2 Analysis of Computational Results

Investigations were also carried out to determine the reason for getting less drop count at higher velocity through the measuring volume. The most obvious reason was due to droplets deposition in the probe (especially near the bend). It was also thought that the droplets might be skewed to the top of the Polytec channel and did not pass the measuring volume, hence undetected. For these matters, the probe and the passage in the Polytec HC-15 (including the measuring volume) were modelled using Computational Fluid Dynamics (CFD) packages; GAMBIT and FLUENT5. There has been a lot of work carried out to investigate fluid motion in curved pipes and particle deposition around bends **(Cheng and Wang, 1975; 1981; Fan *et al.*, 1992; McFarland *et al.*, 1997; Nandakumar and Masliyah, 1982; Pui *et al.*, 1987; Shahnam and Jurewicz, 1986; Yanase *et al.*, 1988; 1989)**. The fluid flow and the particle deposition inside the probe (internal diameter = 9.8 mm and radius of curvature = 40 mm) and the Polytec channel (inner diameter = 7 mm) were investigated at V_s of 1, 1.5 and 3 m/s. From Chapter 2, Section 2.7.2 on sample line losses, it is stated that for Dean number (De) ≤ 370 the flow is considered laminar. From Equation (2.49) the De when V_s = 1.0, 1.5 and 6.0 m/s is 229, 343 and 1372 respectively. The inlet boundary conditions (i.e. V_s), the corresponding velocity through the measuring volume (V_{mv}), Reynolds number (Re_s and Re_m) and the flow models used are listed in Table 7.2.

V_s	Re_s	V_m	Re_m	Model used
1.00	653	1.96	915	Laminar
1.50	980	2.94	1372	Laminar
6.00	3920	11.76	5488	k-ε

Table 7.2: Inlet boundary conditions and the corresponding V_{mv} and Reynolds number used in modelling the fluid flow and drop deposition inside the sampling probe.

The geometry of the probe and the Polytec channel with the various viewing plans (positions where the results will be analysed) is shown in Figure 7.17.

Unstructured hexahedral meshes were used with 2444 cells across the probe inlet with total cells of 2104253. The length of the probe is 107 mm (from inlet middle point to the beginning of Polytec channel). The length of the Polytec channel to the measuring volume is 82 mm. The measuring volume is an interception of the illumination and the observation path with light shined through ellipse (from observation when the Polytec was taken apart). For simplicity, a cuboid is used such that the surface area of the ellipse is the same as one of the surface area of the cuboid. The cuboid length is 3.424 mm and the height and the width is 4.05 mm. It is located in the middle of the Polytec channel cross sectional area.

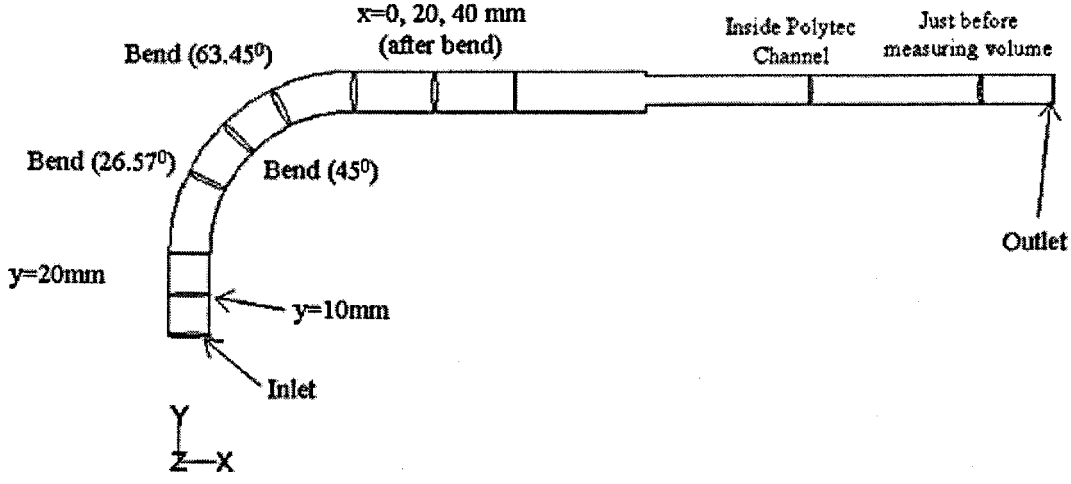

Figure 7.17: Geometry of the probe and Polytec channel modelled with viewing plans labelled.

The fluid flow for V_s of 1.0 and 1.5 m/s are similar, hence for discussion purposes on the fluid flow, only the results at 1.0 and 6.0 m/s are presented to see the effect of laminar and turbulent flow. The axial velocities of V_s = 1.0 and 6.0 m/s are illustrated in Figures 7.18a, b.

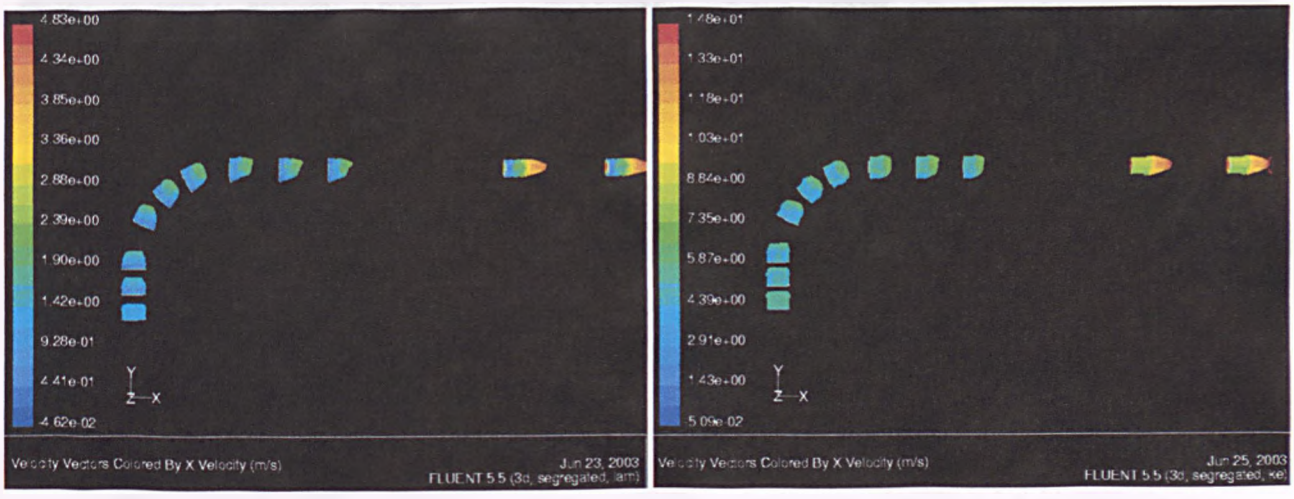

(a) **(b)**

Figure 7.18: Axial velocity profile for (a) V_s = 1.0 m/s and (b) V_s = 6.0 m/s.

For both the cases, there is an increase in velocity in the bend and it becomes more significant straight after the bend. The position of the maximum axial velocity moves toward the outer bend. This is due to the centrifugal force pushing the fluid from the inner bend to the outer bend, hence non-uniform velocity distribution developing in the bend with higher velocity in the outer bend. Due to this, secondary flow $\left(\sqrt{V_y^2 + V_z^2}\right)$started to develop in the bend and the pattern and the magnitude of the secondary flow after the bend were analysed (See Figures 7.19a to 7.22b). It is of more interest to find out the magnitude of the secondary flow compared to the axial flow. If the effect of the secondary flow is significant, at higher sampling velocity, more droplets will be thrown to the probe wall and collected there and this might be the reason for getting less drop count at high V_s. The fluid flow pattern will only be discussed briefly. From Figures 7.19a to 7.22b, it is shown that the strength of the secondary flow is relatively stronger straight after the bend compared to in the Polytec channel. The secondary flow in the Polytec channel can be said to have no effect on the axial flow inside the channel.

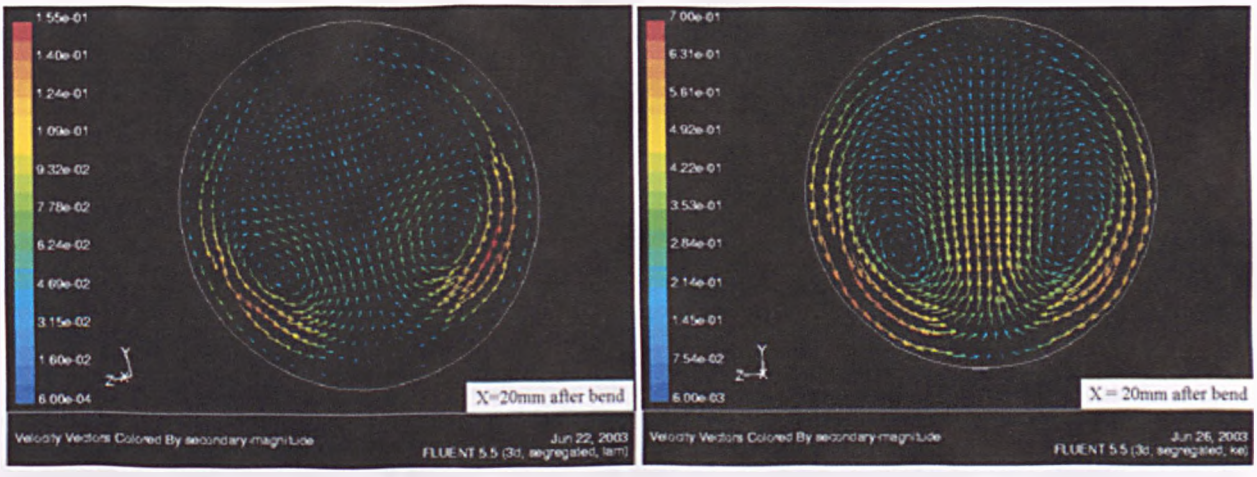

(a) (b)

Figure 7.19: Velocity vectors of the secondary flow when V_s = (a) 1.0 m/s and (b) 6 m/s, 20 mm after the bend.

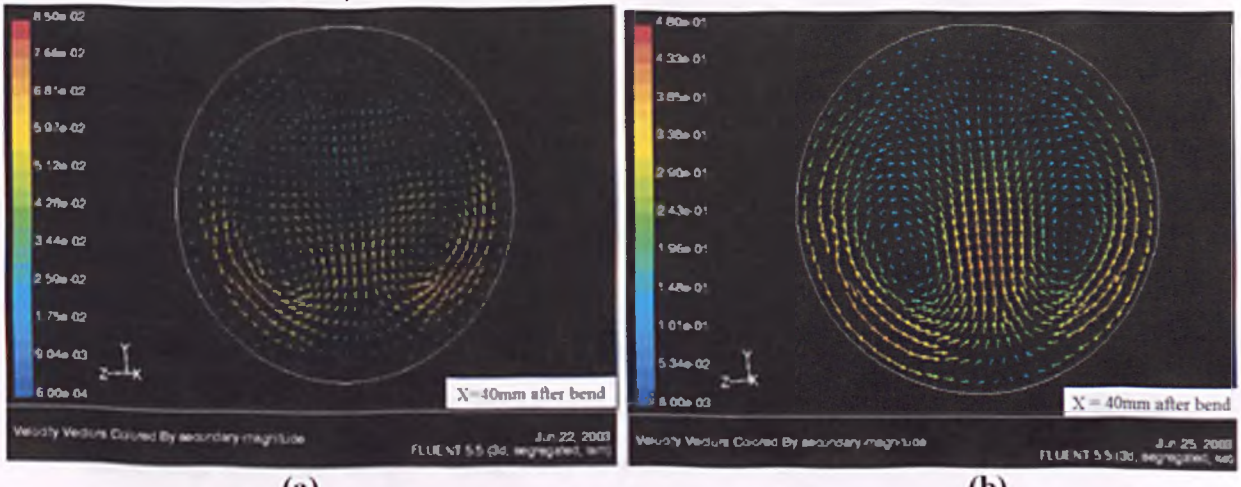

(a) (b)

Figure 7.20: Velocity vectors of the secondary flow when V_s = (a) 1.0 m/s and (b) 6 m/s, 40 mm after the bend.

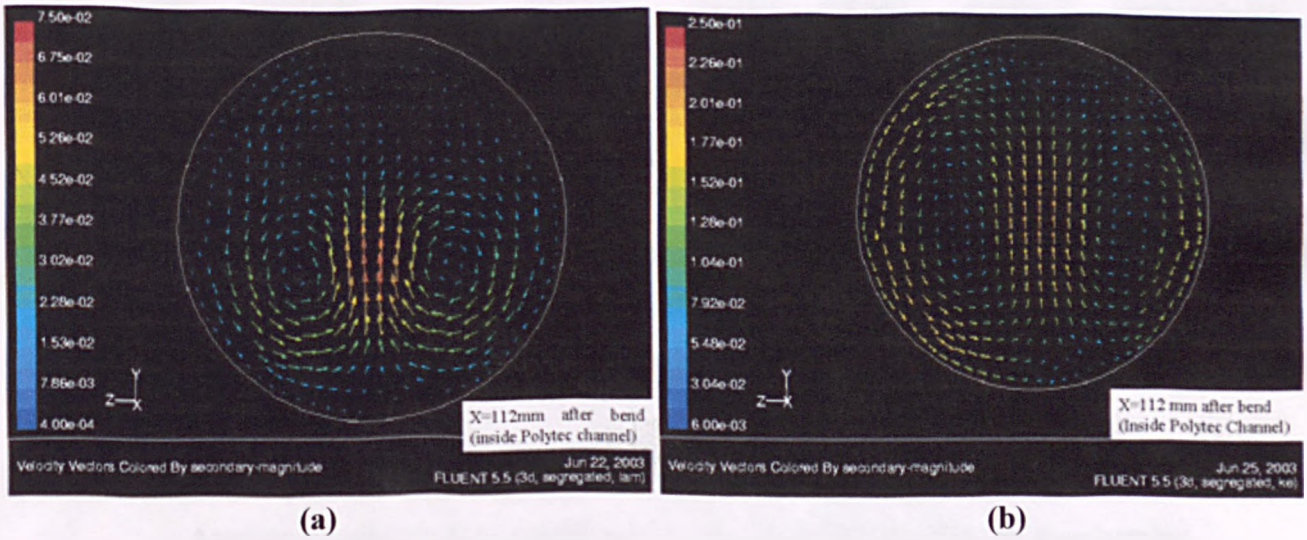

(a) (b)

Figure 7.21: Velocity vectors of the secondary flow when V_s = (a) 1.0 m/s and (b) 6 m/s, 112 mm after the bend (inside the Polytec channel).

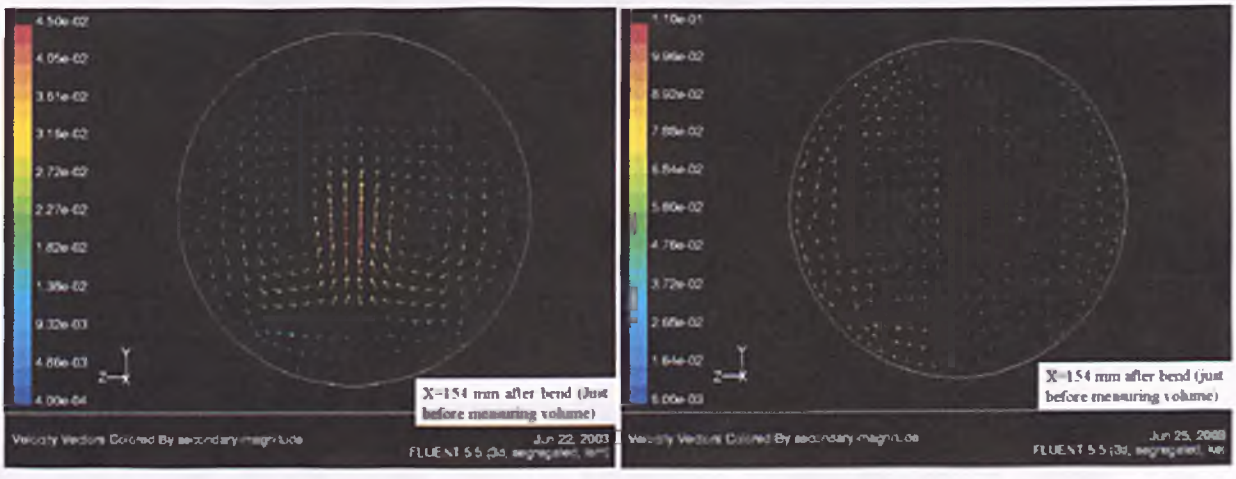

(a) (b)

Figure 7.22: Velocity vectors of the secondary flow when V_s = (a) 1.0 m/s and (b) 6 m/s, 154 mm after the bend (just before measuring volume).

It is noticed that in the laminar flow just after the bend, there is a four-vortex flow. The upper two vortices are very weak compared to the bottom two vortices. **Yanase *et al.* (1989)** also found a four-vortex solution in their investigation on the flow through a curved tube. From their investigation, the four-vortex was unstable to small disturbances. It eventually turned into a two-vortex flow. This is exactly the same result obtained in modelling the sampling velocity at 1.0 m/s. When sampling velocity is at 6 m/s, only a two-vortex secondary flow solution was obtained and the effect of the secondary flow on the axial flow is weaker compared to the laminar model. This might be due to the much stronger axial flow, which damped the secondary flow and the flow is so fast that a four-vortex flow could not be developed in a turbulent flow.

It can be seen that the effect of the secondary flow is more significant straight after the bend, so most of the droplets' deposition will occur here. This will be more significant for larger droplets because their inertia might cause them not to follow the streamlines after turning in the bend and just impact onto the probe wall.

Another possibility that contributes to the sampling error is the overlapping of droplets. If a larger droplet coincidently flows on top of a smaller droplet, the

Polytec will not be able to 'see' the smaller droplet, hence it will not be detected. However, the possibility of two droplets of different sizes moving together at the same velocity might not be too great.

The effect of droplet deposition at various sampling velocities was also investigated using CFD. Droplets that reach the walls of the sampling probe and the Polytec channel are considered lost and those that reach the walls of the measuring volume are considered detected by the Polytec. Those that did not pass through the measuring volume is considered not detected by the Polytec. The percentage deposition is the ratio of the droplets that reached the wall to the incoming drops. The drops are injected uniformly through a bounded plane **(FLUENT, 1998)** with a total of 7992 drops injected for the laminar models and for the turbulent flow stochastic tracking is enabled. Stochastic tracking includes the effect of turbulent velocity fluctuations on the particle trajectories. The number of tries is set to 2, making total of droplets injected 15984. If the number of tries is set to 0, this tells FLUENT to compute the particle trajectory based on the mean continuous phase velocity fields, ignoring the effects of turbulence on the particle trajectories. An input of 1 or greater tells FLUENT to include turbulent velocity fluctuations in the particle force balance. The number of tries was set to 2 because the results did not vary beyond this value. The summary of the detected drops and the deposited drops at sampling velocity of 1.0, 1.5 and 6.0 m/s for various droplet sizes is tabulated in Table 7.3.

Drop Size (μm)	V_s = 1.0 m/s			V_s = 1.5 m/s			V_s = 6.0 m/s		
	% Droplets Deposited	% Droplets Detected	% Droplets Undetected	% Droplets Deposited	% Droplets Detected	% Droplets Undetected	% Droplets Deposited	% Droplets Detected	% Droplets Undetected
0.52	1.86	58.89	39.25	4.07	56.65	39.28	12.52	30.36	57.12
1.00	1.86	58.90	39.24	4.12	56.64	39.24	13.84	30.01	56.15
2.45	1.94	59.10	38.96	4.80	56.65	38.55	15.79	29.47	54.74
3.00	2.01	59.39	38.60	5.01	56.74	38.25	16.87	28.13	55.00
4.26	3.00	59.11	37.89	5.98	57.77	36.25	19.71	27.22	53.07
5.30	3.64	59.10	37.26	6.94	61.07	31.99	22.98	27.56	49.46
7.40	5.09	59.60	35.31	9.68	62.25	28.07	34.02	26.76	39.22
8.25	-	-	-	11.91	62.10	25.99	38.51	25.84	35.65
9.21	6.69	61.49	31.82	15.32	60.67	24.01	47.54	23.79	28.67
10.30	7.62	62.70	29.68	18.43	59.14	22.43	55.08	21.70	23.22
11.49	9.60	67.46	22.94	24.44	56.24	19.32	68.32	16.46	15.22
12.82	11.74	68.67	19.59	30.28	54.17	15.55	79.10	11.21	9.69
14.22	15.87	67.73	16.40	37.09	52.27	10.64	86.95	7.67	5.38

Table 7.3: Summary of the droplet deposition onto the sampling probe, droplets measured and the droplets out of the measuring volume at different sampling velocity.

As expected, the deposition efficiency increases as the velocity and the drop size increase. It was also thought that one of the reasons for getting less drop count at higher velocity was due to the drops not flowing through the measuring volume. From Table 7.3, it can be seen that the amount of drops that bypassed the measuring volume was significant when the sampling velocity is high. At smaller drop size deposition efficiency is not very significant, but there is quite a significant amount of droplets not passing through the measuring volume. This is probably due to the low inertia of smaller droplets and they tend to follow the turning air streamlines inside the bend towards the wall and carried on straight from there.

The CFD results are compared with the models developed by other researchers as discussed in Chapter 2 Section 2.7.2. Equation (2.50) is used to predict the deposition efficiency when the flow is laminar and the Pui *et al.* model is used when the flow is turbulent. The results are tabulated in Table 7.4.

Drop Size (μm)	Deposition efficiency at V_s = 1.0 m/s		Deposition efficiency at V_s = 1.5 m/s		Deposition efficiency at V_s = 6.0 m/s	
	CFD	Model Prediction	CFD	Model Prediction	CFD	Model Prediction
0.52	1.86	0	4.07	0.02	12.52	0.30
1.00	1.86	0	4.12	0.07	13.84	0.99
2.45	1.94	0	4.80	0.35	15.79	5.22
3.00	2.01	0	5.01	0.54	16.87	7.91
4.26	3.00	1.00	5.98	1.03	19.71	14.57
5.30	3.64	1.00	6.94	1.60	22.98	21.58
7.40	5.09	2.00	9.68	3.07	34.02	37.33
8.25	-	-	11.91	3.82	38.51	44.08
9.21	6.69	3.00	15.32	4.75	47.54	51.48
10.00	7.62	4.00	18.43	5.91	55.08	59.35
11.49	9.60	5.00	24.44	7.36	68.32	67.38
12.82	11.74	6.00	30.28	9.16	79.10	75.21
14.22	15.87	8.00	37.09	11.24	86.95	81.95

Table 7.4: Comparison of CFD results with other models on the deposition efficiency inside the sampling probe.

It can be seen from Table 7.4 that the CFD prediction is very close to the models used for laminar flow with increasing discrepancy occurring at the larger drop size and the difference between CFD prediction and the model is more prominent when the sampling velocity is 1.5 m/s compared to 1.0 m/s. This might be due to the ambiguous flow regime at 1.5 m/s. The flow in the sampling probe (Dean number = 343) is just slightly below the laminar flow mark (Dean number = 350), but when the flow is in the Polytec channel, there is a slight reduction in the cross-sectional area and the Dean number inside the channel becomes 480. It is very likely that at sampling velocity of 1.5 m/s, the flow is in the transition regime and there is no appropriate flow model in FLUENT to simulate this condition, hence the discrepancy. Furthermore, the Cheng and Wang model (Equation 2.50) works best when $Re_p << 1.0$ and this corresponds to drop size of 1 μm at 1.0 m/s and 0.7 μm at 1.5 m/s. The CFD prediction and the Pui *et al.* model agree well with each other except for particle size below 1 μm. Therefore, it can be

concluded that the turbulent model is reliable and can be used to predict the deposition of efficiency over a wide range of drop size on the sampling probe. The laminar model, however does not give accurate prediction when $Re_p >> 1.0$.

Thus it is concluded that droplet deposition can be predicted well using CFD except in the transition region. Most of the models developed are restricted to small droplet size (i.e. Stoke flow for $Re_p << 1.0$). Since it has been proved earlier on that isokinetic sampling is not very crucial (i.e. sampling is merely influenced by the velocity through the measuring volume), there will be no difference in the grade efficiency curve even when the deposited drops and the undetected droplets are accounted for because the sampling and velocity through the measuring volume in the inlet and outlets are the same for all the tested flowrates and the drop count was normalised to calculate the grade efficiency.

7.2 Conclusions

The grade efficiency measurements were carried out using Geometry 7a to determine the performance of this design in separating droplets between 0.4 – 20 microns. Initially, the sampling was carried out isokinetically. However, when the inlet velocity was increased, the number of droplets counted reduced significantly especially in the vortex finder. Hence, a flow straightener was put into the vortex finder so that the droplets would be distributed more evenly over the whole cross-sectional area of the tube. It was found out that isokinetic sampling could not be carried out in the vortex finder at high air inlet velocity because this increased the velocity in the vortex finder until it exceeded the limit that the Polytec could handle. Even with the flow straightener in, the amount of drops counted was still low. Therefore, a new approach was taken, which was using non-isokinetic sampling by setting the sampling velocity to be 6, 3, 1.5 and 1.0 m/s by controlling the flowrate going through the probe. The drop size distribution (DSD) curves for both isokinetic and non-isokinetic sampling were compared at the inlet and both the outlets. The DSD curves were very similar.

Therefore, isokinetic sampling was not very crucial in this study. However, it has to be determined whether the sampling was dependent on the sampling velocity, V_S, or the velocity through the measuring volume, V_{mv}. This led to the next approach.

A cone was attached to the tip of the sampling probe to increase the sampling velocity due to the decreased probe inlet area, but keeping the V_{mv} the same as in the previous case (i.e. flowrate going through the probe remained unchanged). From the result, it was shown that the DSD with and without cone were similar. Therefore, it could be concluded that the sampling was dependent on V_{mv}. Measurements were taken 6 times for each different sampling velocity and an arithmetic mean was taken to calculate the grade efficiency curve.

It was also of interest to investigate the reason for getting a smaller droplet count as the velocity increases. Therefore, CFD calculations to simulate the air flow pattern inside the sampling probe were carried out. From the computational work, it was found that the most probable reasons of getting lower counts at high velocities were droplets depositing onto the probe wall and droplets not passing through the measuring volume. These effects were more dominant for larger droplets. It was also thought that the decrease in the drop count was due to the increase of droplet deposition onto the cyclone wall with time and also due to evaporation as the air temperature increases with time. However, these reasoning were found to be invalid after a detailed analysis. Hence, it is concluded that there is inherent variability in the measurements taken.

In the next chapter, the computational work carried out in this project to model the entire cyclone geometry is discussed comprehensively in terms of the pressure drop and the grade efficiency measurements.

Chapter 8

Modelling Cyclone Behaviour

8.1 Introduction to Computational Fluid Dynamics (CFD) Modelling

Apart from using the available empirical relations on empirical data, another approach to designing axial flow cyclones is to model the flow pattern, pressure drop and collection efficiency in these cyclones is using Computational Fluid Dynamics (CFD). Numerical simulation is often used to extend experimental results. CFD offers an alternative way of investigating most aspects of cyclone operation and design (i.e. cyclone performance can be predicted without carrying out experiments for various designs and operating conditions until an optimal result is obtained). Besides saving money, it also reduces the time required for experiments to be carried out. However, one cannot simply depend on computation alone. Experiments are necessary to confirm the corresponding optimal variables and validate the results of the computation. Similar to experiments, computation also requires careful setting up. It is only complete and reliable if the solution converges and is grid independent (i.e. no significant changes in the results when the meshes are further refined).

This chapter discusses CFD modelling of droplet removal, the pressure drop and flow pattern in the tested axial flow cyclone. The cyclone geometry was created and meshed in GAMBIT 2.0. This is the pre-processing stage. The mathematical calculations are then performed using the CFD solver in FLUENT 5 and 6. Simulation results are then compared with the experimental findings from the pressure drop and separation efficiency studies, which were discussed in Chapters 6 and 7.

8.2 Geometry Setup and Grid Generation

Since it was intended only to find out whether typical CFD turbulence models were reliable to accurately predict the pressure drop across the cyclone, not all the experimental results of all the tested geometries needed to be validated against computational results. Only the initial geometry and Geometry 7a were studied. Geometry 7a was of the most interest because it was the most successful design produced. Earlier in the project, the initial geometry was also modelled, using an inferior turbulence model (k-ε turbulence model). The results of these calculations are also reported for completeness. The cyclone geometry created in GAMBIT would have exactly the same dimensions as the experimental setup except where specified. The housing tube was not included in the modelling work, the modelled geometry only included the swirl element, the 52 mm cyclone tube and vortex finder (until the pressure tapping point, PT_C). When generating the grid, attention should be paid to certain aspects, which are discussed below:

- ***Equiangle Skew***

When creating the meshes for the cyclone geometry, the quality of these meshes was checked based on the equiangle skew. This method measures the deviation of the cell angle from the actual angle, for example for triangular and tetrahedral elements, the perfect angle is 60^0 and for quadrilateral and hexahedral elements it is 90^0. The scale of the equiangle skew varies from 0 (equilateral, i.e. perfectly shaped) to 1.0 (degenerate, i.e. poorly shaped element). The equiangle skew should be less than 0.6. Above 0.75, the cell quality is considered poor. If most of the cells are poorly meshed, this will affect the calculation at the later stage, prohibiting accurate results and, in the worst condition, diverging the solution.

- ***Wall Y^+***

Wall y^+ is a non-dimensional parameter defined as $y^+=\rho U_T y_p/\mu$ where U_T is the friction velocity, ρ is the fluid density, y_p is the distance from point P to the wall and μ is the fluid viscosity at point P. Successful computations of turbulent flow require consideration of grid independence during the mesh generation. Due to the strong interaction of the mean flow and turbulence, the numerical results for turbulent flows tend to be more susceptible to grid dependency than those for laminar flows. It is recommended that the near wall region should be resolved using sufficiently fine meshes **(FLUENT Vol. 2, 1998)**. Different y^+ values must be obtained depending on which near wall option is chosen. For the standard wall function the first computational node next to the wall should be in the range of $y^+ > 30 - 60$. However, the value closer to the lower bound, i.e. $y^+ \approx 30$ is most desirable **(FLUENT Vol. 2, 1998)**. Nevertheless, using an excessively fine mesh near the wall should be avoided because the wall functions used in FLUENT cease to be valid in the viscous sublayer. When a two-layer zonal model is employed, y^+ at the wall adjacent cell should be on the order of $y^+ \approx 1.0$. However, a higher y^+ is acceptable as long as it is well inside the viscous sublayer ($y^+ < 4 - 5$).

8.3 The Initial Geometry

There are quite a number of turbulence models that can be used for turbulent flow modelling. These range from the simple k-ε model to complete Reynolds stress models. Unfortunately, there is no single turbulence model that is universally superior for all kinds of problems. The standard k-ε model, where 'k' is the turbulence kinetic energy (m^2/s^2) and 'ε' is the rate of viscous dissipation (m^2/s^3), is the simplest "complete model" of turbulence and is generally used for modelling turbulent flow because it gives reasonable accuracy for a wide range of turbulent flow problems. This model also requires the least computational power and it usually satisfies most of the turbulence cases. However, from Chapter 2 it

was shown that the track record of the k-ε model on swirling flow is very weak. Nevertheless, the k-ε model was chosen to model the fluid flow for this geometry as a practice to get to learn the techniques involved better. Although the k-ε model is the easiest to implement, it is reported that the values of the empirical constants used in them are very problem dependent and inaccuracies of up to 50% **(FLUENT Vol. 2, 1998)**.

The structure created in GAMBIT with the division of the initial geometry is illustrated in Figure 8.1. In 3D geometry, there are 4 different types of meshing; hexahedron, tetrahedron, prism/wedge and pyramid. The initial geometry was divided into 5 different volumes (Figure 8.1) and the details of each division are listed in Table 8.1. The type of mesh used and the details of meshing are listed in Table 8.2. It was ensured that the first computational node next to the wall satisfied the range of y^+ to be between 30 and 60. The description of the element and type of mesh used below can be obtained from the GAMBIT modelling guide **(GAMBIT, 1999)**. The vortex finder length in the CFD study was shorter than the experimental setup. This was because the computational power was low when the work was carried out. However, the pressure drop due to the extra vortex finder length could be accounted for using Equation (8.9), predicting pressure drop due to friction loss.

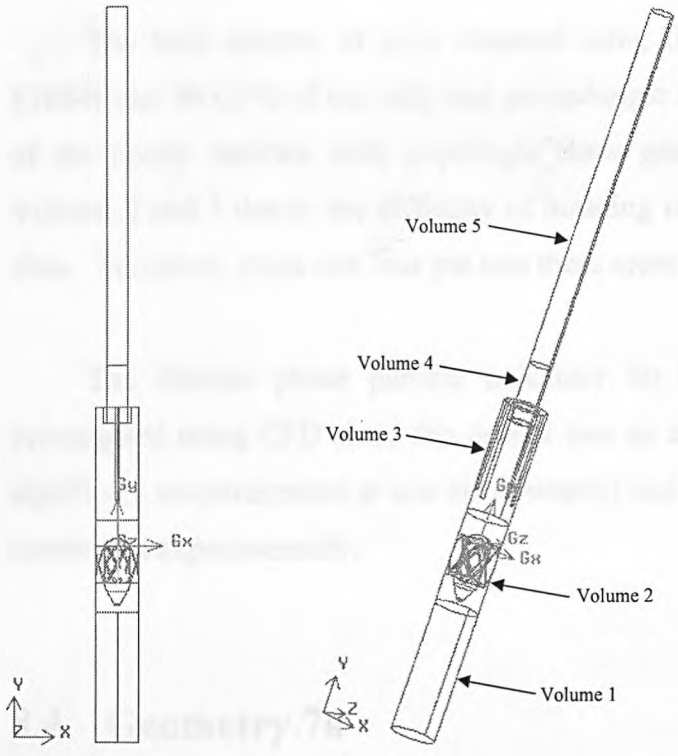

Figure 8.1: Initial geometry created in GAMBIT and the structure division.

Volume	Length (mm)	Section
1	150	Entrance Length
2	110	Vanes and Centre Body
3	135	Separation Length and Slots
4	50	Gas Exit Pipe
5	430	Extension of the Gas Exit Pipe

Table 8.1: Different sections of the initial geometry in GAMBIT.

Volume	Meshing Details	Element	Type	Interval Size
1	Mesh the edge with ratio 1.064	-	-	4 (Interval Size)
	Mesh face	Quad	Map	-
	Mesh Volume	Hex/Wedge	Cooper	-
2	Mesh Volume	Tet/Hybrid	TGrid	3 (Interval Size)
3	Mesh face (for slots only)	Tri	Pave	1.5 (Interval Size)
	Mesh Volume	Tet/Hybrid	TGrid	4 (Interval Size)
4	Mesh the edge with ratio 1.064	-	-	3 (Interval Size)
	Mesh Volume	Hex/Wedge	Cooper	-
5	Mesh Volume	Hex/Wedge	Cooper	5 (Interval Size)

Table 8.2: Details of the meshing process for the initial geometry.

The total number of cells obtained using the above meshing details was 138841 and 99.61 % of the cells had an equiangle skew of less than 0.7. The rest of the poorly meshed cells (equiangle skew greater than 0.7) were found in Volume 2 and 3 due to the difficulty of meshing near the swirling device and the slots. Therefore, extra care was put into these areas when meshing Geometry 7a.

The discrete phase particle trajectory for the initial geometry was not investigated using CFD since this design was an unsuccessful one (i.e. promoted significant re-entrainment at low air flowrates) and a grade efficiency test was not carried out experimentally.

8.4 Geometry 7a

Geometry 7a was far more complex than the initial geometry with the introduction of the tangentially oriented vanes and with the position of the slots in the middle and the end of the cyclone tube, it was a challenge to mesh the whole geometry and maintain the cell equiangle skew to be within 0.5 to 0.6. As the skewness increases, the solution will be inaccurate and a diverged solution is more likely.

The structure of Geometry 7a, which was created in GAMBIT is attached in Appendix K. This geometry was divided into a lot of smaller volumes for easier meshing and the details of each division are shown in Figure 8.2 with the type of mesh used and the details of meshing listed in Table 8.3. Table 8.4 shows the important dimensions of this geometry. This meshing gives a total number of cells of 1130991, 90% of them are hexahedral in shape and 99.07% of the cells have an equiangle skew of less than 0.6. Grid independence was achieved with this meshing because increasing the amount of cell beyond 1130991 did not give a significant change in the results obtained.

After gaining the relevant practice on the initial geometry, for Geometry 7a one of FLUENT's advanced turbulence models (RNG k-ε model, realizable k-ε model or Reynolds stress model) for modelling turbulent flow with a significant amount of swirl (i.e. cyclone flows) was used as suggested **(FLUENT Vol. 2, 1998)**.

After considering the results from previous work discussed in Chapter 2, it was decided to use the RSM turbulence model to solve the steady state continuous gas phase for Geometry 7a since it accounts for the effects of swirl and has greater potential to give accurate predictions for complex flows.

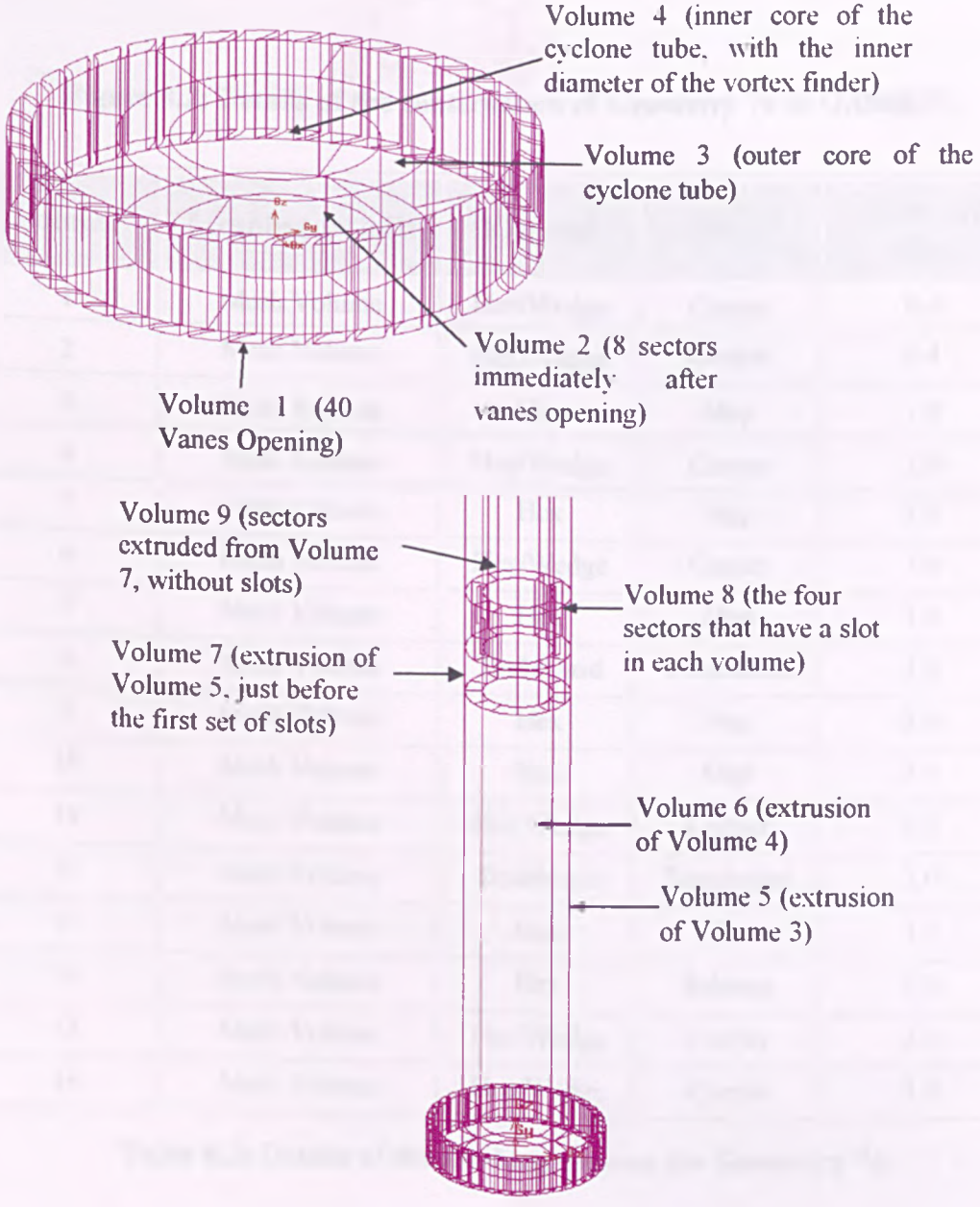

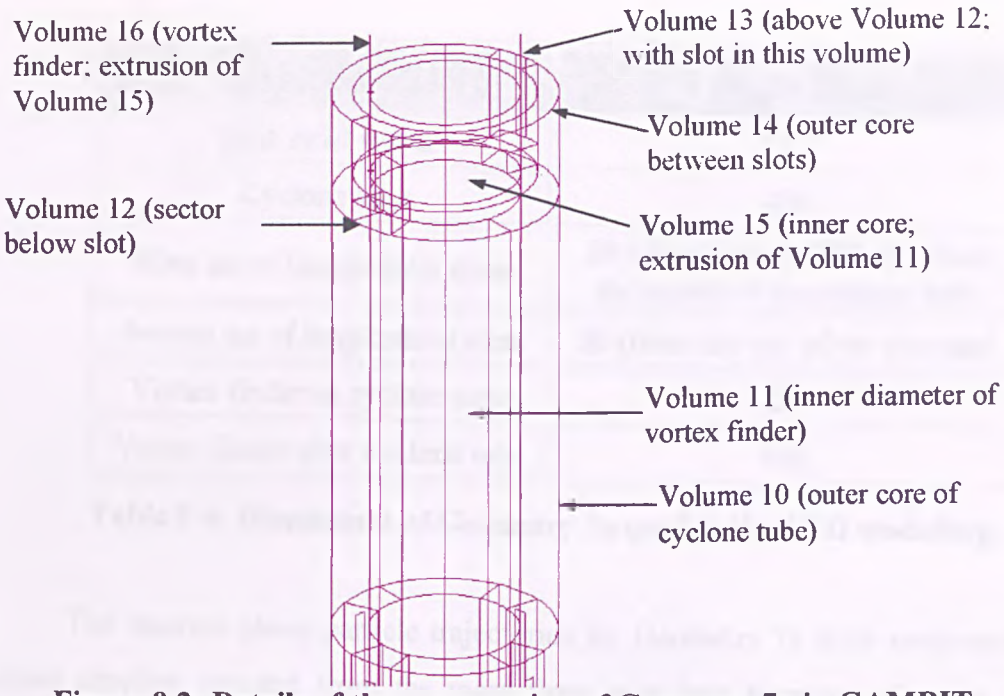

Figure 8.2: Details of the construction of Geometry 7a in GAMBIT.

Volume	Meshing Details	Element	Type	Interval Size
1	Mesh Volume	Hex/Wedge	Cooper	0.4
2	Mesh Volume	Hex/Wedge	Cooper	0.4
3	Mesh Volume	Hex	Map	1.0
4	Mesh Volume	Hex/Wedge	Cooper	1.0
5	Mesh Volume	Hex	Map	1.0
6	Mesh Volume	Hex/Wedge	Cooper	1.0
7	Mesh Volume	Hex	Map	1.0
8	Mesh Volume	Tet/Hybrid	Tetrahedral	1.0
9	Mesh Volume	Hex	Map	1.0
10	Mesh Volume	Hex	Map	1.0
11	Mesh Volume	Hex/Wedge	Cooper	1.0
12	Mesh Volume	Tet/Hybrid	Tetrahedral	1.0
13	Mesh Volume	Hex	Map	1.0
14	Mesh Volume	Hex	Submap	1.0
15	Mesh Volume	Hex/Wedge	Cooper	1.0
16	Mesh Volume	Hex/Wedge	Cooper	1.0

Table 8.3: Details of the meshing process for Geometry 7a.

Cyclone Parts	Length (mm)
Inlet swirl vanes	17.7
Cyclone tube	420
First set of longitudinal slots	20 (slots begin at 250 mm from the mouth of the cyclone tube
Second set of longitudinal slots	20 (from the end of the cyclone)
Vortex finder in cyclone tube	20
Vortex finder after cyclone tube	900

Table 8.4: Dimensions of Geometry 7a used in the CFD modelling.

The discrete phase particle trajectories for Geometry 7a were computed for liquid droplets injected from the mass flow inlet face boundary (i.e. the vane inlets) into the flow domain.

8.5 Mathematical Models

There are three basic flow equations to be solved, which are the continuity, momentum and turbulence equations. For the discrete particle model, Lagrangian particle tracking is used.

8.5.1 Continuity Equation

The continuity equation expresses the conservation of mass. Since the mass is neither created nor destroyed, the net mass flow given by the sum of the masses flowing across the domain is made equal to zero. The general continuity equation is represented by Equation (8.1):

$$\frac{\partial \rho}{\partial x} + \left[\frac{\partial (\rho u)}{\partial x} + \frac{\partial (\rho v)}{\partial y} + \frac{\partial (\rho w)}{\partial z} \right] = 0 \qquad \textbf{- Equation (8.1)}$$

For 3-D incompressible flow, the density is constant. Hence, Equation (8.1) can be simplified to become Equation (8.2).

$$\left[\frac{\partial u}{\partial x}+\frac{\partial v}{\partial y}+\frac{\partial w}{\partial z}\right]=0 \qquad \textbf{- Equation (8.2)}$$

8.5.2 Momentum Equation

The momentum of the fluid must also be conserved. Therefore, the momentum in equals the momentum out. The general momentum equation is represented by Equation (8.3):

$$\frac{\partial \rho u_i}{\partial t}+\frac{\partial(\rho u_i)u_j}{\partial x_j}=-\frac{\partial P}{\partial x_i}+\frac{\partial \tau_{ij}}{\partial x_j}+\rho g_i+F_i \qquad \textbf{- Equation (8.3)}$$

where

P = static pressure

τ_{ij} = stress tensor

$$\tau_{ij}=\mu\left(\frac{\partial u_i}{\partial x_j}+\frac{\partial u_j}{\partial x_i}\right)$$

ρg_i = gravitational body force

F_i = any external body forces impacting the continuous phase

The LHS is the rate of change of momentum per unit fluid volume, which is the transport equation. The RHS is the dynamics equation that is the net force acting per unit fluid volume at position x_i and time, t. The first two terms are the surface force and the remainder is the body force.

8.5.3 Turbulence Model

Turbulence models use the Reynolds-averaged approach whereby instantaneous solution variables consist of the mean and the fluctuating components, e.g. the velocity components as expressed in Equation (8.4).

$$u_i = \bar{u}_i + u'_i \qquad \textbf{- Equation (8.4)}$$

where $\bar{u}_i$ and u'_i are the mean and fluctuating velocity components ($i = 1, 2, 3$). In turbulence flows, additional terms appear in the ensemble-averaged momentum equation (Reynolds stresses) that represent the effects of turbulence and they are modelled using the Boussinesq hypothesis for the standard k-ε model or using the Reynolds stress transport model, particularly for cases that include high swirling flows. Besides the continuity and momentum equations, additional transport equations describing the turbulent kinetic energy, k, and the turbulence dissipation rate, ε, are solved. Turbulent flows are significantly affected by the presence of walls. The near wall treatment for the standard k-ε model is the standard wall function and for RSM it is the enhanced wall treatment.

8.5.4 Discrete Phase Model

The discrete phase model, which follows the Euler-Lagrange approach, was chosen to calculate the droplets' trajectories in the continuous gas phase. It is normal to use this model when the dispersed phase (i.e. water) volume fraction is less than or equal to 10% of the continuous phase (i.e. air) and it is also, in computational terms, the least expensive of all the available multiphase models. The droplets' trajectories are computed using uncoupled calculations between the discrete and the continuous phases, i.e. that the discrete phase does not affect the flow field of the continuous phase. The droplet size considered ranged from 0.47 to 14.22 microns and the droplets are injected into the continuous phase at the same velocity at the gas phase at the inlet to the flow domain. It is assumed that

there is neither mass nor heat transfer between the dispersed and continuous phase. For such a low mass and momentum loadings of the droplets, the use of uncoupled calculations seems logical. This was justified from the rough calculations of the fluid drag and the particles' body force calculations. **Griffiths and Boysan (1996)** also assumed that the presence of particles would not affect the gas flow field in their numerical studies.

The largest droplet size (14.22 microns) was used in the calculation because if this did not affect the gas flow field, then the smaller droplets would not either. The two limits of the air velocity were investigated, i.e. 5 m/s and 20 m/s. The results of the calculations are tabulated in Table 8.5.

Air Velocity, U_g (m/s)	Fluid Drag, $3\pi d_p \mu U_g$, (N)	Body Force, $\pi d_p^3(\rho_p-\rho_g)g/6$, (N)	Fluid Drag / Body Force
5	1.206×10^{-8}	1.474×10^{-11}	818
20	4.825×10^{-8}	1.474×10^{-11}	3273

Table 8.5: Calculations showing the affect of the droplets on the gas flow field.

From this simple calculation, it was shown that the droplets would not have any significant effect on the continuous gas phase. Hence, using uncoupled calculations for the particles' trajectories was acceptable.

The trajectory of a dispersed phase particle is predicted by the integration of the force balance on the particle, which is the particle equation of motion (Equation 2.1) described in Chapter 2. After rearranging Equation (2.1), it becomes Equation (8.5) below (for the x direction in Cartesian coordinates), which is to be solved. This force balance equates the droplet inertia with the forces acting on the droplet (i.e. the drag force, the gravitational force and other additional forces acting on the droplet).

$$\frac{du_d}{dt} = F_D(u-u_d) + \frac{g_x(\rho_d-\rho)}{\rho_d} + F_x \qquad \textbf{- Equation (8.5)}$$

where $F_D(u-u_d)$ is the drag force per unit droplet mass; $F_D = 18\mu C_D Re/24\rho_d d_d^2$, u and u_d are the air and droplet velocity respectively, μ is the dynamic viscosity of air, ρ and ρ_d are the air and droplet density respectively, d_d is the droplet diameter. Re is the relative Reynolds number, which is defined as $\rho d_d|u_d-u|/\mu$ and C_D is the drag coefficient. F_x represents the additional forces acting on the droplet such as the force required to accelerate the fluid surrounding the droplets and force that arises due to pressure gradient in the fluid.

The accuracy of the discrete phase calculation depends on the time accuracy of the integration of Equation (8.5) to yield the droplet trajectory. The time integration of the particle trajectory equation is controlled using two parameters **(FLUENT Vol 3, 1998)**:

(i) The Length Scale controls the time step size for integration. It is equivalent to the distance that the particle will travel before its motion equations are solved again and trajectory is updated. A smaller value for the length scale increases the accuracy of the trajectory for the discrete phase. This was set to 0.001 m, meaning the droplet trajectory was updated every 1 mm.

(ii) The maximum number of time steps allowed for integrating Equation (8.5) before the trajectory computations are aborted and the trajectory fate is reported as "incomplete". This implies that the droplet does not leave the flow domain, possibly being caught in a recirculating region of the continuous phase flow field. This was set to 20,000 because with this value the number of "incomplete" trajectories was insignificant. The limit of the maximum number of steps is 1×10^9. However, the higher the value the more computational power is required.

For turbulent flow, the dispersion of the droplets was modelled using the stochastic tracking or the Discrete Random Walk (DRW) model by computing the trajectory for a sufficient number of representative particles so that the random

effects of the turbulence on the droplet dispersion may be accounted for. The droplets are released from the mass flow inlet boundary surface, hence the number of droplets injected will depend on the number of cells on the inlet surfaces (i.e. the vane surfaces), which were 3888. The number of tries was set to 2. This means that the total number of droplets tracked was 7776 altogether. The number of tries was set to 2 because there was no significant difference in the results obtained when the number was further increased. The injection properties are listed below.

(i) Particle type = An "inert" particle, which is a discrete phase element that obeys the force balance (Equation 8.5). It can be a solid particle, droplet or bubble.
(ii) Particle velocity = Initial droplet velocity is assumed to be equal to the air velocity in the x-direction (corresponds to 600, 1000 and 1400 l/min) and zero velocities in the y- and z-directions.
(iii) Particle diameter = Varies from 0.47 to 14.22 microns.
(iv) Total mass flowrate of particles = Not required for uncoupled calculations.

The fate of a droplet at the different boundary zones is set as follows:

(i) "Reflect" rebounds the particle off the boundary in question with a change in its momentum as defined by the coefficient of restitution. A coefficient of restitution equal to 1.0 implies that particle retains all of its momentum after the rebound (a fully elastic collision) and a value of 0 implies that the particle retains none of its momentum after the rebound (a fully inelastic collision). A value of 0 was used since a water drop would most probably undergo an inelastic collision at the wall.

(ii) "Escape" reports the particle as having escaped when it encounters the boundary in question where the trajectory calculations are terminated. This fate was set through the pressure outlet boundaries (i.e. vortex finder outlet, slots and vane outlets).

8.6 Material Properties, Operating and Boundary Conditions

8.6.1 Material Properties

The fully meshed cyclone geometry was then exported to Fluent Inc.'s FLUENT 6 for subsequent processing. The specified material for the continuous phase is air and for the discrete phase is inert particle. The density and viscosity of air and water are constant and the values are tabulated in Table 8.6.

Fluid Property	Symbol	Value	Units
Air density	ρ_g	1.2	kg/m^3
Air viscosity	μ_g	1.8×10^{-5}	Ns/m^2
Water density	ρ_w	1000	kg/m^3
Water viscosity	μ_w	0.001	Ns/m^2

Table 8.6: Physical constants of gaseous and dispersed phase.

8.6.2 Operating and Boundary Conditions

The operating pressure is taken as the atmospheric pressure 101325 Pa and since both the gas vents flow to the common chamber in the real application the outlet pressures are set to be equal.

For the initial geometry, the v-velocity of the inlet velocity is set to vary from 5 to 20 m/s at an interval of 5 m/s each. The u- and w-velocity are set to be 0 m/s. The use of the k-ε model required inputs of relative turbulence intensity (u'/U) and a length scale (L). The relative turbulence intensity was set at 10% and the length scale was set at 0.052 m. The boundary condition of the slots and the vortex finder outlet is set to be a pressure outlet face boundary. The studies on the

initial cyclone were not as detailed as Geometry 7a. The boundary conditions of the cyclone model (Geometry 7a) are summarised in Table 8.7.

Regions	Boundary Conditions and Inputs
Vane Inlet Surfaces (36 in total)	Mass Flow Inlet face boundary Mass flowrate of continuous phase, M_g For 600 l/min, M_g through each vane = 0.000333 kg/s For 1000 l/min, M_g through each vane = 0.000556 kg/s For 1400 l/min, M_g through each vane = 0.000778 kg/s Turbulent intensity = 5% Hydraulic diameter = 0.006417 m Discrete phase = reflect
Walls	Wall face boundary Discrete phase = reflect
Slots	Pressure Outlet face boundary Gauge pressure = 0 Pa Turbulence Intensity = 5% Hydraulic diameter = 0.005217 m Discrete phase = escape
Vane Outlet Surfaces (4 in total)	Pressure Outlet face boundary Gauge pressure = 0 Pa Turbulence Intensity = 5% Hydraulic diameter = 0.006417 m Discrete phase = escape
Vortex finder	Pressure Outlet face boundary Gauge pressure = 0 Pa Turbulence Intensity = 6% Hydraulic diameter = 0.03454 m Discrete phase = escape
Vortex finder wall	Wall face boundary Discrete phase = escape

Table 8.7: Boundary conditions of cyclone model (Geometry 7a).

The pressures outside the slots and vortex finder were set to be the same because in the real application both vents flow to a common chamber. The pressure drop across the secondary knitted mesh pad (which is not modeled here) is assumed to be insignificant since it will not be seriously flooded.

8.7 Results and Discussions

The results of both the geometries will be presented in two sections; one for the pressure drop calculation and the other one for the particles' trajectories (i.e. the grade efficiency calculation). The results obtained will also be compared with published work of other investigators in the field.

8.7.1 Pressure Drop Calculation

Figure 8.3 compares the Euler number based on the inlet velocity between the k-ε model and experimental data for the initial geometry. It can be seen from Figure 8.3 that the values obtained from the computation deviates from the experimental values by about 28%. This shows that the k-ε model is not very appropriate for predicting the flow behaviour in cyclones. This agrees with the results of other researchers **(Hoekstra *et al.*, 1999; Modigell and Weng, 2000)**. From the experiments, the amount of air going out the vortex finder was about 20% of the total flow going in. From CFD, the percentage going out from the central gas exit pipe was about 27%. Despite this deviation, the CFD and experimental results showed the same trend, which was significantly more air flowed out through the slots.

The pressure drops across the cyclone (Geometry 7a) at an inlet air flowrate of 600, 1000, 1400, 1800 and 2200 l/min are tabulated in Table 8.8 and plotted in Figure 8.4. The pressure drop was measured from the base of the swirl vanes to the vortex finder outlet, which was the pressure tapping point in the experiment. An addition of the pressure drop, which was due to the contraction from the housing pipe to the vanes inlet, has to be added to the numerical results in order to compare the numerical results with the experimental results. This addition of pressure drop can be calculated using the method discussed in Section 8.7.2.

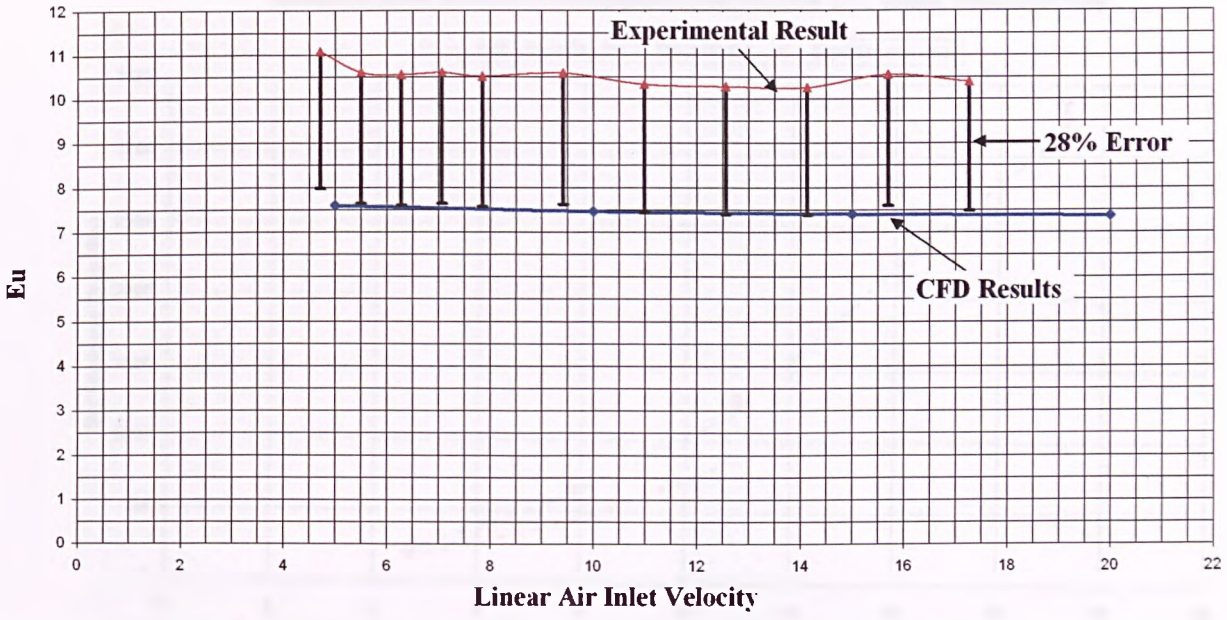

Figure 8.3: Comparing between the Euler number (Eu) as predicted from k-ε simulation and experiment.

Inlet Air Flowrate (l/min)	CFD prediction (RNG k-ε model)	CFD prediction (RSM)	ΔP due to contraction (Pa)	ΔP across cyclone (Pa)		
				Experiment data	RNG	RSM
600	155	205.34	12.39	229.30	167.39	217.73
1000	395	591.89	34.42	658.91	429.42	626.31
1400	800	1143.26	67.46	1289.91	867.46	1210.72
1800	-	2148.67	111.51	2175.08	-	2260.18
2200	-	3008.42	166.58	3255.59	-	3175.00

Table 8.8: Comparison of numerical predictions and experimental measurements of the cyclone pressure drop.

From Figure 8.4, it can be seen that the RSM gives a better prediction of the cyclone pressure drop with an error of approximately 4%. The predicted flow split was around 52 %, which is almost similar to the experimental results, which was 56 %. The RNG k-ε model, however, can be used to obtain a quick, preliminary prediction since it requires less computational power compared to the RSM model.

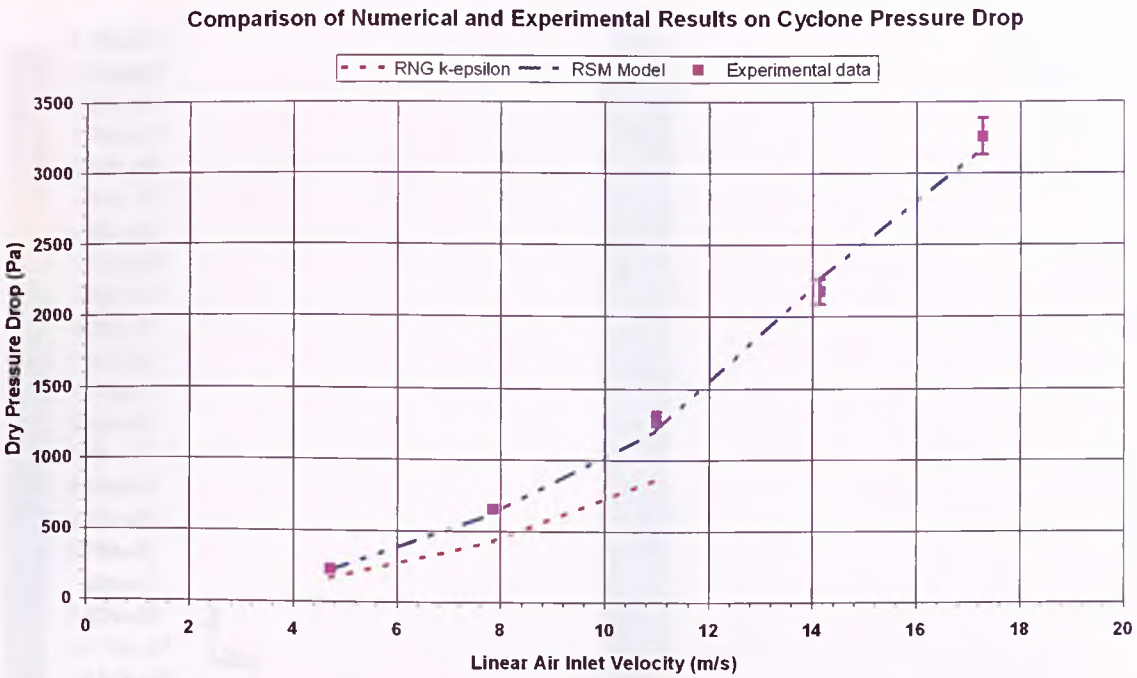

Figure 8.4: Comparison of numerical and experimental data of cyclone pressure drop as a function of inlet air flowrate.

The pressure profile inside the cyclone at an inlet air flowrate of 600, 1000 and 1400 l/min along the center plane of the geometry is shown in Figure 8.5. It can be seen that the highest pressure is the region immediately after the vane openings and the pressure in the middle of the core is the lowest. As the flow progresses along the cyclone tube, the pressure gradient in the radial direction diminishes after the first set of slots and eventually the pressure distribution is fairly uniform across the cross-sectional area of the tube, especially inside the vortex finder. This shows that the vortex strength is decaying as it flows along the cyclone tube. This could justify the re-entrainment occurring at high air flowrates observed from the experimental work carried out. At high air flowrates the liquid was swirled up the cyclone tube, but after the first set of slots the swirl strength decreased, hence the remaining liquid was not entirely thrown out through the second set of slots, resulting in liquid being re-entrained into the vortex finder.

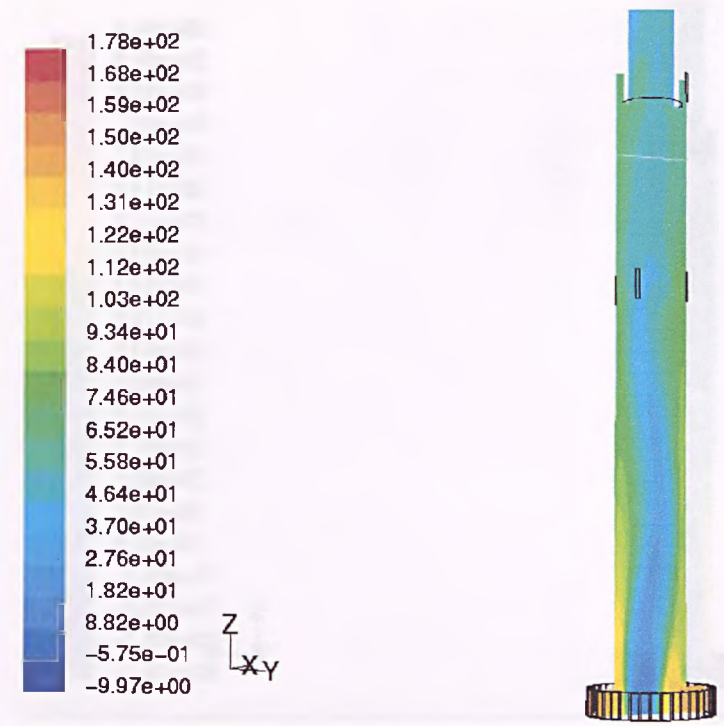
1.78e+02
1.68e+02
1.59e+02
1.50e+02
1.40e+02
1.31e+02
1.22e+02
1.12e+02
1.03e+02
9.34e+01
8.40e+01
7.46e+01
6.52e+01
5.58e+01
4.64e+01
3.70e+01
2.76e+01
1.82e+01
8.82e+00
-5.75e-01
-9.97e+00
Z
X Y
Contours of Total Pressure (pascal)
May 16, 2004
FLUENT 6.1 (3d, segregated, RSM)

(a)

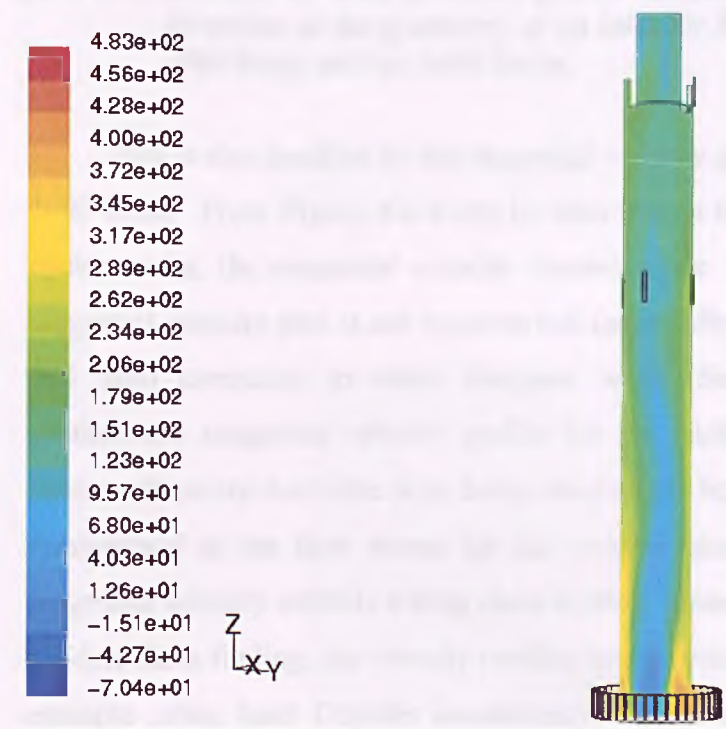
4.83e+02
4.56e+02
4.28e+02
4.00e+02
3.72e+02
3.45e+02
3.17e+02
2.89e+02
2.62e+02
2.34e+02
2.06e+02
1.79e+02
1.51e+02
1.23e+02
9.57e+01
6.80e+01
4.03e+01
1.26e+01
-1.51e+01
-4.27e+01
-7.04e+01
Z
X Y
Contours of Total Pressure (pascal)
May 16, 2004
FLUENT 6.1 (3d, segregated, RSM)

(b)

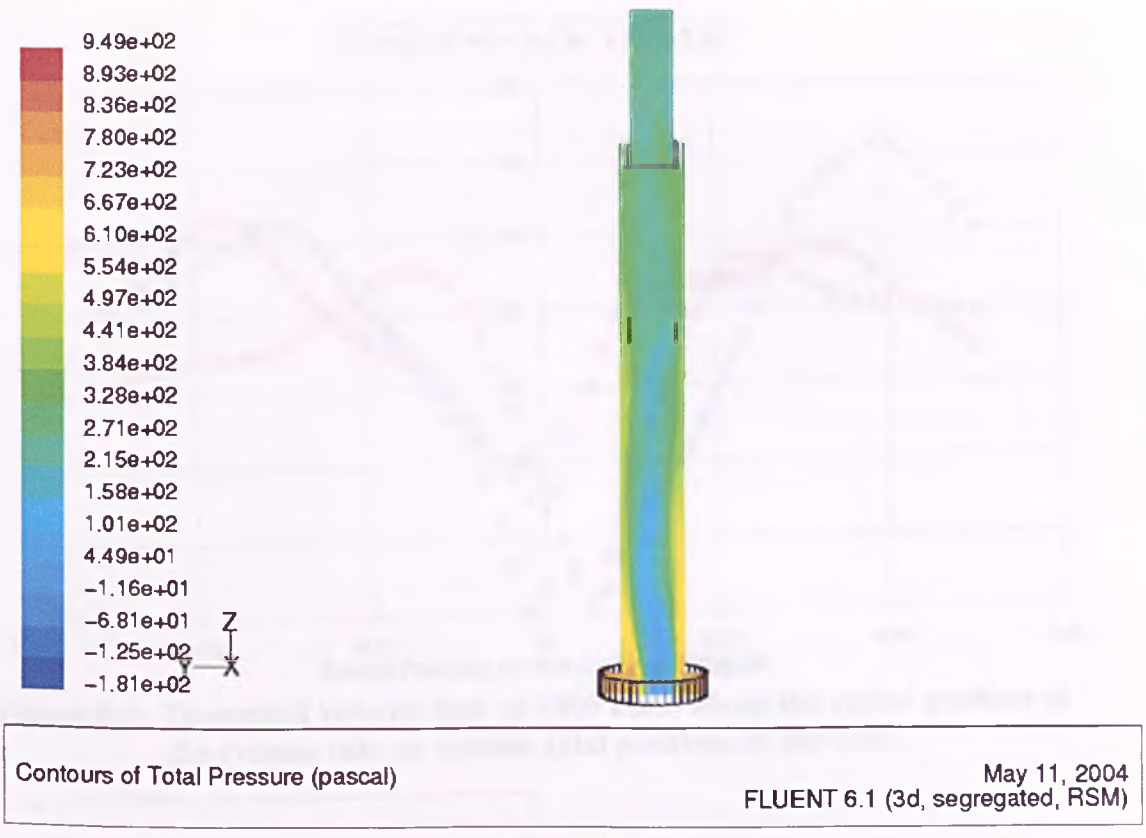

(c)

Figure 8.5: Contour of total pressure profile on the middle plane along the z-direction of the geometry at an inlet air flowrate of (a) 600 l/min, (b) 1000 l/min and (c) 1400 l/min.

This is also justified by the tangential velocity plot along the cyclone tube at 1400 l/min. From Figure 8.6 it can be seen that as the flow progresses along the cyclone tube, the tangential velocity decreases (i.e. the swirl is decaying). The tangential velocity plot is not symmetrical (especially near the inlet slots, e.g. z = 100 mm) compared to other literature work (See Figure 8.7 showing the symmetrical tangential velocity profile for the Axiflow™ cyclone, Figure 8.8) because there are four vane slots being used as the liquid outlet. It becomes more symmetrical as the flow moves up the cyclone tube. Due to wall friction, the tangential velocity exhibits a drop close to the cyclone wall. However, in order to validate these finding, the velocity profiles in the cyclone need to be measured (for example using laser Doppler anemometry). This is outside the scope of this project.

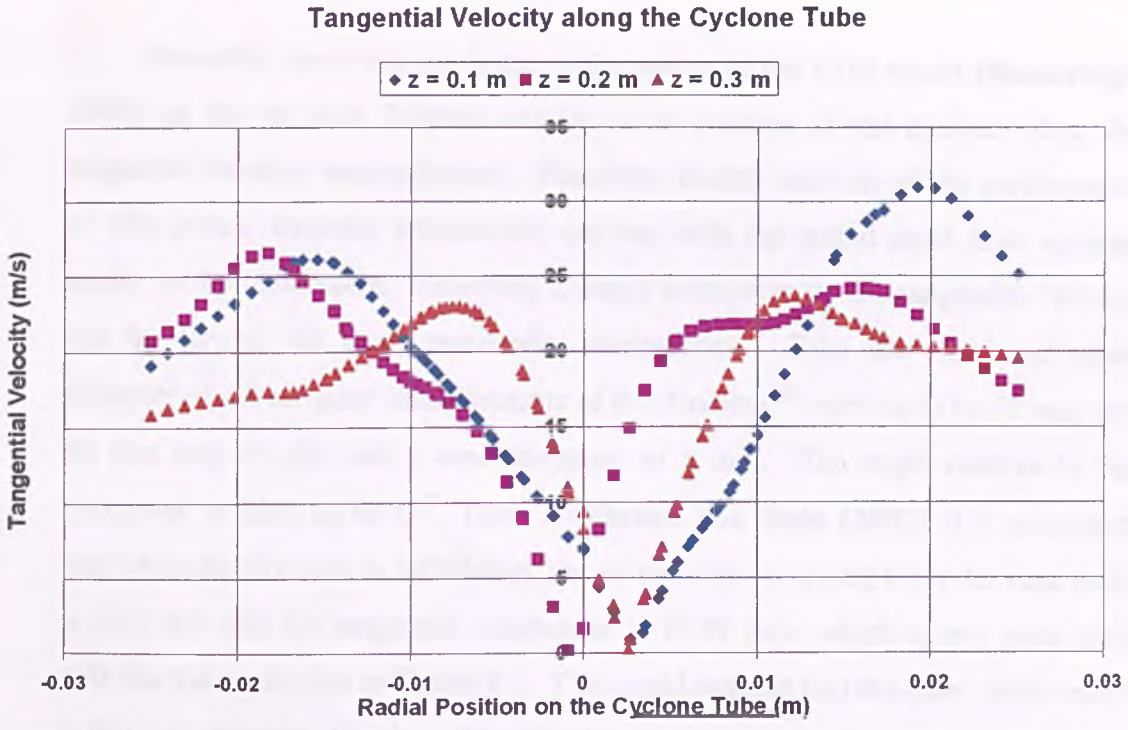

Figure 8.6: Tangential velocity plot at 1400 l/min along the radial position of the cyclone tube at various axial positions of the tube.

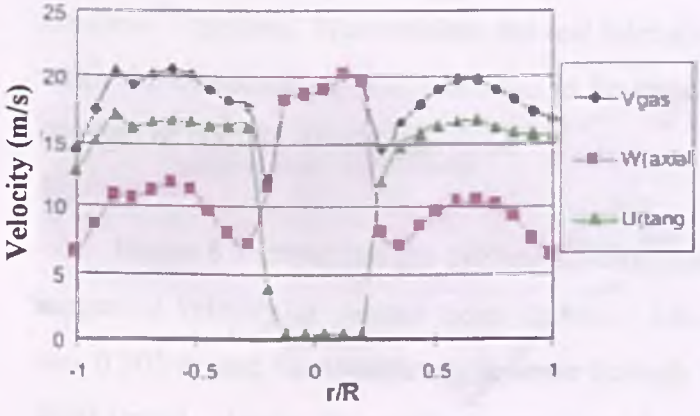

Figure 8.7: Velocity profile in Axiflow™ Cyclone from CDS Engineering (Stanbridge, 2004).

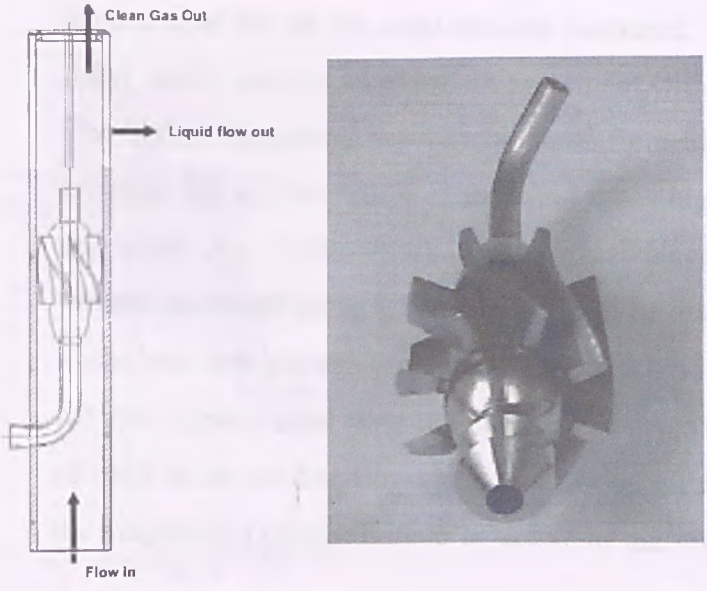

Figure 8.8: (Left) Schematic of the internal arrangement and (right) photograph of swirl element used in Axiflow™ cyclone.

However, there was no further information in the CDS report **(Stanbridge, 2004)** on the air inlet flowrate and the axial position of the cyclone when the tangential velocity was measured. Therefore, further analysis of the performance of this 2-inch diameter commercial cyclone with the tested axial flow cyclone could not be undertaken. However, a rough estimation of the tangential velocity can be carried out using reasonable assumptions. Take the outer and inner diameter of a 8-element vane assembly of the Axiflow^{TM} cyclone to be 52 mm and 30 mm respectively and a vane thickness of 1 mm. The angle relative to the horizontal is taken to be 45^0. From **Hoffmann and Stein (2002)**, it is calculated that when the flowrate is 1400 l/min, the air velocity emerging from the vane pack is 26.6 m/s and the tangential component is 18.81 m/s, which agrees quite well with the values shown in Figure 8.7. This could suggest that the inlet vanes tested in this project were of high quality since the tangential velocity taken further down the cyclone tube (z = 0.1 m) was higher than the velocity obtained using the Axiflow^{TM} cyclone. Nevertheless, the real inlet air flowrate and the geometry used when the measurement was taken has to be known in order to fully evaluate the strength of both the swirling devices.

Figure 8.9 shows the gas cyclone investigated by **Slack *et al.* (2000)** and the tangential velocity at various axial stations. The cyclone diameter investigated was 0.205 m and the volumetric flowrate through the cyclone was 0.08 m^3/s (i.e. 4800 l/min). Again, the results showed that the tangential velocity profiles were symmetrical for all the axial stations measured. This study also showed that the RSM model showed an excellent agreement with the experimental measurements. The highest tangential velocity obtained from Slack's studies was about 38 m/s, however the air flowrate was about 3.4 times higher than the air flowrate used in this study (i.e. 1400 l/min). The highest tangential velocity measured in this project, predicted using CFD was found to be about 25 m/s, which was about 1.5 times less than the value obtained from Slack's investigation. This suggests that the investigated axial flow cyclone has the potential to produce a similar strength of swirl as the reverse flow cyclone at higher air flowrates. The draw back is that the tangential velocity is seen to decay in the tested axial flow cyclone whereas

this effect is not prominent in Slack's work. Nevertheless, the axial flow cyclone would be a more popular choice when a multicyclone arrangement is required, as has been discussed in Chapter 2.

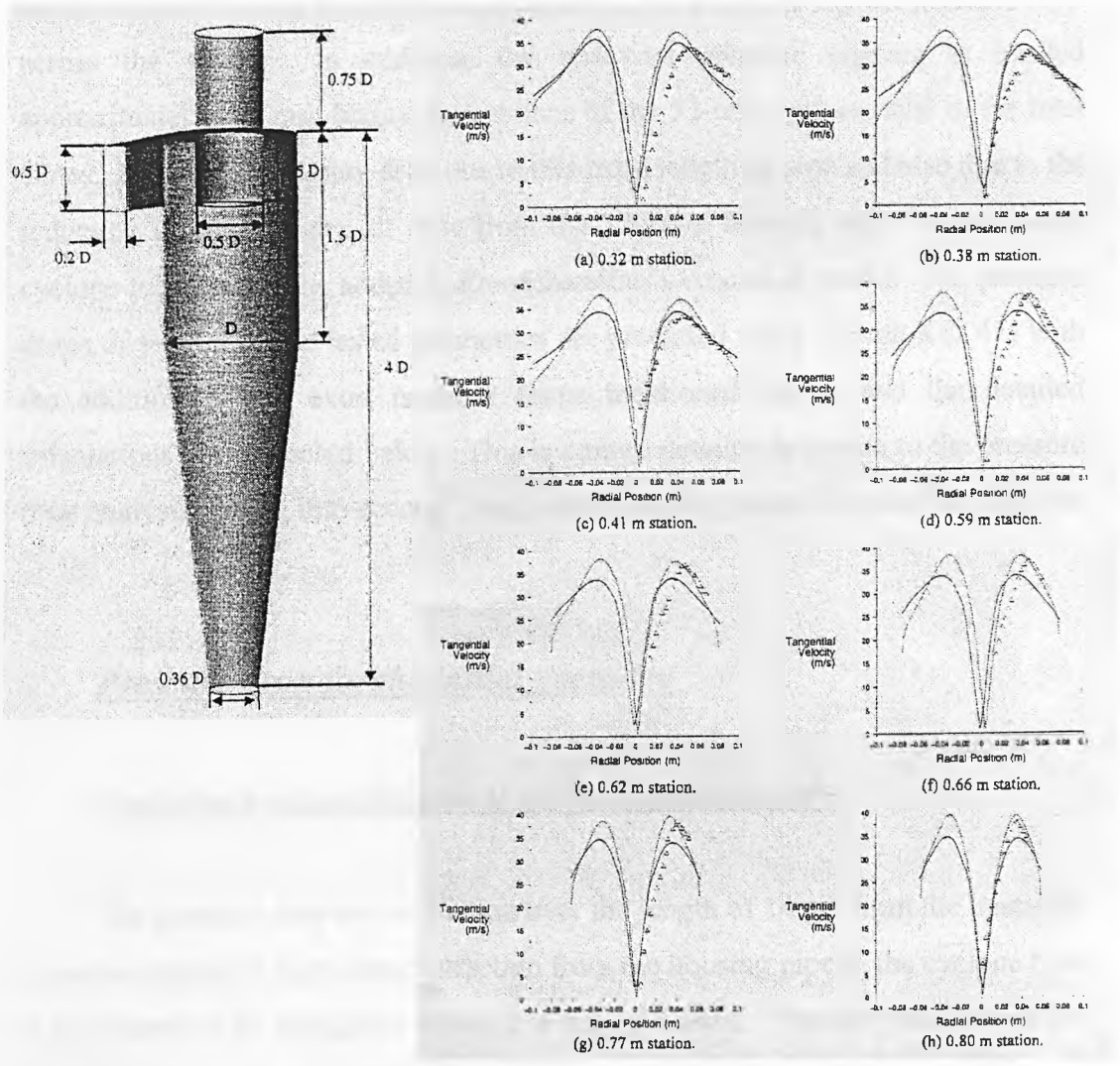

Figure 8.9: (Left) Cyclone investigated by Slack *et al.* (Right) Comparison between tangential velocities at various stations as predicted by RSM model and the experimental data (Δ Experimental data, — RSM model).

8.7.2 Comparison of CFD results with the analytical model of Ramachandran

Ramachandran *et al.* (1991) put forward an empirical model to predict the pressure drop of a rotary flow cyclone. From Figure 2.28, it is clearly seen that the empirical model does not include the pressure drop due to the swirl inside the vortex finder. The important feature in this model is the pitch of the vane and the

model emphasises the pressure loss due to the vanes. Therefore, extra terms for the pressure drop across the vortex finder and the liquid escape slots have to be added to Equation (2.41) to predict the pressure drop for the Sheffield design in order to determine the reliability of Equation (2.41) in predicting the pressure drop across the vanes. In addition, the upstream pressure tapping is located approximately 140 mm before the entrance of the 52-mm cyclone tube or the inlet vanes. Hence, the pressure drop due to this extra length of pipe and also due to the reduction of area for the air flow from the 100-mm housing pipe to the 52-mm cyclone tube have to be added to Ramachandran's empirical model. The pressure drops of several of the tested geometries are predicted using Equation (2.41) with the addition of the extra pressure drops mentioned earlier and the detailed calculations are presented below. This is a more detailed approach to the pressure drop analysis, taking into account every part of the cyclone, compared to Equation (5.3).

- ***Pressure drop for the initial geometry***

  - ***Predicting pressure drop due to abrupt contraction, ΔP_S***

The pressure drop due to friction over the length of 14 cm from the upstream pressure tapping (PT_S) to the contraction from the housing pipe to the cyclone tube is considered to be negligible, hence it is not calculated. The loss coefficients for sudden contraction are given in Figure 8.10.

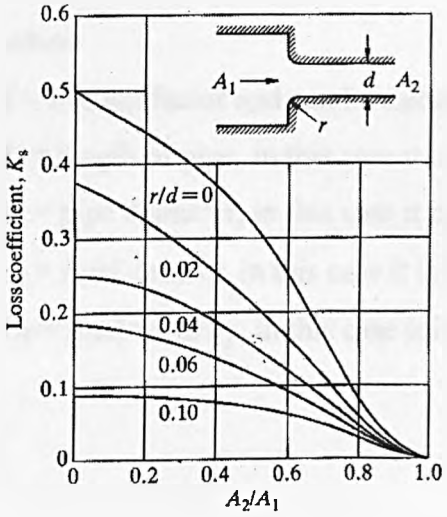

Figure 8.10: Abrupt contraction loss coefficient (based on velocity in A_2) (Miller, 1990).

A_1 is the cross sectional area of the housing pipe (A_H) and A_2 is the cross sectional area of the cyclone tube (A_{CT}). For r/d = 0 and A_2/A_1 = 0.002124/0.008107 = 0.26, the loss coefficient, K_S is 0.42. The pressure drop due to the sudden contraction is expressed as Equation (8.6).

$$\Delta P_S = K_S \frac{\rho_f U_f^2}{2} \qquad \textbf{- Equation (8.6)}$$

where

ρ_f = fluid density, in this case it is the air density = 1.2 kg/m^3

U_f = fluid velocity, in this case it is the air velocity, U_g

Take for example, Q_g = 600 l/min = 0.01 m^3/s.

$U_g = Q_g/A_{CT}$

where $A_{CT} = \pi(D_{CT})^2/4 = \pi(0.052)^2/4 = 0.002124$ m^2

And U_g = 0.01/0.002124 = 4.71 m/s.

Substituting K_S, U_g and ρ into Equation (8.6),

$\Delta P_S = 0.42*0.5*1.2*4.71^2 = 5.59$ Pa.

- ***Predicting pressure drop due to friction loss at the entrance length, $\Delta P_{entrance}$***

The pressure loss over a length of pipe can be estimated using Equation (8.7) below:

$$\Delta P_{entrance} = f \frac{L}{D} \frac{\rho_f U_f^2}{2} \qquad \textbf{- Equation (8.7)}$$

where

f = friction factor and can be calculated using Equation (2.39)

L = length of pipe, in this case it is the length of entrance length = 0.175 m.

D = pipe diameter, in this case it is D_{CT} = 0.052 m

ρ_f = fluid density, in this case it is the air density = 1.2 kg/m^3

U_f = fluid velocity, in this case it is the air velocity in the cyclone tube, U_g

Taking Q_g = 600 l/min,

The Reynolds number will equal to 1.2*4.71*0.052/1.8 x 10^{-5} = 16328 and the friction factor works out to be 0.02715.

Therefore,

$\Delta P_{entrance} = 0.02715*(0.175/0.052)*(1.2*4.71^2/2) = 1.22$ Pa

- ***Predicting pressure drop due to the centre body swirler, ΔP_{CB}***

Equations (2.34) to (2.41) are used to predict the pressure drop across the centre body swirl vane.

Take for example, Q_g = 600 l/min = 0.01 m^3/s.

$U_g = Q_g/A_{CT}$

where $A_{CT} = \pi(D_{CT})^2/4 = \pi(0.052)^2/4 = 0.002124$ m^2

Therefore,

$U_g = 0.01/0.002124 = 4.71$ m/s

From Equation (2.35), U_{avg} can be calculated as follows:

$$U_{avg} = U_g \frac{4\pi}{3R^2 P_t}\left[\left(\frac{P_t^2}{4\pi^2}+R^2\right)^{\frac{3}{2}} - \left(\frac{P_t^2}{4\pi^2}\right)^{\frac{3}{2}}\right]$$

where $P_t = L_V = 0.045$ m and $R = D_{CT}/2 = 0.026$ m

$U_{avg} = 12.48$ m/s

From Equation (2.37) and (2.38), L_{hel} and D_h are obtained as follows:

$$L_{hel} = U_{avg}\left(\frac{H}{U_g}\right)$$

where H = L_V + Length of collection zone = 0.045 + 0.053 = 0.098 m.

$L_{hel} = 0.260$ m

$$D_h = \frac{2\pi R}{\pi+2} = 0.0318 \text{ m}$$

Equation (2.39) calculates the friction factor, f, as shown below:

$$\sqrt{\frac{1}{f}} = -1.8\log_{10}\left[\frac{6.9}{Re_g} + \left(\frac{\varepsilon/D_{CT}}{3.7}\right)^{1.11}\right]$$

where

Air density, ρ_g = 1.2 kg/m^3 and air viscosity, μ_g = 1.8 x 10^{-5} Ns/m^2, Absolute roughness for PVC pipe, ε = 1.5 x 10^{-6} m and

$$Re_g = \frac{\rho_g U_{avg} D_h}{\mu} = 1.2*12.48*0.0318/1.8 \times 10^{-5} = 26458$$

Therefore, f = 0.02408

From Equation (2.41), ΔP across the centre body swirl vanes is as follows:

$$\Delta P_{CB} = \frac{\rho_g U_g^2}{2}\left[\left(\frac{U_{avg}}{U_g}\right)^2\left(1+\frac{L_{hel}}{D_h}f\right)-1\right] = 98.54 \text{ Pa}$$

- ***Predicting the slots pressure drop, ΔP_{slot}***

The slots on the cyclone tube are analogous to an orifice plate with the outlet pipe removed (See Figure 8.11). With the outlet pipe removed from the orifice, the loss coefficient, K_o based on the minimum geometrical area is 2.8 for the orifice **(Miller, 1990)**.

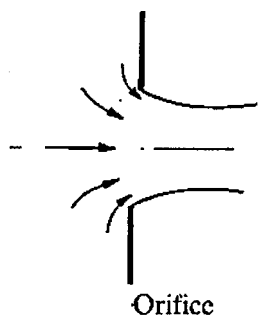

Figure 8.11: Orifice contraction with no outlet pipe.

The pressure drop through the slots can be estimated using Equation (8.8).

$$\Delta P_{slot} = K_o \frac{\rho_f U_f^2}{2} \qquad \textbf{- Equation (8.8)}$$

where

ρ_f = fluid density, in this case it is the air density = 1.2 kg/m^3

U_f = fluid velocity, in this case it is the slot velocity, U_{slot}

For Q_g = 600 l/min with the flow split = 20% for Geometry 1 and assuming that the flow out from the four slots is equally distributed, Q_{slot} = 0.8*0.01/4 = 0.002 m^3/s the velocity in each slot is estimated to be U_{slot} = 0.002/(0.005*0.111) = 3.60 m/s. Therefore,

$$\Delta P_{slot} = 2.8*0.5*1.2*3.60^2$$
$$= 21.77 \text{ Pa}$$

- ***Predicting the pressure drop due to presence of vortex finder, ΔP_{VF}***

Fluid enters the vortex finder (re-entrant inlet) from the end of the cyclone and the side and the flow contracts to half the pipe area. Figure 8.12 gives the loss coefficient for re-entrant inlets, based on the pipe mean velocity. The additional losses as the flow develops in about the first 30 pipe diameters add about 0.1 to the loss coefficient **(Miller, 1990)**.

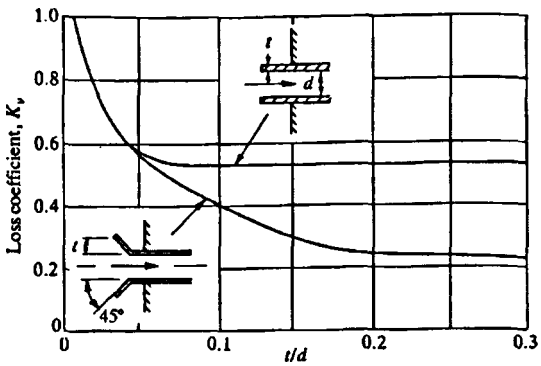

Figure 8.12: Loss coefficients for re-entrant intakes (Miller, 1990).

From Figure 8.12, t and d for the vortex finder are 3.63 mm and 26.14 mm respectively for the initial geometry. The loss coefficient, K_v is 0.52 which corresponds to t/d = 0.139. The pressure drop due to presence of vortex finder can be estimated using Equation (8.9).

$$\Delta P_{VF} = K_{\upsilon} \frac{\rho_f U_f^2}{2} \qquad \textbf{- Equation (8.9)}$$

where

ρ_f = fluid density, in this case it is the air density = 1.2 kg/m^3

U_f = fluid velocity, in this case it is the mean velocity in the vortex finder, U_{VF}

When Q_g = 600 l/min U_C can be estimated as follows:

Since the flow split is 20%, the mean velocity in the cyclone tube is estimated as $0.2*Q_g/A_{VF} = 0.2*0.01/0.000537 = 3.72$ m/s. Therefore,

$\Delta P_{VF} = (0.52+0.1)*0.5*1.2*3.72\text{^}2 = 5.15$ Pa.

Adding up all the pressure drops gives the predicted pressure drop expressed in Equation (8.10).

$$\Delta P_{predicted} = \Delta P_S + \Delta P_{entrance} + \Delta P_{CB} + \Delta P_{slot} + \Delta P_{VF} \qquad \textbf{- Equation (8.10)}$$

Figure 8.13 shows the comparison between the measured experimental pressure drops, the pressure drops with additional terms added to Ramachandran's model for the initial geometry and Geometry 3b and the CFD pressure drop prediction for the initial geometry. It is clearly shown that both the analytical predictions agree very well with the measured data, with a discrepancy of less than 10%, but the CFD prediction has not been able to predict the pressure drop precisely due to the inferior turbulence model used, which has been discussed above. This confirms that the Ramachandran's model for predicting the pressure drop across the swirl vanes with the additional pressure drop terms could be used to predict the pressure drop for cyclone using centre body swirl vanes accurately. It is suggested that it will be more representative to use the distance of the vane from cyclone wall to the centre body rather than the longitudinal length of the vane **(Hoffmann, 2005)**, but in this case, both the values do not differ much, so it will not change the pressure drop calculated significantly.

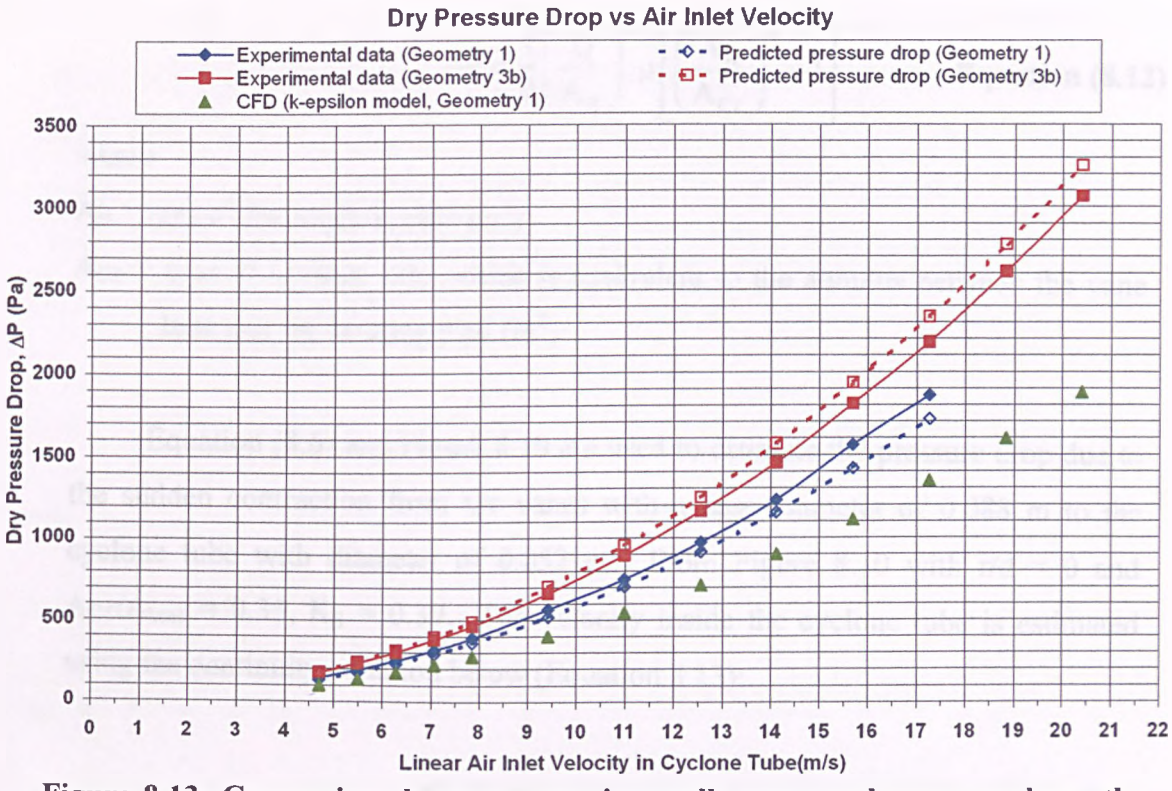

Figure 8.13: Comparison between experimentally measured pressure drop, the numerical prediction and the analytical prediction using Ramachandran's model to predict the pressure drop across the centre body vanes.

- ***Pressure drop for geometries with the tangentially oriented inlet swirl vanes***

It is of interest to determine whether Ramachandran's model is suitable to predict the pressure drop across the tangentially oriented inlet swirl vanes. The method of predicting the pressure drop for these geometries is similar to the one used for the centre body swirl vanes with some simplifications and with an extra term of pressure drop that is due to the area reduction from the housing pipe to the annulus between the base of the vanes and the housing pipe. This pressure drop is calculated based on Bernoulli's theory as follow (Equation 8.11):

$$Q = A_H \sqrt{\frac{2\Delta P}{\rho[(A_H / A_{CT})^2 - 1]}} \qquad \textbf{- Equation (8.11)}$$

Rearranging Equation (8.11) gives the pressure drop expressed as Equation (8.12).

$$\Delta P = \frac{1}{2}\left(\frac{Q}{A_H}\right)^2 \rho \left[\left(\frac{A_H}{A_{CT}}\right)^2 - 1\right] \qquad \textbf{- Equation (8.12)}$$

where

A_H = area of the housing pipe (m^2)

A_{CT} = area of cyclone tube which is equivalent to the annulus between the vane base and the housing pipe (m^2)

Equation (8.6) and Figure 8.10 are used to estimate the pressure drop due to the sudden contraction from the vanes with a base diameter of 0.088 m to the cyclone tube with diameter of 0.052 m. From Figure 8.10 with r/d = 0 and A_{CT}/A_{base} = 0.35, K_S = 0.39. The velocity inside the cyclone tube is estimated using the continuity equation below (Equation 8.13):

$$U_{CT} = U_{vane}(A_{vane}/A_{CT}) \qquad \textbf{- Equation (8.13)}$$

where

$U_{vane} = (Q/n_v A_{vane})$ and n_v is the number of vanes.

A_{vane} = height of vane x minimum distance from one vane to another

= 0.0177 x 0.003 = 0.0000531 m^2

There are 40 vanes altogether, but some of the geometries used two or four of these vanes as additional drainage.

The pressure drop induced by the inlet swirl vanes is estimated using Equation (2.35) to (2.41) with H = height of vane = 0.0177 m, D_{base} = 0.088 m and U_{avg} is taken as the tangential velocity after leaving the vanes ($U_{vane}/\cos 60^0$).

The pressure drop due to friction in the entrance length is calculated using Equation (8.7). It is assumed that the slots are positioned at the end of the tube for the ease of calculation. Therefore the length of the entrance length is the length of the tube minus the length of the slots. When there is an additional drainage route, the area of the vanes used will be accounted for by making the liquid escape slots longer so that the total area for the liquid outlets is unchanged.

The pressure drop across the liquid slots and the vortex finder are accounted for using Equation (8.8) and (8.9). Figure 8.14 illustrates the measured pressure drop, CFD pressure drop prediction of Geometry 7a using RSM model and the predicted pressure drop for Geometry 5a, 6a and 7a with discrepancies of less than 10%. Figure 8.14 indicates that Equation (2.41) predicts the pressure drop across the tangential inlet vanes reasonably well too.

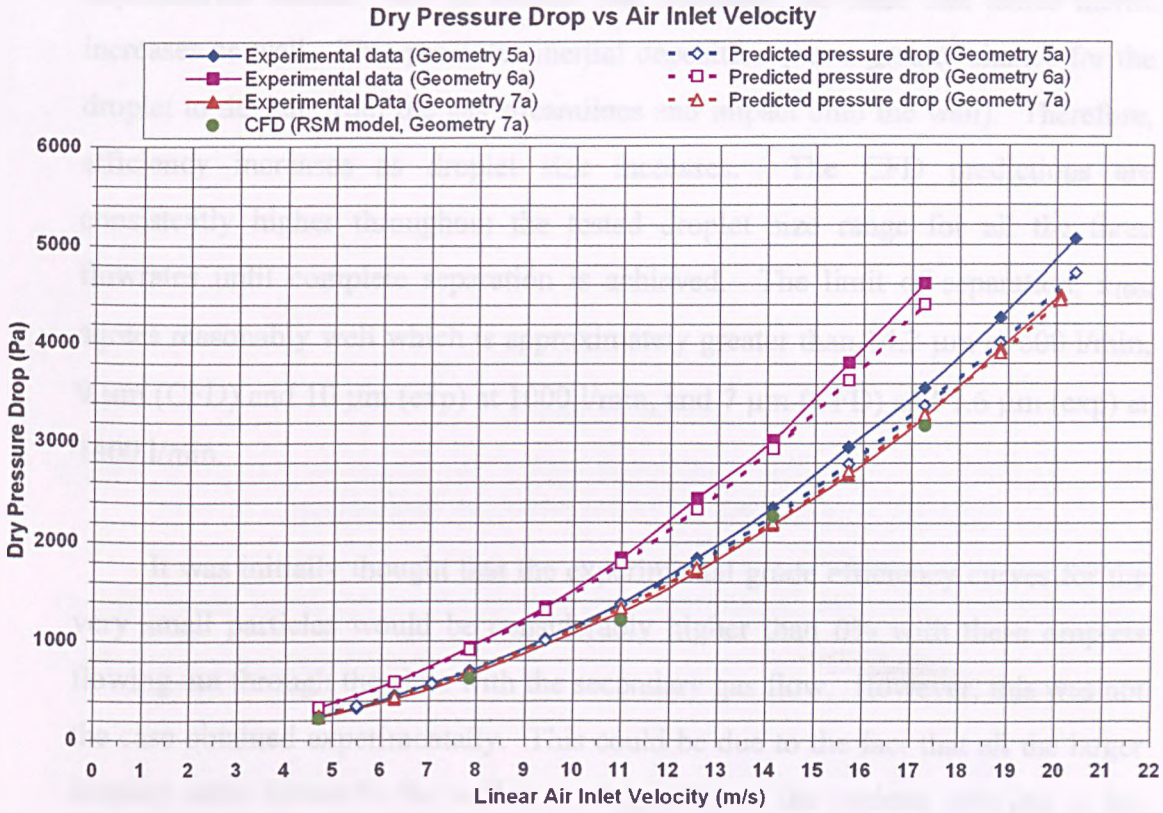

Figure 8.14: Comparison between experimentally measured pressure drop, the numerical prediction and the analytical model using Ramachandran's model for predicting the pressure drop across the tangentially oriented inlet swirl vanes.

8.7.3 Droplet Separation

The droplets were only considered to be separated when they passed through the slots or the vanes outlet. Droplets that hit the wall were to have a coefficient of restitution of 0, meaning that the droplets are deposited. These droplets will then follow the gas flow until they either reach the slots or the vortex finder. Droplets

that flowed into the vortex finder are considered escaped with the gas. For an inlet air flowrate at 600, 1000 and 1400 l/min, the separation efficiency as a function of the droplet size was obtained and plotted in Figure 8.15.

It can be seen in Figure 8.15 that the quantitative prediction of the separation efficiency is rather poor, but qualitatively the CFD prediction is very similar to the experimental results. As the droplet size increases, its mass and hence inertia increases as well. This promotes inertial deposition (i.e. a greater chance for the droplet to deviate from the gas streamlines and impact onto the wall). Therefore, efficiency increases as droplet size increases. The CFD predictions are consistently higher throughout the tested droplet size range for all the three flowrates until complete separation is achieved. The limit of separation, x_{100}, agrees reasonably well which is approximately greater than 14.2 μm at 600 l/min, 9 μm (CFD) and 10 μm (exp) at 1000 l/min, and 7 μm (CFD) and 7.6 μm (exp) at 1400 l/min.

It was initially thought that the experimental grade efficiency curves for the very small particles would be considerably higher than 0% with these droplets flowing out through the slots with the secondary gas flow. However, this was not the case obtained experimentally. This could be due to the fact that all the larger droplets were thrown to the wall in the beginning of the cyclone tube due to the strong vortex flow and were broken up into small droplets (i.e. satellite droplets). When these satellite droplets traveled up the cyclone tube, the swirl decayed hence these droplets just went up straight into the vortex finder giving higher count on the small droplets compared to the inlet giving negative efficiency. Therefore, the tails of all the grade efficiency curves were removed from the grade efficiency plot below and it was the large drop sizes that were of interest since cyclone was not very good in separating droplets less than 1 micron.

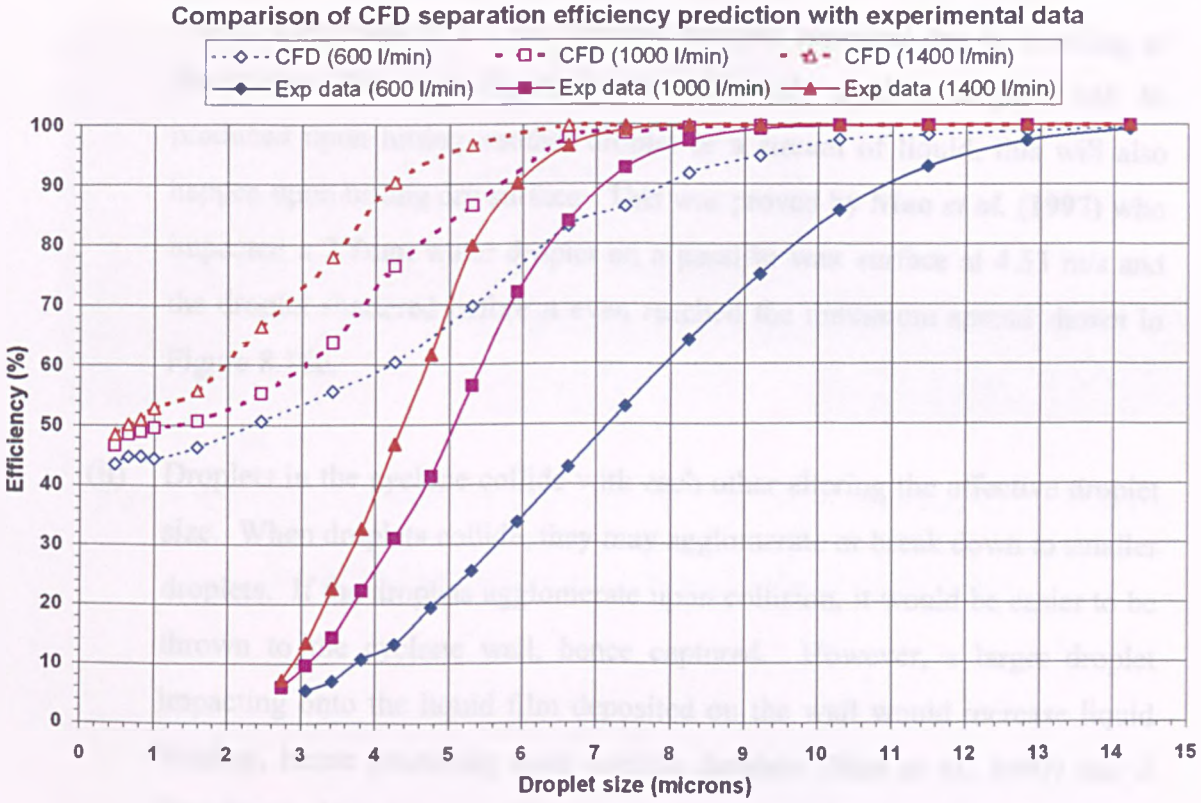

Figure 8.15: Comparison of CFD separation efficiency prediction with experimental data (the tail of all the curves is omitted).

The discrepancies of the prediction and the experimental data may be due to the following reasons/assumptions:

(i) The liquid droplets tend to stick on the cyclone wall and subsequently forming a small stream of liquid. There is a tendency that some small droplets might be stripped off from the liquid stream and then escape with the clean gas through the vortex finder. If the velocity of the liquid film is known then the gas velocity above which will result in ripples on the film surface and eventually leading to formation of smaller droplets can be calculated using the equations in Section 2.7.1. With the highest tangential velocity of 9 m/s at 600 l/min to 25 m/s at 1400 l/min obtained from CFD, it is very likely that small droplets were stripped off from the liquid film because from the work of **Fujimoto *et al.* (2001)** it was found that a droplet impacted with a hemispherical static droplet on a solid at an impact velocity of only 2.1 m/s, the liquid was deformed like a crown on the solid (See

Figure 8.16a) and at 3.1 m/s satellite droplets appeared due to breaking of the crown, shown in Figure 8.16b. Not only satellite droplets will be produced upon hitting another droplet or a stream of liquid, this will also happen upon hitting dry surface. This was proved by **Mao *et al.* (1997)** who impacted a 2.7mm water droplet on a paraffin wax surface at 4.53 m/s and the droplet shattered before it even reached the maximum spread shown in Figure 8.16c.

(ii) Droplets in the cyclone collide with each other altering the effective droplet size. When droplets collide, they may agglomerate or break down to smaller droplets. If the droplets agglomerate upon collision, it would be easier to be thrown to the cyclone wall, hence captured. However, a larger droplet impacting onto the liquid film deposited on the wall would increase liquid breakup, hence producing more satellite droplets **(Mao *et al.*, 1997)** and if they break down into smaller droplets upon collision they have a higher tendency of escaping through the vortex finder. These features (droplets agglomeration and breakage) were absent in the model.

(iii) The fluid dynamics in CFD might not correctly portray what is happening in experiments. To obtain accurate prediction of the efficiency, the process (i.e. the flow) immediately after the swirl vanes has to be modeled very accurately. This can be achieved by greater precision in the modeling of each of the slots of the swirl vanes, which is outside the scope of this project.

(iv) The stochastic spread is not modified (i.e. reduced) in the vicinity of the wall, resulting higher collection efficiency for the small droplets and this has been experience by a lot of researchers **(Hoffmann, 2005)**.

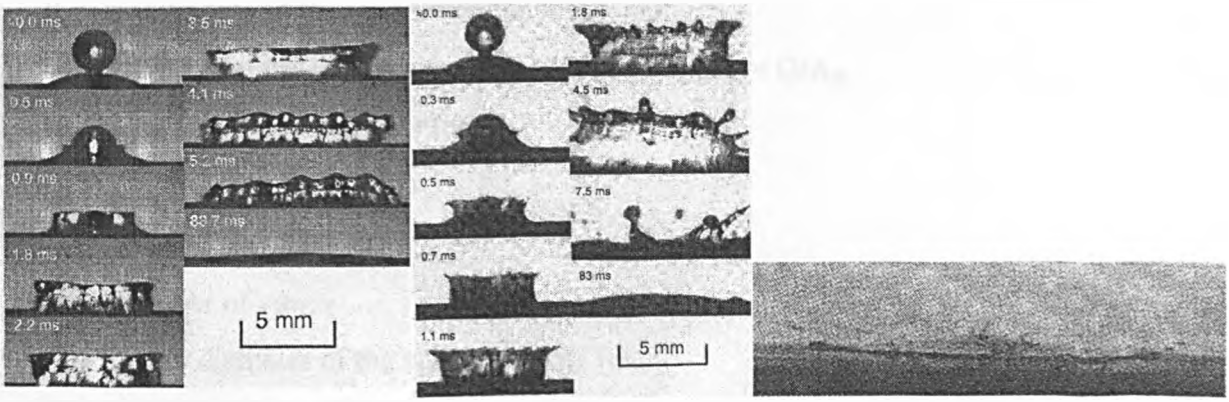

(a) (b) (c)

Figure 8.16: (a) Collision of two droplets for an impact velocity of 2.1 m/s, (b) and 3.1 m/s, (c) Impaction of a 2.7-mm water droplet on a paraffin wax surface at an impact velocity of 4.53 m/s.

8.7.4 Comparison with other work

- ***Comparison of experimental cut sizes with model predictions***

Most of the cyclone models are tailored for the tangential inlet reverse flow cyclones. It is thought that it would be useful to find out whether such cyclone models can predict the performance of the tested axial flow cyclone by calculating an 'equivalent inlet velocity' in the axial flow cyclone and applying it to the cyclone models. From **Peng and Hoffmann (2004)** and **Hoffmann and Stein (2002)**, it was derived that the swirl velocity close to the wall of the axial flow cyclone, $U_{tan,w}$ was (See Equation 8.14):

$$U_{tan,w} = \frac{1}{R_w^n} \cdot \frac{3-n}{3} \cdot U_{tan} \cdot \frac{R_w^3 - R_o^3}{(R_w^{3-n} - R_o^{3-n})} \qquad \textbf{- Equation (8.14)}$$

where

R_w = inner radius of the cyclone wall (m)

R_o = outer radius of the vortex finder (m)

n = calculated using Equation (2.30)

$U_{tan} = U_{th} \cos \beta$

β = exit angle of the vanes with the horizontal

U_{th} = velocity of the jets emerging from the vane pack = Q/A_{th}

Q = volumetric gas flowrate (m^3/s)

$$A_{th} = N_v\left(\frac{\pi D_{mid}}{N_v} - \frac{t}{\sin\beta}\right)\left(\frac{D_{ov} - D_{iv}}{2}\right)\sin\beta$$

N_v = number of vanes

D_{ov} = outer diameter of the vane assembly (m)

D_{iv} = inner diameter of the vane assembly (m)

D_{mid} = geometric mean diameter of the vane = $(D_{ov}\,D_{iv})^{1/2}$

The wall velocity can be taken as a rough estimate of the 'equivalent inlet velocity' to use in the models for reverse flow cyclone and the inlet dimensions are given by the 'inlet velocity' and gas flowrate with the inlet height/inlet width ≈ 2 **(Peng and Hoffmann, 2004)**. This ratio is equivalent to the ratio of the Stairmand high throughput cyclone. Therefore, considering Geometry 7a (the only geometry tested for grade efficiency) with a gas flowrate of 600 l/min with R_w = 0.026 m, R_o = 0.0211 m and U_{tan} as calculated in Section 8.7.2 (referred to as the resultant velocity after leaving the vanes, U_{avg}), $U_{tan,w}$ = 10.03 m/s. The procedure to find the inlet dimensions of the reverse flow cyclone at this velocity is shown below (Equations 8.15, 8.16 and 8.17):

$$Q = U_{tan,w}A \qquad \textbf{- Equation (8.15)}$$

$$A = a \times b \text{ and } a = 2b \qquad \textbf{- Equation (8.16)}$$

Therefore,

$$b = \text{sqrt}\,(A/2) \qquad \textbf{- Equation (8. 17)}$$

This gives 'a' a value of 0.0446 m and 'b' a value of 0.0223 m. For a standard Stairmand high throughput cyclone, the dimensions of various parts of the cyclone are listed in Table 8.9.

Cyclone Part	Dimension (m)
Cyclone diameter, D_C	0.0595
Vortex finder diameter, D_{VF}	0.0446
Inlet height, a	0.0446
Inlet width, b	0.0223
Vortex finder length, L_{VF}	0.0521
Height of cylindrical section, h	0.0893
Height of cyclone, H	0.2380
Underflow diameter, D_{DE}	0.0223

Table 8.9: Dimensions of a reverse flow cyclone that gives an 'equivalent inlet velocity' as the tested axial flow cyclone (Geometry 7a).

The predictions based on Leith-Licht theory (Equation 2.53 to 2.57) and Stenhouse and Trow (Equation 2.62) theoretical model are compared with the experimental results in Figure 8.17. The latter model is actually a model for axial flow cyclones with coaxial discharge.

The Stenhouse and Trow model underpredicts the separation performance of the axial flow cyclone. This might be due to the different type of liquid discharge used for both experiments. Stenhouse's cyclone has a coaxial discharge, which is more prone to re-entrainment at high loadings (See Section 2.6.4). Hence, for the same 'equivalent inlet velocity', the coaxial discharge cyclone will give a higher value of cut size. On the other hand, the Leith-Licht model overpredicts the separation performance. It can be said that models for reverse flow cyclones might not be suitable for predicting the performance of axial flow cyclones. This might be due to the different type of vortex flow in the two types of cyclone. The reverse flow cyclone has an outer and an inner vortex while the axial flow cyclone has only one vortex system. From Figure 8.17, it also suggested that with the same 'inlet velocity' the reverse flow cyclone gives a better performance compared to the axial flow cyclone.

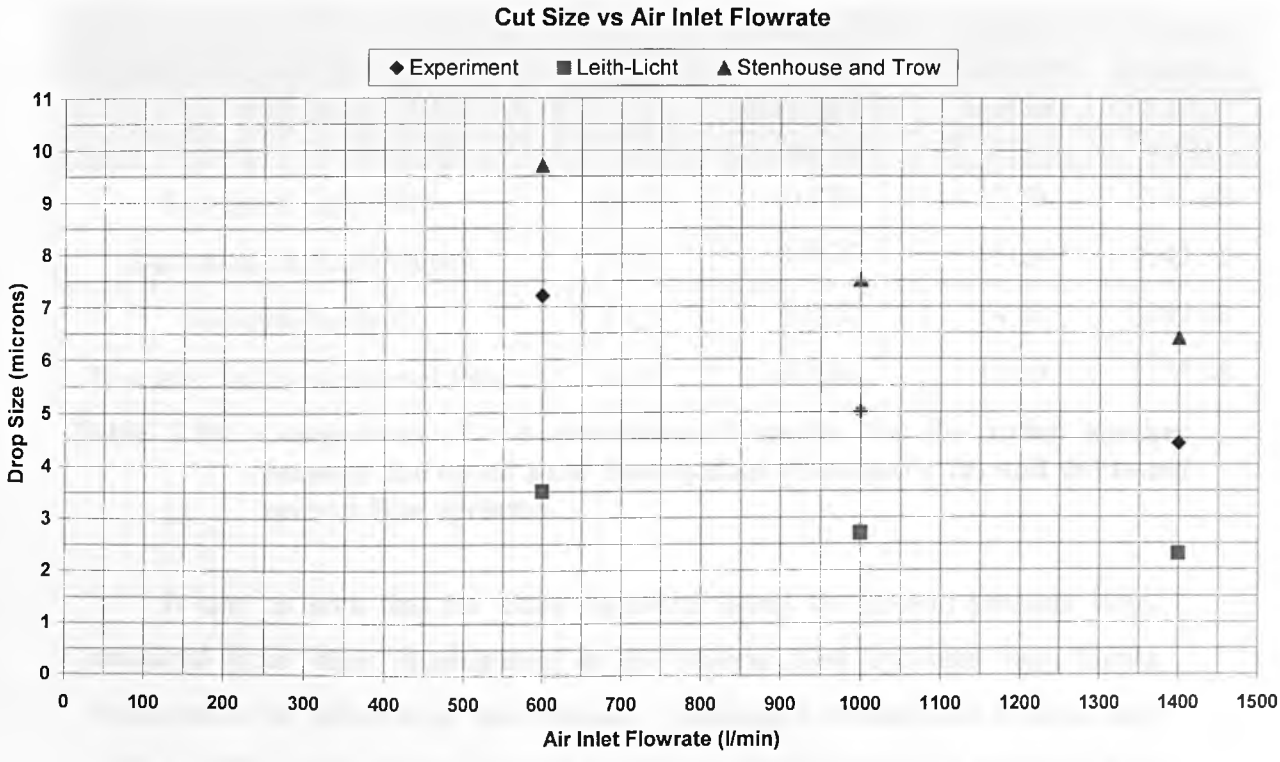

Figure 8.17: Comparison of the experimental results for the cut size with model predictions.

However, this better performance comes with an expense of the pressure drop. Table 8.10 shows the Euler number (Eu) obtained experimentally for reverse flow cyclones investigated by other researchers based on the inlet velocity **(Phillips *et al.*, 1992)** and they are compared with the experimental results obtained using Geometry 7a. The inlet velocity is taken to be the inlet flowrate divided by the inlet cross-sectional area (i.e. the tangential inlet for the reverse flow cyclone). For the tested axial flow cyclone, the inlet area is taken to be the vane inlet (i.e. $36 \times 0.003 \times 0.177 = 1.9116 \times 10^{-3}$ m^2) and the inlet velocity is the inlet flowrate divided by the inlet area.

Tested Cyclone[3] (using air as test gas)	Euler Number (Eu)	Volumetric Gas Flowrate (m^3/s)	Inlet Velocity (m/s)	Dry Pressure Drop (Pa)
Stairmand High Flow	19.71	0.176	15.24	2746.68
Stairmand High Efficiency	30.45	0.0637	15.24	4243.35
Muschelknautz D	18.3	0.102	14.44	2289.48
Geometry 7a (Experimental Data)	14.59	0.030	15.69	2175.08

Table 8.10: Comparison of the experimental results for the Euler number between the tested axial flow cyclone (Geometry 7a) and the tested reverse flow cyclones.

It can be seen that the Euler numbers, hence the system pressure drop, measured from other investigators on the reverse flow cyclones were higher compared to the tested axial flow cyclone. Although a reverse flow cyclone may give a better performance, there is a price to pay in terms of pressure drop generated. The diameter of the reverse flow cyclone, which gives an 'equivalent inlet velocity' as Geometry 7a is bigger. This means if these cyclones were to be nested into a vessel, more axial flow cyclones can be fitted compared to the conventional cyclones hence providing a higher handling capacity. Moreover, there is a greater tendency to get flow maldistribution with tangential inlet.

8.7.5 Comparison with Commercial Cyclones

Every effort has been made to contact companies manufacturing uniflow cyclones in order to compare the performance of the Sheffield design to theirs. However, due to commercial sensitivity it has not proved possible to get a great deal of detail from these companies on their products. Hence an extensive comparison could not be carried out. The available information on the pressure drop and separation efficiency is shown in Table 4.1 and 4.3 respectively. The pressure drop of 'Centrisep' cyclone is very high because the cyclone diameter is

[3] The cyclone dimensions can be found in Appendix L.

only 13 mm, which is 4 times smaller than the tested axial flow cyclone. Two 'Centrisep' cyclones in series separate 12.4 μm particle at 200 l/min. This can be achieved using Geometry 7a at a flowrate higher than 600 l/min with a much lower pressure drop. The 2-inch diameter Spiralflow™ cyclone separates 8 μm droplet at 1520 l/min with a pressure drop of 800 Pa whereas the Sheffield design separates 7.5 μm droplet at 1400 l/min with a pressure drop of 1290 Pa. The separation performance of the Sheffield design is better, but at the expense of pressure drop.

From all the analyses carried out above, the results are suggesting that the Sheffield axial flow cyclone is generally better compared to the equivalent reverse flow cyclone and also among the best of the available commercial cyclones, either in terms of separation efficiency or in terms of the system pressure drop. If more information could be obtained, then it will be more useful to compare the performance of cyclones of different designs and sizes using a Stk-Eu plot as explained in **Hoffmann and Stein (2002)**.

8.8 Conclusion

This chapter aimed to investigate the feasibility of modelling the pressure drop - flowrate characteristics and the grade efficiency of the tested axial flow cyclone, focusing on Geometry 7a because it was the most successful design produced. The initial geometry was also investigated in the very early stage of this project in order to get to learn the software and the techniques involved better.

Initial modelling was undertaken using CFD. The geometry set up and details of the grid generation for both geometries were documented, paying attention to the mesh qualities (i.e. equiangle skew and y^+ value). The mathematical models used were also elaborated, followed by the settings of the material properties, operating and boundary conditions.

The results of the pressure drop predicted using the k-ε model for the initial geometry had a discrepancy of approximately 28%, agreeing with the other researchers that this model was not suitable to accurately predict swirling flows. The flow split calculated was 27% as opposed to 20% obtained from experiments. However, this model took considerably less time to solve compared to the RSM model. Therefore, it could be useful when an accurate prediction is not required.

The pressure drop – flowrate characteristic of Geometry 7a predicted using the RSM model agrees well with the experimental data with a discrepancy of only 4%. The flow split obtained from CFD was 52% compared with about 56% in experiments. The contour plot of the total pressure shows that the pressure is higher near the wall and lower in the core of the cyclone tube. However, the pressure gradient in the radial direction diminishes as the air travels up the cyclone tube indicating decay in the swirl, especially after the first set of slots. This could be the reason for liquid being re-entrained into the vortex finder. Due to the reduced strength, the liquid that swirled past the first set of slots could not be all thrown to the wall and escaped through the second set of slots.

The droplets' predicted trajectories did not agree very well with the experimental results quantitatively. However, qualitatively they showed a similar trend as the experimental results, i.e. efficiency increases as the drop size increases and as the air flowrate increases. The limit of separation for both the prediction and the experimental results were very similar. The discrepancy might be due to the breakage of larger droplets into very fine droplets or production of small satellite droplets from impacting onto the liquid film, hence not being collected in experiments. However all these breakage features were not available in the model. Therefore, the model has over predicted the cyclone's collection efficiency. Another reason could be due to the inaccurate flow field prediction in the cyclone tube because to get an accurate prediction of efficiency, it depends very much upon the flow immediately following the swirl vanes and this could be having to carry out very detailed modeling of each of the slots of the swirl vanes.

The RSM model has accurately predicted the flow split and the pressure drop characteristics of Geometry 7a. However, extensive work can still be carried out to improve the model in predicting the efficiency. Due to the complexity of the turbulence model and the cyclone geometry, it would take up a lot of time in order to solve all the equations involved. Therefore, a lot of computational power will be required. Future work can be carried out on improving the mesh quality in order to reduce the computational time. It is recommended to incorporate models for droplet coalescence, droplet breakage and behaviour of liquid film deposited onto the cyclone wall in order to improve the prediction of the droplets' trajectories.

In the latter part the work on pressure drop analysis, an analytical model (Ramachandran's model) was compared with the pressure drop obtained experimentally. Due to the fact that this model only predicts the pressure drop across the swirling vanes, extra pressure drop terms were added to this model to replicate experimental conditions and the details can be found in Section 8.7.2. This more detailed calculation on the pressure drop takes into account the friction loss along the cyclone tube and all the contractions that exist in the experimental design. From the result of the analysis, it can be seen that Ramachandran's model, with all the extra pressure drop terms, was able to predict the system pressure drop well.

Work was carried out to find out whether cyclone model developed for the conventional cyclone could be used to predict the performance of the tested axial flow cyclone by calculating an 'equivalent inlet velocity'. The cut size predictions used to compare with the experimental findings were based on Leith – Licht theory (for conventional cyclones), and the Stenhouse and Trow model (for uniflow cyclone with coaxial discharge). The results showed that Stenhouse and Trow approach under predicted the cyclone performance and the Leith – Licht model over predicted it. Even though the equivalent conventional cyclone was predicted to perform better than the axial flow cyclone, it was at an expense of the pressure drop, which was not desirable. Efforts were also made to compare the

performance of the tested axial flow cyclone with other commercially available axial flow cyclones. However, extensive analysis could not be carried out due to lack of information from the manufacturers.

The next chapter will cover the methodologies used to integrate individual cyclone tubes into a large separating vessel as well as cyclone optimisation.

Chapter 9

Integration of Individual Tubes into a Separating Vessel and Cyclone Optimisation

One of the important parts of a separation processes is integrating an individual piece of equipment into a large separating vessel: for this case an individual cyclone tube into a multicyclone arrangement. Hence, the tube layout, the number of tubes required and the size of the vessel have to be determined. The cyclone tubes for the purpose of this project are to be operated in parallel inside a separating vessel. It is desired to fit as many tubes as possible inside a vessel so that as high a throughput as possible can be handled. A high flow split is essential if a higher throughput is required so that the load on the secondary mesh is reduced, decreasing the tendency for flooding of this mesh. The methodology used to determine a suitable flow split for a system is described below.

9.1 Determining a suitable flow split

This work describes the methodology used to define a suitable flow split (Q_{VF}/Q_{in}) to enable the demisting system (Figure 4.1) to work effectively over a range of velocities. Frequently used variables are listed in Table 4.2. Some of the introduction to flow split has been discussed in Chapter 4, Section 4.2.2 and it will be used as a reference in this chapter. Equation (4.1) shows the relationship between the flow split, mesh area ratio and the primary to secondary velocity ratio.

The mesh area ratio of A_{PM}/A_{SM} depends on cyclone geometry (i.e. diameter of cyclone tube and vortex finder) and the tube layout in the demisting vessel, which determines the number of tubes to be fitted inside the vessel. If N_t is the number of tubes fitted inside a separating vessel, then the area occupied by the

vortex finders, $N_t \cdot A_{VF}$ and the secondary mesh area, A_{SM} can be calculated using Equation (9.1) and (9.2) respectively.

Total area occupied by vortex finders = N_t x Area of one vortex finder

$$= N_t \times \frac{\pi (d_{o,VF})^2}{4} \quad \textbf{- Equation (9.1)}$$

$$\text{Secondary mesh area, } A_{SM} = \text{Primary mesh area, } A_{PM} - \frac{N_t \cdot \pi (d_{o,VF})^2}{4} \quad \textbf{- Equation (9.2)}$$

$$= \frac{\pi \cdot D_V^2}{4} - \frac{N_t \cdot \pi (d_{o,VF})^2}{4}$$

where

$d_{o,VF}$ = outer diameter of vortex finder (m)

D_V = vessel diameter, which is the diameter of the primary mesh as well (m)

The variation of V_{SM}/V_{PM} with flow split for various area ratios (A_{PM}/A_{SM}) is shown in Figure 9.1 below and it can be seen that to achieve a certain velocity ratio, the flow split required increases as the area ratio increases.

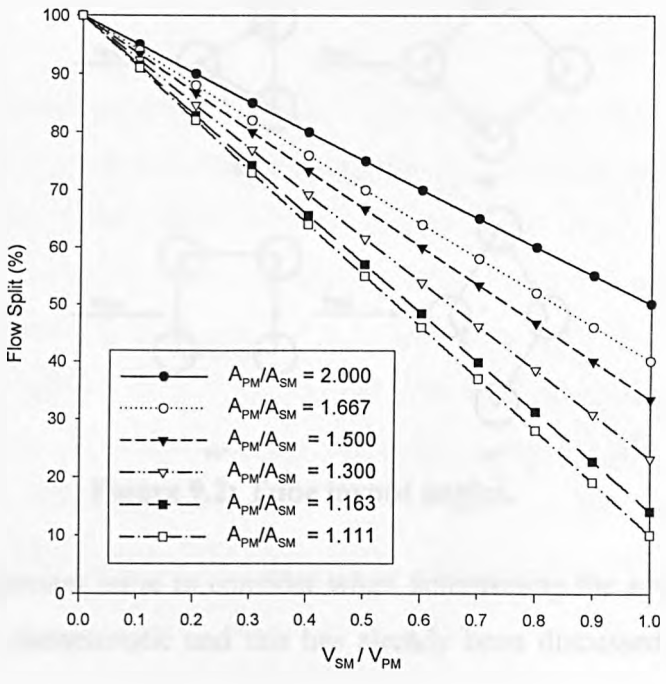

Figure 9.1: A plot showing the relation between mesh velocity ratio and cyclone flow split at different area ratio.

The number of tubes depends upon the vessel diameter and the layout chosen (Figure 9.2). This is analogous to previous work on heat exchangers **(Kakaç and Hongtan, 2002)**, where Equation (9.3) is used to determine the number of tubes required for a system. The equation takes into account incomplete coverage of the vessel area by the tubes resulting from tube pitch separation and edge effects.

$$\text{Number of tubes, } N_t = 0.7854\left(\frac{CTP}{CL}\right)\frac{D_V^2}{(PR)^2 d_o^2} \qquad \textbf{- Equation (9.3)}$$

where

CTP = tube count calculation constant, which depends on the number of tube passes in the heat exchanger (0.93 for one tube pass)

CL = tube layout constant (1.0 for 90^0 and 45^0 layout, 0.87 for 30^0 and 60^0 layout)

D_V = diameter of separating vessel (m)

PR = tube pitch ratio (P_t/d_o),

P_t = tube pitch, distance from one tube to another measured centre to centre (m)

d_o = tube outer diameter (m)

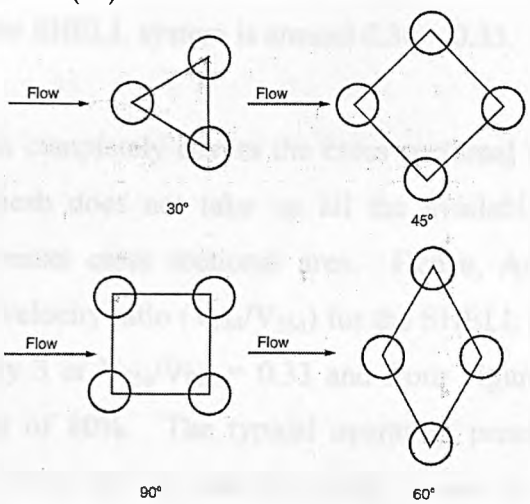

Figure 9.2: Tube layout angles.

Another important issue to consider when determining the appropriate flow split is the mesh characteristic and this has already been discussed in Chapter 2 and Chapter 4.

The next section looks into the typical values used in determining the cyclone arrangement inside the commercial separators and these values were used as a reference in determining the cyclone arrangement for this project.

9.1.1 Typical separators with cyclones used by SHELL

The typical gas-liquid separators incorporating cyclones used by SHELL are equipped with square boxes each with 4 cyclones due to manufacturing requirements, where the net free area per box is approximately 50% **(Hans Nooijen, 2003)**. Net free area (NFA) is generally defined as the ratio of the cross-sectional area available for fluid flow to the entire cross-sectional area which in this case means the cross sectional area of the cyclone tubes, $N_t \cdot A_{CT}$ ('N_t' is the total number of cyclone tubes), to the area of the square box. Since it is not possible to entirely fill a round vessel with square boxes, some of the cross sectional area will be lost. The typical value of the effective NFA (in this case the ratio of $N_t \cdot A_{CT}$ to A_V) for SHELL system is around 0.30 – 0.35.

The primary mesh completely covers the cross sectional area of the vessel, while the secondary mesh does not take up all the available space, typically covering 60% of the vessel cross sectional area. Hence, $A_{SM}/A_{PM} = 0.60$ or $A_{PM}/A_{SM} = 1.667$. The velocity ratio (V_{PM}/V_{SM}) for the SHELL design is aimed at a value of approximately 3 or $V_{SM}/V_{PM} = 0.33$ and from Figure 9.2 or Equation (9.1) gives a flow split of 80%. The typical operating pressure for a subsea separator ranges from 70 to 130 bar and the mesh is said to be in its normal operating range when the gas load factor, k is < 0.1 m/s (corresponds to the 'k' value given by KnitMesh Limited for operation at high pressure, which gives a 'k' value of 0.085).

9.1.2 Sheffield cyclone design

It was desired to find an appropriate flow split for our cyclone design such that it will operate at the same velocity ratio as the SHELL design (i.e. V_{PM}/V_{SM} = 3). At the moment, all the experiments were carried out only at atmospheric conditions with an air-water system.

Assuming that the space available for the secondary mesh is filled up entirely, the secondary mesh area, A_{SM} will depend on the number of cyclone tubes and hence the number of vortex finders fitted in the vessel. It will also depend on the diameter of the vortex finder. The more cyclone tubes that are fitted in the vessel, the smaller the area available for the secondary mesh. Hence, the higher the flow split required to give V_{PM}/V_{SM} =3. The higher the flow split, the higher the system pressure drop, which is undesirable, as discussed previously in Chapter 4. On the other hand, with a higher flow split, the system throughput will increase (i.e. more flow can pass through the system before reaching the flooding velocity of the secondary mesh). In this case, a compromise should be achieved. Therefore, it has been decided to work on the basis that the maximum velocity allowed to flow through the secondary mesh is 80% of U_{cr} as discussed earlier and to achieve V_{PM}/V_{SM} =3, the highest velocity flowing through the primary mesh will be $(3x0.8xU_{cr}) = 2.4U_{cr}$. Depending on the area ratio of the secondary and primary mesh, the flow split that is required to enable the demisting system to work on this basis can then be identified.

9.1.3 Determining the area available for secondary mesh (A_{SM})

An equilateral triangular pitch arrangement was chosen for the cyclone tubes as this arrangement results in the greatest tube density for a specific vessel diameter. Equation (9.3) was then used to calculate the amount of tubes contained within a certain vessel diameter. The number of tubes will effectively determine the area of the secondary mesh, while the inner and outer diameter of the vortex

finder is fixed at 0.03454 m and 0.042 m respectively. This dimension was chosen because it is the largest commercially available tube that can be fitted into a 2-inch cyclone tube (inner diameter = 0.052 m and outer diameter = 0.060 m). Having fixed the cyclone tube, vortex finder, and vane diameter and the gap for gas-liquid intake (s, shown in Figure 9.3), the only variable that could determine the number of tubes is the distance from one set of vanes to another, f. At the moment, only one cyclone tube is being tested; with the cyclone tube and inlet swirl vanes being enclosed inside a housing tube of 0.1016 m inner diameter. The tangentially oriented swirl vanes at the cyclone tube inlet are used to replace the original centre body swirler system due to flooding at low inlet velocities. It should be noted that due to a manufacturing constraint the shortest distance between 2 vanes, w (See Figure 9.3) was limited to 3 mm. The details of the design of the inlet swirl vanes can be found in Chapter 4. The vane base was 0.088 m and this gives a 's' value of (0.1016-0.088)/2 = 0.0068.

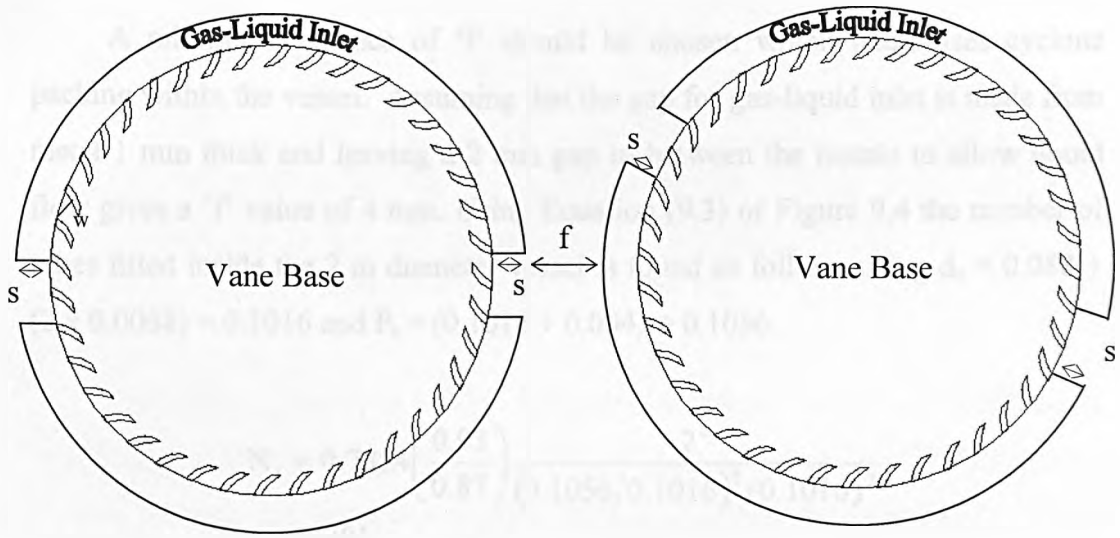

Figure 9.3: Top view of swirling vanes with the gap for gas-liquid intake.

Equation 9.3 was used to calculate the number of tubes in the vessel, and in our case, CL = 0.87 (60^0 layout), $d_o = d_{vane} + 2s$ and $P_t = d_o + f$. All the variables in the equation are defined except 'f'. Assuming that the vessel diameter is 2 m, Figure 9.4 is plotted from Equation (9.3) and determines the number of cyclone tubes in the vessel by varying 'f'.

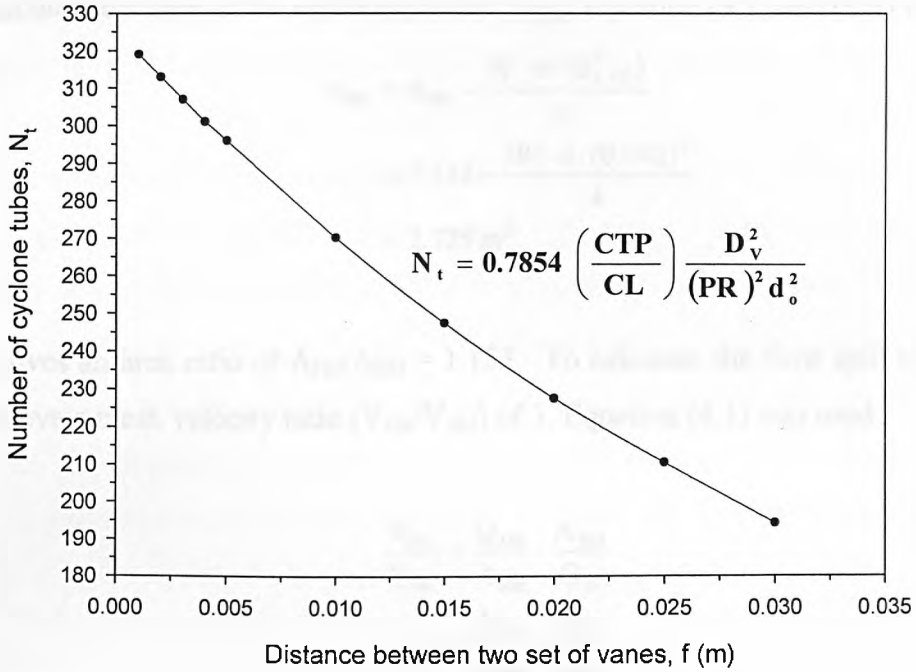

Figure 9.4: Variation of the number of cyclone tubes to be fitted inside a 2 m diameter vessel by varying 'f'.

A minimum distance of 'f' should be chosen which maximises cyclone packing within the vessel. Assuming that the gap for gas-liquid inlet is made from metal 1 mm thick and leaving a 2 mm gap in between the metals to allow liquid flow gives a 'f' value of 4 mm. Using Equation (9.3) or Figure 9.4 the number of tubes fitted inside the 2 m diameter vessel is found as follows using $d_o = 0.088 + (2 \times 0.0068) = 0.1016$ and $P_t = (0.1016 + 0.004) = 0.1056$.

$$N_t = 0.7854\left(\frac{0.93}{0.87}\right)\frac{2^2}{(0.1056/0.1016)^2(0.1016)^2}$$
$$= 301$$

The area of primary mesh, A_{PM}, which is equivalent to the vessel area, A_V, is calculated as follows:

$$A_{PM} = \frac{\pi \cdot D_v^2}{4}$$
$$= \frac{\pi(2)^2}{4}$$
$$= 3.142\,m^2$$

To calculate the area of the secondary mesh, A_{SM}, Equation (9.1) and (9.2) were used.

$$A_{SM} = A_{PM} - \frac{N_t \cdot \pi \cdot (d_{o,VF}^2)}{4}$$
$$= 3.142 - \frac{301 \cdot \pi \cdot (0.042)^2}{4}$$
$$= 2.725\,m^2$$

This gives an area ratio of $A_{PM}/A_{SM} = 1.153$. To calculate the flow split required to achieve a mesh velocity ratio (V_{PM}/V_{SM}) of 3, Equation (4.1) was used.

$$\frac{V_{SM}}{V_{PM}} = \frac{Q_{DS}}{A_{SM}} \cdot \frac{A_{PM}}{Q_{in}}$$
$$= \frac{A_{PM}}{A_{SM}} \cdot \frac{Q_{DS}}{Q_{in}}$$
$$= \frac{A_{PM}}{A_{SM}}(1 - FS)$$

$$\frac{Q_{DS}}{Q_{in}} = \frac{V_{SM}}{V_{PM}} \cdot \frac{A_{SM}}{A_{PM}}$$
$$= \frac{1}{3 \times 1.153}$$
$$= 0.289$$
$$\text{Flow Split, } FS = 1 - 0.289$$
$$= 0.711$$

Therefore, a flow split of 71% is required to enable the demisting system to work adequately with a velocity ratio (V_{PM}/V_{SM}) =3 and the maximum velocity passing through the secondary mesh is 80% of the flooding velocity, U_f, which depends on the operating condition.

9.2 Estimating system pressure drop

A knowledge of the system pressure characteristic is important to avoid liquid in the collection sump travelling up the drainage pipe and flooding the

vessel. This was already discussed in Chapter 4. The methodology used to calculate the pressure drop for the test system investigated is outlined below.

The pressure drop depends on the flow split and mixture density, and while the liquid density does not change significantly the gas density changes as a function of temperature and pressure. Referring to Figure 4.1, the system pressure drop, ΔP, should be less than $h\rho_l g$ in order for the drainage system to work satisfactorily. A typical operating pressure for a subsea separator ranges from 70-130 bar, and assuming an operating condition of 130 bar and 70^0C for methane and oil, the gas density can be estimated using the ideal gas equation (Equation 9.4). Methane density at atmospheric room temperature is 0.68 kg/m^3.

$$P = \rho RT \qquad \textbf{- Equation (9.4)}$$

$$\rho = 0.68 \cdot \frac{130}{1} \cdot \frac{293}{343}$$
$$= 75.5\,\text{kg/m}^3$$

where

P = operating pressure (kPa)

T = operating temperature (K)

R = gas constant (kPa·m^3/kg·K)

ρ = gas density (kg/m^3)

The methane density for the conditions chosen was calculated to be 75.5 kg/m^3 while the oil density was taken as a constant value of 850 kg/m^3. The system pressure drop was then estimated based on the experiments carried out under atmospheric conditions using Euler number, Eu (See Equation 2.25).

There is no experimental data on a cyclone design giving a dry flow split of 71%, but data is available for a dry flow split of 70% (See Appendix K). From the dry pressure drop data for a 70% flow split cyclone design, the Eu number based on velocity going up the vortex finder was 7.74. Unfortunately, there was no wet pressure drop data available for this design, so the dry pressure drop across the cyclone was used to estimate the pressure drop at 130 bar. It was proposed that the

liquid concentration (principally oil) is of order 1-10x10^4 ppm v/v, which converted to a liquid loading of approximately 0.1 % v/v. It is shown in Figure 9.5 that for the design giving a dry flow split of 56%, the pressure drop with 0.100-0.105% liquid loading is lower than the dry pressure drop and so the vessel height calculated using the dry pressure drop data for the 70% flow split should work satisfactorily when liquid is present as well.

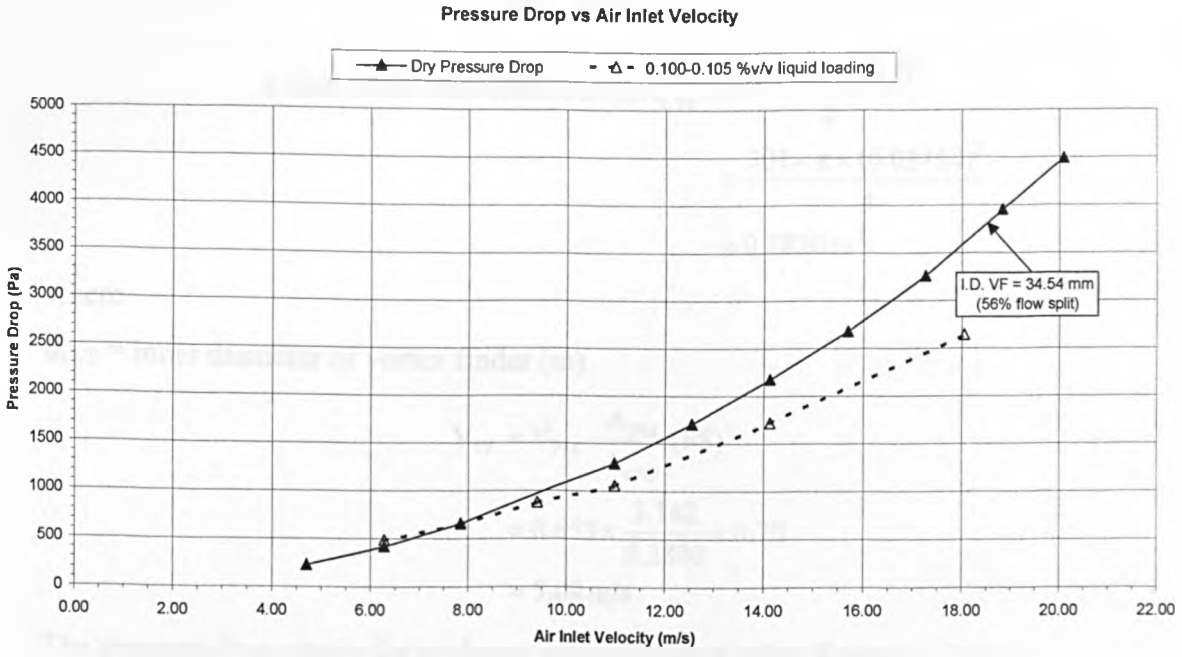

Figure 9.5: Graph showing that the wet pressure drop is lower than the dry pressure drop for a flow split of 56%.

The highest pressure drop occurs when the velocity passing through the secondary mesh is $0.8U_f$ (mesh characteristic section). To calculate the flooding velocity, U_f, Equation (2.15) was used with 'k' = 0.085 m/s and methane and oil density of 75.51 kg/m^3 and 850 kg/m^3 respectively.

$$U_f = 0.085\sqrt{\frac{850 - 75.51}{75.51}}$$
$$= 0.272 \text{ m/s}$$

A flooding velocity, U_f, of 0.272 m/s was calculated, giving the value for the highest velocity going through the secondary mesh as (0.80x0.272) = 0.218 m/s. With a velocity ratio (V_{PM}/V_{SM}) of 3 then the highest velocity going through the

primary mesh is ($2.4xU_f$) = 0.653 m/s. For a 70% flow split, the air velocity inside the vortex finder can be calculated as follows:

$$\frac{V_{VF}}{V_{PM}} = \frac{Q_{VF}}{A_{i,VF}} \cdot \frac{A_{PM}}{Q_{in}}$$

$$= \frac{A_{PM}}{A_{i,VF}} \cdot \frac{Q_{VF}}{Q_{in}}$$

$$\frac{V_{VF}}{V_{PM}} = \frac{A_{PM}}{A_{i,VF}}(FS)$$

$$\text{Vortex finder inner surface area, } A_{i,VF} = \frac{N_t \times \pi \times (d_{i,VF})^2}{4}$$

$$= \frac{301 \times \pi \times (0.03454)^2}{4}$$

$$= 0.2820\ m^2$$

where

$d_{i,VF}$ = inner diameter of vortex finder (m)

$$V_{VF} = V_{PM} \cdot \frac{A_{PM}}{A_{i,VF}}(FS)$$

$$= 0.653 \times \frac{3.142}{0.2820} \times 0.70$$

$$= 5.09\ m/s$$

The pressure drop across the cyclones was calculated using Equation (2.25).

$$\Delta P = Eu \cdot \tfrac{1}{2} \rho_g V_{VF}^2$$

$$\Delta P = 7.74(0.5)(75.51)(5.09)^2$$

$$= 7571\ Pa$$

With V_{PM} = 0.653 m/s, $Q_{PM} = V_{PM} \times A_{PM}$ = 0.653 x 3.142 = 2.052 m^3/s. For a maximum liquid loading of 0.1 % v/v, liquid flowrate, Q_L is determined as follows:

$$\frac{Q_L}{Q_{PM}} \times 100\% = 0.1\%$$

$$\therefore Q_L = \frac{0.1}{100} \times 2.052$$

$$= 0.002052 m^3/s$$

$$= \frac{0.002052 \cdot 3600}{3.142} m^3/m^2hr$$

$$= 2.35 m^3/m^2hr$$

With a liquid loading of 2.35 m^3/m^2 hr (i.e. 0.1% v/v), the pressure drop across the primary mesh (ΔP_{mesh}) is calculated as follows:

Assuming the mesh depth is 10 cm and air (air density = 1.2 kg/m^3) is flowing at 0.7 m/s. Since the liquid loading is very small, the pressure drop is calculated assuming that the air is dry. From Figure 4.3, at gas velocity of 0.7 m/s the dry pressure drop is 6 mm H_2O/m packing and the pressure drop across a 10 cm mesh is about 5.88 Pa. Euler number is calculated below using Equation (2.15):

$$Eu = \frac{5.88}{0.5 \cdot 1.2 \cdot 0.7^2}$$
$$= 20$$

Therefore, the primary mesh pressure drop with methane going through can be determined as follows:

$$\Delta P_{mesh} = 20 \cdot \frac{1}{2} \cdot 75.5 \cdot 0.653^2$$
$$= 322\,Pa$$

When the primary mesh floods, an extra pressure drop due to the head of the liquid in the mesh will occur, which can be calculated as follows:

$$\Delta P = 0.10 \cdot 850 \cdot 9.81$$
$$= 833.85\,Pa$$

Therefore the pressure drop across the primary mesh when it is flooded is (833.85 + 322) = 1155.85 Pa.

As stated previously, in order to have the drainage working properly the system pressure drop (i.e. mesh and cyclone pressure drop) should be less than $h\rho_l g$, allowing the system pressure drop to be not more than (7571 + 1155.85) = 8726.85 Pa. Therefore,

$$h\rho_L g > 8726.85$$
$$h > \frac{8726.85}{850(9.81)}$$
$$h > 1.05\ \text{m}$$

The control volume for the liquid in the sump was taken as the volume collected over 3 minutes **(Hans Nooijen, 2003)**, and the estimated height of liquid collected at the bottom of the vessel was then calculated to be;

Height of collected liquid = Liquid velocity x 3 minutes

Height of collected liquid = (Q_L/A_{PM}) x 3 minutes

$= (0.002052/3.142) \times 180$ s

$= 0.118$ m

The cyclone height is approximately 1 m. The vessel height is approximately (1.05 + 0.118 + 1) = 2.168 m. Therefore, a vessel height of 2.5 m will not induce any drainage problem for methane-oil system operating at 130 bars and 70^0C.

Having done all the calculation to predict the system pressure drop, it can be seen that the pressure drop plays a significant role in determining the height of the vessel rather than the internals of the vessel. Therefore, the pressure drop should be kept to a minimum to keep the vessel height to a minimum because the higher the vessel, the more complications that will be involved in the construction which will evidently increase the capital cost.

9.3 Determining an optimum flow split

This work will look into the impact of mesh area ratio (A_{PM}/A_{SM}) and mesh velocity ratio (V_{PM}/V_{SM}) on the cyclone flow split, which will eventually affect the system pressure drop. It is aimed to determine an optimum flow split, which will be a trade off between system pressure drop, which will in effect determine the vessel height, and the system throughput.

The relation between mesh area ratio, mesh velocity ratio and flow split is expressed in Equation (4.1). The number of tubes that can be fitted into a vessel of certain diameter can be determined using Equation (9.3).

9.3.1 Base Case

The information in this section is from the previous section on the methodology used to define a suitable flow split and to estimate the system pressure drop. This information will be used as the base case in the optimisation exercise, which is discussed in the following sections.

Assuming a vessel diameter of 2 m, for an 'f' value (distance from one set of vanes to another) of 4 mm, the number of tubes that could be fitted into the vessel is 301 and the secondary mesh area is 2.725 m^2. To achieve a mesh velocity ratio (V_{PM}/V_{SM}) of 3, the flow split required is 71 %. The system total pressure drop (i.e. the pressure drop across the primary mesh and the cyclones) for methane-oil system was predicted with the assumption that the operating pressure and temperature are 130 bar and 70^0C. The methane and oil density are 75.5 kg/m^3 and 850 kg/m^3 respectively. The pressure drop was calculated to be 8730 Pa. For this pressure drop, 'h' (distance from surface of the liquid sump to cyclone inlet) needs to be greater than 1.05 m and the total height of vessel is approximately 2.5 m [taken into account the height of cyclones (around 1 m), the height of the liquid sump and also some clearance for the top of the vessel]. At this operating condition, the maximum gas velocity going through the primary mesh is 0.653 m/s, which corresponds to a secondary mesh velocity of 0.218 m/s.

Since there is no information as to which variable is an independent value, all the variables are going to be varied and the impact of the variation on flow split and system pressure drop are analysed and reported in the cases below.

9.3.2 Case 1

Assuming that the vessel diameter and the operating condition remain the same as the base case, the effects of 'f' ('f' will determine the secondary mesh area, hence the mesh area ratio) on flow split and pressure drop are investigated with the mesh velocity ratio (V_{PM}/V_{SM}) fixed at 2, 3, 4 and 5. From Figure 9.6, it is shown that at a fixed mesh velocity ratio (V_{PM}/V_{SM}), the flow split does not change significantly as the distance 'f' is varied. This is because of the slight increase in the secondary mesh area when 'f' is increased. However, the number of cyclone tubes reduces by almost two fold when 'f' increases from 0 to 40 mm (See Figure 9.7). It can also be seen in Figure 9.6 that the rate of increase in flow split reduces as the mesh velocity ratio increases. It is desired to work at a higher flow split so that a higher throughput can be handled. However, this in turn will increase the system pressure drop. From Figure 9.8, it is shown that as the distance 'f' increases, the system total pressure drop increases and the increase is more prominent for higher mesh velocity ratio and this total pressure drop translates into total height of the vessel. From Figure 9.9, it is shown that as velocity ratio increases and as 'f' increases the total vessel height rises significantly. The higher the vessel height, the more complication there will be in manufacture, hence higher capital cost.

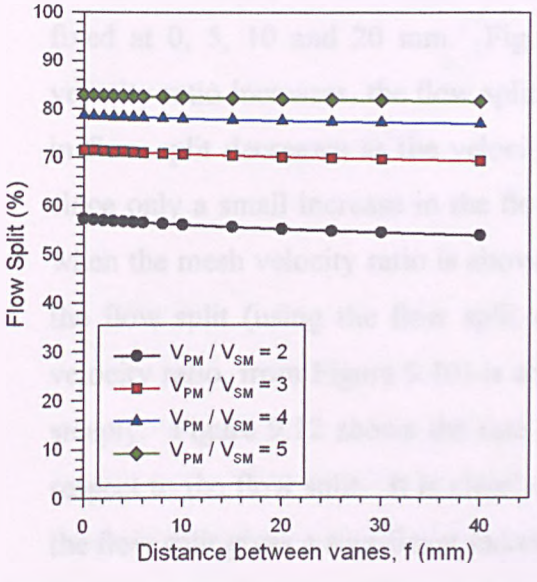

Figure 9.6: Effect of 'f' on flow split at a fixed mesh velocity ratio.

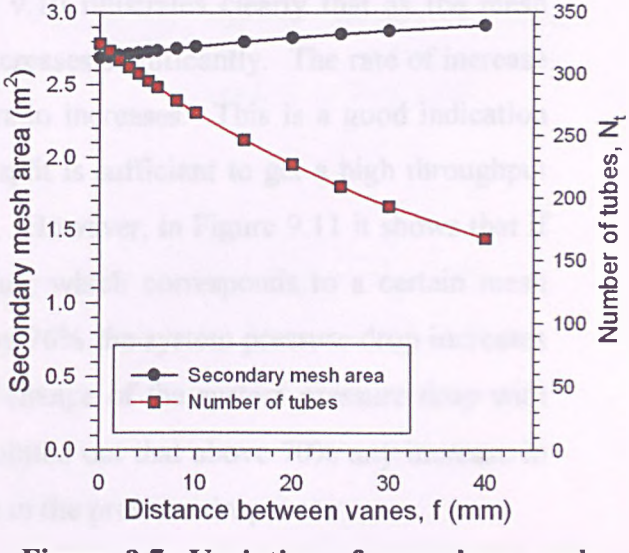

Figure 9.7: Variation of secondary mesh area and number of tubes by varying 'f'.

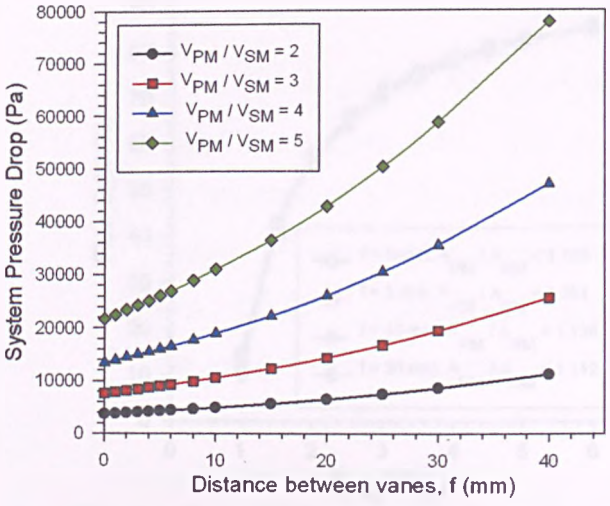

Figure 9.8: Effect of 'f' on system pressure drop at a fixed mesh velocity ratio.

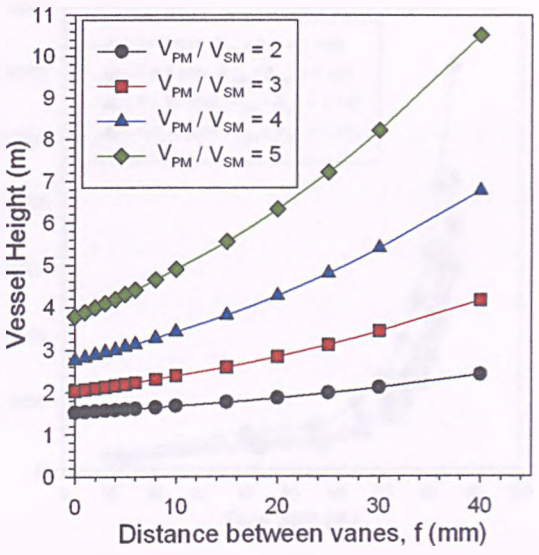

Figure 9.9: Translating Figure 7.8 from system total pressure drop to total vessel height.

9.3.3 Case 2

Assuming that the vessel diameter and the operating condition remain the same as the base case, the effects of mesh velocity ratio (V_{PM}/V_{SM}) on flow split and pressure drop are investigated with the distance between two sets of vanes, f, fixed at 0, 5, 10 and 20 mm. Figure 9.10 illustrates clearly that as the mesh velocity ratio increases, the flow split increases significantly. The rate of increase in flow split decreases as the velocity ratio increases. This is a good indication since only a small increase in the flow split is sufficient to get a high throughput when the mesh velocity ratio is above 3. However, in Figure 9.11 it shows that if the flow split (using the flow split value, which corresponds to a certain mesh velocity ratio, from Figure 9.10) is above 76% the system pressure drop increases steeply. Figure 9.12 shows the rate of change of the system pressure drop with respect to the flow split. It is clearly pointed out that above 70% any increase in the flow split gives a significant increase in the pressure drop.

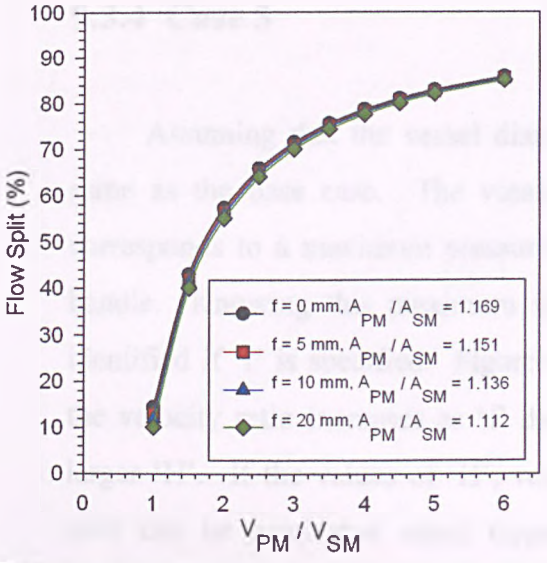

Figure 9.10: Effect of mesh velocity ratio on flow split at a fixed distance between two sets of vanes.

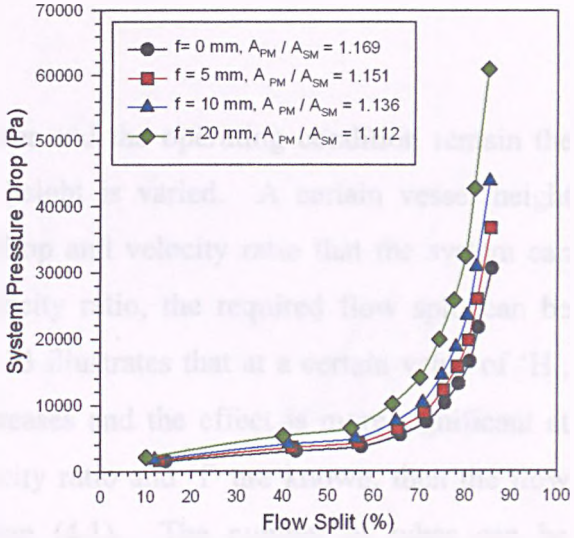

Figure 9.11:Effect of 'f' on system pressure drop corresponding to the mesh velocity ratio in Figure 9.10.

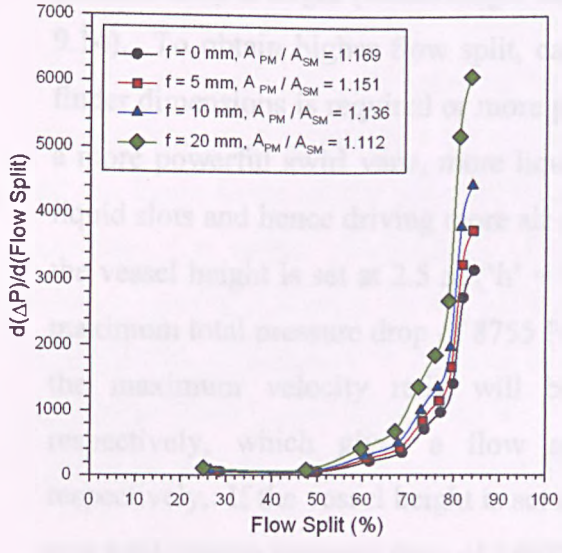

Figure 9.12: Rate of increase of system pressure drop with respect to flow split.

Figures 9.10 and 9.11 suggest that a flow split higher than 70% is undesirable. Although increasing 'f' does not change the flow split significantly, the increase changes system total pressure drop significantly (hence total vessel height) because of the drastic drop in number of tubes and this leads to Case 3 where the height of the vessel is considered an independent variable.

9.3.4 Case 3

Assuming that the vessel diameter and the operating condition remain the same as the base case. The vessel height is varied. A certain vessel height corresponds to a maximum pressure drop and velocity ratio that the system can handle. Knowing this maximum velocity ratio, the required flow split can be identified if 'f' is specified. Figure 9.13 illustrates that at a certain value of 'H', the velocity ratio increases as 'f' decreases and the effect is more significant at larger 'H'. If the values of 'H', velocity ratio and 'f' are known, then the flow split can be calculated using Equation (4.1). The number of tubes can be calculated using Equation (9.3). It is desirable to obtain a high velocity ratio and hence higher throughput. However, the higher the velocity ratio the higher the flow split and the vessel height, hence the capital cost and running cost since the pressure drop is larger (vessel height can be expressed as pressure drop, See Figure 9.14). To obtain higher flow split, careful consideration of the slots and vortex finder dimensions is required or more powerful swirl vanes have to be used. With a more powerful swirl vane, more liquid will be thrown to the wall blocking the liquid slots and hence driving more air into the vortex finder. From Figure 9.13, if the vessel height is set at 2.5 m ('h' = 1.05 m, Figure 9.14), this corresponds to a maximum total pressure drop of 8755 Pa. If the value of 'f' is 0, 5, 10 and 20 mm, the maximum velocity ratio will be approximately 3.2, 3.0, 2.7 and 2.3 respectively, which gives a flow split of 73.3%, 71%, 67.4% and 61% respectively. If the vessel height is set at 3.5 m ('h' = 2 m, Figure 9.14), this gives to a total system pressure drop of 16677 Pa. If the value of 'f' is 0, 5, 10 and 20 mm, the maximum velocity ratio will be approximately 4.6, 4.18, 3.8 and 3.2 respectively, which gives a flow split of 81.4%, 80%, 77% and 72% respectively.

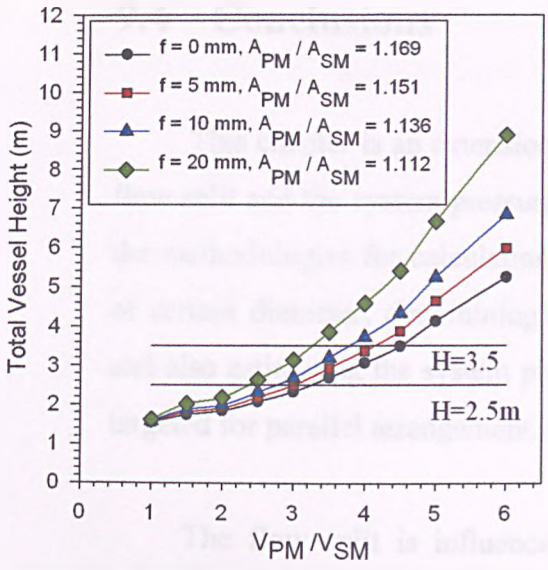

Figure 9.13: Effect of velocity ratio and 'f' on vessel height.

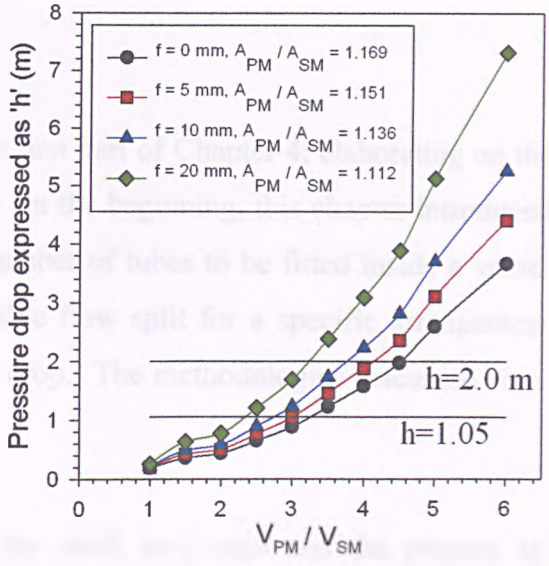

Figure 9.14: Effect of velocity ratio and 'f' on length of drainage pipe. The length gives an indication of the system pressure drop.

It is of interest to keep the pressure drop to a minimum, hence vessel height to minimise capital cost. By reducing the pressure drop, the length of the drainage pipe required to accommodate the drainage head (h) between the cyclone inlets and the liquid sump can be reduced, meaning for a given height more gas can be processed (i.e. higher throughput). From Case 3, if 'H' is 2.5 m to achieve velocity ratio of 3 (similar to the SHELL velocity ratio), a flow split of 71% is required with a minimum 'f' distance of 5 mm. If the flow split is taken as 80% (similar to SHELL flow split), then for 'f' = 5 mm, velocity ratio will be 4.34 and a vessel height of around 3.6 m is required.

If vessel height is 3 m, this gives a velocity ratio of 3.5 when 'f' = 5 mm and the flow split is about 75%. This selection is reasonable since it gives a slightly higher throughput (higher velocity ratio) and lower pressure drop (lower flow split) compared to the typical cyclonic separator used by SHELL.

9.4 Conclusions

This chapter is an extension of the first part of Chapter 4, elaborating on the flow split and the system pressure drop. In the beginning, this chapter introduced the methodologies for calculating the number of tubes to be fitted inside a vessel of certain diameter, determining a suitable flow split for a specific arrangement and also estimating the system pressure drop. The methodologies discussed were targeted for parallel arrangement.

The flow split is influenced by the mesh area ratio and the primary to secondary velocity ratio. Therefore, the mesh area ratio has to be calculated first and this depends on the number of tubes that could be fitted inside a specific vessel, which depends on the geometries of the cyclone tube and the layout chosen. The flow split is important because a higher value will increase the system throughput but at the expense of the system pressure drop and the pressure drop will evidently influence the vessel height. A higher system pressure drop will result in a larger vessel, which will, therefore, increase the capital cost.

Effort was put into estimating the pressure drop in the real application, i.e. a methane – oil system, using the air-water data obtained from the experimental work by relating to the Euler number. The properties of the oil and methane gas were taken at an operating condition of 130 bar and 70^0C. A rough estimate of the vessel height was also carried out based on this operating condition.

In the end of this chapter, optimisation of the flow split was carried out by varying all the variables (i.e. the velocity ratio, the distance between cyclone tubes, vessel height) because there was no information as to which variable is an independent value. It was found that a flow split of around 70% was an optimum value. Any further increase will not benefit a lot from getting a higher velocity ratio, but will significantly increase the system pressure drop. From the optimisation process, it is suggested that the cyclonic system developed in this

project could perform better than the commercially available system, e.g. the typical cyclonic separators used by SHELL.

The next chapter draws out all the conclusions obtained from the investigation carried out on the axial flow cyclone and also outlines the possible areas to be covered as future work.

Chapter 10

Conclusions and Recommendations for Future Work

Conclusions made from the various studies of this research work are presented in the following sections. Recommendations for further development are put forward for possible future work.

10.1 Conclusions

The development of the axial flow cyclone went through seven different designs before arriving at the most recent design that gives a reasonable balance between the flow split, pressure drop, grade efficiency and no re-entrainment within the desired range of liquid loading (0.100 % v/v). The evolution of these cyclone designs and the results are summarised below.

The conclusions of the studies carried out in this project, which can be categorised into three major sections; the flooding/re-entrainment studies, the grade efficiency studies and theoretical modelling are presented below.

10.1.1 Flooding/Re-entrainment Studies

Flooding studies were investigated in terms of the pressure drop-flowrate characteristics, flow split measurement and onset of re-entrainment. The experimental constraint was that the outlet pressure for both the gas vents has to be equal because in the real application both the vents flow to a common chamber. This was achieved by leaving the valve controlling the vortex flow (Valve VC) fully opened while adjusting the valve controlling the flow out through the slots (Valve

VA) until the pressure at both the gas vents is equal. Only then the pressure drop measurements are taken.

- ***Pressure drop – flowrate characteristics (Initial Geometry)***

  - The initial geometry gave a dry flow split of approximately 20%. Flow split is the ratio of the air leaving through the vortex finder to the air supplied. Flow split is a fixed value for a specific cyclone design. When water was added, the slots were partly filled with the liquid and this increased the flow split. The flow split increases as the liquid loading increases.
  - The total pressure drop was estimated to be the sum of the energy required to accelerate liquid within the system ($\frac{1}{2}\rho_f U_{in}^2$), the static liquid hold-up and the swirl losses associated with the air going through the vortex finder. The total pressure drop with presence of liquid (i.e. wet pressure drop) increased about two fold compared to dry conditions at low air flowrates (i.e. when frothing zone occurs). At low liquid loading (0.060 - 0.065 %v/v) and when the air flowrate increased, the wet pressure drop dropped to the condition as if it was dry because the liquid weakened the vortex strength and as the liquid and gas loadings were increased further, the pressure drop increased beyond the dry condition.
  - A frothing zone (i.e. liquid hold-up) was observed directly above the vanes at low inlet flowrates (linear air inlet velocity < 8 m/s). This was a deficiency of the inlet design because the airflow was not high enough to swirl and entrain the liquid, but only enough to prevent the liquid from falling backwards. Liquid built up in the collection zone and overflowed through the slots.
  - When the air flowrate was above 1000 l/min, the vortex strength was high enough to swirl the liquid to the wall, eliminating the frothing zone. At low inlet air flowrate, the total pressure drop was dominated by the liquid

hold-up zone and at higher flowrates it was dominated by the energy transferred to accelerate the liquid and the loss inside the vortex finder.

- ***Pressure drop – flowrate characteristics (Modified Geometries)***

  - With the centre body swirler as the swirling device, the flow split was increased by decreasing the slot's area with everything else remaining unchanged. This drove more flow into the vortex finder, hence increasing the system pressure drop.
  - With the tangentially oriented inlet swirl vanes, a stronger swirl was achieved, which was shown by the increase in the system pressure drop and also the reduction of the flow split from 20% to 14% (using the same cyclone tube as the initial geometry).
  - By adapting a larger vortex finder (from i.d. of 26 mm to 34.5 mm) the pressure drop decreased and the flow split increased to approximately 60% (dry flow split).
  - With four of the slots of the inlet swirl vanes used as additional drainage, the frothing problem was eliminated even at low air flowrates.

- ***Onset of re-entrainment (Initial Geometry)***

  - Re-entrainment is a phenomenon where liquid droplets are detached back to the main air flow from the deposited liquid film on the wall and leave through the vortex finder.
  - Re-entrainment could be detected by observation of liquid drops going into the vortex finder.
  - Three entrainment mechanisms could be identified; direct entrainment due to liquid pulsation, stripping of liquid film on the cyclone wall and re-entrainment due to liquid creeping.

- It was observed that re-entrainment occurred irrespective of the liquid loading at low air velocity (< 8 m/s). This was the region where the frothing zone existed. Droplets were entrained directly into the vortex finder by the liquid pulsation effect.
- The droplets, which were directly entrained into the vortex finder, would not travel very far up the vortex finder. They either stick onto the wall or move up the tube very slowly, agglomerate and the fall back down the vortex finder.
- At higher velocity, the frothing region disappeared because the swirl was strong enough to spin the liquid to the wall. The droplets were re-entrained mostly due to liquid creeping mechanisms and stripping of the liquid film. Direct entrainment might also occur for very fine droplets, but this could not be observed by the naked eye.
- Water droplets travelled across the roof of the cyclone tube and then down the outer wall of the vortex finder until they reached the lip and then formed a film running around the lip of the vortex finder. As the film built up it would reach a point where droplets could be sheared off into the gas stream and take one of two different courses, either flowing outwards towards the wall of the cyclone or creeping into the vortex finder where they impacted on the inside wall. This is re-entrainment due to liquid creeping mechanism.

- ***Onset of re-entrainment (Modified Geometries)***

- When the swirling device was switched to the tangentially oriented inlet swirl vanes and an additional drainage route was introduced, the frothing phenomena was totally eliminated. However, minor re-entrainment still occurred.
- To counteract this, an anti-creep skirt was put around the vortex finder. However, due to the constraint of space between the 52-mm inner

diameter cyclone tube and the 42.2-mm outer diameter vortex finder tube, the angle of the skirt to the axial direction was only about 15^0.

- With the skirt on (Geometry 7b), the re-entrainment problem did not show a significant improvement. It only managed to work up to a linear inlet velocity of 15.5 m/s without re-entrainment below a liquid loading of 0.100 % v/v.

10.1.2 Grade Efficiency Studies

The main objective to carry out the grade efficiency test on the cyclone was to determine the cyclone's collection performance at different air flowrates. The test was only carried out using Geometry 7a since it is the best geometry tested having the highest flow split and working well without re-entrainment over a wide range of air flowrates. Initially, measurements were taken isokinetically. However, it was noticed that it was not feasible to get a representative amount of droplets in the vortex finder at high flowrates. Moreover, the velocities inside the vortex finder at high air flowrates exceeded the limit that the Polytec could handle. Therefore, a flow straightener was put into the vortex finder so that the droplets would be distributed more evenly over the whole cross-sectional area of the tube and a non-isokinetic sampling approach was taken. The drop size distribution (DSD) curves for both isokinetic and non-isokinetic sampling were compared at the inlet and both the outlets and they were found to be very similar. Therefore, isokinetic sampling was not crucial in this study.

Computational Fluid Dynamics was used to simulate the air flow pattern inside the sampling probe in order to investigate the deposition efficiency inside the sampling probe. It was shown that the secondary flow was very weak compared to the axial flow even at the highest measured velocity (i.e. 6 m/s). Therefore, the possibility of droplets recirculating in the probe making the drop count low was very slim. It was found that the most probable reasons for getting lower counts at high

velocities were droplets depositing onto the probe wall especially in the bend and directly after the bend, and droplets not passing through the measuring volume.

The cut size of the grade efficiency curve inside the vortex finder at an air flowrate of 600, 1000 and 1400 l/min was 7.2, 5.0 and 4.4 microns respectively. As for the cut size in the disengagement space, it was found to be 9.0, 6.0 and 5.0 microns. These cut sizes were obtained without a secondary mesh in the disengagement space. With the mesh in it, the cut size at 600 l/min decreased from 9 to 6.75 microns. This suggests that the secondary mesh would be able to trap the droplets leaving through the disengagement space.

10.1.3 Theoretical Modelling

Modelling work was carried out to investigate the practicability of predicting the cyclone's performance, i.e. the system pressure drop and the separation efficiency. The initial geometry was investigated in the early stage using the standard k-ε turbulence model. This model was known to have a weak record on modelling swirling flow. However, it was still chosen as a practice to get to learn the techniques involved better. The main emphasis was put on Geometry 7a since it was the most successful design developed in this project. The geometry was created in GAMBIT and the equations were solved using FLUENT. This geometry was solved using the RSM turbulence model.

As expected, the k-ε model was not able to predict the pressure drop accurately. The difference between the measured and the predicted Euler number was about 28%. On the other hand, the RSM model was able to predict the pressure drop of Geometry 7a accurately with a difference of about 4%. The flow split predicted was 52% and the experimental results gave a value of 56%. Therefore, it can be concluded that the RSM model could predict the pressure drop across the cyclone

very well. The drawback was that it required extensive computational power and time.

While the model was able to predict the system pressure drop accurately, the agreement of the grade efficiency curve between CFD and experimental data was very poor. CFD was only able to predict the limit of separation of the experimental data accurately. Before the limit of separation, CFD has over predicted the efficiency. The contradiction might be due to the breakage of larger droplets into very fine droplets, hence not collected in experiments, giving low separation efficiency at small drop sizes. However this breakage feature was not available in the model. Furthermore, the coefficient of restitution of '0' might not be representative for all droplet sizes over the entire air flowrate tested. Therefore, the model has over predicted the cyclone's collection efficiency. It is suggested to incorporate models for droplet coalescence, droplet breakage and behaviour of liquid film deposited onto the cyclone wall in order to improve the prediction on the droplets' trajectories.

The results obtained from simulation and experiments were also compared to an analytical model developed by other researchers. For the pressure drop prediction, the model developed by **Ramachandran *et al.* (1991)** was used to predict the pressure drop across the vanes with additional terms added to it to calculate the pressure drop across the whole cyclone. The modified Ramachandran's model was able to predict the system pressure drop very accurately (with an error of less than 10%). For the grade efficiency predictions, the cut sizes at different air flowrates were calculated using the Leith-Licht theory and the equation developed by **Stenhouse and Trow (1979)**. The former theory was used on a conventional reverse flow cyclone which had an 'equivalent inlet velocity' as Geometry 7a and it overpredicted the cut sizes, suggesting that a reverse flow cyclone would give a better separation. However, from the pressure drop analysis using empirical and theoretical models developed, it showed that the resistance of this type of cyclone was much higher than the axial flow cyclone. It was also attempted to compare Sheffield cyclone design with the commercially available axial flow cyclones.

However, due to lack of information from the manufacturers, extensive comparison could not be carried out. Nevertheless, from the information available it is suggested that the Sheffield design works better than the commercial cyclone in terms of separation efficiency, but at the expense of pressure drop.

10.2 Future Work

The future work in this section is divided into the further development that can be carried out experimentally and computationally. From the experimental point of view, it was stated in Chapter 9 that to get a velocity ratio (V_{PM}/V_{SM}) of 3.0 (i.e. similar to the ratio obtained by SHELL) the flow split required was 70% and if flow split is higher than 70% this will increase the velocity ratio (i.e. higher throughput). To increase the flow split, there are three ways to achieve this, i.e. using a larger vortex finder, reducing the slot area and using a more efficient swirling device. The first method is not feasible with the 52 mm diameter cyclone tube because the largest tube commercially available, which has an outer diameter of 42.2 mm and an inner diameter of 34.54 mm, has been used (Geometry 7a).

Figure 10.1 shows the variation of flow split when the slot area is reduced. The data points are based on all the tested geometries in this project. The slot area required to give a flow split of 70% (Geometry 8) is about 375 mm^2 with the area of the vortex finder being 937 mm^2 (i.d. 34.54 mm). The pressure drop characteristic of Geometry 8 is given in Appendix M. From the plot, to get a flow split of 80% the slot area has to be reduced to 234 mm^2. There is one problem that is very likely to occur with the reduction of the slot area; re-entrainment of liquid into the vortex finder. For Geometry 7a with a total slot area of 570 mm^2, re-entrainment occurred above a linear air inlet velocity of 15.5 m/s (i.e. around 2000 l/min) for a liquid loading of 0.100 – 0.105 v/v%. Therefore, it is envisaged that for a slot area of less than 570 mm^2, re-entrainment would occur at an even lower velocity. However, re-entrainment tests should be carried out to verify this conclusion. If this is true then

reducing the slot area will narrow the safe operability range of the cyclonic system, i.e. lowering the system throughput, which is undesirable. Hence, the last alternative is to increase the flow split without reducing the operability range, which is to develop a stronger swirling device. Therefore, further work can be carried out focussing on the design of the swirling device. A swirler providing a stronger vortex would also increase the collection efficiency due to the stronger centrifugal force throwing the droplets to the wall and out through the slots.

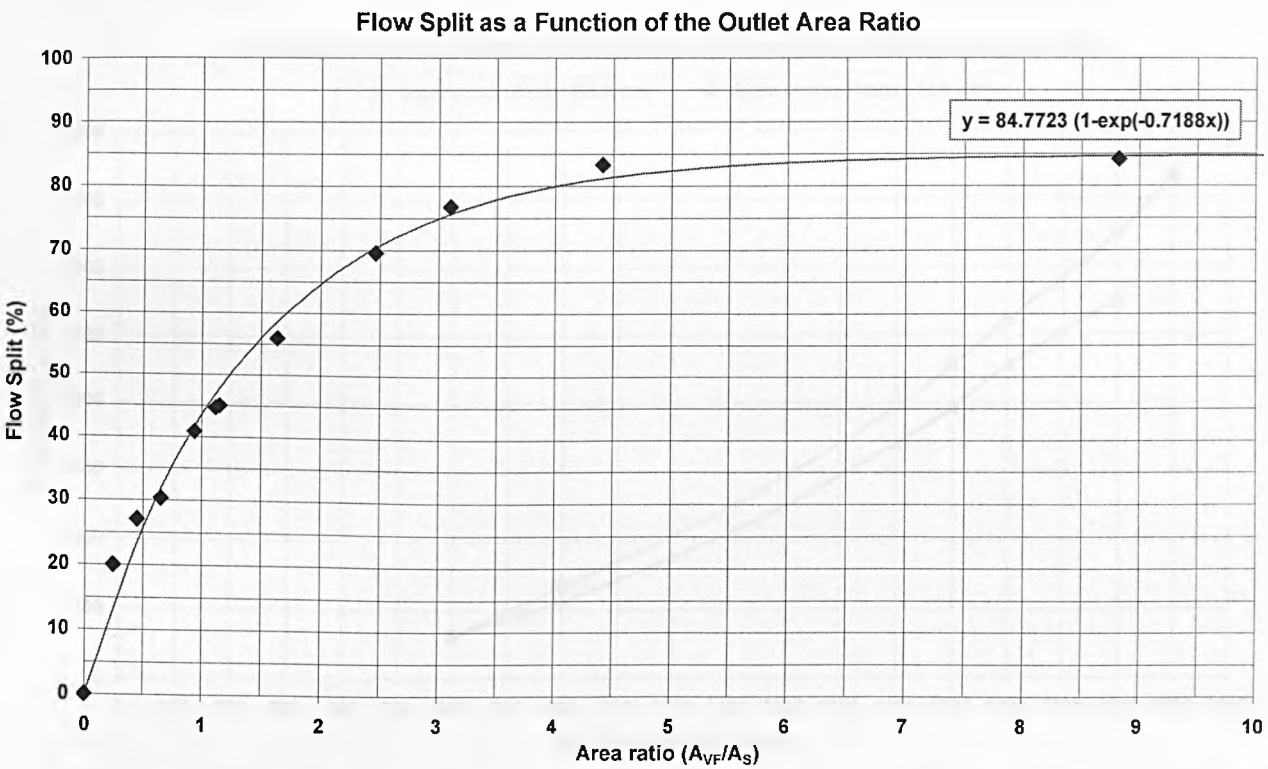

Figure 10.1: Variation of flow split as a function of the total slot area.

The vortex finder length used for all the experimental tests was 90 cm. In the real application, the vortex finder only has to exceed the height of the secondary mesh in order to hold the mesh in position. The length should be made as short as possible since it is shown in Figure 10.2 that a shorter length gives a lower pressure drop when all the slots are blocked, i.e. all the air leaves through the vortex finder. The difference between the two pressure drops is about 18%.

It was observed experimentally that the liquid had to swirl quite a long way before it reached the liquid drainage slots. It was also discussed previously that the

swirl decayed as the flow past the first set of slots. The current entrance length for Geometry 7a is 250 mm. It might be useful to reduce the entrance length to widen the cyclone operability range (i.e. higher velocity could be used without re-entrainment since most of the liquid could be thrown to the wall and out through the slots before the swirl decayed). Shortening the entrance length could also reduce the pressure drop due to friction, similar to shortening the vortex finder discussed earlier on, although the reduction might not be very significant.

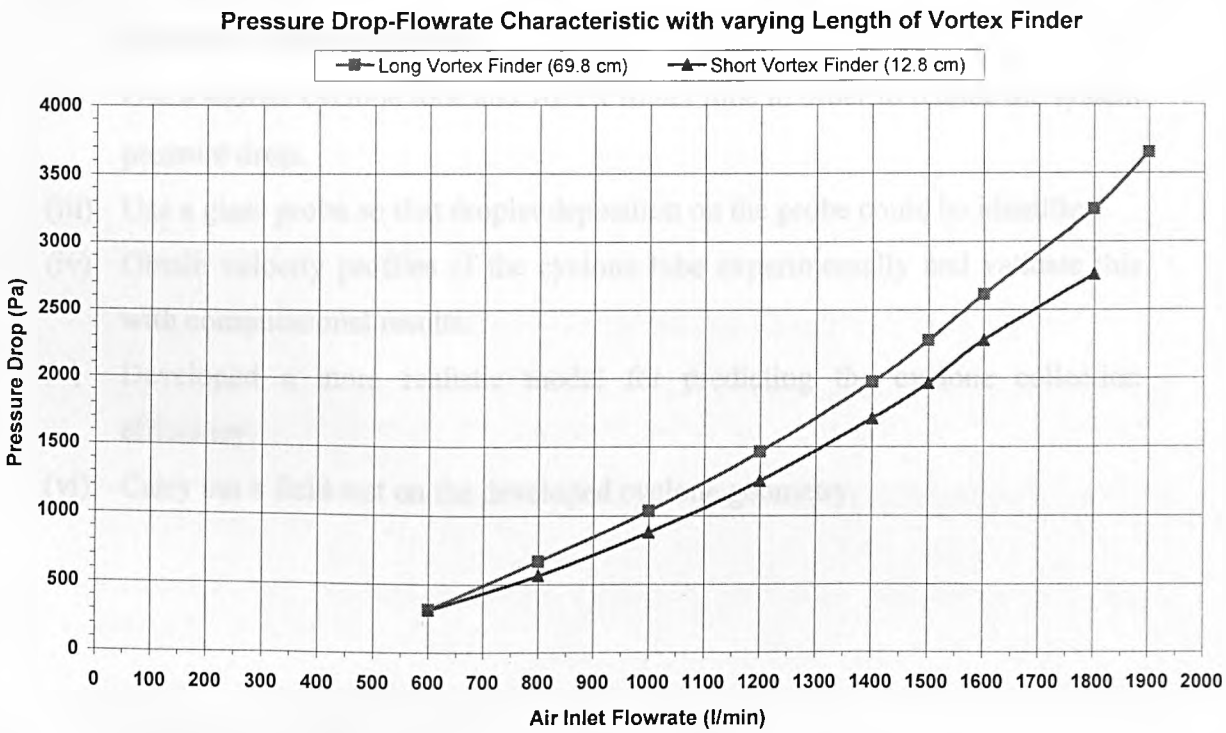

Figure 10.2: The pressure drop characteristic when the vortex finder length is varied.

It is also proposed to use a glass probe in the future for grade efficiency measurements so that any droplet deposition could be identified and also the observation could be verified with the computational results. As for the computational work, it is recommended to develop a more suitable model to investigate droplet collection efficiency in terms of droplet breakage, coalescence and droplet stripping from the liquid film on the cyclone wall. The velocity profile inside the cyclone tube has to be measured experimentally as well in order to validate the computational results. This is essential because to get accurate predictions of the grade efficiency, it requires accurate prediction of the cyclone

fluid dynamics and this could go into extend of very detailed modelling of the flow after each of the slots of the inlet swirl vanes. It will also be beneficial to carry out a field test on the developed geometry in the future.

The future work discussed above could be summarised as follows:

(i) Develop a more efficient swirling device in order to increase the flow split and also the collection efficiency.
(ii) Use a shorter cyclone tube and vortex finder tube in order to reduce the system pressure drop.
(iii) Use a glass probe so that droplet deposition on the probe could be identified.
(iv) Obtain velocity profiles of the cyclone tube experimentally and validate this with computational results.
(v) Developed a more realistic model for predicting the cyclone collection efficiency.
(vi) Carry out a field test on the developed cyclone geometry.

Bibliography

Akiyama, T. and Marui, T. (1989). "Dust Collection Efficiency of a Straight-Through Cyclone - Effects of Duct Length, Guide Vanes and Nozzle Angle for Secondary Rotational Air Flow." Powder Technology **58**: 181-185.

Akiyama, T., Marui, T. et al. (1986). "Experimental Investigation on Dust Collection Efficiency of Straight-Through Cyclone with Air Suction by Means of Secondary Rotational Air Charge." Industrial Engineering Chemistry Process Design and Development **25**(4): 914-918.

Alexander, R. M. (1949). "Fundamentals of Cyclone Design and Operation." Proceedings of Australian Institute of Mining Metallic Processes **152**: 203-228.

Allen, R. W. K. (2001). Lecture notes: CPE 407 Environment - Particulate Emissions, University of Sheffield, U.K.

Allen, R. W. K. (2003, 2004). Personal Communication, University of Sheffield, U.K.

Andreussi, P. (1980). "The Onset of Droplet Entrainment in Annular Downward Flows." The Canadian Journal of Chemical Engineering **58**: 267-270.

Armand, P., Boulaud, D. et al. (1998). "Two-fluid modeling of aerosol transport in laminar and turbulent flows." **29**(8): 961-983.

Brunazzi, E. and Paglianti, A. (1998). "Design of Wire Mesh Mist Eliminators." AIChE Journal **44**(3): 505-512.

Brunazzi, E. and Paglianti, A. (2000). "Design of Complex Wire-Mesh Mist Eliminators." AIChE Journal **46**(6): 1131-1137.

Buttner, H. and Ebert, F. (1989). "Particle Collection in Small Laboratory Cyclones as a Basis for the Design of Large Scale Cyclones." Chemical Engineering Technology **12**: 295-301.

Calvert, S. (1978). "Guidelines for Selecting Mist Eliminators." Chemical Engineering **85**(5): 109-112.

Carpenter, C. L. and Othmer, D. F. (1955). "Entrainment Removal By A Wire-mesh Separator." AIChE Journal **1**(4): 549-557.

Casal, J. and Martinez-Benet, J. M. (1983). "A Better Way to Calculate Cyclone Pressure Drop." Chemical Engineering **90**(2): 99-100.

Cheng, Y. S. and Wang, C. S. (1975). "Inertial Deposition of Particles in a Bend." Journal of Aerosol Science **6**: 139-145.

Cheng, Y. S. and Wang, C. S. (1981). "Motion of Particles in Bends of Circular Pipes." Atmospheric Environment **15**: 301-306.

Clift, R., Ghadiri, M. et al. (1991). "A Critique of Two Models for Cyclone Performance." AICHE Journal **37**(2): 285-289.

Coulson, J. M., Richardson, J. F. et al. (1999). Coulson & Richardson's Chemical Engineering Volume 1, Fluid Flow, Heat Transfer and Mass Transfer, Butterworth Heinemann.

Daniels, I. (2004). Private Communication. Natco Group, U.K.

Daniels, T. C. (1957). "Investigation of a Vortex Air Cleaner." The Engineer **203**: 358-362.

Davies, G. (2000). Private Communication. UMIST, Manchester, U.K.

Davies, G. A. and Papadopoulos, D. (2000). Optimal Design For Wire Mesh Mist Eliminators, Advanced Research Partnership, Design and Instrumentation for Process Separation Systems (DIPSS). **2000**.

Dean, W. R. (1927). "Note on the motion of fluid in a curved pipe." Philosophical Magazine **4**(20): 208-223.

Dean, W. R. (1928). "The stream-line motion of fluid in a curved pipe." Philosophical Magazine 7th Series **5**(30): 673-695.

Dennis, S. C. R. and Ng, M. (1982). "Dual solutions for steady laminar flow through a curved tube." Quarterly Journal of Mechanics and Applied Mathematics **35**(3): 305-324.

Dietz, P. W. (1981). "Collection Efficiency of Cyclone Separators." AIChE Journal **27**(6): 888-892.

Dirgo, J. and Leith, D. (1985). "Cyclone Collection Efficiency - Comparison of Experimental Results with Theoretical Predictions." Aerosol Science and Technology **4**(4): 405-415.

Dobbins, R. A., Conti, K. A. et al. (1979). "Performance Analysis of Axial Flow Dust Separators." The Second World Filtration Congress 1979: 145-150.

Fan, B., McFarland, A. R. et al. (1992). "Aerosol-Particle Losses in Isokinetic Sampling Probe Inlets." Environmental Science of Technology **26**(2): 390-394.

Feord, D., Wilcock, E. et al. (1996). "A Stochastic Model To Describe The Operation Of Knitted Mesh Mist Eliminators, Computation Of Separation Efficiency." Trans IChemE **71**(Part A): 282-294.

FLUENT 5 User's Guide, Volume 2, 1998, Fluent Europe Ltd., Sheffield, U.K.

FLUENT 5 User's Guide, Volume 3, 1998, Fluent Europe Ltd., Sheffield, U.K.

FLUENT 5 User's Guide, Volume 4, 1998, Fluent Europe Ltd., Sheffield, U.K.

Fujimoto, H., Ogino, T. et al. (2001). "Collision of a droplet with a hemispherical static droplet on a solid." International Journal of Multiphase Flow **27**: 1227-1245.
Gambit User's Guide, 1999, Fluent Europe Ltd., Sheffield, U.K.

Gauthier, T. A., Briens, C. L. et al. (1990). "Uniflow Cyclone Efficiency Study." Powder Technology **62**(3): 217-225.

Gauthier, T. A., Briens, C. L. et al. (1992). "Study of the Gas Circulations Patterns in a Uniflow Cyclone." Canadian Journal of Chemical Engineering **70**(2): 209-215.

Gil, A., L. Romeo, M. et al. (2002). "Effect of the solid loading on a pressurised fluidised bed combustors cyclone with pneumatic extractions of solids." Chemical Engineering and Technology **25**(4): 407-415.

Gore, R. and Jurewicz, J. T. (1983). "A Numerical Model For Fluid-Particle Motion Near The Inlet Of An Aspirating Probe." American Society of Mechanical Engineers (Fluids) **10**: 47-52.

Griffiths, W. D. and Boysan, F. (1996). "Computational Fluid Dynamics (CFD) and empirical modelling of the performance of a number of cyclone samplers." Journal of Aerosol Science **27**(2): 281-304.

Hinds, W. C. (1999). Aerosol Technology - Properties, Behaviour, and Measurement of Airborne Particles, John Wiley & Sons Inc.

Hoekstra, A. J., Derksen, J. J. et al. (1999). "An Experimental and Numerical Study of Turbulent Swirling Flow in Gas Cyclones." Chemical Engineering Science **54**(13-14): 2055-2065.

Hoffmann, A.C. (2005). Private Communication. University of Bergen, Norway.

Hoffmann, A. C., Vansanten, A. et al. (1992). "Effects of Geometry and Solid Loading on the Performance of Gas Cyclones." Powder Technology **70**(1): 83-91.

Hoffmann, A. C., Dejonge, R. et al. (1995). "Evidence of the Natural Vortex Length and its Effect on the Separation Efficiency of Gas Cyclones." Filtration and Separation **32**(8): 799-804.

Hoffmann, A. C., de Groot, M. et al. (1996). "The Effect of the Dust Collection System on the Flow Pattern and Separation Efficiency of a Gas Cyclone." The Canadian Journal of Chemical Engineering **74**: 464-469.

Hoffmann, A. C., de Groot, M. et al. (2001). "Advantages and Risks in Increasing Cyclone Separator Length." AICHE Journal **47**(11): 2452-2460.

Hoffmann, A. C. and Stein, L. E. (2002). Gas Cyclones and Swirl Tubes - Principles, Design and Operation. Berlin, Springer-Verlag.

Iozia, D. L. and Leith, D. (1989). "Effect of Cyclone Dimensions on Gas Flow Pattern and Collection Efficiency." Aerosol Science and Technology **10**(3): 491-500.

Ishii, M. and Grolmes, M. A. (1975). "Inception Criteria for Droplet Entrainment in Two-Phase Concurrent Film Flow." American Insitute of Chemical Engineer Journal **21**(2): 308-318.

Jackson, R. (1963). Mechanical Equipment For Removing Grit and Dust from Gases, The British Coal Utilisation Research Association.
Kakaç, S. and Hongtan, L. (2002). Shell-and-Tube Heat Exchangers. Heat Exchangers: Selection, Rating and Thermal Design, CRC Press: 302-303.

Kim, H. T., Lee, K. W. et al. (2001). "Exploratory design modifications for enhancing cyclone performance." Journal of Aerosol Science **32**(10): 1135-1146.

Klujszo, L. A. C., Rafaelof, M. et al. (1999). "Dust collection performance of a swirl air cleaner." Powder Technology **103**: 130-138.

Klujszo, L. A. C., Songfack, P. K. et al. (1999). "Design Of A Stationary Guide Vane Swirl Air Cleaner." Minerals Engineering **12**(11): 1375-1392.

KnitMesh Catalogue (2001). Demisters-Knitmesh Demisters for separation of liquid entrainment and pollution control.

König, C. (1991). "Design Data for Cyclones." Particle and Particle Systems Characterization **8**(4): 301-307.

Krishnan, T. (1999). Determination of the on-set of re-entrainment and grade efficiency of demisting cyclones. Chemical and Process Engineering. Sheffield, University of Sheffield.

Lees, F. P. (1996). Fire. Loss Prevention in the Process Industries : Hazard identification, assessment and control., Butterworth Heinemann. **2:** 99.

Leith, D. and Licht, W. (1972). "The Collection Efficiency of Cyclone Type Particle Collectors - A New Theoretical Approach." AIChE Symposium Series **68**(126): 196-206.

MacInnes, J. (2000). Private Communication. University of Sheffield, Sheffield, U.K.

Mao, T., Kuhn, C. S. et al. (1997). "Spread and Rebound of Liquid Droplets upon Impact on Flat Surfaces." AIChE Journal **43**(9): 2169-2179.

McFarland, A. R., Gong, H. et al. (1997). "Aerosol deposition in bends with turbulent flow." **31**(12): 3371-3377.

Miller, D. S. (1990). Internal Flow Systems, BHRA (Information Services).

Mitchell, J. P. and Morris, K. (1994). SPS MINI-MANUAL 1: The Practical Determination of Gas and Particle Properties Part 8: Particle Size. Oxfordshire, AEA Technology.

Mitchell, J. P., Nichols, A. L. et al. (1989). "The Characterisation of Water-Droplet Aerosols by Polytec Optical Particle Analysers." Particle and Particle System Characterisation **6**(3): 119-123.

Modigell, M. and Weng, M. (2000). "Pressure Loss and Separation Characteristics Calculation of a Uniflow Cyclone with a CFD method." Chemical Engineering and Technology **23**(9): 753-758.

Mycock, J. C., McKenna, J. D. et al. (1995). Handbook of Air Pollution Control Engineering and Technology, Lewis Publishers.

Nandakumar, K. and Masliyah, J. H. (1982). "Bifurcation in steady laminar flow through curved tubes." Journal of Fluid Mechanics **119**: 475-490.

Ng, S. Y., Priestman, G. H. et al. (2003a). Investigation of Axial Flow Cyclones for Use in Oil and Gas Applications. FILTECH EUROPA 2003: International Conference and Exhibition Filtration and Separation Technology, CCD. Congress Center Dusseldorf, Germany.

Ng, S. Y., Priestman, G. H. et al. (2003b). Performance Analysis of Axial Flow Cyclones: Pressure Drop Characteristic and Collection Efficiency. Britain's Younger Engineers, House of Commons, London, United Kingdom.

Nooijen, H. (2003). Private Communication. SHELL International, The Netherlands.

Peng, W. and Hoffmann, A. C. (2004). "Separation Characteristics of Swirl-Tube Dust Separators." AIChE Journal **50**(1): 87-96.

Phillips, H. W., Abrahamson, J. A. et al. (1992). Cyclones. Separation Processes Service (SPS) Gas Cleaning Manual. **II**.

Pokusevski, Z. (2001). Private Communication. UMIST, Manchester, U.K.

Priestman, G. (2001). Private Communication. University of Sheffield, Sheffield, U.K.

Pui, D. Y. H., Romay-Novas, F. et al. (1987). "Experimental Study of Particle Deposition in Bends of Circular Cross Section." Aerosol Science and Technology **7**: 301-315.

Ramachandran, G., Leith, D. et al. (1991). "Cyclone Optimization based on a New Empirical Model for Pressure Drop." Aerosol Science and Technology **15**(2): 135-148.

Ramachandran, G., Raynor, P. C. et al. (1994). "Collection Efficiency and Pressure Drop for a Rotary-Flow Cyclone." Filtration and Separation **31**: 631-636.

Rhodes, M. J. and Laussmann, P. (1992). "A simple non-isokinetic sampling probe for dense suspensions." Powder Technology **70**: 141-151.

Robinson, K. S. (1985). "Spray Elimination and Demisting." Separation Processes Service (SPS) State of Art Report **SPS SAR44**(G 3375).

Shahnam, M. and Jurewicz, J. T. (1986). "Particle Motion Near The Inlet of a Sampling Probe." American Society of Mechanical Engineers (Fluids) **35**: 145-150.

Shepherd, C. B. and Lapple, C. E. (1939). "Flow Pattern and Pressure Drop in Cyclone Dust Collectors." Industrial and Engineering Chemistry **31**(8): 972-984.

Slack, M. D., Prasad, R. O. et al. (2000). "Advances in Cyclone Modelling Using Unstructured Grids." Trans. Institution of Chemical Engineers **78**(A): 1098-1104.

Souders, M. and Brown, G. G. (1934). "Design of Fractionating Columns, I. Entrainment and Capacity." Industrial and Engineering Chemistry **26**(1): 98-103.
Sparks, L. (1984). Particle Sampling and Analysis. Handbook of Air Pollution Technology, John Wiley and Sons: 785-832.

Stallard, P., Scowen, P. et al. The Development of a Multi-Tube Axial Flow Cyclone Separator System for Use in Nuclear Gas Cleaning Systems. 20th DOE/NRC Nuclear Air Cleaning Conference.

Stanbridge, D. (2004). Private Communication. CDS Engineering, U.K.

Stairmand, C. J. (1949). "Pressure Drop in Cyclone Separator." Engineering **168**: 409-412.

Stairmand, C. J. (1951). "The Design and Performance of Cyclone Separators." Trans. Institution of Chemical Engineers **29**: 356-383.

Stenhouse, J. I. T. and Trow, M. (1979). "The Behaviour of Uniflow Cyclones." The Second World Filtration Congress 1979: 151-156.

Stern, A. C., Caplan, K. J. et al. (1955). "Cyclone Dust Collectors (Report on Removal of Particulate Matter From Gaseous Wastes)." American Petroleum Institute.

Strauss, W. (1977). Mist Elimination. Air Pollution. A. Stern, C,, Academic Press. **4**: 294-326.

Sumner, R. J., Briens, C. L. et al. (1987). "Study of a Novel Uniflow Cyclone Design." Canadian Journal of Chemical Engineering **65**(3): 470-475.

Svarovsky, L. (1981). Handbook of Powder Technology, Elsevier.

Swanborn, R. A. (1988). A new approach to the design of gas-liquid separators for the oil industry, University of Delft, The Netherlands.

Tippetts, J. (2001). Private Communication. University of Sheffield, Sheffield, U.K.

Tsai, C.-J. and Pui, D. Y. H. (1990). "Numerical Study of Particle Deposition in Bends of a Circular Cross-Section - Laminar Flow Regime." Aerosol Science and Technology **12**(4): 813-831.

Van Dongen, J. R. J. and Ter Linden, A. J. (1958). "The Application of Gas/Liquid Cyclones in Oil Refining." Trans. ASME **80**: 245-251.

Wang, W. and Davies, G. A. (1996). "CFD Studies of Separation of Mists from Gases Using Vane-Type Separators." Trans. IChemE. **74**(Part A): 232-238.

Wark, K., Warner, C. F. et al. (1998). Particulate Control. Air Pollution: Its Origin and Control, Addison-Wesley.

Yanase, S., Goto, N. et al. (1988). "Stability of dual solutions of the flow in a curved circular tube." Journal of the Physical Society of Japan **57**(8): 2602-2604.

Yanase, S., Goto, N. et al. (1989). "Dual solutions of the flow through a curved tube." Fluid Dynamics Research **5**: 191-201.

York, O. H. (1954). "Performance of Wire-mesh Demisters." Chemical Engineering Progress **50**(8): 421-424.

York, O. H. and Poppele, E. W. (1963). "Wire Mesh Mist Eliminators." Chemical Engineering Progress **59**(6): 45-50.

York, O. H. and Poppele, E. W. (1970). "Two-Stage Mist Eliminators For Sulfuric Acid Plant." Chemical Engineering Progress **66**(11): 67-72.

Yuu, S., Jotaki, T. et al. (1978). "The Reduction of Pressure Drop due to Dust Loading in a Conventional Cyclone." Chemical Engineering Science **33**: 1573-1580.

Zhao, Z. M. and Pfeffer, R. (1997). "A simplified model to predict the total efficiency of gravity settlers and cyclones." Powder Technology **90**(3): 273-280.

Appendix A: Calibration curve of the flowrate-pressure characteristics of the spray nozzles

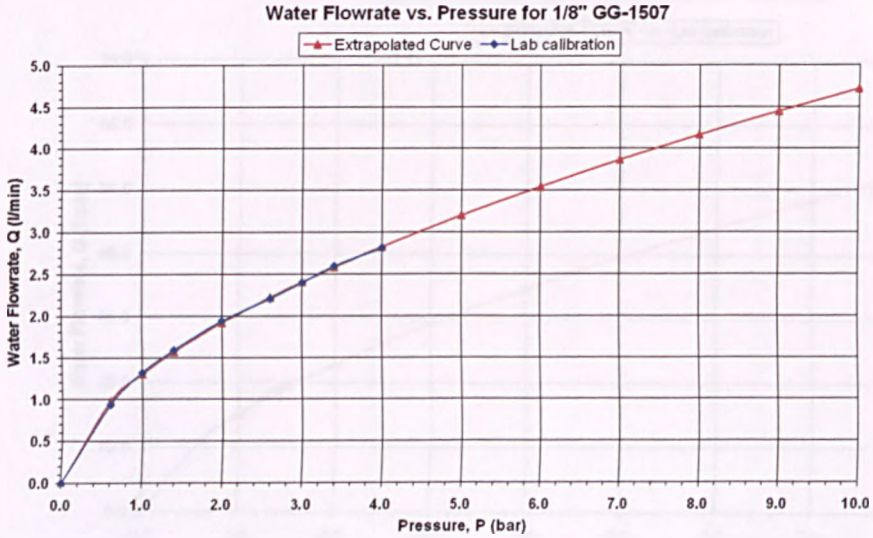

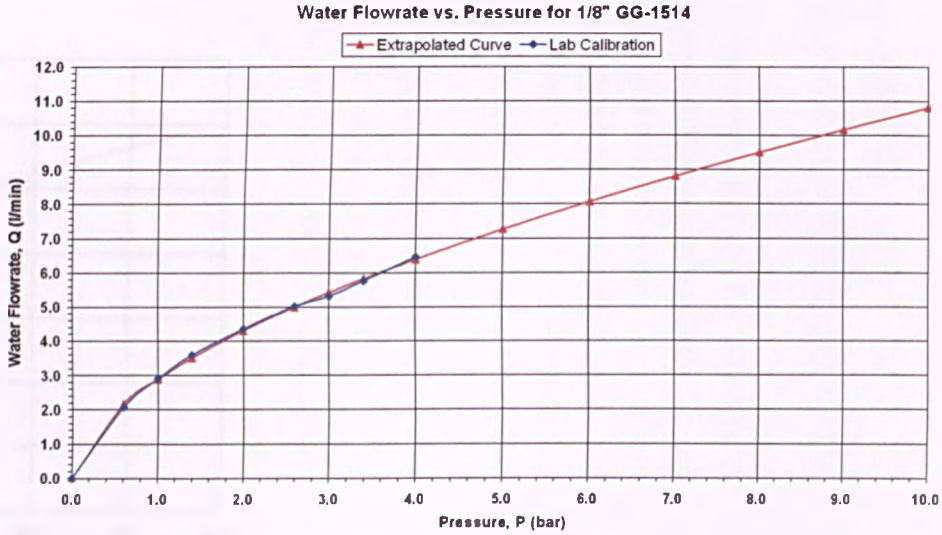

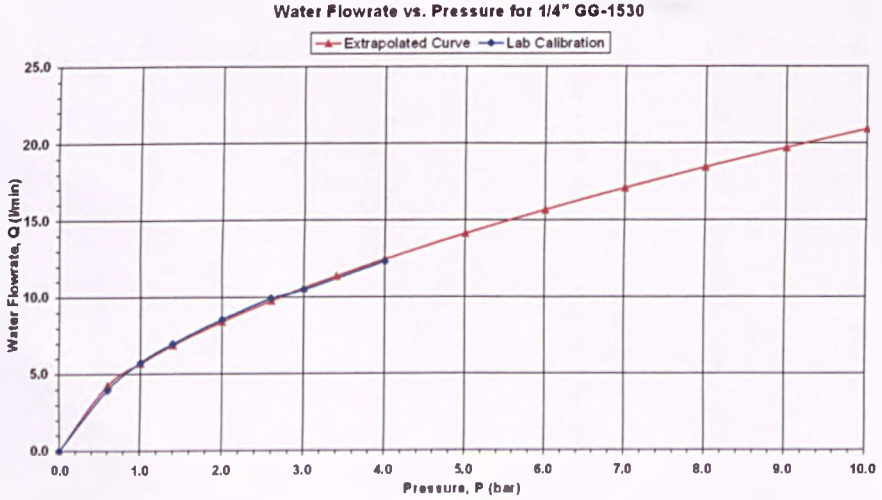

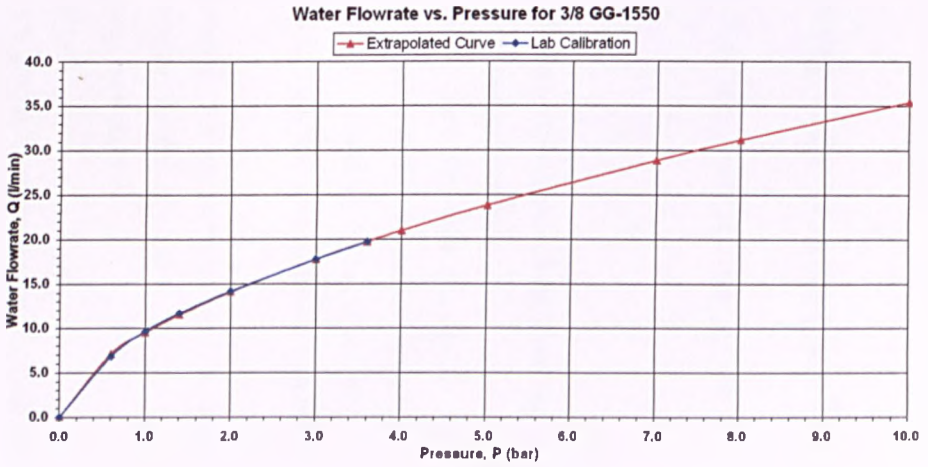

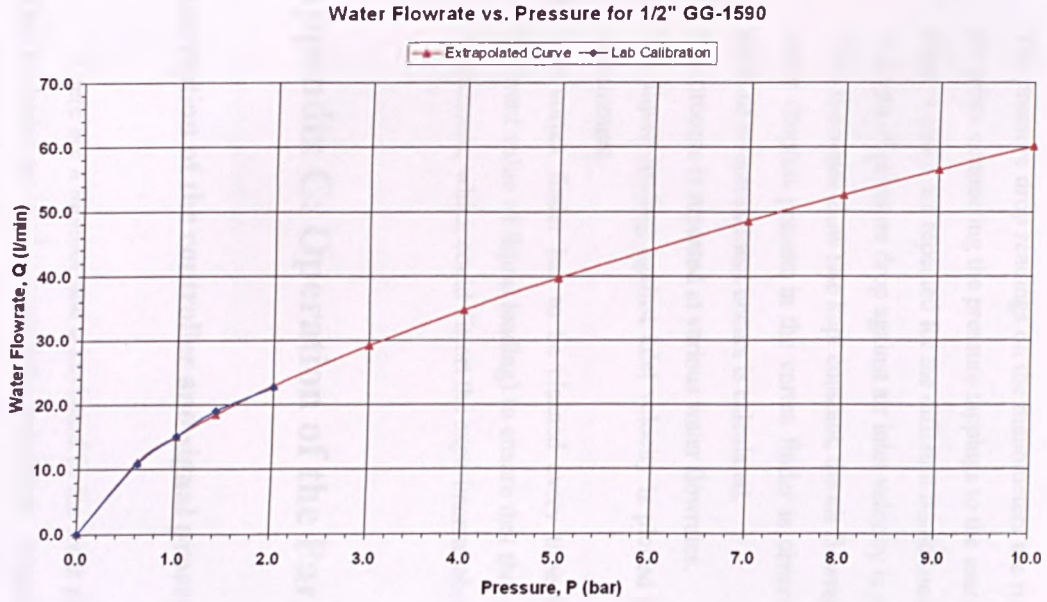
Water Flowrate vs. Pressure for 1/2" GG-1590
Extrapolated Curve
Lab Calibration
Water Flowrate, Q (l/min)
70.0
60.0
50.0
40.0
30.0
20.0
10.0
0.0
0.0
1.0
2.0
3.0
4.0
5.0
6.0
7.0
8.0
9.0
10.0
Pressure, P (bar)

Appendix B:
Experimental Procedures for Flooding/Re-entrainment Test

1. Before switching on the fan, the manometers are checked so that they are level and that the reading on the manometer is zero.
2. The fan is then switched on.
3. The water tap is then turned on.
4. The required air flowrate is adjusted using the gate valve and the required water flow rate is manipulated via the pressure regulator to match the liquid loading required.
5. Valve VC is fully opened and Valve VA is adjusted until the total pressure in the disengagement space and the vortex finder is the same because in the real demisting system, both the gas vents would be flowing to a common chamber. Therefore, ΔPT_{SA} (from inlet to pressure tapping point in the disengagement space) and ΔPT_{SC} (from inlet to pressure tapping point in the vortex finder) should be equal.
6. The pressure drop readings on the manometers are recorded. It is important to make sure that the tubes connecting the pressure tappings to the manometers are free of water.
7. Steps 4 and 5 are repeated for the different liquid loadings investigated.
8. A graph of pressure drop against air inlet velocity is plotted.
9. With the water flow rate kept constant, the air flowrate is gradually increased; the first train of water droplets present in the vortex finder is observed and noted. The inlet velocity when onset of re-entrainment occurs is calculated.
10. The process is repeated at various water flowrates.
11. The liquid loading against inlet velocity is plotted to get the phase diagram of onset of re-entrainment.
12. The vortex finder has to be cleaned every time before starting a new experiment (with different value of liquid loading) to ensure that there are no water droplets from the previous experiment, which could distort the experimental observations.

Appendix C: Operation of the Particle Analyser [(c)]

Description of the controller and signal processor

There are a monitor and a keyboard in the front plate of the signal processor. The 16 keys of the keyboard are used to control the instrument. Alternatively, an external computer can be used as the controller for automatic operation.

[(c)] This information was extracted from the Polytec HC – 15 Manual

Operation of the signal processor

The signal processor mains switch is on the rear of the instrument next to the power connector. A moment after switching on, the directory is displayed on the screen. The brightness of the screen can be controlled with the intensity potentiometer on the side of the signal processor. The RESET button below the intensity potentiometer is used when faults occur (i.e. if the system hangs) or if the directory does not appear after switching on.

Input of measurement parameters

In the directory, four different functions can be selected. By pressing '1' the routine for input of measurement parameters is called up. Key '2' is for initialising the measurement. Key '3' and '4' are for analysis and output, and utilities respectively.

There are 8 blocks in which every block has a list of parameters in which the measurement will be made must be typed in. After choosing a block, the parameter, which has to be changed or defined, is called by pressing the respective number on the keyboard. Each input is ended by pressing the RETURN key.

Parameter

1. Sample Identification

This is for identification purposes. It can consists up to a maximum of 8 numbers.

2. Flow Velocity

The approximate velocity of the flow can be typed in for reference purposes. This input has no influence on the measurement and calculation of the results.

3. Photomultiplier Voltage

After pressing 3, the following selections are displayed in the bottom line of the screen that read "Input HV (0 = Low, 1 = High, 2 = Ref)". When 0 is pressed, the high voltage for the latex calibration curve for the large particles diameter will be selected. The LOW photomultiplier voltage is associated with a relative value of 50. The HIGH photomultiplier voltage is associated with a relative value of 255. By pressing 1 (HIGH) the voltage for the calibration curve with the small particles is selected. Calibration curves are stored in the

instrument for both these voltages. The particles diameter can only be displayed on the screen when one of these voltages is selected. By pressing 2, a relative value for the voltage between 1 and 255 may be keyed in. With the photomultiplier voltages HIGH and LOW, particles over the whole measuring range of the instrument can be measured. So, the input of a relative value is only necessary in exceptional cases.

4. Total Counts (*128)

The measurement can be stopped after a selected number of pulses. As the instrument has 128 storage channels for every range of input number is the average number of pulses per channel. However, only 127 of the 128 channels are displayed. In the first channel only noise pulses are counted. In the last channel all particles are counted which are larger than the maximum size of the selected measuring range. The number of these particles is counted, but they are not classified in size.

5. Total Time (sec)

The measurement can be stopped after a preset time. The longest selectable time is 65535 seconds. The input must be terminated with the return key. If both the stop after time and stop after counts were selected, the measurement will stop whichever the first of these conditions is fulfilled.

0. OK – Return to Main Menu

After inputting all the required parameters, by pressing '0' will go back to the main directory.

Making a Measurement

After inputting the measurement parameters, the measurement can be initialised by pressing '2'. The relevant memory block should be called up by pressing a key (1-8). After selecting the block, a message will be shown in the bottom line that states, "wait – lamp warm up or key". User will go back to the main menu if any key is pressed. Otherwise the instrument will be ready for operation after 10 seconds. The lamp is switched off after the end of any measurement, which takes longer than 60 seconds. As long as the lamp is a light, the word "LAMP" is displayed in the top line of the screen.

At the top of the screen, the parameters chosen for the particular measurement are displayed which are the identification, the velocity, the high voltage, the block and the conditions for ending the measurement. The START/STOP key initiates a measurement. After the measurement is

stopped either by the preset time or the preset counts, with key '0', one can select the data to be presented either in the form of a cumulative or a differential curve. By pressing key '1', the units on the x-axis can be selected to:

1. Display quantity of particles with respect to the channel number.
2. Display quantity of particles with respect to the diameter.
3. Display quantity of particles with respect to the voltage.

The condition under which the measurement was ended is displayed in the bottom line. When no parameter is given to end the measurement, it can be stopped by pressing the START/STOP key. When more than 65280 pulses occur in one of the channels, the measurement is stopped by channel overflow. One can return to the directory after the end of measurement by pressing any key.

Analysis of Measurement

The analysis software is called when 3 is pressed. The following selection will appear on the monitor;

(1) Differential and Cumulative
(2) Background Subtraction
(3) Channel Contents Table
(4) Degree of Separation
(0) Return to Main Menu

In the analysis mode, after pressing 1, the required data block (1-8) should be selected. The measured values are displayed as differential or cumulative distribution. Unlike the display during a measurement, the normalised distribution is shown, which is the division by the total number of particles has also been made. Options 2 and 4 are rarely used.

When key 3 is pressed, the contents of the channels of data block 1 to 8 depending which block you select are displayed. When 0 is pressed, the number of particles counted in each channel is displayed. CH # is the number of the channel and Ni is the number of particles in the channel. The mean value $\overline{U}$ (in volts), the median value U_{50} (in volts) and the standard deviation S_i ($=\ln(U_{84}/U_{50}) = \ln(U_{50}/U_{16})$ are also displayed below the table on the monitor.

When 1 is pressed, the differential distribution against the diameter is displayed. The mean value $\bar{x}$ (in μm), the median value x_{50}(in μm) and the standard deviation S_i ($=\ln(x_{84}/x_{50})$ $=\ln(x_{50}/x_{16})$) are displayed under the table.

By pressing 2, the differential distribution against the voltage is displayed. By pressing 4, the width of the channels in μm is displayed. Key 5-8 are rarely used.

Software Utilities

While in the main directory, the utilities are called by pressing 4. On the screen, the following display appears;

(1) Set Date and Time
(2) Data Transfer to Host
(3) Lamp on/off
(4) HV on/off
(5) Calibration 1/2
(0) Return to Main Menu

Setting up the date and time

While in the utility mode, the software for setting date and time is called up by pressing key 1. In the bottom of the screen, "year" is displayed. It is just required to type in the last 2 digits of the actual year (99 for 1999). Then, enter the two numbers corresponding to the month (e.g. 03 for March) and then the two numbers for the day. A similar procedure is used for keying in hours, minutes and seconds. Once everything has been inserted, the date and time will be displayed in the top right hand corner of the screen. Option 2 is seldom utilised.

Switching the lamp on and off

Whilst in the utilities mode, by pressing 3 the lamp can be switched off and on. If the lamp is switched off when a measurement is started the polytec allows 10 seconds warm-up time for the lamp. If the lamp has been on for more than 60 seconds when the measurement is ended or interrupted, the lamp is switched off automatically. Otherwise it remains on until 60 seconds have elapsed in order to extend the working life of the lamp. If the lamp is switched on manually by

pressing key 3 it must also switched off manually. In the top line of the screen the word "LAMP" always appears when the lamp is lit.

Switching the high voltage on and off

The selected high voltage is normally switched on and off automatically when a measurement is taken. The high voltage can be switched manually independently from the lamp by pressing key 4. The automatic "LAMP ON/OFF" function is independent from the manual switching of the high voltage.

Selection of Calibration Curve

In the PSE 1500, two standard calibration curves are stored, one for latex spheres (1) and one for liquid droplets (2). Whilst in the utility mode, the current calibration curve number is displayed on line 5. In order to change the calibration curves, key 5 is pressed once. Key 0 will return you to the main menu when pressed.

All the parameters to enter into the data block, making measurement and analysis of the measurement can be done from an external computer as well. The PSE controller contains a hardcopy-program. This means that all displays on the screen can be printed out by pressing the PRINT key. Print out can be interrupted by pressing the CLEAR key.

Appendix D:
Specification of the latex cocktail provided by LGC Promochem

The cocktail should comprise the components (1.0, 2.0 and 5.0 microns latex particles) at number concentrations of 4×10^8 particles ml^{-1}. This number concentration was chosen to produce singlet to multiplet ratio of 0.99 when the suspensions are converted to aerosol form by means of conventional medical nebulisers that produce sprays with droplet volume equivalent diameter and geometric deviation of 3 microns and 2.0 respectively.

Appendix E:
Experimental Procedures for Grade Efficiency Test

1. The glycerol-water mixture is prepared just before the experiment started. 13% glycerol by volume is mixed with 87% distilled water.
2. Make sure the tip of the probe is aligned parallel to the bulk flow in the middle of the inlet/outlet pipe.
3. Make sure the cooling water for the Polytec is turned on before the Polytec is switched on.
4. Polytec is switched on and then the computer. Details on operating the Polytec are available in Appendix F.
5. Fan is switched on and the required flowrate is adjusted using gate valve.
6. The nebuliser is turned on and measurement is taken at inlet.
7. Measurements are taken for 4 minutes.
8. After the inlet measurement is taken, the platform is then raised to take data at both the outlets (vortex finder and disengagement space). The procedure for lifting and lowering the platform is included in Appendix G.
9. Measurements are repeated at various air flowrates to see the effect of air velocity to the separation efficiency.
10. Measurements are repeated for each condition 6 times altogether on different days.
11. The inlet and outlets counts are normalised and the inlet/outlets size distributions are plotted.
12. The grade efficiency for each drop size, η_d, is given by Equation (E.1) where N_{od} and N_{id} is the normalised number of drops of diameter, d, in the outlet and inlet respectively:

$$\eta_d = 1 - \frac{N_{od}}{N_{id}} \qquad \textbf{- Equation (E.1)}$$

Appendix F: Polytec HC-15 Operating Procedure

1. Cooling water for the Polytec is turned on before the Polytec is switched on.
2. Polytec has to be switched on before entering the operating programme in the computer.
3. At c: prompt, type **polytec** to execute the operating programme.
4. Press **1** to run and start the programme.
5. At this stage, make sure that the Polytec is not in data transfer mode. If it is, press the **Clear** key.
6. Press I to initialise the Polytec. When another screen comes up, press **1** to use latex calibration or **2** for water calibration curve.

7. After choosing the calibration curve, a number of options will appear. Press F1 to set the block parameters.
8. Return to main menu when all the blocks have been set up. Press F2 to initiate the measurement.
9. Press 2 for consecutive counting.
10. Always make sure that the Polytec is not in the data transfer mode before hitting any key to start measurement. Press CLEAR if it is in data transfer mode.

Appendix G:
Procedure for lifting and lowering the Polytec platform

Lifting the platform

1. The sampling probe has to be disconnected from the Polytec.
2. The platform is raised using the controller to a distance where the sampling probe can be taken out from the inlet sampling point easily.
3. The sampling probe is placed in the outlet sampling point. Make sure that the probe is pushed to the back of the tube so that it does not block the movement of the platform.
4. The platform should be raised until it is well above the marked position for the outlet sampling point so that the adjustable supports can be locked into position easily.
5. After securing the platform supports, the platform is lowered.
6. The position of the Polytec is adjusted so that it is aligned to the probe position.
7. The sampling probe is connected to the Polytec and measurements can now be taken.

Lowering the platform

1. The sampling probe is disconnected from the Polytec.
2. The platform is raised slightly above the platform supports.
3. The supports are unlocked and are rested at the bottom of the framework.
4. The platform is lowered until the position where the sampling probe can be taken out easily.
5. The probe is then placed at the inlet measuring point. Make sure the probe is pushed to the back of the tube.
6. The platform is lowered until it touched the platform supports at the bottom of the frame.
7. The Polytec position is then adjusted until it is aligned to the sampling probe at the inlet.
8. The sampling probe is then connected to the Polytec before any measurement is taken.

Appendix H:
Video clip showing the frothing zone and the re-entrainment of liquid into the vortex finder of the initial geometry (In CD attached)

Appendix I:
Video clip showing the serious flooding of the vortex finder for Geometry 3a (In CD attached)

Appendix J:
Video clips showing liquid pulsation and re-entrainment of liquid into the vortex finder for Geometry 4 (In CD attached)

Appendix K:
The view of the entire cyclone length of Geometry 7a created in GAMBIT

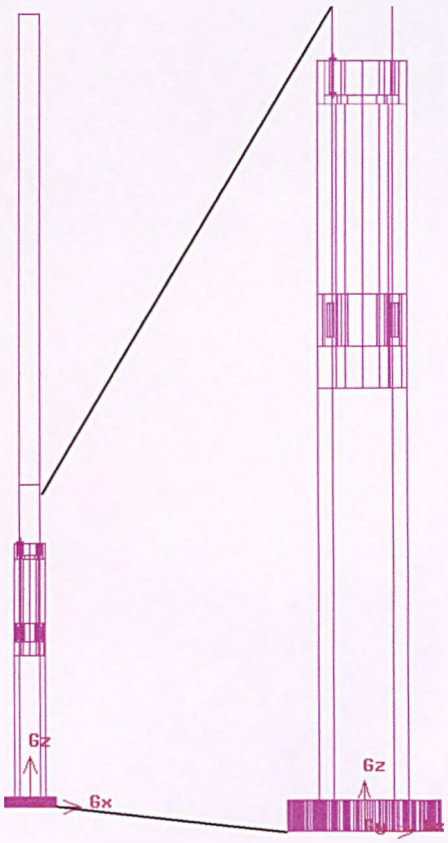

Appendix L:
Dimensions of the reverse flow cyclones investigated by other researchers (Phillips, 1992)

Cyclone Type / Geometry	Stairmand High Flow	Stairmand High Efficiency	Muschelknautz D
Barrel diameter	0.203	0.203	0.3
Gas exit diameter	0.152	0.102	0.1
Gas exit length	0.178	0.102	0.267
Overall height	0.812	0.812	0.72
Barrel length	0.305	0.305	0.22
Entrance height	0.152	0.102	0.157
Entrance width	0.076	0.041	0.045
Dust exit diameter	0.076	0.076	0.2

Appendix M:
Pressure Drop – Flowrate Characteristics of a Geometry Giving 70% Dry Flow Split

The area of the slots in Geometry 7a was further decreased. This geometry with four slots of 3 x 11 mm in the middle of the tube and 2 x 6 mm at the rear gave a dry flow split of 70%. Table M.1 below shows the pressure drop characteristics of this geometry.

Q_S (l/min)	Q_A (l/min)	Q_C (l/min)	ΔP_{Ssa} (cm H2O)	ΔP_{Ssa} (Pa)	ΔP_{Ssc} (cm H2O)	ΔP_{Ssc} (Pa)	U_C (m/s)	U_A (m/s)	0.5*pho* (U_C^2-U_A^2)	% central air outflow
600	180	420	2.4	235.37	2.75	269.69	7.47	0.45	33.37	70.00
800	240	560	4.49	440.33	5.1	500.16	9.96	0.60	59.32	70.00
1000	310	690	7.33	718.85	8.25	809.08	12.27	0.77	90.03	69.00
1200	375	825	10.58	1037.58	11.9	1167.03	14.67	0.93	128.69	68.75
1400	445	955	14.22	1394.56	15.97	1566.18	16.99	1.11	172.40	68.21
1600	490	1110	18.82	1845.68	21.2	2079.08	19.74	1.22	233.01	69.38
1800	555	1245	23.57	2311.51	26.55	2603.76	22.15	1.38	293.11	69.17
2000	600	1400	29.26	2869.53	33.05	3241.21	24.90	1.49	370.75	70.00
2200	650	1550	35.12	3444.22	39.75	3898.28	27.57	1.61	454.52	70.45
2400	720	1680	41.86	4105.21	47.30	4638.71	29.88	1.79	533.87	70.00

Q_S (l/min)	Vel. in the housing, U_S (m/s)	Inlet velocity in 2" pipe, U_{in} (m/s)	ΔP_{TAC} (Pa)	0.5*pho* (U_H^2-U_A^2)	Total Pressure Drop, ΔP_{TSA} (Pa)	0.5*pho* (U_H^2-U_C^2)	Total Pressure Drop, ΔP_{Tsc} (Pa)	Eu_{VF}
0	0	0	0	0	0	0	0	
600	1.23	4.71	0.96	0.79286019	236.16	-32.574309	237.12	7.08
800	1.64	6.28	0.50	1.40952923	441.74	-57.909883	442.25	7.43
1000	2.06	7.85	0.20	2.17979984	721.03	-87.845466	721.23	7.98
1200	2.47	9.42	0.77	3.13061287	1040.71	-125.55607	1041.48	8.06
1400	2.88	10.99	-0.78	4.23660135	1398.79	-168.16568	1398.01	8.07
1600	3.29	12.56	0.40	5.60219578	1851.28	-227.40618	1851.68	7.92
1800	3.70	14.13	-0.86	7.07491649	2318.58	-286.03568	2317.72	7.88
2000	4.11	15.70	0.94	8.80955767	2878.34	-361.93677	2879.28	7.74
2200	4.52	17.27	-0.45	10.7080768	3454.93	-443.80944	3454.47	7.57
2400	4.93	18.83	-0.37	12.685763	4117.90	-521.18895	4117.52	7.68

Table M.1: Pressure characteristics of a cyclone design giving 70% dry flow split.